GFZ Helmholtz Centre Potsdam

Institute of Earth and Environmental Science

Universität Potsdam

Analytical and numerical elastic dislocation models of volcano deformation processes

Mehdi Nikkhoo

May, 2019

Cumulative dissertation
to obtain the academic degree
"doctor rerum naturalium" (Dr. rer. nat.)
in the scientific discipline Geophysics

Submitted to the
Faculty of Mathematics and Natural Sciences
at the University of Potsdam, Germany

Primary advisor: Priv. Doz. Dr. Thomas R. Walter
Co-advisor: Prof. Dr. Torsten Dahm

Reviewers: Dr. François Beauducel
Dr. Matthias Ohrnberger
Priv. Doz. Dr. Thomas R. Walter

Examining committee: Prof. Dr. Bodo Bookhagen
Dr. Matthias Ohrnberger
Priv. Doz. Dr. Thomas R. Walter
Prof. Dr. Max Wilke
Prof. Dr. Gert Zöller

Published online at the
Institutional Repository of the University of Potsdam:
https://doi.org/10.25932/publishup-42972
https://nbn-resolving.org/urn:nbn:de:kobv:517-opus4-429720

Statement of originality

I hereby declare that this thesis is the product of my own work. All the assistance received in preparing this thesis and the sources used have been acknowledged.

Mehdi Nikkhoo Potsdam, May 2019

Abstract

The advances in modern geodetic techniques such as the global navigation satellite system (GNSS) and synthetic aperture radar (SAR) provide surface deformation measurements with an unprecedented accuracy and temporal and spatial resolutions even at most remote volcanoes on Earth. Modelling of the high-quality geodetic data is crucial for understanding the underlying physics of volcano deformation processes. Among various approaches, mathematical models are the most effective for establishing a quantitative link between the surface displacements and the shape and strength of deformation sources. Advancing the geodetic data analyses and hence, the knowledge on the Earth's interior processes, demands sophisticated and efficient deformation modelling approaches. Yet the majority of these models rely on simplistic assumptions for deformation source geometries and ignore complexities such as the Earth's surface topography and interactions between multiple sources.

This thesis addresses this problem in the context of analytical and numerical volcano deformation modelling. In the first part, new analytical solutions for triangular dislocations (TDs) in uniform infinite and semi-infinite elastic media have been developed. Through a comprehensive investigation, the locations and causes of artefact singularities and numerical instabilities associated with TDs have been determined and these long-standing drawbacks have been addressed thoroughly. This approach has then been extended to rectangular dislocations (RDs) with full rotational degrees of freedom. Using this solution in a configuration of three orthogonal RDs a compound dislocation model (CDM) has been developed. The CDM can represent generalized volumetric and planar deformation sources efficiently. Thus, the CDM is relevant for rapid inversions in early warning systems and can also be used for detailed deformation analyses. In order to account for complex source geometries and realistic topography in the deformation models, in this thesis the boundary element method (BEM) has been applied to the new solutions for TDs. In this scheme, complex surfaces are simulated as a continuous mesh of TDs that may possess any displacement or stress boundary conditions in the BEM calculations.

In the second part of this thesis, the developed modelling techniques have been applied to five different real-world deformation scenarios. As the first and second case studies the deformation sources associated with the 2015 Calbuco eruption and 2013–2016 Copahue inflation period have been constrained by using the CDM. The highly anisotropic source geometries in these two cases highlight the importance of using generalized deformation models such as the CDM, for geodetic data inversions. The other three case studies in this thesis involve high-resolution dislocation models and BEM calculations. As the third case, the 2013 pre-explosive inflation of Volcán de Colima has been simulated by using two ellipsoidal cavities, which locate zones of pressurization in the volcano's lava dome. The fourth case study, which serves as an example for volcano-tectonics interactions, the 3-D kinematics of an active ring-fault at Tendürek volcano has been investigated through modelling displacement time series over the 2003–2010 time period. As the fifth example, the deformation sources associated with North Korea's underground nuclear test in September 2017 have been constrained. These examples demonstrate the advancement and increasing level of complexity and the general applicability of the developed dislocation modelling techniques.

This thesis establishes a unified framework for rapid and high-resolution dislocation modelling, which in addition to volcano deformations can also be applied to tectonic and human-made deformations.

Zusammenfassung

Fortschritte in modernen geodätischen Techniken wie dem globalen Navigationssatellitensystem (GNSS) und dem Synthetic Apertur Radar (SAR), liefern Messungen der Oberflächenverformung mit einer beispiellosen Genauigkeit sowie zeitlichen und räumlichen Auflösungen, selbst an abgelegensten Vulkanen. Die Modellierung von hochqualitativen geodätischen Daten ist entscheidend für das Verständnis der zugrundeliegenden Physik der Verformungsprozesse an diesen Vulkanen. Um eine quantitative Verbindung zwischen den Oberflächenverschiebungen und der Form und Stärke von Verformungsquellen herzustellen, sind mathematische Modelle am effektivsten. Die Fortschnitte in geodätischen Datenanalysen und damit das Wissen über die Prozesse im Inneren der Erde erfordern ausgefeilte und effiziente Ansätze der Verformungsmodellierung. Die meisten dieser Modelle beruhen jedoch auf vereinfachten Annahmen der Geometrien der Verformungsquellen und ignorieren Komplexitäten wie die Erdoberflächentopographie und Wechselwirkungen zwischen mehreren Quellen.

Diese Doktorarbeit befasst sich mit diesem Problem im Kontext der analytischen und numerischen Vulkanverformungsmodellierung. Im ersten Schritt wurden neue analytische Lösungen für dreieckige Dislokationen (triangular dislocation-TD) im gleichförmigen elastischen Voll- und Halbraum entwickelt. Durch eine umfassende Untersuchung wurden die Orte und Ursachen von TDs verbundenen Artefaktsingularitäten und numerischen Instabilitäten identifiziert und diese Problematik gelöst. Dieser Ansatz wurde dann auf rechteckige Dislokationen (rectangular dislocation-RD) mit vollen Rotationsfreiheitsgraden erweitert. Unter Verwendung dieser Lösung in einer Konfiguration von drei orthogonalen RDs wurde ein "Zusammengesetztes Dislokationsmodel" (compound dislocation model-CDM) entwickelt. Das CDM kann verallgemeinerte volumetrische und planare Verformungsquellen effizient darstellen. Somit ist das CDM für schnelle Inversionen in Frühwarnungssystemen relevant und kann auch für detaillierte Verformungsanalysen verwendet werden. Um komplexe Quellengeometrien und eine realistische Topographie in den Verformungsmodellen dieser Untersuchung zu berücksichtigen, wurde die Randelementmethode (REM) auf die neuen Lösungen für TDs angewendet. In diesem Schema werden komplexe Oberflächen als ein kontinuierliches Netz von DVs simuliert, die in den REM-Berechnungen beliebige Verschiebungs- oder Spannungsgrenzbedingungen aufweisen können.

Als Beispiele wurden die entwickelten Modellierungstechniken auf fünf verschiedene reale Verformungsszenarien angewendet. Das erste und zweite Beispiel, die Calbuco-Eruption 2015 und die 2013–2016 Copahue-Aufwölbungsperiode, wurden durch die Verwendung des CDM näher beschrieben. Die hoch anisotropen Quellengeometrien in diesen beiden Fällen unterstreichen die Bedeutung der Verwendung verallgemeinerter Verformungsmodelle wie dem CDM für geodätische Dateninversionen. Weitere Fallstudien dieser Doktorarbeit umfassen hochauflösende Versetzungsmodelle und REM-Berechnungen. Die Aufwölbung 2013 am Volcán de Colima wurde simuliert, indem zwei ellipsoidale Quellen verwendet wurden, die Druckzonen im Lavadom des Vulkans lokalisieren. Danach, als Beispiel für Vulkantektonik-Interaktionen, wurde die 3-D-Kinematik einer aktiven Ringstörung am Tendürek-Vulkan durch Modellierung von InSAR-Zeitreihen über die Zeitperiode 2003–2010 simuliert. Als letztes Beispiel wurden die Verformungsquellen, die im Zusammenhang mit Nordkoreas unterirdischem Atomtest im September 2017 stehen, simuliert und der Einsatz der verwendeten Methoden auch in nicht vulkanischen Terrain gezeigt. Diese Beispiele zeigen den Fortschritt und das zunehmende Niveau der Komplexität und die allgemeine Anwendbarkeit der entwickelten Dislokationsmodellierungs-

techniken.

Diese Doktorarbeit unterstreicht die Anwendung von neuer schneller und hochauflösender Dislokationsmodellierung, die neben Vulkanverformungen auch auf tektonische und vom Menschen verursachte Verformungen angewendet werden kann.

Acknowledgment

Firstly, I would like to express my appreciation to my advisor Thomas R. Walter for his valuable advice, his encouragement and his continuous support of my research during my PhD studies. Also, my sincere thanks go to Valerio Acocella and Torsten Dahm for their knowledge and for their kind support.

I am indebted to Eleonora Rivalta, Birger Lühr and Rongjiang Wang for their endless guidance and care and also for being such great mentors and inspirations to me.

I am grateful to Mahmood Mohammad-Karim and Amir M. Abolghasem for their profound belief in my abilities and for the wonderful discussions we had together, all of which inspired me, leading me to pursue a life in science.

Last but not least, I would like to extend my deepest gratitude to all those whose moral support and nurturing, made the completion of this dissertation possible: my friends and colleagues, particularly those in Helmholtzstraße 6/7, and my family, especially my parents.

Contents

Chapter 1

Introduction

1.1 Motivation

Volcanic eruptions, tectonic earthquakes and landslides have caused numerous catastrophes throughout the history and contemporary records and yet continue to do so. These natural hazards have constantly put human lives and civilizations subject to a very high risk in many areas all over the world (Auker et al., 2013; Bilham, 2013). The risk due to these natural hazards is becoming even higher with the growing population of humans in the world. This ever increasing population, within 100 km of active volcanoes alone, is more than 800 million people (Brown et al., 2015). In particular, the large number of inhabitants and infrastructures of the large cities located in areas such as the close vicinity of $\sim$ 600 active volcanoes (Dvorak and Dzurisin, 1997), along the subduction zones and near tectonic faults are susceptible to at least one of these natural hazards. Comprehensive plans for disaster and risk management can save millions of lives and prevent massive economical losses in these areas. Effective forecasting and early warning systems and timely assessment of the mentioned natural hazards are essential for this purpose. All these, however, rely on our understanding of the underlying physical causes, precursors and consequences of these processes. Thus, scientific research in these fields is crucial for a sustainable human life and development.

The driving forces of volcanic eruptions and earthquakes cannot be directly observed, hence any knowledge about these processes can merely be acquired through the causal relationship between the driving forces and the impacts that they have on the Earth's crust. The Earth's crust is made up of various kinds of rocks, which deform whenever they are subjected to surface and body forces (Lisowski, 2007; Dzurisin, 2007; Segall, 2010). The deformation can be observed in the form of relative displacements and rotations of some fixed control points on the rock body. The precision geodetic techniques have enabled us to measure these quantities in a reliable manner, mostly but not exclusively, at the Earth's surface. These deformations may well be related to their underlying forces and described through mathematical models. Depending on the time span of the deformations, the mathematical models simulate the Earth's crust as an elastic, viscoelastic or plastic continuum with some discontinuities, which represent the internal sources of deformation. These models can extrapolate the Earth's deformations in space and time and allow predictions, on the behaviour of the deformation sources in the past and future, to be made. Prerequisite to this, however, is that the models be geologically plausible and consistent with physical grounds, and also be validated through the present-day geodetic observations. Such models can perform as a basis for hazard forecast and assessment in early warning systems in order to decrease the risk and vulnerability associated with volcanic eruptions and earthquakes and also for crisis management and civil protection from these natural disasters.

Thanks to the rapid development of terrestrial and spaceborne geodetic techniques in the recent decades, heterogeneous geodetic observations with unprecedented spatial and temporal

resolutions are being collected worldwide. Amongst the modern geodetic techniques, particularly the global navigation satellite system (GNSS) and interferometric synthetic aperture radar (InSAR) have provided extremely valuable displacement datasets, using which a better understanding of sources of earthquakes and volcanoes has been acquired. These techniques have revolutionized the deformation monitoring of numerous case studies including those in the most remote areas, which is a remarkable achievement especially for volcano geodesy. Maintaining this remarkable quality data collection mechanism continues to be a challenge for volcano geodesy; however, the more important challenge is the data interpretation through deformation modelling (Poland et al., 2006; Fernández et al., 2017).

Volcano deformation may occur due to various magmatic and tectonic processes. Migration of magma and magmatic fluids and heat transfer within the plumbing system of active volcanoes, emplacement of magmatic intrusions and hydro-fractures in the host rock, magmatic extrusions and activation of local tectonic faults and surficial fractures comprise some of these processes, which may produce detectable surface deformation. The geometry, temporal and spatial evolution, physical and chemical characteristics of the magma reservoirs and dynamics of magma transport therein comprise fundamental themes and areas of active research in volcanology (Poland et al., 2006). The main objective of the volcano deformation modelling is to learn about the underlying deformation processes through inferring the location and orientation of their driving internal forces, which form a deformation source, and the intensity thereof. Besides the knowledge on volcanic processes that is acquired through geological and petrological investigations of erupted materials and exposed volcanic reservoirs, respectively, volcano deformation modelling provides constraints on geometry, location and physical and chemical characteristics of magma reservoirs and subsurface magmatic processes that occur beneath active volcanoes (Poland et al., 2006). Techniques such as analogue modelling, which consists of controlled lab experiments using scaled materials that are analogue to those in nature, provide qualitative physical explanations for the processes (see Galland et al., 2015). However, a detailed quantitative analysis and interpretation of the geodetic data relies on mathematical deformation models. These models are mostly developed based on the mathematical theory of linear elasticity (Love, 1944). Applying these models to long-term displacement time series has further improved the understanding of the temporal evolution of deformation sources and their mutual interactions (see Fernández et al., 2017; Dvorak and Dzurisin, 1997). Most of the existing methods for this purpose belong to one of the extreme ends, being either simplistic and fast or sophisticated and slow. However, proper exploitation of the available high-resolution geodetic data can be attained only through intense calculations by using sophisticated methods. These methods must allow implementing complex geometries and physical constraints in the deformation models conveniently. Nevertheless, to achieve this goal new developments in modelling techniques are necessary.

This dissertation is well motivated by the rising demand for developing more flexible and, yet reasonably efficient and rigorous modelling approaches. This includes both analytical and numerical deformation modelling techniques as both of them in essence belong to a more inclusive class of techniques, namely "the quantitative deformation modelling methods". The first step to meet this demand is addressing some long-standing issues in the mathematical formulations of a few analytical models, which as fundamental solutions, form the basis for developing other analytical and numerical modelling techniques. Artefact singularities and numerical instabilities in the associated deformation-field calculations and geometrical limitations in the spatial orientation of the source models comprise some of the challenging issues. The next step is developing sophisticated numerical models, which account for complexities such as mixed displacement and traction boundary conditions, topographic effects and arbitrary magma reservoir geometries and interactions thereof. These numerical models must also be efficient for intense computations. Nevertheless, the main goal is to gain a deeper knowledge

on the physics of volcano deformation processes through developing new modelling techniques. The developments are also intended to enhance the capabilities of a broader audience of Earth scientists in implementing the required physical constraints, routinely, in the crustal deformation models. This way a greater impact on the quality of deformation modelling in the Earth science community, as a whole, and in individual research projects is sought. To achieve this goal, the present work delivers new modelling techniques along with their application to a number of selected example case studies. These real-world examples demonstrate applications of the new modelling techniques to volcano and man-made deformation processes. These techniques with minor modifications can also be applied to earthquake and landslide studies.

The modelling techniques that are developed in this work mainly focus on deformation sources that yield detectable displacements over time periods from a few seconds to some decades. Thus, the deformations that the Earth's crust undergoes over geologic time scales and their respective underlying processes have not been considered.

Similar to other sub-disciplines of geophysics, two general approaches of inverse and forward modelling are used in volcano geodesy to analyse the deformation data. The inverse modelling in volcano geodesy is the process of inferring the shape, location and physical properties of the subsurface deformation sources through inverting the geodetic observations (see Dzurisin, 2007). This involves utilizing linear, and mostly non-linear inversion schemes (see Lisowski, 2007). Forward modelling, however, is used to find a theoretical prediction of the deformation field parameters such as displacements, strains, stresses and so on, that corresponds to some assumed deformation sources and material properties of the crust (see Dzurisin, 2007). The techniques developed in this research contribute to both the inverse and forward modelling applications with knowledge of the crucial role of both of these approaches in volcano geodesy.

The following parts of this chapter give an overview on the principal concepts and general features of analytical and numerical volcano deformation modelling techniques along with advantages and disadvantages of each. Details on more specific contributions of this dissertation and the addressed questions therein conclude this chapter.

1.2 Analytical volcano deformation modelling

Analytical deformation models are closed-form algebraic representations of displacement and strain fields associated with the deformation sources in a usually elastic, or occasionally viscoelastic crust model. The *a priori* geometry and spatial orientation and the force distribution associated with the deformation sources may be modified through some scaling parameters, which are known as the source parameters. The analytical models are multi-variable functions of the source and crust model parameters. The deformation problems, which involve complex source geometries or complex crust models are not algebraically tractable, therefore, analytical models only exist for simple-geometry sources in an isotropic homogeneous crust model. For instance, analytical models of deformation due to pressure change in a magmatic or hydrothermal reservoir are the uniformly pressurized spherical (Mogi, 1958; McTigue, 1987) or ellipsoidal (Davis, 1986; Yang et al., 1988) cavity models in a homogeneous elastic half-space (see Segall, 2010). All of these models, however, are approximate in that they only approximately meet the boundary conditions on the cavity walls. The Mogi (1958) and Davis (1986) models are point-source approximations, which are accurate for simulating only the far-field displacements and stresses associated with the reservoirs. The McTigue (1987) and Yang et al. (1988) models, however, are finite models, which provide estimations of both the near-field and far-field deformations up to a varying level of accuracy that is a function of the depth and dimensions of the reservoir (see Segall, 2010). Other examples of analytical volcano deformation models in a linear elastic half-space are the Bonaccorso and Davis (1999) uniformly expanding open pipe

and uniformly pressurized closed pipe models, which are associated with vertical magma conduits, and the tensile rectangular dislocation (Davis, 1983; Okada, 1985, 1992) and uniformly pressurized penny-shaped crack (Fialko et al., 2001) models, which are associated with thin reservoirs and magmatic intrusions such as dikes, sills and eruptive fissures. A small number of analytical volcano deformation models consider the crust model as a linear viscoelastic half-space (Bonafede et al., 1986; Bonafede and Ferrari, 2009). A more sophisticated model, which is supported by physical arguments and petrological observations is the Dragoni and Magnanensi (1989) finite pressurized spherical cavity that is surrounded by a viscoelastic shell in a linear elastic full-space. The elastic moduli of the viscoelastic shell in this model are different from those of the rest of the full-space. The far-field approximation of the Dragoni and Magnanensi (1989) model has been extended to the half-space (see Bonafede and Ferrari, 2009; Segall, 2010, 2016).

The analytical volcano deformation models divide into the two categories of exact and approximate models. This is merely based on how the mathematical formulation of the models fit the respective model boundary conditions: exactly or approximately. The exact analytical solutions are essential tools in the validation process of other models, including numerical models, and are also the basis for the derivation of the approximate analytical models. However, there are no exact analytical solutions for cavity problems in the half-space. This is a caveat against using these exact solutions for field-based research, where gaining a better insight on the pressurization process of volumetric volcanic reservoirs through their signatures in surface deformations is intended. In such problems, the ability of the analytical model in fitting to the boundary conditions on the cavity walls is of secondary importance, but as a necessity, the model must fit the boundary conditions associated with the stress-free surface of the Earth's crust. Only the approximate analytical models in the half-space meet this requirement. These analytical models, however, have significantly contributed to the research on the sources of volcanic deformations and unrest. Because of their concise formulation, analytical models are especially well-suited for inverse modelling. However, many forward modelling attempts using cavity and conduit models, in some cases combined with analytical solutions for vertical surface loads (see Boussinesq, 1878; Flamant, 1892; Pinel and Jaupart, 2003) that simulates the loading and unloading of volcanic edifices (see Pinel and Jaupart, 2003), have been used to explain the general behaviour of the underlying processes of various volcano deformation scenarios. Some examples of these processes are the formation of cone sheets and ring dikes (Anderson, 1936), the effect of stress concentration on magma reservoir intrusion and extrusion frequencies (Gudmundsson, 1988), the effect of a thermal metamorphic shell on the time-dependent deformation field (Dragoni and Magnanensi, 1989; Segall, 2016), the magma chamber instability and failure (Parfitt et al., 1993; Pinel and Jaupart, 2003, 2005) and the cyclic activity and deformation rate of a magma chamber-conduit system (Maeda, 2000). These models are mostly used to explain the general behaviour of various geological and physical processes. Nonetheless, the distinctive applications and advantages of both categories of analytical models justify undertaking new parallel efforts for addressing possible mathematical shortcomings in their formulation, and developing more flexible analytical models.

A surface of discontinuity in displacements, across which the two sides have been shifted with respect to each other is called a dislocation (see Hirth and Lothe, 1982). In general, dislocation surfaces may have any arbitrary geometry. The angular and polygonal dislocations (Yoffe, 1960; Brown, 1975; Comninou and Dundurs, 1975) are the only family of finite analytical models for which exact closed-form solutions are available in both the full-space and half-space. As a result, dislocations of simple geometry, namely triangular dislocations (Yoffe, 1960; Comninou and Dundurs, 1975) and rectangular dislocations (Okada, 1985, 1992) have been extensively used as basic components in numerical simulations of sources and surfaces of complex geometries (see Jeyakumaran et al., 1992; Kuriyama and Mizuta, 1993; Thomas, 1993; Cayol and Cornet, 1997;

Jónsson et al., 2002; Maerten et al., 2005). Therefore, the dislocation models seem to be a good basis upon which flexible analytical and also numerical volcano deformation frameworks can be established. However, this should be started with validating the existing dislocation models and improving the mathematical formulation of these models to achieve efficient solutions for higher qualities in modelling purposes.

Elastic dislocation modelling

Mathematical elastic volcano deformation models can be expressed in terms of the fundamental solutions for point forces (Kelvin, 1848; Mindlin, 1936) or their derivatives, which are the force couples with or without moment (Mindlin, 1936; Love, 1944) and the double couples (Aki and Richards, 2002). A point dislocation is a certain combination of these force models with a cancelling moment (Aki and Richards, 2002), which simulates the relative motion of two sides of an infinitesimal discontinuity in an elastic medium. The vector which shows the relative motion of the two sides of the dislocation is known as the *Burgers* vector. Any finite dislocation can be considered as a continuous distribution of the basic point dislocations (Aki and Richards, 2002). Thus, the mathematical formulation of a finite dislocation can be derived through integration of the basic point dislocations over the surface of the finite dislocation (Aki and Richards, 2002). Integrating the same point dislocations with a constant Burgers vector over the surface of an angular dislocation, and hence triangular and rectangular dislocations, leads to exact closed-form expressions in both the full-space and half-space (see Yoffe, 1960; Comninou and Dundurs, 1975; Hirth and Lothe, 1982). This has significantly motivated utilizing these finite dislocations as individual magmatic intrusion source models and especially, as fundamental solutions in numerical deformation modelling schemes.

Elastic dislocation models can be further improved at different levels. First, the mathematical imperfections, which may potentially cause numerical instabilities in the calculations associated with the triangular and rectangular dislocations must be addressed. These drawbacks, which were not as evident in the past decades, have emerged with the much higher recent demand for applying high-resolution deformation models more frequently. Second, the straightforward geometrical understanding associated with dislocations explains their extensive applications in deformation models. For the same reason, a unique dislocation model that is capable of simulating both planar intrusions and volumetric volcanic sources of pressurization can be of great interest to the users of the analytical models in the volcano deformation modelling community.

1.3 Numerical volcano deformation modelling

The analytical volcano deformation models are fairly efficient in addressing a wide range of problems. Nevertheless, for many case studies these models can only provide a first-order approximation. For instance, complexities such as the rough topography, material heterogeneity of the host rock, non-planar intrusions, pressurized volcanic cavities of various aspect ratios and sometimes of amorphous geometries and multiple interacting deformation sources, which are common in many volcanic areas, cannot be considered efficiently in analytical models. It can be difficult, or mostly impossible, to find accurate closed-form solutions for these problems, which involve complex geometries and complicated physical boundary conditions that cannot be expressed in terms of simple mathematical equations. These problems can be addressed by making use of the numerical models. These models subdivide the elastic medium into several non-overlapping smaller elements and find an approximate solution for the unknown deformation field parameters within each element for a certain number of representative points

known as the nodes. This is accomplished by solving a linear system of equations in which the known boundary conditions at the nodes of each element are linked to the unknown parameters of all of the nodes in the model. The coefficients of each equation in the linear system are calculated from a simple discretized form of the governing differential or integral equation, or if available, from an analytical solution for each element (see Dieterich and Decker, 1975; Crouch and Starfield, 1983; Cayol and Cornet, 1997).

Numerical models are excellent tools for forward modelling purposes. In these cases, based on some *a priori* knowledge on volcano deformation source geometries and their respective boundary conditions, the deformation field for a limited number of model set-ups is calculated. These models are mostly used to explain the general behaviour of various geological and physical processes. For instance, detailed studies on problems such as the relation between the ratio of horizontal to vertical displacements and the aspect ratios of magma reservoir (Dieterich and Decker, 1975), the effect of rheological layering on the surface deformations (Trasatti et al., 2003; Manconi et al., 2007; Long and Grosfils, 2009), the initiation and evolution of ring-faults and collapse calderas (Komuro et al., 1984; Saunders, 2001; Walter, 2008; Holohan et al., 2011; Grosfils et al., 2015), propagation of dikes and sills (Dahm, 2000; Mériaux and Lister, 2002; Kühn and Dahm, 2004; Maccaferri et al., 2011), emplacement of radial and circumferential dikes (Chestler and Grosfils, 2013; Grosfils et al., 2015), magma chamber instability and failure (Sartoris et al., 1990; Grosfils, 2007; Hurwitz et al., 2009; Long and Grosfils, 2009; Grosfils et al., 2015), stress transfer and interaction of multiple magma bodies (Albino and Sigmundsson, 2014; Pascal et al., 2014), the link between eruptive activity and edifice growth (Pinel et al., 2010), stress trajectories due to edifice loading and formation and propagation of fractures (Chevallier and Verwoerd, 1988; Muller et al., 2001; Grosfils, 2007; Hurwitz et al., 2009), flank instability (Martel and Muller, 2000), have significantly contributed to the knowledge on these volcanic processes. The wide variety of these examples and also the detailed information that they provide reaffirms that the numerical models are indeed superior to the analytical models for forward modelling applications. However, compared to the analytical models, a practical utilization of the numerical volcano deformation models requires a deeper understanding of various technical computational details. Moreover, most of the efficient numerical volcano deformation modelling software are not freely available to the vast majority of scientists. These drawbacks become more noticeable for the inverse modelling applications due to the large number of observation-based case studies.

The finite element method (FEM) and the boundary element method (BEM) are the two most popular and most frequently used numerical methods for volcano deformation studies. As pioneer works in numerical volcano deformation modelling, Dieterich and Decker (1975) used the FEM to study the implications of various magma reservoir geometries in the interpretation of the surface deformations, and Pollard and Holzhausen (1979) used the BEM to study dikes in volcanic rift zones. Similarly, other FEM and BEM simulations have been used to quantify the effects of irregular topographies (Cayol and Cornet, 1998a; Williams and Wadge, 1998; Trasatti et al., 2003; Currenti et al., 2007), viscoelastic shells surrounding magma reservoirs (Newman et al., 2001) and vertical and lateral heterogeneities and rheological layering (Trasatti et al., 2003) on the host rock deformations and gravity changes due to the pressurization of magma reservoirs. In all cases, the accuracy of the numerical models depends on many factors, the most important of which are the size and distribution of the model elements, the number of the representative points on each element and the extent of the discretized area or the model size. Thus, using the numerical models any desirable accuracy is achievable, however, at the expense of longer calculation times. Nonetheless, the experience from many case studies show that the numerical models have proven to be highly flexible and efficient tools that are able to tackle with the wide variety of complexities in volcano deformation modelling.

Besides the flexibility of the numerical models, the technological advancements in remote sensing and the accessible computational power in recent years, have enormously contributed to the growing demand for utilizing the numerical models. The introduction of the spaceborne interferometric synthetic aperture radar (InSAR) to volcano sciences has allowed accurate imaging of the surface deformations at most of the active volcanoes on the planet (Massonnet et al., 1995). These high-resolution images contain millions of data points and allow the detection of sub-centimetre surface movements in the satellite look direction. This abundance of observations has significantly increased the degree of freedom for volcano deformation modelling. Provided that all model parameters are associated with some physical grounds, models with a higher number of free parameters deliver a more accurate interpretation of deformation sources. Davis (1986) showed that a nine-parameter ellipsoidal pressure centre outperforms its four-parameter spherical counterpart, that is the Mogi (1958) model, as the Davis (1986) model fitted the data significantly better and its increased parametrization was justified by an F-test. The Davis (1986) model also provided a more realistic picture of the involved active magmatic and seismic sources of deformation. It is much easier to increase the number of parameters in numerical models, owing to their high flexibility. Physically-guided and properly parametrized numerical models provide the capacity to exploit the deformation data more efficiently. This breakthrough is indeed promoted by the present-day growing computational power and has led to the extraction of detailed source images from the surface deformation data, especially from the SAR imagery (see Amelung et al., 2000; Fukushima et al., 2005; Yun et al., 2006).

The boundary element method

Using the *elastostatic Green's functions*, namely the Kelvin (1848) and Mindlin (1936) fundamental solutions for the elastic full-space and half-space, respectively, the solutions for many elastic models can be represented by an integral over the boundaries of the deformation sources and interfaces in the model (Segall, 2010). In this boundary integral representation the displacement at any point on the boundaries is expressed as a weighted mean of the displacement and stress boundary values, where the weight functions are the traction and displacement fundamental solutions, respectively. For general problems of arbitrary geometries the boundary integrals cannot be performed analytically. Alternatively, rather than finding an exact solution, that is the final displacements everywhere on the boundaries, an approximate solution for a discrete number of points, called nodes, can be sought. To do so, first the boundaries of the model are divided into a number of elements and on each element a certain number of nodes are considered. Using the discretized form of the governing boundary integral equation, the known boundary values at each node are equated with a linear combination of unknown displacements of all nodes. The coefficients of the linear combination, which are referred to as the influence coefficients, are simple functions of the fundamental solutions that are calculated for the nodes of each element. Following the same procedure for all elements and nodes leads to a linear system of equations with the approximate solution to the boundary integral. This numerical scheme of solving the boundary integral is known as the boundary element method (BEM; Sadd, 2009).

The numerical methods such as the finite element method (FEM) use a discrete form of the partial differential equations of elasticity in their formulation and thus, require the discretization of the entire domain and the boundaries in the model. These methods are highly efficient in simulating complex rheological heterogeneities in the medium, however, this is achieved at the expense of long calculation times. By using a boundary integral statement of elasticity, the BEM reduces the discretization and the corresponding calculations only to the boundaries of the model. This also applies to the interfaces between rheological heterogeneities, if they be present in the model. Therefore, for most applications the discretization and geometrical

model set-up associated with a boundary element model is more convenient to perform than that of a finite element model. This is more evident for three dimensional models, where the discretization of volumes and surfaces are required for the finite and boundary element models, respectively.

As mentioned earlier in this section, the calculation procedure with both the finite and boundary element methods leads to a linear system of equations, where the number of equations and unknowns are proportional to the number of elements in the model. Between the finite element and boundary element models of a single case study, the boundary element model often has a smaller number of elements and hence, a much smaller system of equations. Therefore, to achieve any specific level of accuracy for the modelling outputs, the BEM requires a significantly shorter calculation time as compared to the FEM.

In some special formulations of the boundary element method, exact analytical solutions for some finite sources may replace the Kelvin (1848) and Mindlin (1936) fundamental solutions. For instance, the displacement discontinuity method (DDM) is a special case of the BEM in which the exact solutions for finite dislocations are used as the fundamental solutions (Dunbar and Anderson, 1981; Crouch and Starfield, 1983). The dislocations are mostly the *Volterra* type dislocations, which have a uniform slip or more precisely a constant Burgers vector everywhere on their surface (see Volterra, 1907). The centroids of the dislocations in the model are used as the computational nodes of the DDM. Both displacement and traction boundary conditions can be assigned to these nodes. Due to the mathematical structure of the dislocations the displacement boundary conditions are met on the entire dislocation surface, however, the traction boundary conditions are met only at the node on each dislocation, that is the dislocation centroid. As a great advantage, in a displacement discontinuity model both the crack-like and volumetric sources of deformation can be represented by using appropriate meshes of dislocations along with proper boundary values. The open meshes can represent curved surfaces of deformation sources such as magmatic intrusions and faults and fractures, whereas the closed meshes can represent boundaries of volumetric sources such as pressurized cavities and magma reservoirs (see Thomas, 1993; Maerten, 2010). Any polygonal dislocation can be used for constructing these meshes, however the triangular dislocations (Yoffe, 1960; Comninou and Dundurs, 1975; Jeyakumaran et al., 1992; Meade, 2007) are more favourable because by using them any open and closed surfaces of any complex geometry can be simulated without any discontinuity in the final model (see Thomas, 1993; Maerten, 2010).

Computer programs that are based on the BEM and are developed for the geomechanical and crustal deformation studies are commonly either based on the DDM (see Thomas, 1993; Maerten, 2010) or use it to model crack-like sources (see Cayol and Cornet, 1997). In addition to the general advantages of the BEM such as the simple model geometry and the efficiency in fast calculations, the DDM has a few other beneficial factors. The DDM utilizes a universal approach for modelling crack-like and volumetric deformation sources and its fundamental solutions, that are the Volterra dislocations, have a clear geometrical understanding associated with them. This makes the interpretation of the modelling outputs more convenient. Also, the same model set-up that uses the DDM, without any changes, can also use other dislocation modelling techniques such as the distributed slip method. This provides the possibility of integrating some features of these dislocation models in the DDM and vice versa. Because of this clear advantages, the DDM seems to be an appropriate method as a basis for developing modelling software packages that meet the special requirements of the forward and inverse volcano deformation modelling.

1.4 Research questions and outline

This thesis consists of two main parts, which include Chapters 2 and 3 and Chapters 4 to 7, respectively. In Part *I*, considering the present requirements of the volcano deformation modelling problems new solutions for dislocation models have been developed. These solutions build up on earlier works in this field and address some long-standing artefact singularities and geometrical limitations in the mathematical formulations of the triangular and rectangular Volterra (1907) dislocations. These solutions form the basis for analytical compound dislocation models and the displacement discontinuity method, which is a special case of the boundary element method. In Part *II* of this thesis, the newly developed analytical and numerical models have been established for practical applications through applying them to selected real-world case studies in various geological settings.

The main theme of the following chapters ranges from developments in analytical modelling and developments in numerical modelling to the applications of the models to individual ground deformation datasets, respectively. These case studies are mostly, but not exclusively, volcano deformation scenarios. Each of these chapters has already been published as an article in a peer-reviewed journal and therefore can be read through separately. A summary of each chapter and the key research questions of this dissertation are stated in the following:

1. Numerical instabilities and singularities in deformation field calculations associated with triangular and rectangular dislocations have been reported and partly addressed in a few research publications (see Thomas, 1993; Gimbutas et al., 2012; Okada, 1992). These solutions, however, do not address these drawbacks in a comprehensive manner. The validation tests in the early stage of this research, which were conducted on the available solutions for triangular and rectangular dislocations revealed further singularities and numerical instabilities. These issues were evident especially in high-resolution dislocation models that involved a higher number of dislocations. The validation tests led to the conclusion that correcting the mathematical formulation of the dislocation solutions is a necessity for achieving reliable results from the dislocation models, and hence the first research question in this thesis:

   - What are the underlying causes of the singularities and numerical instabilities associated with the mathematical formulation of the triangular and rectangular dislocations and how could these drawbacks be addressed comprehensively?

   In Chapter 2, new analytical solutions for triangular dislocations (TDs) in both full-space and half-space have been elaborated. These solutions are free of the numerical instabilities and the artefact singularities that in other solutions exist, respectively near and on the continuations of the sides and above and beneath the vertices of the triangular dislocations. These artefact-free solutions have been validated by using other well-known analytical solutions. The solutions are scale-independent and can be used in small and large scale problems without any further modification. The MATLAB codes that allow calculation of the displacement and stress fields have been published with this work. Nevertheless, the mathematical and geometrical details of the employed algorithms along with their flowcharts in this chapter allow straightforward computer implementation of the developed algorithms in any other programming language.

2. Rapid inversions of surface displacements to infer the unknown parameters and to interpret the underlying processes of the associated deformation sources are crucial for hazard and risk assessments and early warning purposes in volcanic areas. Due to their concise formulations and fairly short calculation times, analytical deformation models suit this purpose very well. However, selecting the appropriate analytical source model among multiple available

solutions (see Section 1.2; Lisowski, 2007; Dzurisin, 2007) is often challenging. Rectangular dislocations (RDs) have been used as a model for magmatic intrusions (see Segall, 2010). A configuration of three mutually orthogonal tensile dislocations has been shown to have the same far-field displacements as the Mogi (1958) model, that is an isotropic point source (Bonafede and Ferrari, 2009). Therefore, such configurations of dislocation models can potentially simulate volumetric deformation sources. This gives rise to the next question:

- How can a dislocation model be extended to a generalized analytical source model for both planar and volumetric deformation sources? Does the application of generalized source models to volcano deformations lead to significant improvements in our understanding of physical processes in magmatic and hydrothermal systems?

In Chapter 3, the work in Chapter 2 has been extended to new solutions for rectangular dislocations with full rotational degrees of freedom. Using these new solutions in a configuration of three mutually orthogonal tensile dislocations a new compound dislocation model (CDM) has been developed. Replacing the finite dislocations in the CDM configuration with point tensile dislocations, the point-source version of the CDM, that is referred to as the *point CDM*, has also been developed. It has been shown that both of these models can represent pressurized ellipsoidal cavities of any aspect ratios in the far field and that the CDM can also represent simple planar intrusions in the near field. After discussing the range of applicability of the CDM and point CDM in detail, these models have been applied to the 2015 co-eruptive surface displacements of Calbuco volcano in Chile. The modelling outputs have been then compared with those of other simple analytical sources and the implications have been discussed. The MATLAB codes associated with the CDM and point CDM have been published with this chapter.

In Chapter 4, the details and implications of the deformation source models associated with the inflation period from 2011 to 2016 at Copahue volcano, located on the edge of the Agrio-Caviahue caldera along the border between Chile and Argentina, have been discussed. The time-series of the surface displacements have been derived from satellite and airborne synthetic aperture radar (SAR) imagery through applying interferometric techniques. The posterior probability density functions (PDFs) of the source parameters have been estimated by applying the compound dislocation models (CDMs) to the displacement rates in a Bayesian inference approach based on the Markov Chain Monte Carlo (MCMC) sampling. The spatial distribution of the volcano tectonic earthquakes and the surface fault motion in the region have been compared with the location and orientation of the deformation sources and the consequent Coulomb stress change, respectively. The deformation model that consists of two CDMs roughly images the active part of the magmatic plumbing system in Copahue volcano as a narrow transfer region between a deeper, unresolved magma reservoir beneath the caldera and a shallow reservoir beneath Copahue's summit.

3. Precise calculations of volcano deformations often rely on accounting for realistic surface topography, complex source geometries and interactions between multiple sources in deformation models. These complexities are present in the majority of volcanic areas and their influence on the deformation field parameters may be very significant (see Cayol and Cornet, 1998a,b; Pascal et al., 2014). This is especially relevant for the case studies that involve shallow deformation sources and steep-sided flanks (see Cayol and Cornet, 1998a; Segall, 2010). The main questions in this regard are:

   - How does accounting for the mentioned complexities in deformation models improve the inferred picture of underlying volcano deformation processes? Can high-resolution dislocation models account for these complexities in an efficient manner?

In Chapter 5, the displacement discontinuity method based on the new TD solution developed in Chapter 2 has been applied to the 2013 pre-explosive surface deformation of the summit of Vólcan de Colima in Mexico. The geometry of the conduit system within the "perched" lava dome has been inferred through inverse modelling of the surface displacements, which have been estimated through interferometric processing of a pair of satellite synthetic aperture radar (SAR) images. The data inversion has been performed by using the genetic algorithm method. The deformation modelling suggests that the surface deformation had most likely been due to the pressurization of a shallow source within the dome and a deeper source beneath the summit centre at the upper conduit. This deformation model is also backed by the location, intensity and frequency of the summit explosions that are recorded through optical imagery.

In Chapter 6, dislocation modelling of interferometric synthetic aperture radar (InSAR) time-series and sandbox analogue modelling of caldera collapse processes along with the field constraints on the geological structures have been used to investigate the three dimensional geometry of an active caldera ring-fault at Tendürek volcano in Turkey. For this purpose, using the displacement discontinuity method based on the new TD solution in Chapter 2 and the genetic algorithm, the InSAR time-series have been inverted for the deformation source parameters. In these models, the geometrical degrees of freedom for the ring-fault have been constrained through the outcomes of the sandbox experiments and other geological evidences from similar case studies. Also, the shape of the upper rim of the ring-fault has been constrained with the mapped surface fractures and displacement residuals of previous analytical source models. It has been shown that the subsidence and westward motion of a large area that encompasses the volcano edifice may have been promoted by the compaction or contraction of a deep reservoir along with the slip on a ring-fault that is composed of outward-inclined reverse segments on the western flanks and inward-inclined normal segments on its eastern flanks of Tendürek.

4. Scientific investigations on the crustal deformations due to volcanic activities, earthquakes and human activities, collectively benefit from dislocation theory (see Lisowski, 2007; Segall, 2010). Therefore, the dislocation modelling techniques, which are developed for volcanic applications in this dissertation may also be applicable to crustal deformations of other origins. Analogies between the underlying processes of such crustal deformations and their volcanic counterparts have been shown to provide significant implications and feedback for volcano deformation studies (see Howard, 2010). This gives rise to the following questions on the range of applicability of the new dislocation models:

   - To what extent the findings of this research on volcano deformation modelling can be generalized and extended to other crustal deformation studies?

   In Chapter 7, elastic dislocation models and seismic focal mechanism solutions have been developed and jointly analyzed to decipher the nature of multiple processes associated with the 3 September 2017 underground nuclear test in North Korea. The 3-D surface displacements have been measured through applying the pixel offset tracking technique to 4 tracks of high-resolution spotlight images acquired by the German TerraSAR-X satellite. Using a sophisticated dislocation model based on both the new TD solutions and the CDM developed in Chapters 2 and 3, respectively, the horizontal location and depth of the detonation chamber have been constrained. It has been shown that the observed displacement field is due to cumulative effects of inflation, collapse and compaction processes at the explosion site over the $\sim$1 week period of time right after the explosion. The analysis of seismic data from local and regional seismic records has revealed the full moment tensor solutions associated with the explosion and collapse events, the relative horizontal location of these two events

and the explosive yield of the nuclear device. The remarkable agreement between the the geodetic and seismic analyses' results demonstrates the capability of unravelling complex deformation processes through joint modelling of the data from SAR imagery and seismic networks.

In Chapter 8, the concluding remarks of this thesis and the outlook for the future research have been mentioned.

1.5 Author's contributions and publications

The chapters 2-7 of this thesis are each a peer-reviewed article in a scientific journal. These articles and the author's contributions therein are listed below:

- Chapter 2:

  Nikkhoo, M., Walter, T. R. (2015): Triangular dislocation: an analytical, artefact-free solution. - Geophysical Journal International, 201 (2), 1117-1139. doi:10.1093/gji/ggv035

  - The author, MN, developed the mathematical concepts in this article and prepared the associated MATLAB codes and wrote up the manuscript, implementing comments from his Ph.D. adviser and co-author, TRW.

- Chapter 3:

  Nikkhoo, M., Walter, T. R., Lundgren, P. R., Prats-Iraola, P. (2017): Compound dislocation models (CDMs) for volcano deformation analyses. - Geophysical Journal International, 208 (2): 877-894. doi:10.1093/gji/ggw427

  - The author, MN, developed the mathematical concepts in this article and prepared the associated MATLAB codes and wrote up the manuscript, implementing comments from his Ph.D. adviser and co-author, TRW. The other co-authors PRL and PP-I processed and commented on the InSAR data, which is used in this article.

- Chapter 4:

  Lundgren, P., Nikkhoo M., Samsonov S. V., Milillo P., Gil-Cruz F., Lazo J. (2017): Source model for the Copahue volcano magma plumbing system constrained by InSAR surface deformation observations. - Journal of Geophysical Research. Solid Earth, 122, 5729-5747. doi:10.1002/2017JB014368

  - This article is another application of the CDM, which is elaborated on in Chapter 3 of this thesis. Together with PL, the first author of this article, MN did the modelling. MN also contributed to the figures and discussions on the results and implications of this study.

- Chapter 5:

  Salzer, J. T., Nikkhoo, M., Walter, T. R., Sudhaus, H., Reyes-Dávila, G., Bretón, M., Arámbula, R. (2014): Satellite radar data reveal short-term pre-explosive displacements and a complex conduit system at Volcán de Colima, Mexico. - Frontiers in Earth Science, 2, p. 1-11; doi:10.3389/feart.2014.00012

  - This article is the first application of the TDs, which is discussed in Chapter 2 of this thesis. MN did the modelling of this work and contributed to the modelling-related text and figures as well as the discussions on the modelling results.

- Chapter 6:

  Bathke, H., Nikkhoo, M., Holohan, E., Walter, T. R. (2015): Insights into the 3D architecture of an active caldera ring-fault at Tendürek volcano through modelling of geodetic data. - Earth and Planetary Science Letters, 422, 157-168; doi:10.1016/j.epsl.2015.03.041

  - This article is another application of the TDs, which is discussed in Chapter 2 of this thesis. Together with HB, the first author of this article, MN did the modelling. MN also contributed to the text and figures and discussions on the results and implications of this study.

- Chapter 7:

  Wang, T., Shi, Q., Nikkhoo, M., Wei, S., Barbot, S., Dreger, D., Bürgmann, R., Motagh, M., Chen, Q.-F. (2018): The rise, collapse, and compaction of Mt. Mantap from the 3 September 2017, North Korean nuclear test. - *Science*, 361, No. 6398, 166-170; doi:10.1126/science.aar7230

  - This article is another application of both the TDs and the CDM, which are discussed in Chapters 2 and 3 of this thesis, respectively. Together with SB, another co-author of this article, MN did the modelling of the geodetic data. MN also contributed to the modelling-related text and figures and discussions on the results and implications of this study.

The following works have benefited from the author's contribution and have been published in the course of his Ph.D. research, however, they are not included as a part of this thesis:

- Prats-Iraola, P., Nannini, M., Yague-Martinez, N., Scheiber, R., Minati, F., Vecchioli, F., Costantini, M., Borgstrom, S., De Martino, P., Siniscalchi, V., Walter, T. R., Nikkhoo, M., Foumelis, M., Desnos, Y. (2016): Sentinel-1 tops interferometric time series results and validation. - 2016 IEEE International Geoscience and Remote Sensing Symposium (IGARSS) : proceedings; July 10-15, 2016, Beijing, China, IEEE, p. 3894-3897. doi:10.1109/IGARSS.2016.7730011

- Richter, N., Nikkhoo, M., de Zeeuw-van Dalfsen, E., Walter, T. R. (2016): Terrestrial laser scanner data covering the summit craters of Láscar Volcano, Chile. GFZ Data Services: Potsdam doi:10.5880/GFZ.2.1.2016.002

- Sharifi, M., Forootan, E., Nikkhoo, M., Awange, J., Najafi-Alamdari, M. (2013): A pointwise least squares spectral analysis (LSSA) of the Caspian Sea level fluctuations, using TOPEX/Poseidon and Jason-1 observations. - Advances in Space Research, 51, 5, pp. 858-873; doi:10.1016/j.asr.2012.10.001

- Abbaszadeh, M., Sharifi, M., Nikkhoo M. (2013), A comparison of the estimated effective elastic thickness of the lithosphere using terrestrial and satellite-derived data in Iran, Acta Geophysica, 61, 3; doi:10.2478/s11600-012-0089-6

Part I

Method development

Chapter 2

Triangular dislocation: an analytical artefact-free solution

Abstract

Displacements and stress-field changes associated with earthquakes, volcanoes, landslides and human activity are often simulated using numerical models in an attempt to understand the underlying processes and their governing physics. The application of elastic dislocation theory to these problems, however, may be biased because of numerical instabilities in the calculations. Here, we present a new method that is free of artefact singularities and numerical instabilities in analytical solutions for triangular dislocations (TDs) in both full-space and half-space. We apply the method to both the displacement and the stress fields. The entire 3-D Euclidean space $\mathbb{R}^3$ is divided into two complementary subspaces, in the sense that in each one, a particular analytical formulation fulfils the requirements for the ideal, artefact-free solution for a TD. The primary advantage of the presented method is that the development of our solutions involves neither numerical approximations nor series expansion methods. As a result, the final outputs are independent of the scale of the input parameters, including the size and position of the dislocation as well as its corresponding slip vector components. Our solutions are therefore well suited for application at various scales in geoscience, physics and engineering. We validate the solutions through comparison to other well-known analytical methods and provide the MATLAB codes.[1]

[1]Originally published as: Nikkhoo, M., Walter, T. R. (2015): Triangular dislocation: an analytical, artefact-free solution. - Geophysical Journal International, 201 (2), 1117-1139. doi:10.1093/gji/ggv035

2.1 Introduction

Crustal deformations associated with earthquakes, volcanoes, landslides and human activities can be observed at a high level of detail using modern geodetic techniques, including synthetic aperture radar interferometry (InSAR) and GPS (Segall, 1997; Bürgmann et al., 2000). These deformation data are often analysed using modelling techniques that are typically very computationally intense. The primary objective of such modelling is to understand the underlying processes through indirect imaging of the so-called sources, such as seismogenic faults, magma chambers and other reservoirs. The position and geometry of these sources, as well as the slip or the forces acting on them, are typically regarded as the source parameters. The source parameters, in other words, the outputs of the implemented modelling, are relevant to earthquake aftershock studies, the assessment of volcanic eruption precursors, tsunami modelling and many other applications (Feigl et al., 2002).

The majority of methods that are applied for crustal deformation modelling are based on the theory of elasticity in general and the concept of dislocations in particular (Segall, 2010). Elastic dislocation theory concerns the state of deformations in a strained solid body that is subject to the action of a dislocation embedded inside it (Love, 1944). The Volterra model (Volterra, 1907) describes a dislocation as a surface of displacement discontinuity with a uniform distribution of the slip throughout. The edges of the Volterra dislocation, also known as dislocation lines, are intrinsic singularities because of their corresponding displacements, which are essentially indeterminate (Steketee, 1958). Consequently, the displacements, strains and stresses are singular on the dislocation lines, and numerical calculations are instable in the vicinity of these singularities.

Apart from these singular dislocation lines and their differential neighbourhoods, the analytical solutions of the general Volterra dislocations are continuous and well-behaved functions elsewhere, including the dislocation surface itself (Segall, 2010). In geophysics, Volterra's dislocation theory is therefore used extensively, following the Green's function method of Steketee (1958), which describes a general point-source dislocation in an isotropic elastic half-space.

Integration of the fundamental point-source dislocations gives rise to analytical solutions for finite dislocations such as rectangular dislocations (RDs; Okada, 1992) or triangular dislocations (TDs; Jeyakumaran et al., 1992; Meade, 2007). Since the derivation of these solutions, they have been used directly as simple analytical models and also as the basis for more sophisticated numerical models, such as distributed slip models (Wald and Heaton, 1994) and the boundary element method (BEM; Cayol and Cornet, 1997). The possibility of simulating any arbitrarily curved surface in terms of a continuous triangular mesh is a clear advantage of the implementation of the TD approach over the RD approach and has led to the consideration of complex dislocation geometries (Maerten et al., 2005; Meade, 2007).

However, the existence of the artefact singularities and numerical instabilities that affect the calculation of the displacements and stresses associated with a TD has posed an obstacle to the geometrical flexibility and applicability of TDs. The more TDs are present in a model, the higher is the probability of obtaining erroneous results at various calculation points. Therefore, an artefact-free solution for TDs is of great relevance. In contrast to the intrinsic singularities, there is no theoretical basis to explain the artefact singularities, which are produced only through imperfections in numerical calculation. The analytical solutions for TDs are derived either through direct analytical integration over the surface of the triangle (Crouch and Starfield, 1983) or by superposing basic dislocations with known analytical solutions, as has been considered for segment dislocation in a full-space (Hirth and Lothe, 1982), angular dislocation in a full-space (Yoffe, 1960) and angular dislocation in a half-space (Comninou and Dundurs, 1975). A general problem that is encountered in either case, however, is related to the artefact singularities and numerical instabilities that lie along the sides of a TD in full-space and also below

and above the vertices of a TD in a half-space. Despite a few previous attempts, in which either the artefact singularities have been addressed only in part (Thomas, 1993) or a combination of analytical and numerical quadrature rules along with a Taylor series expansion has been proposed to approximately correct for the effects of the artefact singularities (Gimbutas et al., 2012), the problem of artefact singularities for TDs has not yet been analytically addressed. Cai et al. (2006) have summarized some methods that attempt to address the intrinsic singularities and have also developed a novel, elegant formulation for the stress field of a segment dislocation in a full-space. Although this solution is free of intrinsic and artefact singularities, it lacks the displacement equations and is not applicable to a half-space (Cai et al., 2006).

In this paper, we present a fully analytical, artefact-free solution for the displacement and the strain and stress fields associated with a TD in a full-space and half-space. This paper is organized as follows:

First, we generalise the solution, following (Yoffe, 1960), to a generic TD in a full-space and elaborate on the necessary coordinate systems and transformations. Secondly, we address the problem of artefact singularities and numerical instabilities along with presenting the analytical solution for a TD in a full-space (Yoffe, 1960). We then use the full-space artefact-free solution to develop an analytical artefact-free solution for a TD in a half-space. Finally, we evaluate our solution through comparison to other analytical solutions for finite dislocations, followed by a discussion section.

2.2 A triangular dislocation in a full-space

The full-space solution is a relatively simple model that not only can be directly used in several geophysical applications but also is the basis for the more realistic half-space model (Comninou and Dundurs, 1975). Additionally, as the basis for numerical approaches such as the BEM, the full-space solution can be used to simulate realistic topography in related models (Cayol and Cornet, 1997). Here, we develop a generic solution for a triangular dislocation (TD) in a full-space as a superposition of three angular dislocations, following Yoffe (1960), and elaborate on the necessary coordinate systems and the coordinate transformations between them. The implemented coordinate transformation scheme, which is the most fundamental concept underlying the development of the solution, is detailed in Appendix 2.A. We also develop a so-called 'alternative solution' that is equivalent to the first solution but possesses singularities along completely different directions. Using a geometric technique, we present an artefact-free solution that is a combination of these two equivalent solutions. Improvements on the Burgers function equation are used in the displacement calculations associated with a TD. These new improvements allow for faster calculations and eliminate the numerical instabilities in the calculation of the Burgers function in the Yoffe (1960) solution.

2.2.1 The general solution for a TD in a full-space

2.2.1.1 The structure of the solution

An angular dislocation is composed of two semi-infinite straight dislocation lines that meet at the point of origin (Fig. 2.1a). The analytical solution of an angular dislocation in a full-space was first developed by Yoffe (1960), employing Burgers' method (Burgers, 1939). The equations of the displacement and stress field of an angular dislocation, which we have corrected for a few misprints, are provided in Appendix 2.B accompanying this paper. These equations are valid in the angular dislocation coordinate system (ADCS), which is a right-handed Cartesian coordinate system with the x-axis normal to the page (Fig. 2.1a). Here, the coordinates of the Burgers vector of the angular dislocation represented by (b_x, b_y, b_z) are composed of the opening

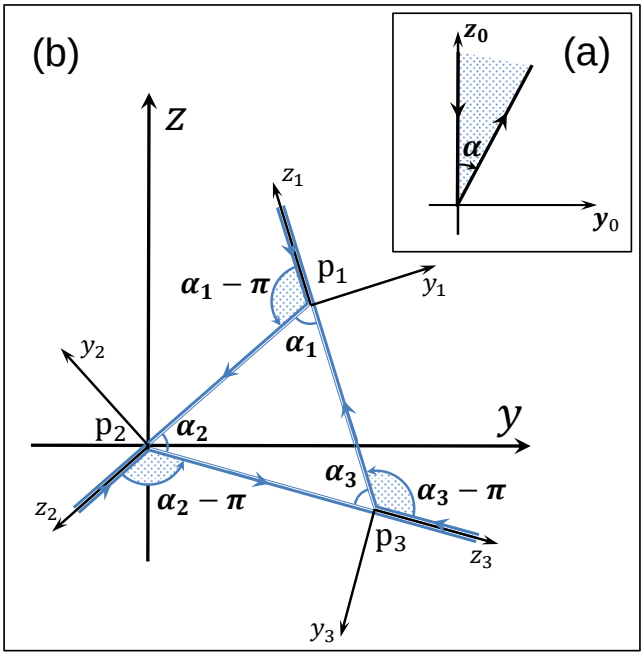

Figure 2.1: (a) Angular dislocation in a full-space following Yoffe (1960); the x_0 axis is perpendicular to the plane and forms a right-handed coordinate system. The angle α is measured clockwise. (b) Yoffe (1960) configuration for a triangular dislocation (TD) in a full-space. It consists of the three angular dislocations that form the external angles of the triangle $P_1P_2P_3$. The third axis of each angular dislocation coordinate system (ADCS) lies along one side of the TD, and the first axis of each of these right-handed coordinate systems is perpendicular to the plane. The x-, y- and z-axes of the triangular dislocation coordinate system (TDCS) are normal to the plane, parallel to the strike direction and parallel to the dip vector, respectively. The vertex P_2 of the TD is the origin of the TDCS.

and slip components along the y and z directions, respectively. The Burgers vector, also known as the slip vector, essentially represents the relative motion of the two sides of a dislocation.

Yoffe (1960) also derived the first analytical solution for a particular case of an equilateral TD in a full-space by superposing the displacement and stress fields of the three angular dislocations that form the exterior angles of the TD (Fig. 2.1b). All three angular dislocations share the same slip vector, which is the slip vector of the TD. Here, we generalize the solution, following Yoffe (1960), to a generic TD in a full-space and elaborate on the details of our work.

We specify the components of the slip vector of the TD, that is the strike slip, the dip slip and the opening, with respect to the triangular dislocation coordinate system (TDCS). The TDCS is a right-handed Cartesian coordinate system with the second vertex of the TD as its origin (Fig. 2.1b). The y-, z- and x-axes of the TDCS align with the strike, dip and normal to the TD directions. We consider the same conventions for the strike, dip and normal directions that are defined for an RD (Okada, 1985) to facilitate comparison with the RD case. For the vertices of the TD, however, as well as the calculation points, the coordinates are given in an Earth-fixed coordinate system (EFCS) with the X- and Y-axes pointing towards the east and north, respectively, and the Z-axis pointing upwards. The diagram presented in Fig. 2.2 summarizes all necessary coordinate transformations used in this paper. Here, we first transform the coordinates of the calculation points and the TD vertices from the EFCS into the TDCS. The next step is to transform the coordinates of the calculation points and the components of the TD slip vector from the TDCS into each ADCS separately. Then, it is possible to calculate the displacement and stress fields of each angular dislocation in its own ADCS, which, in the next step, are all transformed back into the TDCS. As the final step, after superposing the contributions of all three angular dislocations, we transform the displacement and stress field of the TD into the EFCS.

2.2.1.2 The implementation procedure

We adopt $\{\vec{e}_X, \vec{e}_Y, \vec{e}_Z\}$ as the basis for the EFCS, $\{\vec{e}_n, \vec{e}_s, \vec{e}_d\}$ as the basis for the TDCS, and, finally, $\{\vec{e}_{x_1}, \vec{e}_{y_1}, \vec{e}_{z_1}\}$, $\{\vec{e}_{x_2}, \vec{e}_{y_2}, \vec{e}_{z_2}\}$ and $\{\vec{e}_{x_3}, \vec{e}_{y_3}, \vec{e}_{z_3}\}$ as the bases for the three ADCSs. To apply the transformations illustrated in Fig. 2.2, we first determine the necessary transformation matrices (Appendix 2.A). We also adopt the right-hand rule, that is when the curl of the fingers of the right hand represents the vertex ordering, then the normal vector of the TD points along the thumb. Therefore, if $\vec{r}_{P_1}$, $\vec{r}_{P_2}$ and $\vec{r}_{P_3}$ are the position vectors of the TD vertices in the EFCS, then the normal vector can be defined as $\vec{e}_n = (\vec{r}_{12} \times \vec{r}_{13}) / \|\vec{r}_{12} \times \vec{r}_{13}\|$, which is the normalized cross product of the vectors $\vec{r}_{12} = \vec{r}_{P_2} - \vec{r}_{P_1}$ and $\vec{r}_{13} = \vec{r}_{P_3} - \vec{r}_{P_1}$, that is the vectors along the P_1P_2 and P_1P_3 sides, respectively. The unit strike vector is then defined as $\vec{e}_s = (\vec{e}_Z \times \vec{e}_n) / \|\vec{e}_Z \times \vec{e}_n\|$. Finally, $\vec{e}_d = \vec{e}_n \times \vec{e}_s$ represents the unit dip vector. As a result, the transformation matrix for the direct transformation from the TDCS into the EFCS will be

$$A_{TE} = \begin{pmatrix} X_n & X_s & X_d \\ Y_n & Y_s & Y_d \\ Z_n & Z_s & Z_d \end{pmatrix}. \tag{2.1}$$

The three columns of A_{TE} are the coordinates of the vectors $\vec{e}_n$, $\vec{e}_s$ and $\vec{e}_d$ in the EFCS. Recall that the origin of the TDCS is the second vertex of the TD, which is P_2; thus, the translation matrix for the direct position vector transformation in eq. (2.A.4) is $r_{P_2} = (X_{P_2}\, Y_{P_2}\, Z_{P_2})^T$, which is precisely the coordinates of P_2 in the EFCS. For the inverse transformation in this case, we use eq. (2.A.5) and eq. (2.A.9) for the free vectors and the position vectors, respectively. For the transformation of the strain and stress tensors, eq. (2.A.10) is used.

To use the equations associated with each angular dislocation, we must transform the coordinates of the calculation points and the TD slip vector from the TDCS to each ADCS. Because the TDCS and the ADCS share the same x-axis, it is obvious that $\vec{e}_{x_1} = \vec{e}_n$. Moreover, from the configuration of the TD in Fig. 2.1(b), it is clear that $\vec{e}_{z_1}$ is aligned with the P_3P_1 side and thus that $\vec{e}_{z_1} = \vec{r}_{31} / \|\vec{r}_{31}\|$, where $\vec{r}_{31} = \vec{r}_{P_1} - \vec{r}_{P_3}$. Because the ADCS as a right-handed coordinate system, we can write the third equation as $\vec{e}_{y_1} = \vec{e}_{z_1} \times \vec{e}_{x_1}$. The columns of the transformation matrix A_{AT_1} for the direct transformation from the first ADCS into the TDCS are the coordinates of $\vec{e}_{x_1}$, $\vec{e}_{y_1}$ and $\vec{e}_{z_1}$ in the TDCS:

$$A_{AT_1} = \begin{pmatrix} 1 & 0 & 0 \\ 0 & z_{P_1} - z_{P_3} & y_{P_1} - y_{P_3} \\ 0 & y_{P_3} - y_{P_1} & z_{P_1} - z_{P_3} \end{pmatrix}. \tag{2.2}$$

A_{AT_2} and A_{AT_3}, which correspond to the second and third ADCSs, are defined similarly. As the origins of the ADCSs are the vertices of the TD (Fig. 2.1b), the translation matrices in eq. (2.A.4) will be the coordinates of $\vec{r}_{P_1}$, $\vec{r}_{P_2}$ and $\vec{r}_{P_3}$ in the TDCS. For the inverse transformations in these cases, we also use eqs (2.A.5) and (2.A.9) for the free vectors and the position vectors, respectively. For the transformation of the strain and stress tensors, we again use eq. (2.A.10).

The size of the angle with the appropriate algebraic sign is the final input parameter that we need to calculate for each angular dislocation. The internal angles of the TD can be calculated as follows:

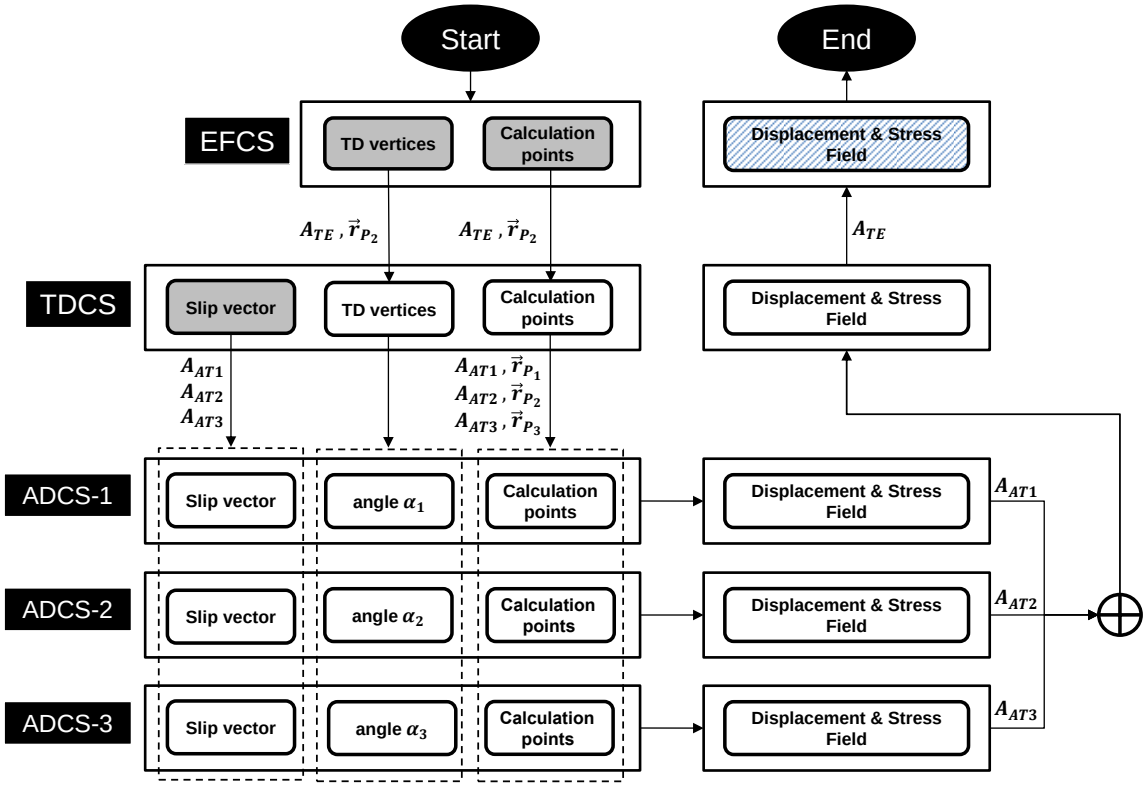

Figure 2.2: Flowchart for calculating the displacement and stress field of a triangular dislocation (TD) in an Earth-fixed coordinate system (EFCS) using the full-space Yoffe (1960) solution. The black box at the left side of each row specifies the coordinate system corresponding to that row. The grey boxes represent the inputs, and the blue box represents the final output. The coordinates of the calculation points and the TD vertices are first transformed from the EFCS into the triangular dislocation coordinate system (TDCS) using A_{TE} and $\vec{r}_{P_2}$ in eq. 2.A.9. These coordinates, along with the slip vector, are then transformed into each angular dislocation coordinate system (ADCS) (see eqs 2.A.9 and 2.A.5 in Appendix 2.A). After the contribution of each angular dislocation is calculated, the results are transformed into the TDCS (see also eqs 2.A.4 and 2.A.10 in Appendix 2.A). Finally, the superposition of the results is transformed into the EFCS.

$$\begin{aligned}\alpha_1 &= \cos^{-1}\left(\vec{e}_{12}\cdot\vec{e}_{13}\right)\\ \alpha_2 &= \cos^{-1}\left(\vec{e}_{21}\cdot\vec{e}_{23}\right)\\ \alpha_3 &= \cos^{-1}\left(\vec{e}_{13}\cdot\vec{e}_{23}\right),\end{aligned}$$

where

$$\begin{aligned}\vec{e}_{12} &= \left(\vec{r}_{P_2}-\vec{r}_{P_1}\right)/\left\|\vec{r}_{P_2}-\vec{r}_{P_1}\right\|\\ \vec{e}_{13} &= \left(\vec{r}_{P_3}-\vec{r}_{P_1}\right)/\left\|\vec{r}_{P_3}-\vec{r}_{P_1}\right\|\\ \vec{e}_{23} &= \left(\vec{r}_{P_3}-\vec{r}_{P_2}\right)/\left\|\vec{r}_{P_3}-\vec{r}_{P_2}\right\|\end{aligned}$$

are the unit vectors along the sides of the TD and '.' represents the dot product of the vectors. The angles that must be used in the calculations are the supplementary angles of α_1, α_2 and α_3 measured clockwise, that is $\alpha_1-\pi$, $\alpha_2-\pi$ and $\alpha_3-\pi$, respectively (Fig. 2.1b).

Now, we calculate the 'incomplete' displacements (see Appendix 2.B) and the stresses associated with each angular dislocation using eqs (2.B.2) and (2.B.4), respectively. Subsequently, after transforming the results from each ADCS into the TDCS, we calculate the complete displacements as follows:

Table 2.1: The parameters of the two configurations illustrated in Fig. 2.3.

	Angular dislocation vertex	Input angle	z-axis direction
Config-1	P_1	$-\pi+\alpha_1$	P_3P_1
	P_2	$-\pi+\alpha_2$	P_1P_2
	P_3	$-\pi+\alpha_3$	P_2P_3
Config-2	P_1	$-\pi+\alpha_1$	P_1P_3
	P_2	$-\pi+\alpha_2$	P_2P_1
	P_3	$-\pi+\alpha_3$	P_3P_2

$$
\begin{aligned}
u &= b_x\varphi_{TD} + \sum_{i=1}^{3} u_i^0 \\
v &= b_y\varphi_{TD} + \sum_{i=1}^{3} v_i^0 \\
w &= b_z\varphi_{TD} + \sum_{i=1}^{3} w_i^0,
\end{aligned} \tag{2.3}
$$

where u_i^0, v_i^0 and w_i^0 are the components of the incomplete displacements of the i-th angular dislocation and φ_{TD} is the Burgers function (Burgers, 1939) that corresponds to the TD. We elaborate on the calculation of φ_{TD} in Section 2.2.3. Note that in eq. (2.3), we use the components of the slip vector and the incomplete displacement vector in the TDCS. The outcome of this step is the displacement and stress fields of the TD in the TDCS. As a final step, we transform these results into the EFCS.

2.2.2 Developing an artefact-free solution for a TD in a full-space

The analytical solutions for a TD in a full-space contain artefact singularities on the extensions of the sides of the TD (Kuriyama and Mizuta, 1993). Similar difficulties also exist in the general solution of the previous section. In the following, we describe a geometric method for developing a fully analytical solution that is free of such artefact singularities.

The semi-infinite dislocation lines with opposite polarities that are shown in Fig. 2.1(b) must theoretically cancel each other outside the TD. However, because the contribution of each angular dislocation is calculated separately, the singular terms in the displacement and stress equations remain in the final results, giving rise to artefact singularities. Moreover, each dislocation line possesses a $1/r$ singularity, where r is the distance from the dislocation line (Segall, 2010). Therefore, numerical instabilities are also observed everywhere in the vicinity of the semi-infinite dislocation lines.

As the first step in eliminating the artefact singularities, we reconfigure the angular dislocations as illustrated in Fig. 2.3. The input parameters of both configurations are presented in Table 2.1. Clearly, these two solutions are equivalent. The artefact singularities in these two configurations, however, occur in completely different locations. As a result, if the calculation point, for example, point P in Fig. 2.3(a), lies on or in the vicinity of the lines of the artefact singularities, we can successfully avoid any computational problems by using the other configuration depicted in Fig. 2.3(b).

To choose between the two configurations for any arbitrary calculation point, we consider

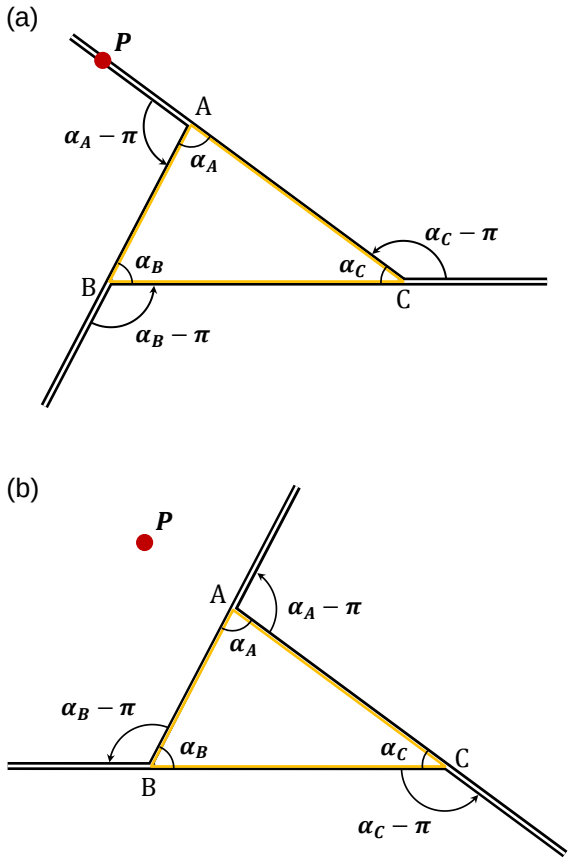

Figure 2.3: Two different configurations for the triangular dislocation ABC. Apart from the placements of the semi-infinite dislocation lines, these configurations are equivalent and can be used interchangeably. (a) The calculation point P in the plane of the triangle intersects one of the dislocation lines. (b) In the 'alternative' configuration for the angular dislocations, point P is located at the maximum possible distance from such lines. Through the selection of the appropriate configuration, any artefact singularity or numerical instability can be avoided.

the orthogonal projection of the point onto the TD plane, which we hereafter refer to as 'the projection point'. We also subdivide the plane of the TD into six partitions using the medians of the TD sides (Fig. 2.4). When this approach is taken, each line of artefact singularity is located in one and only one of the six partitions. For the projection points outside the TD, we use the configuration whose lines of artefact singularity do not lie in the same partition as the projection point. For the projection points inside the TD, either configuration can be used. Following this strategy, we always maintain the maximum distance from the dislocation lines, regardless of whether the point of calculation lies on the plane of the TD. As a consequence, we avoid both artefact singularities and numerical instabilities for any on- or off-plane calculation points.

To implement this strategy, we must be able to identify the partition in which the projection point is located. For this purpose, we use the special barycentric coordinates of the projection points (Ungar, 2010). The barycentric coordinate system efficiently represents the coordinates of points in the plane of a triangle with respect to the position of the vertices of the triangle. Further details concerning the barycentric coordinate system can be found in Appendix 2.C. The very simple and often symmetric form of the equations of geometric shapes in this coordinate system makes it the most appropriate system for many problems related to the geometrical properties of a triangle (Bottema, 2008).

For an arbitrary point $P(x_P, y_P)$ and a triangle with vertices $A_1(x_1, y_1)$, $A_2(x_2, y_2)$ and $A_3(x_3, y_3)$ in a 2-D Cartesian coordinate system, (μ_1, μ_2, μ_3), the normalized barycentric coordinates of P with respect to $A_1A_2A_3$, are calculated as follows:

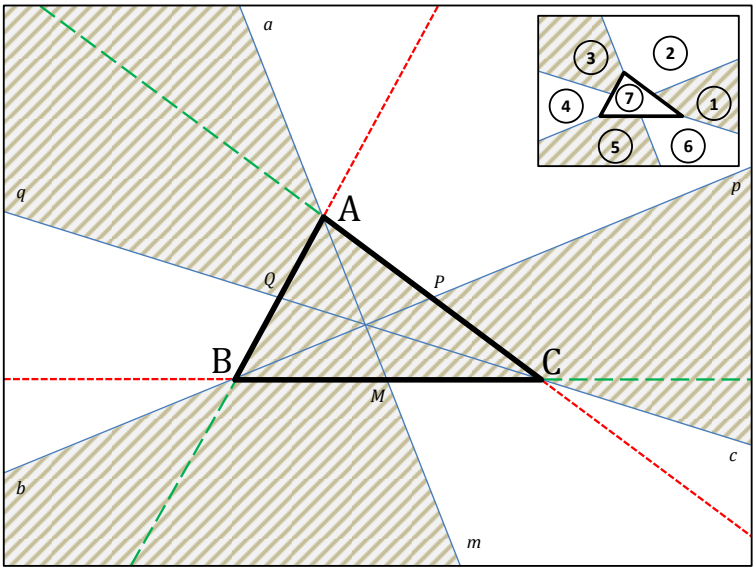

Figure 2.4: The seven partitions in the plane of the triangular dislocation (TD) formed by AM, BP and CQ, which are the medians of the TD extended through the plane on both sides (the solid concurrent lines). The green dashed lines and the red dotted lines represent the lines of singularities corresponding to the two configurations of Fig. 2.3. Each line of singularity lies in only one of the partitions. To avoid artefact singularities and numerical instabilities, we use the configuration corresponding to the red dotted lines for the projection points that lie in the dark partitions and the configuration corresponding to the green dashed lines for the remaining points. Either configuration can be used for the points inside the TD. The subpanel on the top right shows the numbers assigned to the partitions, which are used in Table 2.2.

$$\mu_1 = \frac{\begin{vmatrix} x_P - x_3 & x_2 - x_3 \\ y_P - y_3 & y_2 - y_3 \end{vmatrix}}{\begin{vmatrix} x_1 - x_3 & x_2 - x_3 \\ y_1 - y_3 & y_2 - y_3 \end{vmatrix}}, \tag{2.4}$$

$$\mu_2 = \frac{\begin{vmatrix} x_1 - x_3 & x_P - x_3 \\ y_1 - y_3 & y_P - y_3 \end{vmatrix}}{\begin{vmatrix} x_1 - x_3 & x_2 - x_3 \\ y_1 - y_3 & y_2 - y_3 \end{vmatrix}}, \tag{2.5}$$

and

$$\mu_3 = 1 - \mu_1 - \mu_2, \tag{2.6}$$

where the symbol '$|.|$' represents the determinant of the matrix. The equations $\mu_1 = \mu_2$, $\mu_1 = \mu_3$ and $\mu_2 = \mu_3$ represent the medians of the triangle (Ungar, 2010). Using this equations and the barycentric coordinates of each projection point with respect to the TD vertices, we develop a set of simple inequalities that enable us to identify the partition corresponding to each projection point. The inequalities corresponding to the partitions illustrated in Fig. 2.4 are summarized in Table 2.2. The necessary computation time for the transformation of the primary Cartesian coordinates into the barycentric coordinate system is negligible.

Table 2.2: The inequalities that define the partitions in the special barycentric coordinate system illustrated in Fig. 2.4.

Zone number	Zone corners	Inequalities specifying the zone I	II	III	Artefact-free configuration in the zone
1	cCPp	$\mu_3 \geqslant \mu_1$	$\mu_1 \geqslant \mu_2$	$\mu_2 < 0$	Config-2
2	pPAa	$\mu_1 \geqslant \mu_3$	$\mu_3 \geqslant \mu_2$	$\mu_2 < 0$	Config-1
3	aAQq	$\mu_1 \geqslant \mu_2$	$\mu_2 \geqslant \mu_3$	$\mu_3 < 0$	Config-2
4	qQBb	$\mu_2 \geqslant \mu_1$	$\mu_1 \geqslant \mu_3$	$\mu_3 < 0$	Config-1
5	bBMm	$\mu_2 \geqslant \mu_3$	$\mu_3 \geqslant \mu_1$	$\mu_1 < 0$	Config-2
6	mMCc	$\mu_3 \geqslant \mu_2$	$\mu_2 \geqslant \mu_1$	$\mu_1 < 0$	Config-1
7	ABC	$\mu_1 > 0$	$\mu_2 > 0$	$\mu_3 > 0$	Config-1 and Config-2

2.2.3 Improvement on the Burgers function formulation

The Burgers function (Burgers, 1939), which appears in the displacement equations associated with any dislocation, is the only term that allows for a discontinuity across the dislocation surface (Brown, 1975). The strain and stress equations, however, as functions of the partial derivatives of the displacements, include the partial derivatives of the Burgers function.

For an arbitrary calculation point $P\,(x_P, y_P, z_P)$, the Burgers function φ^P is proportional to the solid angle Ω^P subtended at P by the dislocation (Burgers, 1939):

$$\varphi^P = \frac{\Omega^P}{4\pi}. \tag{2.7}$$

In other words, the dislocation is observed from the point P through the solid angle.

To calculate the displacements associated with a triangular dislocation (TD), we use eq. (2.3). Yoffe (1960) calculated the Burgers function corresponding to a TD, that is φ^P_{TD}, in terms of the superposition of the Burgers functions of three angular dislocations forming a configuration such as that illustrated in Fig. 2.1(b). This approach, however, results in an incorrect value for φ^P_{TD} because the angular dislocations are the external angles of the TD, and therefore, the calculated φ^P_{TD} corresponds to the entire $x = 0$ plane except the TD surface.

In the following, we apply the equation developed by Van Oosterom and Strackee (1983) to calculate φ^P_{TD}, which is the Burgers function associated with the TD. Using the same equation, we then develop a new equation for φ^P_A, which is the Burgers function associated with the angular dislocation. Eventually, we verify our approach by calculating and comparing the partial derivatives of our new equation for φ^P_A to the Yoffe (1960) equations.

For an arbitrary triangle ABC in Fig. 2.5(a), the corresponding solid angle Ω^P_{ABC} is equal to the area of the spherical triangle $A'B'C'$, which is the orthogonal projection of ABC onto the unit sphere centred at P (Van Oosterom and Strackee, 1983). As depicted in Fig. 2.5(a), A', B' and C' are the points at which the position vectors $\vec{r}_{PA}$, $\vec{r}_{PB}$ and $\vec{r}_{PC}$, respectively, meet the surface of the sphere.

Van Oosterom and Strackee (1983) developed an efficient equation for the calculation of Ω^P_{ABC}:

$$\Omega^P_{ABC} = 2\tan^{-1}\left[\frac{\vec{r}_{PA}\cdot(\vec{r}_{PB}\times\vec{r}_{PC})}{r_{PA}r_{PB}r_{PC} + (\vec{r}_{PA}\cdot\vec{r}_{PB})\,r_{PC} + (\vec{r}_{PA}\cdot\vec{r}_{PC})\,r_{PB} + (\vec{r}_{PB}\cdot\vec{r}_{PC})\,r_{PA}}\right], \tag{2.8}$$

where r_{PA}, r_{PB} and r_{PC} are the $L2$-norms of $\vec{r}_{PA}$, $\vec{r}_{PB}$ and $\vec{r}_{PC}$, respectively. The term in the

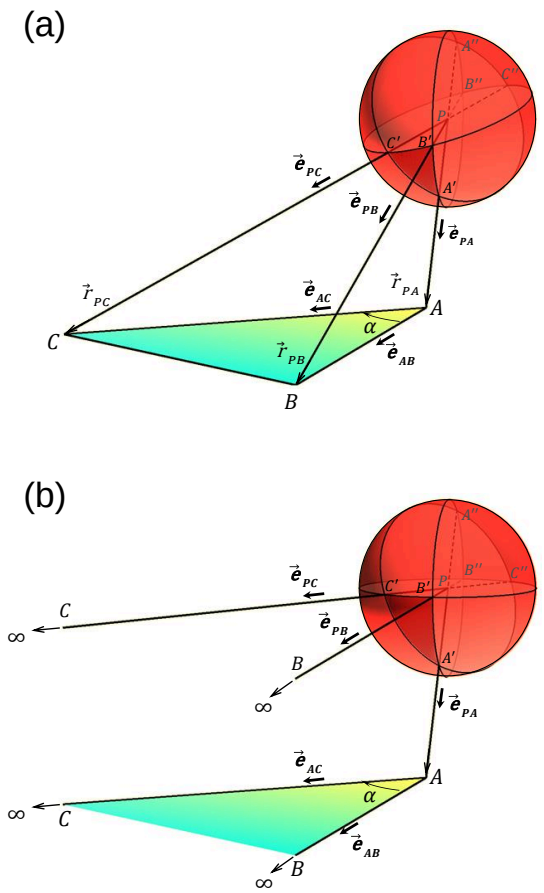

Figure 2.5: (a) The solid angle subtended at point P, the centre of the unit sphere, by the triangular dislocation ABC. This solid angle is equal to the area of the spherical triangle $A'B'C'$, which is the orthogonal projection of the TD onto the unit sphere. (b) The solid angle subtended at point P by the angular dislocation A, shown as the limit of the TD solid angle as the vertices B and C approach infinity along the positive directions of $\vec{e}_{AB}$ and $\vec{e}_{AC}$, respectively. By definition, two parallel lines intersect at infinity.

numerator, that is $\vec{r}_{PA} \cdot (\vec{r}_{PB} \times \vec{r}_{PC})$, represents the scalar triple product of the vectors.

To calculate φ^P_{TD}, the Burgers function corresponding to any TD at an arbitrary point P, we first apply eq. (2.8) to calculate Ω^P_{TD}, which is the corresponding solid angle. We then use eq. (2.7) to calculate φ^P_{TD}. Note that for calculations based on eq. (2.8), the four-quadrant inverse tangent (e.g., the atan2 function in MATLAB) must be used, which accounts for the signs of the numerator and denominator of the fraction.

We now use eq. (2.8) to derive the equation of the solid angle and, subsequently, the Burgers function associated with an angular dislocation. For this purpose, we first replace the position vectors in eq. (2.8) with $r_{PA}\vec{e}_{PA}$, $r_{PB}\vec{e}_{PB}$ and $r_{PC}\vec{e}_{PC}$, where $\vec{e}_{PA}$, $\vec{e}_{PB}$ and $\vec{e}_{PC}$, respectively, are the unit vectors along the position vectors. This replacement results in an equation that is equivalent to eq. (2.8) but is now based only on the unit vectors:

$$\Omega^P_{ABC} = 2\tan^{-1}\left[\frac{\vec{e}_{PA} \cdot (\vec{e}_{PB} \times \vec{e}_{PC})}{1 + \vec{e}_{PA} \cdot \vec{e}_{PB} + \vec{e}_{PA} \cdot \vec{e}_{PC} + \vec{e}_{PB} \cdot \vec{e}_{PC}}\right]. \tag{2.9}$$

As illustrated in Fig. 2.5(b), if the vertices B and C are shifted along the positive directions of the $\vec{e}_{AB}$ and $\vec{e}_{AC}$ vectors, respectively, to infinity, an angular dislocation is formed that originates at A. For this angular dislocation, we adopt the coordinate system convention used in Yoffe (1960), where the z-axis coincides with the AB side and the x-axis points upwards. Because B and C are already at infinity, $\vec{e}_{PB}$ and $\vec{e}_{PC}$ are parallel to the sides of the angular

dislocation, and therefore, the coordinates of the unit vectors in this coordinate system are $\vec{e}_{PA} = -(x_P, y_P, z_P)/r_P$, $\vec{e}_{PB} = (0, 0, 1)$ and $\vec{e}_{PC} = (0, \sin\alpha, \cos\alpha)$. If we substitute these coordinates into eqs (2.9) and (2.7) and use the half-angle trigonometry formulae, it follows that the Burgers function at the calculation point P that corresponds to the angular dislocation with $\alpha > 0$ is

$$\varphi_A^P = \frac{1}{2\pi}\tan^{-1}\left[\frac{x_P}{(r_P - z_P)\cot(\alpha/2) - y_P}\right]. \tag{2.10}$$

Negating the numerator and the denominator of eq. (2.10) while using the four-quadrant tangent function also enables calculations for values of $\alpha < 0$.

The partial derivatives of this function with respect to x, y and z are

$$\begin{aligned}
\frac{\partial\varphi_A^P}{\partial x} &= \frac{1}{4\pi}\left[\frac{\eta_p}{r_P(r_P - \zeta_P)} - \frac{y_p}{r_P(r_P - z_P)}\right] \\
\frac{\partial\varphi_A^P}{\partial y} &= \frac{1}{4\pi}\left[\frac{x_p}{r_P(r_P - z_P)} - \frac{x_p\cos\alpha}{r_P(r_P - \zeta_P)}\right] \\
\frac{\partial\varphi_A^P}{\partial z} &= \frac{1}{4\pi}\frac{x_p\sin\alpha}{r_P(r_P - \zeta_P)},
\end{aligned} \tag{2.11}$$

where $\zeta_P = y_P\sin\alpha + z_P\cos\alpha$.

All partial derivatives in eq. (2.11) are identical to those given by Yoffe (1960). Because the Burgers function does not include any constant term (see eq. 2.10), the equality of the partial derivatives verifies eq. (2.8) and guarantees the validity of our approach.

These equations contain only one arc-tangent term, which makes them very efficient to calculate. Moreover, eq. (2.10) remains single-valued everywhere and also addresses the numerical instabilities of the Brown (1975) equation near $x = 0$. Below, we will use eq. (2.10) in our artefact-free solution for a TD in a half-space.

2.3 A triangular dislocation in a half-space

In many geophysical applications of dislocation theory, because no stress is transferred from the solid earth to the atmosphere, the earth's surface is simulated as a free surface (Segall, 2010).

Following Jeyakumaran et al. (1992) and Meade (2007) and using the coordinate transformation scheme presented in Section 2.2.1, we now develop a general solution for a triangular dislocation (TD) in a half-space. We use this general solution merely to calculate the effect of a free surface on a TD and then develop an artefact-free solution in a half-space by using the method of images.

2.3.1 The general solution for a TD in a half-space

2.3.1.1 The structure of the solution

By applying the method of images to the Yoffe (1960) solution in a full-space, Comninou and Dundurs (1975) developed the mathematical equations associated with an angular dislocation in a half-space that are applied for displacement calculations at the surface and at depth as well as calculations of the strain and rotation tensor at the surface only. The solution was developed for an angular dislocation with a vertical leg (perpendicular to the surface) and an angle that is restricted to the interval $[-\pi/2, \pi/2]$, as shown in Fig. 2.6. Therefore, the dislocation lines

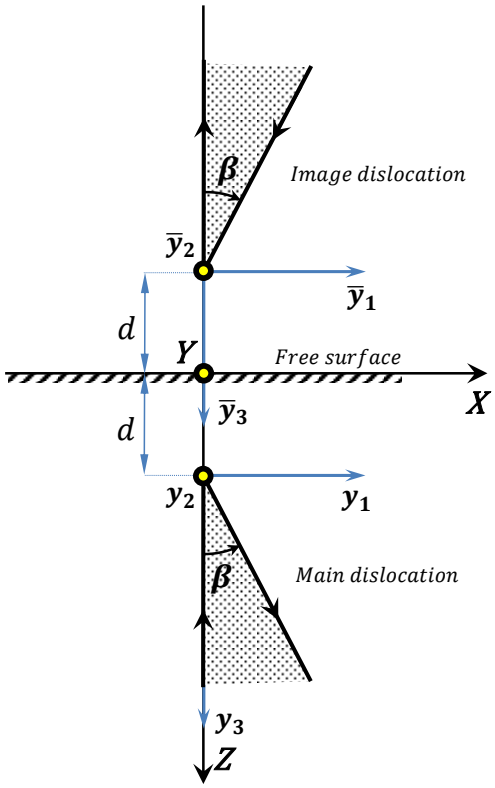

Figure 2.6: Half-space formulation of an angular dislocation, composed of the main dislocation, the image dislocation and a harmonic potential function (Comninou and Dundurs, 1975). The image dislocation (here, the dislocation on the upper side) is the mirror image of the main dislocation (here, the dislocation on the lower side), whose origin is located at a depth d. All coordinate systems shown here are right-handed, and the y_2-, $\bar{y}_2$- and Y-axes, which are shown as black-and-yellow circles, are normal to the plane and point outwards. Following the convention of Comninou and Dundurs (1975), in this figure, the positive direction of the Z-axis points downwards and $Z = 0$ defines the free surface. The half-space equations give the displacements and stresses in terms of $y_1y_2y_3$, which is the main dislocation coordinate system.

of the angular dislocation never intersect the surface, unless the origin is located at the surface and the angle is exactly $\pm\pi/2$. The equations in Comninou and Dundurs (1975) are given in the ADCS, which is detailed in Section 2.2.1 and is shown as the $y_1y_2y_3$ coordinate system in Fig. 2.6. The y_1, y_2 and y_3 axes of this figure correspond to the y-, x- and z-axes, respectively, that are used by Yoffe (1960).

The solution for the angular dislocation in a half-space consists of three parts: the main dislocation, the image dislocation and a harmonic function (Comninou and Dundurs, 1975). The image dislocation, which is the mirror image of the main dislocation with respect to the free surface, cancels the surface shear traction of the main dislocation but doubles the surface normal traction. The harmonic function eliminates the resultant surface normal traction to fulfil the zero-traction boundary condition at the free surface (Comninou and Dundurs, 1975). Therefore, the half-space solutions for the displacement vector $\vec{d}$ and the stress tensor S can be written as follows:

$$\vec{d} = \vec{d}^{MD} + \vec{d}^{ID} + \vec{d}^{HF}, \tag{2.12}$$

$$S = S^{MD} + S^{ID} + S^{HF}. \tag{2.13}$$

The superscripts *MD*, *ID* and *HF* of the terms on the right-hand sides of eqs (2.12) and (2.13)

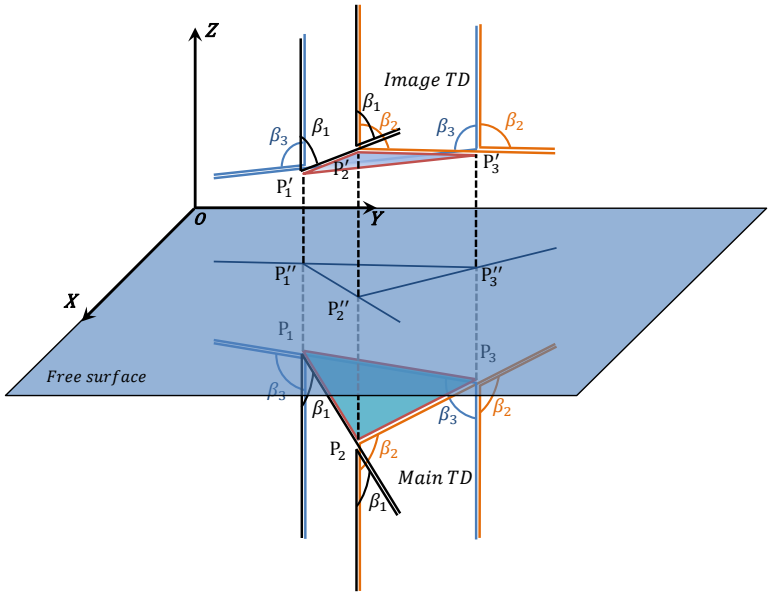

Figure 2.7: Half-space formulation of a triangular dislocation (TD), modified from Jeyakumaran et al. (1992). The triangles $P_1P_2P_3$ and $P_1^{'}P_2^{'}P_3^{'}$ are the main and image TDs, respectively, and $P_1^{''}P_2^{''}P_3^{''}$ is their projection onto the free surface. The solid lines connected to P_1, P_2 and P_3 form the first set of artefact singularities, and the other solid lines, connected to $P_1^{''}$, $P_2^{''}$ and $P_3^{''}$, form the second set of artefact singularities discussed in Section 2.3.2. These artefact singularities affect the displacements, strains and stresses. The vertical dashed lines indicate the locations of the artefact singularities, which affect the strains and stresses only.

represent the contributions of the main dislocation, the image dislocation and the harmonic function, respectively. To calculate the contributions of the main and image dislocations, the full-space solution detailed in Appendix 2.B must be used, whereas the contributions of the harmonic function to eqs (2.12) and (2.13) are given by Comninou and Dundurs (1975) and Meade (2007), respectively.

A solution for a TD in a half-space was developed by Jeyakumaran et al. (1992) through the superposition of six angular dislocations in the half-space. The complete strain equations along with the details of the method used to construct the solution in the half-space are given by Meade (2007).

Here, we first follow the same approach used in these earlier studies and combine it with the coordinate transformation approach (Appendix 2.A). In this manner, we develop a general solution for a TD in a half-space with the configuration depicted in Fig. 2.7. In our conventions, the EFCS is defined with the positive Z-axis pointing upwards. Therefore, the vertices of the TD in the half-space have Z components that are negative or, in case that the free surface is reached, zero. The procedure for the calculations associated with a TD in a half-space is summarized in the diagram presented in Fig. 2.8. When considering the new ADCS in the half-space, we simply use the direct transformation between the EFCS and the ADCS. However, we transform the slip vector from the TDCS into the EFCS and then from the EFCS into the ADCS of each angular dislocation. Thus, the EFCS plays the role of both an intermediate and the final coordinate system.

2.3.1.2 The implementation procedure

To construct the transformation matrices, we first calculate the strike, dip and normal to the TD vectors, using the right-hand rule for vertex ordering. Therefore, the transformation matrix of eq. (2.1) can be used for direct transformation from the TDCS into the EFCS. The details regarding the calculation of the components of this transformation are presented in Section 2.2.1. Now, using A_{TE} in eq. (2.A.3), we can transform the slip vector from the TDCS into

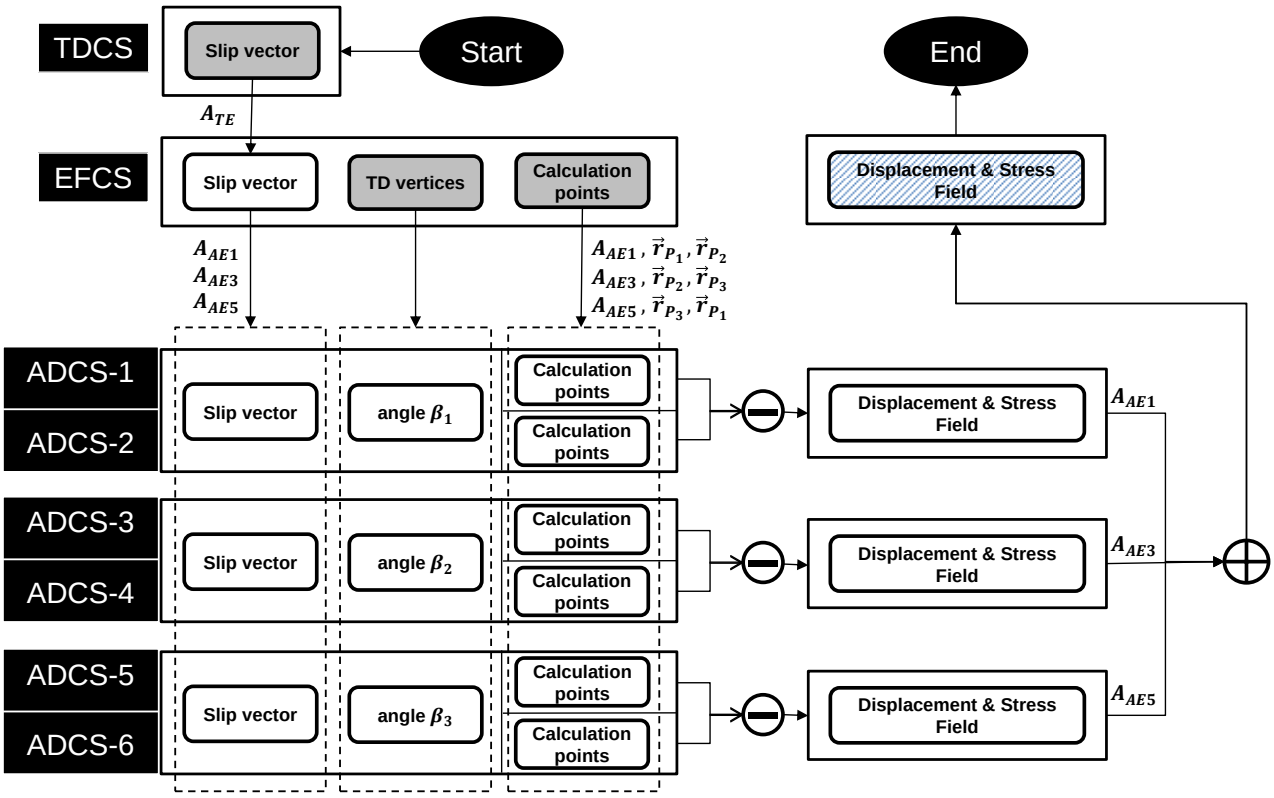

Figure 2.8: Flowchart for calculating the displacement and stress field of a triangular dislocation (TD) in an Earth-fixed coordinate system (EFCS) in a half-space. The first box on the left side of each row indicates the coordinate system corresponding to the other boxes in that row. The grey boxes represent the inputs, and the blue box represents the final output. The coordinates of the slip vector in the triangular dislocation coordinate system (TDCS) are first transformed into the EFCS (see eq. 2.A.3 in Appendix 2.A). The coordinates of the calculation points and the TD vertices are then transformed from the EFCS into each of the six angular dislocation coordinate systems (ADCSs; see eqs 2.A.9 and 2.A.5 in Appendix 2.A). After the contribution of each angular dislocation is calculated, the results are transformed into the EFCS (see eqs 2.A.4 and 2.A.10 in Appendix 2.A). The superposition of the individual contributions of the angular dislocations yields the final result.

the EFCS.

The transformation matrices $A_{AE_1},\ldots,A_{AE_6}$ for the direct transformation from each ADCS into the EFCS consist of the coordinates of $\{\vec{e}^{\,k}_{y_1},\vec{e}^{\,k}_{y_2},\vec{e}^{\,k}_{y_3}\}$ for k =1,2,...,6, which are the unit vectors along the axes of the ADCS that correspond to each of the six angular dislocations. It can be observed in Fig. 2.7 that along each side of the TD in the half-space, there is a pair of coplanar angular dislocations whose origins are located at the vertices of that side of the TD. These two angular dislocations have the same angles but opposite slip vectors (Fig. 2.9a). The ADCSs of these two angular dislocations have parallel axes, and their y_1-axis is parallel to the projection of the corresponding side of the TD onto the free surface. Considering the TD depicted in Fig. 2.7, if we represent the coordinates of P_1, P_2 and P_3 in the EFCS as $r_{P_1}=(X_{P_1}\,Y_{P_1}\,Z_{P_1})^T$, $r_{P_2}=(X_{P_2}\,Y_{P_2}\,Z_{P_2})^T$ and $r_{P_3}=(X_{P_3}\,Y_{P_3}\,Z_{P_3})^T$, respectively, then the coordinates of their respective projections onto the free surface, P_1'', P_2'' and P_3'', will be $r''_{P_1}=(X_{P_1}\;Y_{P_1}\;0)^T$, $r''_{P_2}=(X_{P_2}\;Y_{P_2}\;0)^T$ and $r''_{P_3}=(X_{P_3}\;Y_{P_3}\;0)^T$. As a result, the unit vectors $\vec{e}^{\,k}_{y_1}$ for k =1,2,...,6, which are the unit vectors along the projections of P_1P_2, P_2P_3 and P_3P_1, are $\vec{e}^{\,1}_{y_1}=\vec{e}^{\,2}_{y_1}=(\vec{r}''_{P_2}-\vec{r}''_{P_1})/\|\vec{r}''_{P_2}-\vec{r}''_{P1}\|$, $\vec{e}^{\,3}_{y_1}=\vec{e}^{\,4}_{y_1}=(\vec{r}''_{P_3}-\vec{r}''_{P_2})/\|\vec{r}''_{P_3}-\vec{r}''_{P_2}\|$ and $\vec{e}^{\,5}_{y_1}=\vec{e}^{\,6}_{y_1}=(\vec{r}''_{P_1}-\vec{r}''_{P_3})/\|\vec{r}''_{P_1}-\vec{r}''_{P_3}\|$. We number the angular dislocations along the P_1P_2 side with the vertices P_1 and P_2 as their origins as the first and second angular dislocations, respectively. The third and fourth angular dislocations are those along the P_2P_3 side with the vertices P_2 and P_3, respectively, as their origins. Finally, the fifth and sixth angular dislocations

are those along the P_3P_1 side with the vertices P_3 and P_1, respectively, as their origins. However, $e^k_{y_3} = (0 \;\; 0 \;\; -1)^T$ clearly holds because these unit vectors are oriented along the vertical legs of the angular dislocations and point downwards. Because the $y_1y_2y_3$ coordinate system is right-handed, it also holds that $\vec{e}^k_{y_2} = \vec{e}^k_{y_3} \times \vec{e}^k_{y_1}$, which completes the construction of the required transformation matrices. Starting from the coordinates of the TD vertices in the EFCS and using $A_{AE1}, \ldots, A_{AE6}$ in eqs (2.A.4) and (2.A.6), we can transform the coordinates of the slip vector and the calculation points from the EFCS into each ADCS. The angles of the six angular dislocations can be calculated using $\beta_1 = \cos^{-1}(-\vec{e}_{12} \cdot \vec{e}_Z)$, $\beta_2 = \cos^{-1}(-\vec{e}_{23} \cdot \vec{e}_Z)$ and $\beta_3 = \cos^{-1}(-\vec{e}_{13} \cdot \vec{e}_Z)$, where $\vec{e}_{12} = (\vec{r}_{P_2} - \vec{r}_{P_1}) / \|\vec{r}_{P_2} - \vec{r}_{P_1}\|$, $\vec{e}_{13} = (\vec{r}_{P_3} - \vec{r}_{P_1}) / \|\vec{r}_{P_3} - \vec{r}_{P_1}\|$ and $\vec{e}_{23} = (\vec{r}_{P_3} - \vec{r}_{P_2}) / \|\vec{r}_{P_3} - \vec{r}_{P_2}\|$ are the unit vectors along the sides of the TD.

To calculate the final results, the contribution of each angular dislocation to the displacements and the stresses must first be transformed into the EFCS. Superposition of the individual contributions yields the final results.

2.3.2 Developing an artefact-free solution for a TD in a half-space

With regard to the geometry and configuration of the angular dislocations in the half-space solution presented in Figs 2.6 and 2.7, we find that the results are subject to even more artefact singularities than the full-space solution. In this case, in addition to those on the extensions of the sides of the TD, additional artefact singularities are present beneath and above the vertices of the TD. These artefact singularities are indicated by the solid and dashed lines around the TD in Fig. 2.7. The first set of solid lines represents the slant and vertical legs of the main angular dislocations, which cause problems similar to those encountered in the full-space case. The second set of solid lines constitutes those at the free surface, representing the harmonic function, which eliminates the normal traction of the free surface. The artefact singularities on these lines and the numerical instabilities in their vicinity emerge whenever at least one of the sides of the main TD intersects the free surface or when the dislocation is very shallow. The vertical dashed lines above the TD vertices represent the artefact singularities arising from the miscalculation of the Burgers function or its partial derivatives.

We develop an artefact-free solution in a half-space by applying the method of images directly to the TDs (Fig. 2.7). We note that the final result of the superposition of the six TDs in the half-space can also be written in the form of eqs (2.12) and (2.13). In this case, the first and second terms represent the contributions of the main and image TDs, respectively, which are shown in Fig. 2.7 as $P_1P_2P_3$ and $P_1'P_2'P_3'$, respectively. The third term expresses the contribution of the harmonic function associated with the main and image TDs and is virtually represented by $P_1''P_2''P_3''$ in Fig. 2.7. Accordingly, we propose our artefact-free solution in a half-space in two steps. In step 1, we calculate the artefact-free contributions of the main and image TDs. In step 2, we calculate the artefact-free contribution of the harmonic function to the displacements and stresses that correspond to the TD. The superposition of the outputs of these two steps yields the final results.

2.3.2.1 Step 1

In step 1, we use the same EFCS in which the positive Z-axis points upwards and $Z = 0$ represents the free surface. We calculate the contribution of the main and image TDs using the full-space artefact-free solution that we developed in Section 2.2.2. The horizontal coordinates of the vertices of the main and image TDs in the EFCS are the same, whereas the values of their vertical components are additive inverses. Therefore, to obtain consistent results, with the exception of the Z coordinates of the vertices, which are opposite, we consider the same input parameters for the main and image TDs, including the same vertex ordering and the same slip vectors. According to this model framework and the conventions that we adopted for

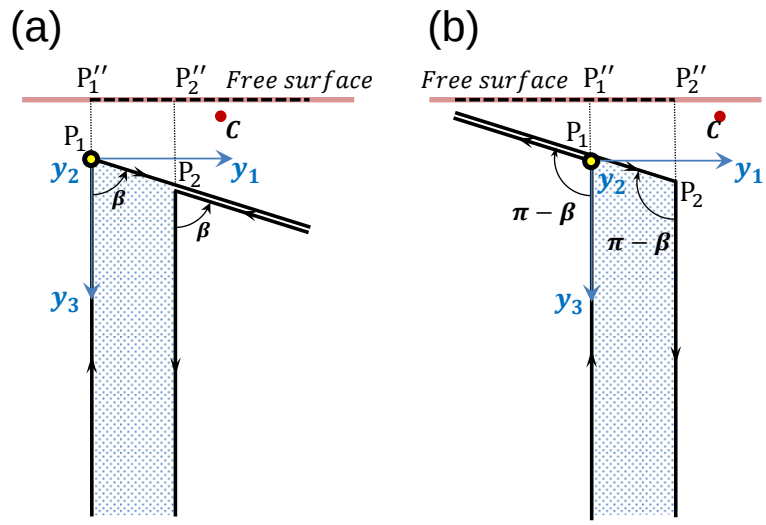

Figure 2.9: Two equivalent configurations associated with the pair of angular dislocations along the side P_1P_2. The dashed line along $P_1^{''}P_2^{''}$ is the projection of the dislocation lines onto the free surface. Here, $y_1y_2y_3$ is the angular dislocation coordinate system (ADCS) of the angular dislocation at P_1. The configuration depicted in (a) is used for points with negative y_1 coordinates, and the configuration depicted in (b) is used for points with positive y_1 coordinates. For points such as C, we avoid the artefacts along the dashed lines by using this technique to calculate the contribution of the harmonic function in our artefact-free half-space solution.

the TDCS, the strike vectors of the main and image TDs have parallel but opposite directions. However, our convention for a completely horizontal TD produces the same strike vectors for both the main and image TDs. We correct for this exceptional case by negating the components of the strike vector for the image TD after calculating the normal vector. The dip vector is then calculated as the cross product of the normal and strike vectors.

Now, we calculate the contributions of the main and image dislocations using our artefact-free solution for a TD in a full-space. Consequently, the artefact singularities along the first set of solid lines and the dashed lines will no longer exist in the model.

2.3.2.2 Step 2

In step 2, we recall from Section 2.3.1.1 that $\vec{d}^{HF}$ and S^{HF} are the contributions of the harmonic function to the displacement and stress fields, respectively, of an angular dislocation in a half-space. Now, we calculate the contributions of the harmonic function to the displacements and stresses associated with a triangular dislocation in a half-space by applying the technique discussed in Section 2.3.1, only now we apply it to the $\vec{d}^{HF}$ and S^{HF} terms in eqs (2.12) and (2.13). However, this calculation is still subject to the artefacts represented by the solid lines on the free surface in Fig. 2.7, as discussed before. These lines are the projections of the plunging legs of the pairs of angular dislocations along the sides of the main TD. The two configurations represented in Fig. 2.9 can be used equivalently to calculate the contribution of each pair of angular dislocations along each side of the TD in the half-space. Note that to use the second alternative in Fig. 2.9, the angle β must be replaced by the opposite of its supplementary angle, $\beta - \pi$, while the other inputs remain unchanged. According to Fig. 2.9, for the calculation points, which have positive y_1 coordinates, we must use the alternative configuration in Fig. 2.9(b), whose artefacts extend along the negative y_1-axis, and vice versa. In this manner, we can always avoid the artefacts on the free surface.

Superposing the outputs of Sections 2.3.2.1 and 2.3.2.2 produces the final solution for a TD in a half-space, which is free from all the various artefacts that we discussed before.

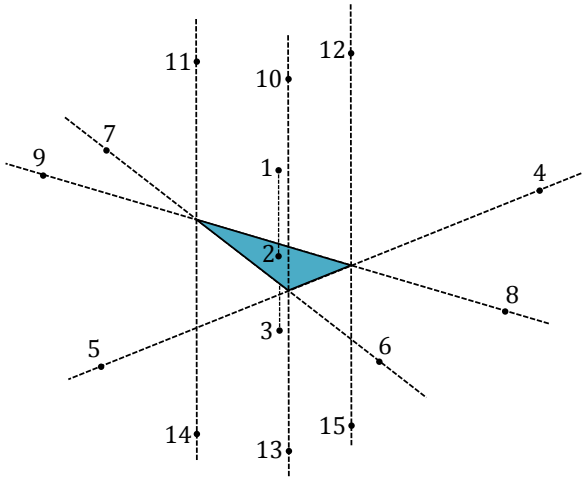

Figure 2.10: The triangular dislocation (TD) in a half-space and the calculation points on the artefact singularities that are used for the validation and comparison of the results of our method with respect to the Meade (2007) solution.

2.4 Validation of the new artefact-free solutions

With regard to the lengthy equations associated with a TD in either a full space or half-space and with regard to the procedure that we applied to address the artefacts in these equations, analytical verification of our method is not feasible. One approximate method of verification consists of comparing the results to those of the available numerical methods for dislocation model calculations (Jeyakumaran et al., 1992). However, the absolute precision of the solution may arguably remain unresolved in this case. A superior alternative applied in other, earlier works by Thomas (1993) and Meade (2007) is to validate the solution using the analytical solution for a rectangular dislocation (RD) in a half-space, as summarized by Okada (1992).

Here, we first compare our solution for a TD in a half-space to the solution of Meade (2007). The purpose of this comparison is to validate our solution for the regular calculation points, those that do not lie near the artefact singularities. This comparison also demonstrates the ability of our method to address the artefacts. For this purpose, we consider the TD and calculation points shown in Fig. 2.10. The coordinates and the first components of the displacement vector and the strain tensor that correspond to the calculation points are listed in Table 2.3. The first three points, which form a line parallel to the Z-axis, are located at the centroid of the TD, above it, and underneath it. The next six points are located on the extensions of the sides of the TD, and the remaining six lie above or underneath the vertices.

In Table 2.3, the results of our method are presented as u and ϵ_{XX}, which represent the first displacement component and the first strain component, respectively; the corresponding outputs obtained using the Meade (2007) code are presented as $u^{'}$ and $\epsilon^{'}_{XX}$. For the calculations, we consider a Poisson's ratio of 0.25. The coordinates of the vertices of the TD are $(-1, -1, -5)$, $(1, -1, -5)$ and $(-1, 1, -4)$. In our calculations, the coordinates of the TD vertices and the coordinates of the calculation points share the same unit of length, which may be any unit that is desired. The components of the TD slip vector, which correspond to the strike slip, the dip slip and the opening, are 1, -1 and 2, respectively. The components of the TD slip vector and of the displacement vector also share the same arbitrary unit.

The calculated displacements and strains for points No. 1, No. 2 and No. 3 in Table 2.3 demonstrate that the results of our method compare very well with the outputs of the Meade (2007) code. The differences of less than 10^{-15} indicate excellent agreement between the two approaches for calculation points far from the artefact singularities.

As another reference for the validation of our method, we use the solution of Okada (1992)

Table 2.3: The coordinates, displacements and strains corresponding to the points shown in Fig. 2.10. The 'NaN' values and the grey fields in the table indicate the artefact singularities and numerical instabilities in the Meade (2007) code. Note that our approach allows for valid computation of these points. For the first three points, both approaches retrieve the same results, demonstrating the correctness of both methods at calculation points that are not subject to artefact singularities.

#	X	Y	Z	u (this paper)	u' (Meade 2007)	ϵ_{XX} (this paper)	ϵ'_{XX} (Meade 2007)
1	-1/3	-1/3	-3	0.0352311877319734	0.0352311877319732	0.0481047005255181	0.0481047005255181
2	-1/3	-1/3	-14/3	-0.509465745232405	-0.509465745232405	-0.244188978214975	-0.244188978214977
3	-1/3	-1/3	-6	-0.0450664903903138	-0.0450664903903139	0.0546831404832553	0.0546831404832554
4	7	-1	-5	-0.00230579292792908	NaN	0.000829157341339727	NaN
5	-7	-1	-5	0.00401472894583963	0.00401472894583941	0.00114439668841158	NaN
6	-1	-3	-6	0.00483219740842196	NaN	-0.00386292388925956	NaN
7	-1	3	-3	0.00261498816660580	0.00261498816660530	-0.00243788640223540	NaN
8	3	-3	-6	-0.00498017723062124	0.0498371783469113	0.000706397690338731	142952905402461
9	-3	3	-3	0.00469791958297159	0.00469791958297180	0.000211254167350266	0.00431126958717604
10	-1	-1	-1	0.00147786823004841	0.00147786823004838	0.00650800501584133	NaN
11	-1	1	-1	0.00374844575688324	0.447846746319388	0.000922452413344460	NaN
12	1	-1	-1	0.0166558386729541	-0.427442461889551	0.00441202690885827	NaN
13	-1	-1	-8	-0.00656347406353817	NaN	0.00330232019558791	NaN
14	-1	1	-8	-0.0105680479573571	NaN	0.00876398663844928	NaN
15	1	-1	-8	-0.00213929091658054	NaN	-0.000914111766849476	NaN

for an RD. We construct the displacement field of an RD by superposing the displacements of two TDs in a half-space that form exactly the same RD (Fig. 2.11a; see also Meade (2007)). We use the same conventions for the units of the various quantities as those used in the first part of this section. The midpoint of the upper edge of the RD is located at a depth of 2 beneath the origin of the EFCS. The RD has a dip angle of 30 degrees, a strike angle of 10 degrees, and a length and width of 1.5 and 0.75, respectively. We consider a unit slip vector with a rake angle of 90 degrees on the RD and calculate the corresponding displacements on a 2×2 grid beneath the RD, centred on the origin of the EFCS. The approximate coordinates of the vertices of the RD are P_1 (0.1302, 0.7386, −2.0000), P_2 (−0.1302, −0.7386, −2.0000), P_3 (0.5094, −0.8514, −2.3750), and P_4 (0.7699, 0.6258, −2.3750). The precise coordinates can be calculated using the RD parameters that we specified earlier. As shown in Fig. 2.11(a), $P_1P_2P_3$ and $P_3P_4P_1$ are the two TDs that, together, are geometrically equivalent to the RD. These TDs share the same slip vector, (0, 1, 0). We calculate and superpose the displacements of the TDs on the same grid using our artefact-free solution for the two TDs in the half-space. The displacements of the TDs and the RD, as well as the differences between the two, are illustrated in Fig. 2.11. The results are comparable, and the differences are on the order of 10^{-15}. The same order of accuracy has been reported by Meade (2007) for various calculation points at the surface.

As we have used our artefact-free solution for a TD in a full-space to develop the artefact-free solution in a half-space, the presented validation test can be regarded as a simultaneous verification of the artefact-free solutions in both full space and half-space. All results presented and discussed here can be reproduced using our MATLAB codes, which accompany this paper.

2.5 Discussion

In this paper, we developed fully analytical, artefact-free solutions for a TD in a full-space and half-space. Our solution in a full-space consists of two equivalent configurations of three angular dislocations (Yoffe, 1960). Each of these configurations is free of any artefact singularities in its domain of definition. These domains of definition are complementary, that is they cover the entire $\mathbb{R}^3$ space. We also replaced the Burgers function equation in Yoffe (1960) with a more efficient equation based on Van Oosterom and Strackee (1983). This new equation,

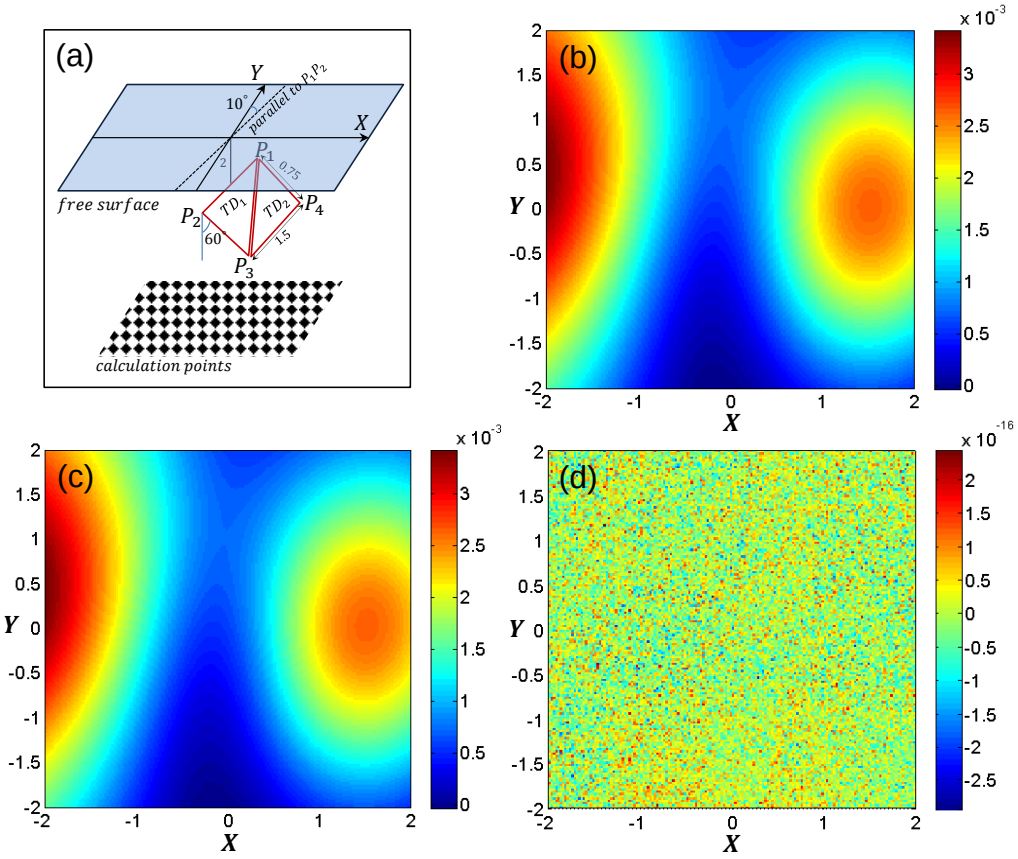

Figure 2.11: The validation of our approach against the Okada (1992) solution by superposing two triangular dislocations to construct a rectangular dislocation in a half-space with a slip vector of (0, 1, 0). (a) The model set-up. (b) The first component of the displacements on the grid shown in panel (a), calculated using our method. (c) The first component of the displacements on the calculation points, calculated using the Okada (1992) method. (d) The differences between (b) and (c). The X and Y coordinates have the same unit as the dislocation dimensions. The colour bars indicate the calculated displacements, which have the same unit as the slip vector components (see Section 2.4).

which we verified analytically, also addresses the problem of the Burgers function producing multiple outputs for a single input (Brown, 1975). Using this new full-space solution in the method of images, along with the harmonic function given by Comninou and Dundurs (1975), we developed a new artefact-free solution in a half-space. There is no rigid-body motion associated with our half-space solution because of the new configurations of the superposed angular dislocations.

2.5.1 Limitations of the method

The solutions that we developed for TDs in this paper are Volterra dislocations (Volterra, 1907). Therefore, a general disadvantage of our solution is that it can only account for a uniform slip on each TD surface. In other words, no variation in the slip on the surface of a single TD is allowed. As a result, because of the existing discontinuity of the slip vector components at the dislocation boundaries, the stresses there become unbounded. This may be inconvenient when calculating the displacements and stresses in the near field, for example, when considering the crack tip in a crack propagation problem. As a rule of thumb, the average length of the TD sides can be regarded as the characteristic distance that should exist between the calculation points and the dislocation boundaries to obtain accurate results (Crouch and Starfield, 1983). However, this rule does not apply to the centroid of the TD, for which the results are absolutely valid. Developing analytical solutions that allow for slip variations on the dislocation surface

as a linear function, for example, can address the problem.

In the development of the MATLAB codes, we frequently used the vectorisation technique, thus making the codes highly optimized for ordinary desktop computers. However, these vectorisation techniques are not supported by the parallel calculation functionalities of MATLAB. Therefore, the current version of our codes is not suited to parallel calculations in MATLAB on computers with multicore CPUs.

2.5.2 Improvements on and comparison to earlier works

The previous analytical solutions for the TD case, as mentioned above, are subject to various artefact singularities. The Yoffe (1960) approach, which was the first solution for TDs in a full space and is detailed in Section 2.2.1, exhibits artefact singularities on the extensions of the sides of the TD, as shown in Fig. 2.3. The other shortcoming of the Yoffe (1960) approach is related to the Burgers function producing multiple outputs at a single calculation point, as first considered by Brown (1975). Crouch and Starfield (1983) developed an alternate solution for a TD in a full-space, which was later utilised in a BEM implementation developed by Kuriyama and Mizuta (1993). The latter also reported the existence of singularities on the extensions of the sides of the TD, which is considered to be a major shortcoming of the method.

Jeyakumaran et al. (1992) developed the first solution for a TD in a half-space using the method detailed in Section 2.3.1. Nonetheless, as discussed in Section 2.3.2, the solution of Jeyakumaran et al. (1992) possesses new artefact singularities below and above the vertices of the TD, in addition to those present in the Yoffe (1960) full-space solution (Fig. 2.7). Thomas (1993) developed Poly3D, which is a BEM implementation written in the C programming language and is based on the Jeyakumaran et al. (1992) method. Using the geometric method elaborated on here in Section 2.3.2.2, Poly3D removes the artefact singularities on the extensions of the sides of the TD. However, the singularities below and above the vertices still remain. Meade (2007) also implemented the Jeyakumaran et al. (1992) approach using MATLAB and elaborated the method in greater detail. Although the Meade (2007) approach exhibits considerably higher accuracy than the Thomas (1993) outputs, none of the artefact singularities are addressed. To illustrate the effect of these singularities on the calculations, we recall the results of the validation test presented in Section 2.4 (see Table 2.3 and Fig. 2.10).

Comparing the displacements first, we find differences of less than 10^{-15} for the first three points (No. 1, No. 2 and No. 3), thus observing excellent agreement between the two methods. This is because these points are far from any artefact singularities. The singular results in the Meade (2007) outputs are represented by 'NaN', which stands for 'Not a Number'. We observe artefact singularities for all points underneath the vertices of the TD as well as along the downwards-dipping extensions of the TD sides. Because of the limited accuracy of the values stored in the computer, the point No. 8 in the Meade (2007) code is considered to be located not on the downwards-dipping line of the artefact singularity but merely in its vicinity. Therefore, the Meade (2007) approach produces an incorrect output that exhibits the numerical instability discussed in Section 2.3. Finally, we observe incorrect displacements for points No. 11 and No. 12, which are above the vertices of the TD. Although there are no artefact singularities near points No. 11 and No. 12, the miscalculation of the Burgers function in the Meade (2007) code results in a discontinuity in the displacements. This discontinuity is more apparent in Fig. 2.12, where we show the first component of the displacement vector in the neighbourhood of point No. 12.

When considering the calculated strains, for the first three points (No. 1, No. 2 and No. 3), we also detect differences of less than 10^{-15}. Nevertheless, for the remainder of the calculation points, apart from points No. 8 and No. 9, which exhibit large numerical instabilities, the output of the Meade (2007) code is 'NaN', reflecting the singularity of the calculations. This is partially

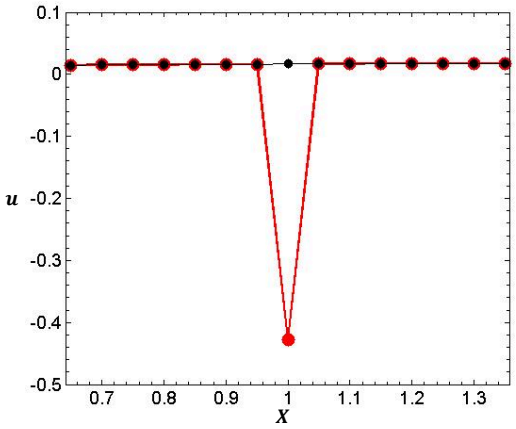

Figure 2.12: The discontinuity in the first component of the displacement ($\boldsymbol{u}$) along the X axis in the neighbourhood of point No. 12 above one of the vertices of the triangular dislocation (TD) depicted in Fig. 2.10 caused by the miscalculation of the Burgers function. The black line shows the results of our code, and the red curve shows the output of the Meade (2007) code. The axes may have any arbitrary units of length (see Section 2.4).

attributable to the artefact singularities beneath the vertices and along the downwards-dipping extensions of the TD sides. For the remaining calculation points, however, the singularity of the strain calculations is caused by the use of inappropriate partial derivatives of the Burgers function rather than eq. (2.11). Apart from the artefact singularities discussed here, the results of our code and those of the Meade (2007) code at any other calculation point in a half-space exhibit perfect agreement on the order of 10^{-15}, which is the accuracy of double-precision numbers near unity in MATLAB.

Gimbutas et al. (2012) applied a combination of analytical and numerical quadratures to the Green's function for full-space (Kelvin, 1848) and half-space (Mindlin, 1936) point sources to develop the corresponding solutions as well as corresponding FORTRAN codes for a TD in a full-space and half-space. To address the problem of artefact singularities in a full-space, Gimbutas et al. (2012) approximated the solution using a Taylor series expansion inside the cones that encircle the extension of each TD side. These cones have a vertex angle of 2×10^{-8} rad, and their origins are the TD vertices (Gimbutas et al., 2012). Similar to other solutions based on numerical quadrature schemes, the presence of a fixed number for the vertex angle serves as a threshold for this approach and results in scale-dependent outputs. To remove the artefact singularities and obtain the half-space solution, a fully numerical adaptive quadrature rule for calculating the image dislocation and the contribution of the potential function is applied (Gimbutas et al., 2012). This technique, although it offers certain advantages, yields low-quality results for calculation points and TDs near the free surface where the main and image dislocations are very close to each other. In particular, the calculations at the centroid of a TD that lies at the free surface become either singular or ill-posed.

The artefact-free solutions for a TD in a full-space and half-space that we developed in this paper are fully analytical, and no approximations or series expansion methods are applied in our approach. Consequently, our solutions are independent of the units of the input parameters, and the accuracy of the results, as discussed in Section 2.4, is on the order of 10^{-15}, equivalent to the accuracy of double-precision values for numbers near unity. By reducing the number of arc-tangent terms present in the equations that we used for the calculation of the Burgers function in the displacement calculations, we addressed the problem of multi-valuedness in the displacements. Moreover, we modified the equations in accordance with the effect of the free surface presented in Meade (2007) by manually grouping similar terms in the equations. We also used eq. (2.10) for the calculation of the contributions of the Burgers function to these equations. As a result, these equations became much less complex, and we thereby reduced the

time required for large calculations by a factor of three. We developed optimized MATLAB codes to calculate the displacement, strain and stress fields associated with a TD in a full-space and half-space. These codes are available in the Supporting Information of this paper.

2.5.3 Application possibilities

Our solutions can be applied to a wide range of problems in modelling, including nano- and micro-fracturing and dislocations in engineering and physics as well as geological faults with an extent of several tens of kilometres. This wide range of applicability is because of the fully analytical approach that we used and also the scale-independent techniques that we developed for the removal of the artefact singularities. Our approach also allows for the use of complex meshes of any size for the TDs and can thus be used for the simulation of any curved surface in various disciplines. Our solutions can be used as the basis for other numerical methods, such as BEM, which utilize TDs as fundamental elements. Inverting the coseismic surface deformation for the slip on complex curved faults associated with earthquakes (Maerten et al., 2005), analysing the deformations and stress fields of volcanoes arising from fractures and pressurized reservoirs underneath realistic edifice topographies (Cayol and Cornet, 1997), and evaluating the excavation-induced displacements and stresses near man-made cavities (Kuriyama and Mizuta, 1993) are a few examples of the possible applications of this approach.

2.5.4 Implications and further work

TDs have the advantage that they can be used to simulate sources with complex geometries, such as reservoirs, cavities and curved fault zones, without leaving any discontinuities in the model. Considering the high performance of computational facilities that are available even on desktop computers and the availability of high-resolution observation techniques, the need for more sophisticated and more accurate modelling methods that can integrate many TDs is emerging more strongly than before. The ability to achieve quality calculations in such models is guaranteed by the application of our solutions, first, because the calculations involved in our solutions are not affected by the previously discussed artefact singularities and numerical instabilities (see Sections 2.2 and 2.3), and second, because our solutions are independent of the scale of the model parameters, including the number and size of the TDs in a model. Therefore, especially for high-resolution models, our solutions strongly improve model handling and results.

In the present work, we addressed only the problem of artefact singularities for a Volterra-type TD. For a more realistic simulation of natural processes, however, the intrinsic singularities at the edges of the TDs should also be taken into consideration, because these singularities result in infinite stresses accumulated at a single point in models, which are unlikely to arise in nature. Considering earlier attempts to remove these intrinsic singularities, since the 1960s, Cai et al. (2006) developed a non-singular analytical solution for the stress field of a straight segment dislocation in full space. For this purpose, the Burgers vector, which, in the classical definition of Volterra (1907), is concentrated at the points of a dislocation line, is given a new definition in which it is isotropically spread about every point within a certain spreading radius (Cai et al., 2006). In general, it is possible to use segment dislocations to construct a TD (Hirth and Lothe, 1982). Therefore, the segment solution of Cai et al. (2006) can also be used to develop a singularity-free solution for a TD in a full-space. However, because Cai et al. (2006) provided only the stress equations, the displacement equations would first need to be determined. Using these equations along with the coordinate transformation scheme (see Appendix 2.A) and the contributions of the Burgers function (see Section 2.2.3), the development of such a solution seems straightforward. However, reasonable values for the spreading function that corresponds

to the Cai et al. (2006) solution and its physical interpretations in various applications, such as those in geophysics, remain to be discussed. Moreover, for the half-space solution, new equations for the harmonic potential function in accordance with the new singularity-free equations provided in Cai et al. (2006) also have yet to be developed.

2.6 Conclusion

Our work builds on earlier developments and addresses some of the major limitations of commonly used solutions for a TD in a full-space and half-space. We developed piecewise analytical solutions without applying any analytical or numerical approximations. Our solutions consist of two sets of equivalent closed-form equations, each of which is free of artefact singularities and numerical instabilities on one of two complementary subspaces of the entire elastic medium. Using the barycentric coordinate system, we developed simple inequalities that allow for the selection of the optimal configuration for each calculation point. The new equations for the Burgers functions associated with the angular and triangular dislocations that we presented in this paper are more computationally efficient than previous equations for this purpose.

Our solutions are fully generic and highly flexible, in the sense that they do not demand any special care with regard to artefact singularities, unique ill-posed geometries or numerical-scale dependencies. Therefore, these solutions can be applied to a variety of problems in geophysics, engineering and physics, without requiring any alterations in the units of the input data or the geometric structures of the triangular dislocations.

Based on the details of the techniques and the flowchart guidance provided here, computer codes that implement our method can be easily written in any desired programming language. We also developed highly optimized MATLAB functions that facilitate the use of our solution in practice, making these codes very suitable for use as a basis for the development of implementations of other numerical approaches, such as the BEM, that must be run repeatedly over large data sets, especially to solve inverse problems.

The numerical validation of our solution using the widely used analytical solution for an RD in half-space (Okada, 1992) demonstrated excellent agreement between the two solutions up to the round-off error of double-precision values.

Appendix

2.A General scheme for the coordinate transformation

To transform coordinates between two Cartesian coordinate systems, we utilize vector linear algebra operations. By using this method, we can avoid the presence of rotation matrices in the equations and perform the transformations more efficiently using a single transformation matrix rather than three rotation matrices. If $\{\vec{e}_1, \vec{e}_2, \vec{e}_3\}$ and $\{\vec{f}_1, \vec{f}_2, \vec{f}_3\}$ are two arbitrary orthonormal bases for $\mathbb{R}^3$ that represent two Cartesian coordinate systems, then any arbitrary vector $\vec{r}$ can be represented as a linear combination of the basis vectors as follows:

$$\vec{r} = \gamma_1\vec{e}_1 + \gamma_1\vec{e}_2 + \gamma_1\vec{e}_3 \tag{2.A.1}$$

or

$$\vec{r} = \delta_1\vec{f}_1 + \delta_1\vec{f}_2 + \delta_1\vec{f}_3. \tag{2.A.2}$$

We define $r_1 = (\gamma_1\ \gamma_2\ \gamma_3)^T$ and $r_2 = (\delta_1\ \delta_2\ \delta_3)^T$ as the coordinates of $\vec{r}$ in the first and second coordinate systems, respectively. If the columns of the matrix

$$A = \begin{pmatrix} m_1 & n_1 & k_1 \\ m_2 & n_2 & k_2 \\ m_3 & n_3 & k_3 \end{pmatrix}$$

represent the coordinates of $\vec{e}_1$, $\vec{e}_2$ and $\vec{e}_3$ in the second coordinate system, then we can write

$$\begin{cases} \vec{e_1} = m_1\vec{f}_1 + m_2\vec{f}_2 + m_3\vec{f}_3 \\ \vec{e_2} = n_1\vec{f}_1 + n_2\vec{f}_2 + n_3\vec{f}_3 \\ \vec{e_3} = k_1\vec{f}_1 + k_2\vec{f}_2 + k_3\vec{f}_3 \end{cases}$$

Substituting these terms into eq. (2.A.1) and regrouping the result, we obtain

$$\begin{aligned} \vec{r} = &(\gamma_1 m_1 + \gamma_2 n_1 + \gamma_3 k_1)\,\vec{f}_1 + \\ &(\gamma_1 m_2 + \gamma_2 n_2 + \gamma_3 k_2)\,\vec{f}_2 + \\ &(\gamma_1 m_3 + \gamma_2 n_3 + \gamma_3 k_3)\,\vec{f}_3, \end{aligned}$$

which, using matrix notation, can be written as

$$r_2 = Ar_1. \tag{2.A.3}$$

Therefore, eq. (2.A.3) performs the direct vector transformation from the first coordinate system into the second, and the matrix A is the transformation matrix. Note that eq. (2.A.3) is used only for the transformation of free vectors, such as displacement vectors, which do not depend on the origin of the coordinate system. For the transformation of a position vector of

a calculation point or a TD vertex, we use the following equation:

$$r_2 = Ar_1 + r_{02}, \tag{2.A.4}$$

where r_{02} is the translation matrix and includes the coordinates of the origin of the first coordinate system in the second coordinate system. Moreover, because of the orthonormality of the bases, it is straightforward to show that $AA^T = AA^{-1} = I$, where I is the identity matrix. Therefore, the inverse vector transformation for a displacement vector will be

$$r_1 = A^T r_2. \tag{2.A.5}$$

Similarly, we write the inverse vector transformation for a position vector as

$$r_1 = A^T r_2 + r_{01}, \tag{2.A.6}$$

where r_{01} is the translation matrix, which includes the coordinates of the origin of the second coordinate system in the first coordinate system. By substituting eq. (2.A.6) into eq. (2.A.4), it is straightforward to show that

$$r_{02} = -Ar_{01}, \tag{2.A.7}$$

or equivalently,

$$r_{01} = -A^T r_{02}. \tag{2.A.8}$$

When eq. (2.A.8) is substituted into eq. (2.A.6), the latter can be written in the form

$$r_1 = A^T \left(r_2 - r_{02}\right), \tag{2.A.9}$$

which can be used independently from eq. (2.A.6) whenever r_{02} is given.

Finally, the transformation equation for a second-rank tensor S_1 from the first coordinate system into the second is as follows (Segall, 2010):

$$S_2 = AS_1A^T. \tag{2.A.10}$$

2.B The angular dislocation equations

Yoffe (1960) developed the equations for the displacement and stress fields of an angular dislocation in a full-space, as illustrated in Fig. 2.1(a). Here, we provide the complete set of these equations, which we have corrected for a few misprints (in bold). In the following, (x, y, z) are the coordinates of the calculation point, (b_x, b_y, b_z) are the coordinates of the slip vector, and φ is the Burgers function at the calculation point corresponding to the angular dislocation (Yoffe, 1960), which can be calculated using eq. (2.10) in Section 2.2.3.

For each component of the displacement vector (u, v, w), we consider the contributions of the slip vector components separately, as follows:

$$u_x = \frac{b_x}{8\pi\left(1-\nu\right)}\left[\frac{xy}{r\left(r-z\right)} - \frac{x\eta}{r\left(r-\zeta\right)}\right]$$

$$v_x = \frac{b_x}{8\pi\left(1-\nu\right)}\left[\frac{\eta\sin\alpha}{r-\zeta} - \frac{y\eta}{r\left(r-\zeta\right)} + \frac{y^2}{r\left(r-z\right)}\right.$$

$$
\begin{aligned}
&+ (1-2\nu)\left(\cos\alpha \ln(r-\zeta) - \ln(r-z)\right)\Bigg] \\
w_x &= \frac{b_x}{8\pi(1-\nu)}\left[\frac{\eta\cos\alpha}{r-\zeta} - \frac{y}{r} - \frac{\eta z}{r(r-\zeta)} - (1-2\nu)\sin\alpha\ln(r-\zeta)\right] \\
u_y &= \frac{b_y}{8\pi(1-\nu)}\left[\frac{x^2\cos\alpha}{r(r-\zeta)} - \frac{x^2}{r(r-z)}\right. \\
&\left. - (1-2\nu)\left(\cos\alpha\ln(r-\zeta) - \ln(r-z)\right)\right] \\
v_y &= \frac{b_y x}{8\pi(1-\nu)}\left[\frac{y\cos\alpha}{r(r-\zeta)} - \frac{\sin\alpha\cos\alpha}{r-\zeta} - \frac{y}{r(r-z)}\right] \\
w_y &= \frac{b_y x}{8\pi(1-\nu)}\left[\frac{z\cos\alpha}{r(r-\zeta)} - \frac{\cos^2\alpha}{r-\zeta} + \frac{1}{r}\right] \\
u_z &= \frac{b_z\sin\alpha}{8\pi(1-\nu)}\left[(1-2\nu)\ln(r-\zeta) - \frac{x^2}{r(r-\zeta)}\right] \\
v_z &= \frac{b_z x\sin\alpha}{8\pi(1-\nu)}\left[\frac{\sin\alpha}{r-\zeta} - \frac{y}{r(r-\zeta)}\right] \\
w_z &= \frac{b_z x\sin\alpha}{8\pi(1-\nu)}\left[\frac{\cos\alpha}{r-\zeta} - \frac{z}{r(r-\zeta)}\right],
\end{aligned}
\tag{2.B.1}
$$

where $\eta = y\cos\alpha - z\sin\alpha, \zeta = y\sin\alpha + z\cos\alpha, r = \sqrt{x^2+y^2+z^2}$ and ν is the Poisson's ratio.

Now, if we define the 'incomplete' displacement vector components as

$$
\begin{aligned}
u^0 &= u_x + u_y + u_z \\
v^0 &= v_x + v_y + v_z \\
w^0 &= w_x + w_y + w_z,
\end{aligned}
\tag{2.B.2}
$$

then the complete displacement vector components can be calculated as follows:

$$
\begin{aligned}
u &= b_x\varphi + u^0 \\
v &= b_y\varphi + v^0 \\
w &= b_z\varphi + w^0.
\end{aligned}
\tag{2.B.3}
$$

By comparing eqs (2.B.2) and (2.B.3), it can be observed that the final displacements are the sum of the incomplete displacements and the product of the slip vector (b_x, b_y, b_z) with the Burgers function φ.

The strain-field equations are functions of the partial derivatives of the displacements. The final strain equations, after the simplification and regrouping of several algebraic terms in the partial derivatives of the displacements, can be represented as follows:

$$
\begin{aligned}
\epsilon_{xx} &= b_x\frac{\partial\varphi}{\partial x} \\
&+ \frac{b_x}{8\pi(1-\nu)}\left[\frac{\eta}{\xi r} + \frac{\eta x^2}{\xi^2 r^2} - \frac{\eta x^2}{\xi r^3} + \frac{y}{r(r-z)} - \frac{x^2 y}{r^2(r-z)^2} - \frac{x^2 y}{r^3(r-z)}\right] \\
&- \frac{b_y x}{8\pi(1-\nu)}\left[\left(\frac{2\nu+1}{\xi r} + \frac{x^2}{\xi^2 r^2} - \frac{x^2}{\xi r^3}\right)\cos\alpha + \frac{2\nu+1}{r(r-z)} - \frac{x^2}{r^2(r-z)^2}\right.
\end{aligned}
$$

$$
\begin{aligned}
&- \frac{x^2}{r^3\left(r-z\right)}\Bigg] + \frac{b_z x \sin\alpha}{8\pi\left(1-\nu\right)}\left(\frac{2\nu+1}{\xi r} + \frac{x^2}{\xi^2 r^2} - \frac{x^2}{\xi r^3}\right)\\
\epsilon_{yy} &= b_y \frac{\partial\varphi}{\partial y}\\
&+ \frac{b_x}{8\pi\left(1-\nu\right)}\Bigg[\left(\frac{1}{\xi r} + \frac{\left(r\sin\alpha - y\right)^2}{\xi^2 r^2} - \frac{y^2}{\xi r^3}\right)\eta + \frac{\left(2\nu+1\right)y}{r\left(r-z\right)} - \frac{y^3}{r^2\left(r-z\right)^2}\\
&- \frac{y^3}{r^3\left(r-z\right)} - \frac{2\nu\cos\alpha\left(r\sin\alpha - y\right)}{\xi r}\Bigg] - \frac{b_y x}{8\pi\left(1-\nu\right)}\Bigg[\frac{1}{r\left(r-z\right)}\\
&- \frac{y^2}{r^2\left(r-z\right)^2} - \frac{y^2}{r^3\left(r-z\right)} + \left(\frac{1}{\xi r} + \frac{\left(r\sin\alpha - y\right)^2}{\xi^2 r^2} - \frac{y^2}{\xi r^3}\right)\cos\alpha\Bigg]\\
&+ \frac{b_z x \sin\alpha}{8\pi\left(1-\nu\right)}\left[\frac{1}{\xi r} + \frac{\left(r\sin\alpha - y\right)^2}{\xi^2 r^2} - \frac{y^2}{\xi r^3}\right]\\
\epsilon_{zz} &= b_z \frac{\partial\varphi}{\partial z}\\
&+ \frac{b_x}{8\pi\left(1-\nu\right)}\left[\frac{\eta}{\xi r} + \frac{\eta\left(r\cos\alpha - z\right)^2}{\xi^2 r^2} - \frac{\eta z^2}{\xi r^3} + \frac{yz}{r^3} + \frac{2\nu\sin\alpha\left(r\cos\alpha - z\right)}{\xi r}\right]\\
&- \frac{b_y x}{8\pi\left(1-\nu\right)}\left[\left(\frac{1}{\xi r} + \frac{\left(r\cos\alpha - z\right)^2}{\xi^2 r^2} - \frac{z^2}{\xi r^3}\right)\cos\alpha + \frac{z}{r^3}\right]\\
&+ \frac{b_z x \sin\alpha}{8\pi\left(1-\nu\right)}\left[\frac{1}{\xi r} + \frac{\left(r\cos\alpha - z\right)^2}{\xi^2 r^2} - \frac{z^2}{\xi r^3}\right]\\
\epsilon_{xy} &= \frac{1}{2}b_x\frac{\partial\varphi}{\partial y} + \frac{1}{2}b_y\frac{\partial\varphi}{\partial x}\\
&- \frac{b_x}{8\pi\left(1-\nu\right)}\Bigg[\frac{xy^2}{r^2\left(r-z\right)^2} - \frac{\nu x}{r\left(r-z\right)} + \frac{xy^2}{r^3\left(r-z\right)} - \frac{\nu x\cos\alpha}{\xi r}\\
&+ \frac{\eta x\left(r\sin\alpha - y\right)}{\xi^2 r^2} + \frac{\eta x y}{\xi r^3}\Bigg] + \frac{b_y}{8\pi\left(1-\nu\right)}\Bigg[\frac{x^2 y}{r^2\left(r-z\right)^2} - \frac{\nu y}{r\left(r-z\right)}\\
&+ \frac{x^2 y}{r^3\left(r-z\right)} + \frac{\nu\cos\alpha\left(r\sin\alpha - y\right)}{\xi r} + \frac{x^2\cos\alpha\left(r\sin\alpha - y\right)}{\xi^2 r^2} + \frac{x^2 y\cos\alpha}{\xi r^3}\Bigg]\\
&- \frac{b_z\sin\alpha}{8\pi\left(1-\nu\right)}\left[\frac{\nu\left(r\sin\alpha - y\right)}{\xi r} + \frac{x^2\left(r\sin\alpha - y\right)}{\xi^2 r^2} + \frac{x^2 y}{\xi r^3}\right]\\
\epsilon_{xz} &= \frac{1}{2}b_x\frac{\partial\varphi}{\partial z} + \frac{1}{2}b_z\frac{\partial\varphi}{\partial x}\\
&- \frac{b_x}{8\pi\left(1-\nu\right)}\left[-\frac{xy}{r^3} + \frac{\boldsymbol{\nu} x\sin\alpha}{\xi r} + \frac{\eta x\cos\alpha}{\xi^{\mathbf{2}} r} - \frac{\eta x z}{\xi^2 r^2} + \frac{\eta x z}{\xi r^3}\right]\\
&+ \frac{b_y}{8\pi\left(1-\nu\right)}\Bigg[-\frac{x^2}{r^3} + \frac{\nu}{r} + \frac{\nu\cos\alpha\left(r\cos\alpha - z\right)}{\xi r} + \frac{x^2\cos\alpha\left(r\cos\alpha - z\right)}{\xi^2 r^2}\\
&+ \frac{x^2 z\cos\alpha}{\xi r^3}\Bigg] - \frac{b_z\sin\alpha}{8\pi\left(1-\nu\right)}\left[\frac{\nu\left(r\cos\alpha - z\right)}{\xi r} + \frac{x^2\left(r\cos\alpha - z\right)}{\xi^2 r^2} + \frac{x^2 z}{\xi r^3}\right]
\end{aligned}
$$

$$
\begin{aligned}
\epsilon_{yz} = & \frac{1}{2} b_y \frac{\partial \varphi}{\partial z} + \frac{1}{2} b_z \frac{\partial \varphi}{\partial y} \\
& + \frac{b_x}{8\pi (1-\nu)} \left[\frac{y^2}{r^3} - \frac{\nu}{r} - \frac{\nu \cos\alpha (r\cos\alpha - z)}{\xi r} + \frac{\nu \sin\alpha (r\sin\alpha - y)}{\xi r} \right. \\
& \left. + \frac{\eta \sin\alpha \cos\alpha}{\xi^2} - \frac{\eta (y\cos\alpha + z\sin\alpha)}{\xi^2 r} + \frac{\eta y z}{\xi^2 r^2} - \frac{\eta y z}{\xi r^3} \right] - \frac{b_y x}{8\pi (1-\nu)} \left[\frac{y}{r^3} \right. \\
& \left. + \frac{\sin\alpha \cos^2\alpha}{\xi^2} - \frac{\cos\alpha (y\cos\alpha + z\sin\alpha)}{\xi^2 r} + \frac{y z \cos\alpha}{\xi^2 r^2} - \frac{y z \cos\alpha}{\xi r^3} \right] \\
& - \frac{b_z x \sin\alpha}{8\pi (1-\nu)} \left[\frac{yz}{\xi r^3} - \frac{\sin\alpha \cos\alpha}{\xi^2} + \frac{y\cos\alpha + z\sin\alpha}{\xi^2 r} - \frac{yz}{\xi^2 r^2} \right],
\end{aligned}
\tag{2.B.4}
$$

where $\xi = y\sin\alpha + z\cos\alpha - r$.

The partial derivatives of the Burgers function, that is $\frac{\partial \varphi}{\partial x}$, $\frac{\partial \varphi}{\partial y}$ and $\frac{\partial \varphi}{\partial z}$, which appear in eq. (2.*B*.4), must be calculated from eq. (2.11) in Section 2.2.3.

Finally, the stresses can be calculated using the isotropic form of Hooke's law (Segall, 2010):

$$
\begin{aligned}
\sigma_{xx} &= 2\mu\epsilon_{xx} + \lambda (\epsilon_{xx} + \epsilon_{yy} + \epsilon_{zz}) \\
\sigma_{yy} &= 2\mu\epsilon_{yy} + \lambda (\epsilon_{xx} + \epsilon_{yy} + \epsilon_{zz}) \\
\sigma_{zz} &= 2\mu\epsilon_{zz} + \lambda (\epsilon_{xx} + \epsilon_{yy} + \epsilon_{zz}) \\
\sigma_{xy} &= 2\mu\epsilon_{xy} \\
\sigma_{xz} &= 2\mu\epsilon_{xz} \\
\sigma_{yz} &= 2\mu\epsilon_{yz},
\end{aligned}
\tag{2.B.5}
$$

where μ and λ are the Lamé coefficients; μ is the shear modulus.

2.C The barycentric coordinate system

The barycentric coordinate system is an efficient way to represent the coordinates of points in the plane of a triangle with respect to its vertices. The very simple and often symmetric form of the equations of geometric objects in this coordinate system makes it the most appropriate system for many problems in analytical geometry and computer sciences that are related to the geometrical properties of a triangle (Bottema, 2008).

It is well known from mechanics that for a point G that is the centre of mass, or the barycentre, of three masses m_1, m_2 and m_3 that are attached to the vertices of a triangle $A_1A_2A_3$, respectively, we can write

$$
\vec{r}_G = \frac{m_1\vec{r}_1 + m_2\vec{r}_2 + m_3\vec{r}_3}{m_1 + m_2 + m_3},
\tag{2.C.1}
$$

where all vectors are the position vectors in an arbitrary two-dimensional coordinate system in the plane of the triangle. By generalizing this concept to include negative weights as well, the barycentric coordinates of an arbitrary point P in the plane of an arbitrary triangle $A_1A_2A_3$ with respect to this triangle can be regarded as the ordered triple (m_1, m_2, m_3), which is composed of the weights that are placed on the vertices of $A_1A_2A_3$; point P then becomes the centre of mass of the system of masses (Ungar, 2010). Here, we use the normalized barycentric coordinates (μ_1, μ_2, μ_3), also known as areal coordinates, which are calculated by dividing each coordinate

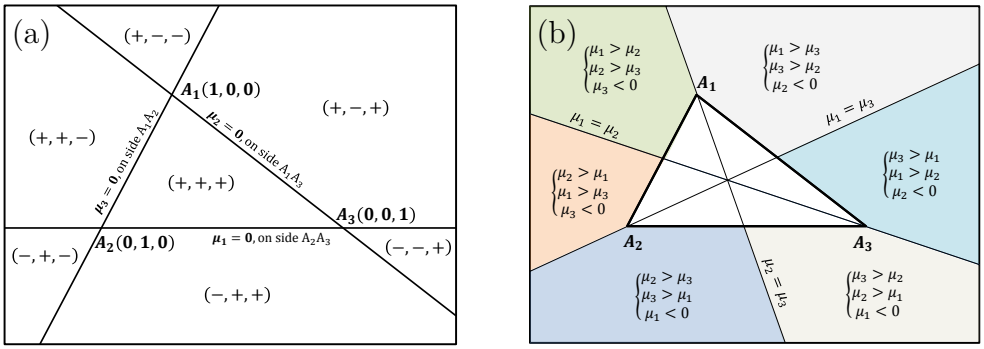

Figure 2.C.1: (a) Geometrical properties of the barycentric coordinate system. The barycentric coordinates of the vertices, the equations of the sides and the signs of the components of the barycentric coordinates of the points in the various partitions delimited by the sides of the triangle $A_1A_2A_3$. (b) Certain geometrical properties of the barycentric coordinate system. The equations of the medians of the triangle $A_1A_2A_3$ and the inequalities that define the partitions illustrated in Fig. 2.4.

by the sum of all three (Coxeter, 1969); we can then write

$$\mu_1 + \mu_2 + \mu_3 = 1, \tag{2.C.2}$$

where

$$\mu_i = \frac{m_i}{\sum_{i=1}^{3} m_i}, \tag{2.C.3}$$

for $i = 1, 2, 3$.

Considering eq. (2.C.1) for point P together with eq. (2.C.2), we obtain

$$\begin{pmatrix} x_P \\ y_P \end{pmatrix} = \begin{pmatrix} \mu_1 x_1 + \mu_2 x_2 + (1 - \mu_1 - \mu_2)\, x_3 \\ \mu_1 y_1 + \mu_2 y_2 + (1 - \mu_1 - \mu_2)\, y_3 \end{pmatrix}, \tag{2.C.4}$$

or equivalently,

$$\begin{pmatrix} \mu_1 \\ \mu_2 \end{pmatrix} = \begin{pmatrix} x_1 - x_3 & x_2 - x_3 \\ y_1 - y_3 & y_2 - y_3 \end{pmatrix}^{-1} \begin{pmatrix} x_P \\ y_P \end{pmatrix}. \tag{2.C.5}$$

It is now quite straightforward to calculate μ_3 from eq. (2.C.2) after replacing μ_1 and μ_2 with their values calculated from eq. (2.C.5). Note that although the barycentric coordinates are expressed in terms of three components, they represent the position of a point in a 2-D space. This fact is also indicated by eq. (2.C.2), which shows that these components are not independent.

We summarize certain properties of the normalized barycentric coordinate system in Fig. 2.C.1. Independent of the Cartesian coordinates of the vertices, the normalized barycentric coordinates of the vertices are always $(1, 0, 0)$, $(0, 1, 0)$ and $(0, 0, 1)$, and $\mu_i = 0$ is the equation of the line that contains the side opposite to vertex A_i, for $i = 1, 2, 3$ (Ungar, 2010). The plus and minus signs in the parentheses in Fig. 2.C.1(a) represent the signs of the barycentric coordinates of the points in each of the partitions formed by these lines, which pass through each pair of vertices in the plane of the triangle $A_1A_2A_3$. Each of the other partitions in Fig. 2.C.1(b), which are formed by the medians of the triangle $A_1A_2A_3$, is represented by a set of three simple inequalities. It is also trivial to show that $\mu_1 = \mu_2$, $\mu_1 = \mu_3$ and $\mu_2 = \mu_3$ are the equations of the medians (Ungar, 2010).

Chapter 3

Compound dislocation models (CDMs) for volcano deformation analyses

Abstract

Volcanic crises are often preceded and accompanied by volcano deformation caused by magmatic and hydrothermal processes. Fast and efficient model identification and parameter estimation techniques for various sources of deformation are crucial for process understanding, volcano hazard assessment and early warning purposes. As a simple model that can be a basis for rapid inversion techniques, we present a compound dislocation model (CDM) that is composed of three mutually orthogonal rectangular dislocations (RDs). We present new RD solutions, which are free of artefact singularities and that also possess full rotational degrees of freedom. The CDM can represent both planar intrusions in the near field and volumetric sources of inflation and deflation in the far field. Therefore, this source model can be applied to shallow dikes and sills, as well as to deep planar and equidimensional sources of any geometry, including oblate, prolate and other triaxial ellipsoidal shapes. In either case the sources may possess any arbitrary orientation in space. After systematically evaluating the CDM, we apply it to the co-eruptive displacements of the 2015 Calbuco eruption observed by the Sentinel-1A satellite in both ascending and descending orbits. The results show that the deformation source is a deflating vertical lens-shaped source at an approximate depth of 8 km centred beneath Calbuco volcano. The parameters of the optimal source model clearly show that it is significantly different from an isotropic point source or a single dislocation model. The Calbuco example reflects the convenience of using the CDM for a rapid interpretation of deformation data.[1]

[1]Originally published as: Nikkhoo, M., Walter, T. R., Lundgren, P. R., Prats-Iraola, P. (2017): Compound dislocation models (CDMs) for volcano deformation analyses. - Geophysical Journal International, 208 (2): 877-894. doi:10.1093/gji/ggw427

3.1 Introduction

Since their early development, analytical models of crustal deformation have been used to interpret volcano deformation processes (Segall, 2010; Lisowski, 2007). Despite their simplicity, the widespread application of these models has proven that they are notably useful tools as first-order approximations for studying physical processes at volcanoes. These models are based entirely on the mathematical theory of elasticity applied to the deformation of the Earth's surface and its interior due to forces or dislocations (Love, 1944). The diversity of volcano deformation processes (see Segall, 2010) requires a flexible representation of the wide variation in source geometries in elastic media. Despite being in use for decades, some basic analytical models based on either concepts of dislocations (Okada, 1985, 1992) or forces (Davis, 1986) include numerical artefacts and structural imperfections that are to be addressed in this paper.

The simplest models of planar volcanic sources, namely, dikes and sills, are those based on rectangular dislocations (RDs) with only a prescribed uniform opening (Segall, 2010). One limitation of the existing RD solutions (Okada, 1985, 1992) is that they lack full rotational degrees of freedom. The reason for this limitation is that in these solutions, two parallel edges of an RD can be dipping at any arbitrary angle, but the other two edges, which are perpendicular to the first two, have to be parallel to the free surface. The existence of the artefact singularities along the edges and below and above the vertices is the other problem with these RD solutions. Okada (1992) reported this problem and addressed it in a small neighbourhood of the artefact singularities. The predefined size of the neighbourhood, however, makes the Okada (1992) analytical solution scale dependent, which means that the solution depends on the dimensions of the RDs and on the distribution of the calculation points in a model. Bradley and Segall (2012) addressed the artefact singularities along the edges of RDs but not below and above their vertices. Nevertheless, neither of these attempts fully addressed the problem of artefact singularities.

The widely known point-source models of pressurized cavities are based on force dipoles. The simplest case in this group of cavity models is the centre of dilatation, referred to as the Mogi model (Mogi, 1958). The Mogi model is a point-source approximation that is suitable only for deep spherical sources (Segall, 2010). Comparatively, the Davis (1986) point ellipsoidal cavity model is a point-source approximation for deep triaxial ellipsoidal sources, which also includes the spherical cavities as a special case. Nonetheless, compared to the Mogi model, the Davis (1986) solution has not yet been adopted as a routine modelling tool.

These issues also affect other analytical and numerical solutions. It has been shown that a certain combination of a few dislocations can reproduce the same displacement and stress fields as that of an isotropic pressurized point source (Bonafede and Ferrari, 2009). Had this model been generalized, it could have replaced most of the volcano deformation analytical models, which are based on either concepts of dislocations or forces.

Given the problems and imperfections in the aforementioned analytical solutions, developing new solutions that first enhance the functionality and improve the performance of these analytical solutions and then make the application of such solutions more convenient is of relevance.

In the following, we first develop new solutions for the surface, internal displacement and stress fields of RDs with full rotational degrees of freedom in both full-space and half-space. We address the problem of artefact singularities along the edges and below and above the vertices of the RDs. Using our RD solutions, we develop a compound dislocation model (CDM) as an alternative generalized source model of pressurized cavities and compare the CDM with analytical and numerical solutions. Finally, we apply the CDM to the 2015 April 22 co-eruptive displacements of Calbuco volcano in Chile. The application of the CDM to the Calbuco case study supports a vertically elongated lens-shaped source, which is significantly different from both spherical and planar volcanic sources. We show that the CDM can be simply integrated in

any optimization algorithm to invert the observed displacements for the unknown parameters of various deformation sources.

3.2 Methods

In this section, we develop new analytical solutions for RDs in a full-space and half-space based on the earlier works of Comninou and Dundurs (1975) and Nikkhoo and Walter (2015). We then elaborate a CDM, which is a generalization of the Bonafede and Ferrari (2009) dislocation source.

3.2.1 New analytical, artefact-free solutions for rectangular dislocations

We develop new artefact-free solutions for the displacement and stress fields associated with RDs with full rotational degrees of freedom in an elastic full-space and half-space.

In the first step, we construct two different but mathematically equivalent configurations of angular dislocations in a full-space (Fig. 3.1a). The double dislocation lines in Fig. 3.1(a) show the lines of artefact singularities. These lines in the first configuration are extended in directions that completely differ from those in the second configuration (Fig. 3.1a). The edges of the RD and their perpendicular bisectors, as well as the bisectors of the RD external angles, mark the boundaries between the two complementary partitions (white and dark shadings in Fig. 3.1b). Clearly, the artefact singularities of each configuration remain inclusively inside one of the two partitions. Additionally, the orthogonal projection of any calculation point onto the RD plane falls into only one of the two partitions. In the new RD solution, we first specify the partition that includes the projection of the calculation point, and then we use the configuration that is located in the other partition. In this way, we always avoid all of the artefact singularities in our RD solution. Moreover, we calculate the Burgers function associated with the RD as the sum of the Burgers functions of two triangular dislocations or four angular dislocations that form exactly the same RD (Nikkhoo and Walter, 2015).

In the second step, we apply the method of images directly to the new RD full-space solution and develop an artefact-free solution for an RD in a half-space (see Nikkhoo and Walter, 2015). For this purpose, using the artefact-free solution for RDs in a full-space, we calculate the main and image dislocation contributions. The sum of these two together with the free surface potential function contribution (Comninou and Dundurs, 1975) completes the solution for the RD in a half-space. Using this technique, we are able to calculate displacement and stress fields at depth and on the surface of a half-space.

As the final step, using the Comninou and Dundurs (1975) solution for an angular dislocation in a half-space, we develop another solution only for the surface displacement and stress fields associated with an RD with full rotational degrees of freedom in a half-space. Implementing two configurations and switching between them in a method similar to the full-space case, we remove the artefact singularities that appear when one of the RD edges is in the vicinity of or breaches the free surface (see Nikkhoo and Walter, 2015).

The geometrical parameters of the Okada (1985, 1992) and the new RD solutions are illustrated in Fig. 3.2. The strike angle (α) and the dip angle (δ) determine the orientation of the plane upon which the RD is located. We introduce a new parameter that controls the orientation of the RD in this 'extended RD plane'. This parameter, which we call the 'plunge angle' (θ), is the angle between the upper edge of the RD and the intersection of the free surface with the extended RD plane (see Fig. 3.2). The possibility of having a plunging upper edge in the new RD solutions allows them to possess full rotational degrees of freedom. In other words, the new RD solutions that we developed here extend the well-known Okada (1985, 1992) solutions by addressing the numerical artefacts and the geometrical limitation problem in their structure.

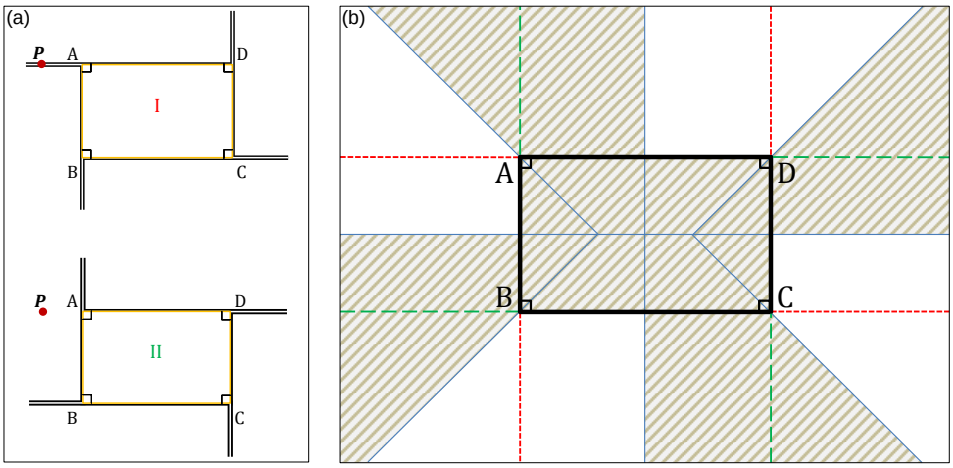

Figure 3.1: Addressing the problem of artefact singularities and numerical instabilities for rectangular dislocations (RDs). (a) Two different configurations for the RD, named by $ABCD$, are depicted. Apart from the placements of the semi-infinite dislocation lines, these two configurations are equivalent and can be used interchangeably. The calculation point **P** in the plane of the RD intersects one of the dislocation lines of the configuration **I**. For the 'alternative' configuration **II**, the point **P** is located at the maximum possible distance from the dislocation lines. Through the selection of the appropriate configuration, any artefact singularity or numerical instability can be avoided. (b) The partitions in the plane of the RD formed by the RD angle bisectors and the RD perpendicular bisectors (the solid blue lines). The red short dashed lines and the green dashed lines represent the lines of singularities of the RD configurations **I** and **II** in (a), respectively. Each line of singularity lies in only one of the partitions. To avoid artefact singularities and numerical instabilities, we use configuration **I** for the calculation points in which their orthogonal projection onto the RD plane falls in the dark partitions, and for the other calculation points, we use configuration **II**. Either configuration can be used for the points inside the RD.

3.2.2 The compound dislocation model

The displacement field of three mutually orthogonal square dislocations with the same prescribed uniform opening is equivalent to that of the Mogi model (Bonafede and Ferrari, 2009). We generalize this concept and use three mutually orthogonal RDs to develop a source model that can represent planar and volumetric sources of various aspect ratios. As a result of utilizing the RD solutions of Section 3.2.1 in its configuration, this generalized model may possess any arbitrary size and orientation in space (Fig. 3.3). We refer to this new model as the compound dislocation model (CDM).

In the following, we adopt two coordinate systems (see Fig. 3.3). The x, y and z axes, which lie on the CDM axes, establish a Cartesian coordinate system, which its origin is located on the CDM centroid. The lengths of the CDM semi-axes along the x, y and z axes (Fig. 3.3a) are equal to a, b and c, respectively. The RDs labelled as 'A', 'B' and 'C' are perpendicular to the x, y and z axes and their dimensions are $(2b, 2c)$, $(2a, 2c)$ and $(2a, 2b)$, respectively. The origin of the XYZ coordinate system is at the Earth's surface and the positive X, Y and Z axes point to the east, north and up, respectively. Therefore, the XYZ coordinate system is a local Earth-fixed Cartesian coordinate system and the XY plane represents the free surface. We use the XYZ coordinate system as the reference frame to define the orientation and location of the CDM and the xyz coordinate system. The clockwise rotations of ω_X, ω_Y and ω_Z about the X, Y and Z axes, respectively, specify the orientation of the CDM in space (see Fig. 3.3). Notice that before applying the rotations the xyz and XYZ coordinate systems are coincident (see Fig. 3.3a) and after applying the rotations these coordinate systems still share the same origin (see Fig. 3.3d). The translation vector that moves the CDM to its final location in space is $(X_0, Y_0, -d)$, where X_0, Y_0 and d are the east and north coordinates and the depth of the CDM centroid, respectively, in the XYZ coordinate system. Considering the angles of rotation in Figs 3.2 and 3.3 it can be shown that $\omega_X = \theta_A$, $\omega_Y = \frac{\pi}{2} - \delta_A$ and $\omega_Z = \alpha_A$, where θ_A, δ_A and α_A

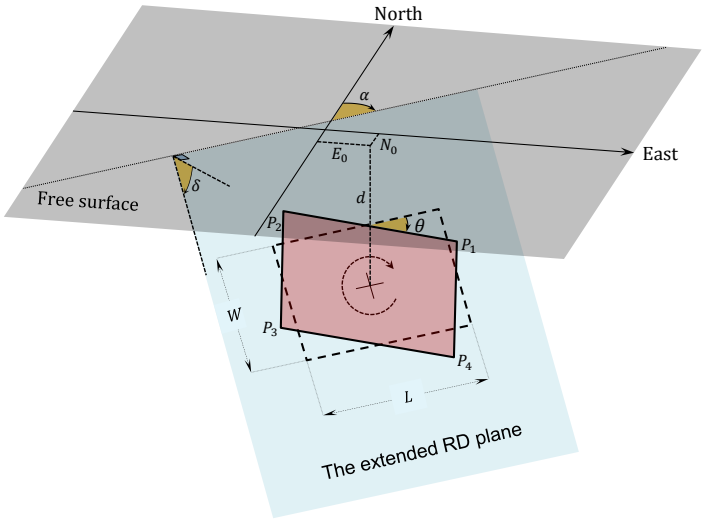

Figure 3.2: The geometry of the Okada (1985, 1992) solutions (dashed line) and the new solution (solid line) for a rectangular dislocation (RD) in a half-space. E_0, N_0 and d are the coordinates of the RD centroid, and L and W are the RD length and width, respectively. δ and α, which define the orientation of the RD plane, are the dip and strike angles, respectively. The plunge angle, θ, which only exists in the new solution, can change the orientation of the RD within the RD plane. Note that the upper edge of the Okada (1985, 1992) RD solutions is always parallel to the free surface. Because of having the plunge angle in its geometrical configuration, the new RD solution possesses full rotational degrees of freedom.

are the plunge angle, dip angle and strike angle of the first RD of the CDM, which is labelled as 'A' in Fig. 3.3. The RDs that form the CDM all have the same amount of uniform opening u. Therefore, the CDM has a total number of 10 parameters that include the CDM centroid location (X_0, Y_0, d), the CDM rotation angles $(\omega_X, \omega_Y, \omega_Z)$, the CDM semi-axes (a, b, c) and the opening (u).

If we consider the long-wavelength components of the displacement signal associated with a CDM in the far field only, then the model will effectively be a point source (Aki and Richards, 2002). Then, the CDM can be considered as a system of force dipoles located at its centroid, with a moment tensor equal to the integral of the moment density over the CDM surface (Aki and Richards, 2002). Due to the linearity of the integral operator, the moment tensor of the effective point source is equal to the sum of the moment tensors of the individual RDs in the model. Without loss of generality, we derive the moment tensor of the CDM in Fig. 3.3 with respect to the 'CDM-fixed', xyz coordinate system. For this CDM, the areas of the RDs 'A', 'B' and 'C' are equal to $S_A = 4bc$, $S_B = 4ac$ and $S_C = 4ab$, respectively, and u is the uniform opening of all three RDs. Based on the moment tensor density of a tension crack after Aki and Richards (2002), the moment tensor of the CDM in the xyz coordinate system will be

$$
\begin{aligned}
M^{CDM} = &\begin{pmatrix} (\lambda+2\mu)\,uS_A & 0 & 0 \\ 0 & \lambda u S_A & 0 \\ 0 & 0 & \lambda u S_A \end{pmatrix} \\
&+ \begin{pmatrix} \lambda u S_B & 0 & 0 \\ 0 & (\lambda+2\mu)\,uS_B & 0 \\ 0 & 0 & \lambda u S_B \end{pmatrix} \\
&+ \begin{pmatrix} \lambda u S_C & 0 & 0 \\ 0 & \lambda u S_C & 0 \\ 0 & 0 & (\lambda+2\mu)\,uS_C \end{pmatrix},
\end{aligned} \tag{3.1}
$$

where μ, known as the shear modulus, and λ are the Lamé coefficients.

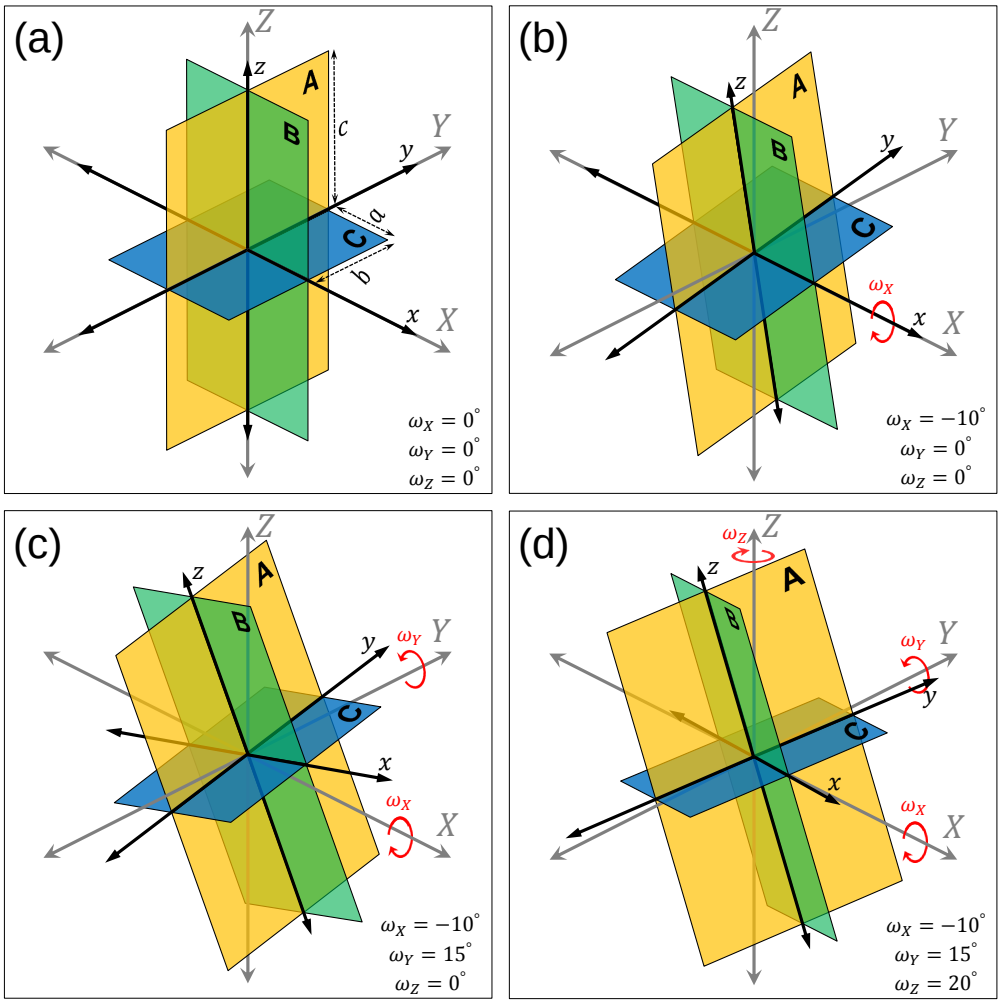

Figure 3.3: The geometrical structure and rotation angles of a compound dislocation model (CDM) composed of three rectangular dislocations (RDs), labelled as 'A', 'B' and 'C' (the yellow, green and blue planes). The origin of the XYZ coordinate system is at the Earth's surface and the positive X, Y and Z axes point to the east, north and up, respectively. The origin of the xyz coordinate system is located on the CDM centroid and the x, y and z axes are normal to 'A', 'B' and 'C', respectively. The xyz coordinate system is fixed to the CDM. The a, b and c are the semi-axes of the CDM along the x, y and z axes, respectively. The ω_X, ω_Y and ω_Z are angles of rotation about the X, Y and Z axes, respectively. Positive values of these angles correspond to clockwise rotations. (a) The initial orientation of the CDM. (b) The orientation of the CDM after applying ω_X. (c) The orientation of the CDM after applying ω_X and ω_Y. (d) The final orientation of the CDM. The numerical values of the rotation angles for this given example are denoted on the bottom right of each panel.

The contraction of the eq. (3.1) is

$$M^{CDM} = u \begin{pmatrix} \lambda S + 2\mu S_A & 0 & 0 \\ 0 & \lambda S + 2\mu S_B & 0 \\ 0 & 0 & \lambda S + 2\mu S_C \end{pmatrix}, \tag{3.2}$$

where $S = S_A + S_B + S_C = 4(ab + bc + ac)$.

Moreover, eq. (3.2) can be written as

$$M^{CDM} = \begin{pmatrix} \lambda\, \Delta V + 2\mu\, \Delta V_A & 0 & 0 \\ 0 & \lambda\, \Delta V + 2\mu\, \Delta V_B & 0 \\ 0 & 0 & \lambda\, \Delta V + 2\mu\, \Delta V_C \end{pmatrix}, \tag{3.3}$$

where $\Delta V_A = uS_A$, $\Delta V_B = uS_B$ and $\Delta V_C = uS_C$ are the potencies of the three RDs that compose the CDM and $\Delta V = \Delta V_A + \Delta V_B + \Delta V_C$ is the potency of the CDM. The *potency* is the product given by area × slip, which describes the strength of a dislocation source and holds the dimensions of volume change (Aki and Richards, 2002). The potency of a tensile dislocation is given by area × opening. From eq. (3.3), we can write

$$\Delta V = \frac{M_{kk}^{CDM}}{3K}, \tag{3.4}$$

where M_{kk}^{CDM} is the sum of the diagonal components of M^{CDM} and $K = \lambda + \frac{2}{3}\mu$ is the bulk modulus. The fact that M_{kk}^{CDM} is the first invariant of M^{CDM} shows that eq. (3.4) is independent of the coordinate system.

In the case of a CDM that simulates an inflating crack-like or volumetric cavity, the potency ΔV represents the volume available to host new fluids intruding into the cavity from the outside (Bonafede and Ferrari, 2009). The potency, however, must not be confused with the actual volume change δV, which represents the expansion that a deformation source applies to the surrounding elastic medium (see Aki and Richards, 2002; Kumagai et al., 2014; Ichihara et al., 2016).

3.2.2.1 The point CDM

We develop another source model by replacing the finite RDs in the CDM configuration with point tensile dislocations (Okada, 1992). This model is a point-source version of the CDM and we refer to it as the point CDM. Similar to other point sources such as the Mogi (1958) and Davis (1986) models the point CDM is exactly equivalent to a single moment tensor that represents a system of three mutually orthogonal force dipoles in a half-space (see Aki and Richards, 2002; Bonafede and Ferrari, 2009). In the far field, the point CDM and CDM are equivalent and therefore share the same moment tensor in eq. (3.3). The point CDM, from a geometrical point of view and by using the concept of the calculus of infinitesimals, can be visualized as the CDM in Fig. 3.3(a), but with the semi-axes a, b and c replaced with 'differential' semi-axes da, db and dc, respectively. Because the point CDM is inherently a point source, the differential semi-axes tend to zero, that is $da \longrightarrow 0$, $db \longrightarrow 0$ and $dc \longrightarrow 0$, respectively. However, the potencies of the point dislocations, that form the point CDM, and the ratios of the differential axes, that determine the geometrical shape of the point CDM, can be different from zero. The parameters that specify the location and spatial orientation of the point CDM are the same as those of the CDM. These parameters and the potencies of the point dislocations are the 9 parameters that uniquely specify the point CDM. Considering the definition of potency, it is straightforward to show that the axes ratios of the point CDM also can be calculated as ratios of the point dislocation potencies.

3.3 Evaluation of the compound dislocation model

In this section, we evaluate the CDM through comparisons with analytical and numerical solutions. We compare the CDM to point and finite ellipsoidal sources and assess the ability of the CDM to simulate deformation sources of various geometries and depths in the near field and far field.

3.3.1 The CDM and point ellipsoidal source comparison

Moment tensors reveal the far-field behaviour of their corresponding deformation sources (Aki and Richards, 2002) and can therefore be used for a quantitative assessment of these deformation sources. To better understand the performance of the CDM, we compare its moment tensor to that of the Davis (1986) point ellipsoidal cavity. Because the CDM and point CDM share the same moment tensors (see Section 3.2.2), the results of the comparison in this section, which are presented in Fig. 3.4, apply to both the CDM and point CDM.

The equivalent moment tensor M^E for the point ellipsoidal cavity after Davis (1986) is

$$M^E = \sigma^T V, \tag{3.5}$$

where σ^T is the transformation stress and V is the volume of the ellipsoid (see Segall, 2010).

To calculate σ^T, we implement the Carlson (1995) algorithms for numerical computation of elliptic integrals and the Eshelby (1957) transformation strain equations in a MATLAB function. Using eq. (3.2) and eq. (3.5), we calculate the moment tensors M^{CDM} and M^E that cover the entire range of various aspect ratios of the CDM and the Davis (1986) point ellipsoidal cavity. By applying the Trasatti et al. (2009) convention to the eigenvalues of the calculated moment tensors, we can represent the domains of moment eigenvalue ratios that correspond to the CDM and point ellipsoidal cavity in a Poisson solid, where $\mu = \lambda$ (Fig. 3.4). Clearly, the CDM possesses a wider domain, which as its subset also encompasses the domain of the ellipsoidal cavity model. This implies that corresponding to any arbitrary point ellipsoidal cavity, there is a CDM with the same moment tensor; however, the reverse statement does not necessarily hold. To derive the direct relationship, we assume that the diagonal moment tensor

$$M = \begin{pmatrix} M_{11} & 0 & 0 \\ 0 & M_{22} & 0 \\ 0 & 0 & M_{33} \end{pmatrix} \tag{3.6}$$

represents a point ellipsoidal cavity with arbitrary dimensions in the same xyz coordinate system introduced in Section 3.2.2. The potencies of the RDs that compose a CDM with the same moment tensor M are uniquely determined through comparing eq. (3.3) and eq. (3.6) as

$$\Delta V_A = \frac{1}{2\mu}\left(M_{11} - \frac{\lambda}{3K}M_{kk}\right),$$

$$\Delta V_B = \frac{1}{2\mu}\left(M_{22} - \frac{\lambda}{3K}M_{kk}\right),$$

$$\Delta V_C = \frac{1}{2\mu}\left(M_{33} - \frac{\lambda}{3K}M_{kk}\right), \tag{3.7}$$

where $M_{kk} = M_{11} + M_{22} + M_{33}$.

We find that eqs (3.3) and (3.7) establish a one-to-one relationship between any point ellipsoidal cavity and a CDM in the far field (see also Fig. 3.4). Moreover, it is straightforward to calculate the aspect ratios of the CDM from eq. (3.7). Using eqs (3.5) and (3.7) and the MATLAB function that we mentioned above, we also develop MATLAB functions for forward-model

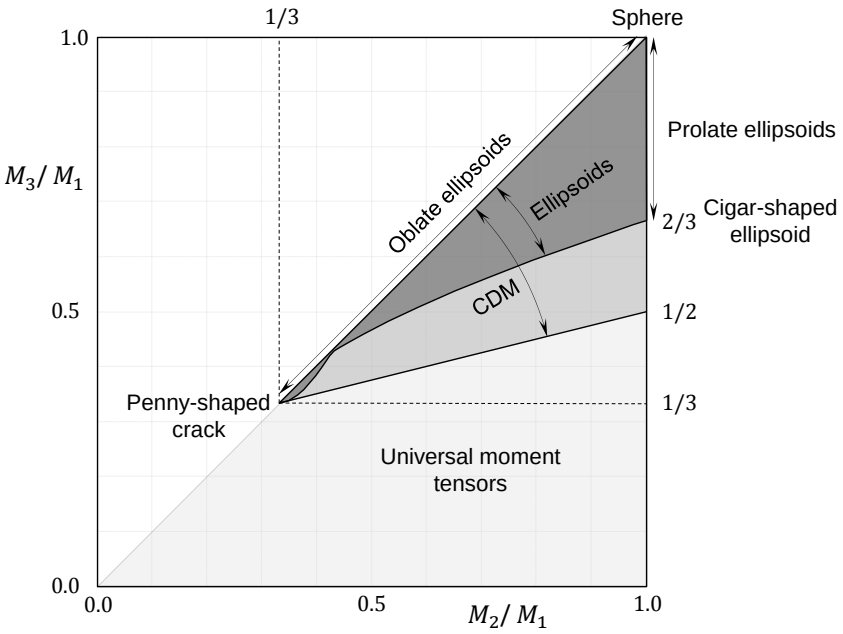

Figure 3.4: The moment tensor spectrum of the compound dislocation model (CDM) and point ellipsoidal cavity models in a Poisson solid ($\mu = \lambda$) as a function of M_2/M_1 and M_3/M_1, where M_1, M_2 and M_3 are the eigenvalues of the moment tensors and $M_1 \geq M_2 \geq M_3$ holds (Trasatti et al., 2009). The lower right-triangle area on the plot represents the universal set of moment tensors. The CDM possesses a wider moment tensor spectrum (light and dark gray area), which encompasses that of the ellipsoidal cavity (dark grey area) as a subset.

calculations associated with point ellipsoidal cavities.

The uniform pressure p on the walls of a pressurized ellipsoidal cavity with a volume of V is related to the actual volume change δV^E of the cavity through

$$\frac{\delta V^E}{V} - \epsilon^T_{kk} = -\frac{p}{K}, \tag{3.8}$$

where ϵ^T_{kk} is the sum of the diagonal components of the transformation strain (Segall, 2010). By using the isotropic form of Hooke's law (Segall, 2010), and assuming the bulk modulus to be the same inside and outside the cavity, it can be shown that

$$\epsilon^T_{kk} = \frac{\sigma^T_{kk}}{3K}, \tag{3.9}$$

where σ^T_{kk} is the sum of the diagonal components of the transformation stress. Combining eq. (3.4), eq. (3.5), eq. (3.8) and eq. (3.9) yields

$$\Delta V^E = \delta V^E + \frac{pV}{K}, \tag{3.10}$$

where ΔV^E is the potency of the ellipsoidal cavity.

The potency and actual volume change of the ellipsoidal cavity, and consequently, its corresponding CDM, are related through eq. (3.10). It is straightforward to show that for the Mogi model, eq. (3.10) can be written as $\Delta V^{Mogi} = \left(1 + \frac{4\mu}{3K}\right) \delta V^{Mogi}$, which in a Poisson solid with $\mu = \lambda$ will be reduced to $\Delta V^{Mogi} = 1.8 \delta V^{Mogi}$ (Bonafede and Ferrari, 2009).

3.3.2 The CDM and finite ellipsoidal source comparison

To evaluate the efficiency of the CDM in a more general sense, we compare the surface displacement fields associated with finite ellipsoidal cavities and their corresponding CDMs, the results of which are presented in Figs 3.5-3.7. For this purpose, we calculate the surface displacements associated with the ellipsoidal cavities using a numerical approach based on the boundary element method (BEM) after Kuriyama and Mizuta (1993). In the following comparisons, the moment tensor and depth to the centre of the corresponding ellipsoids and CDMs are identical. We calculate the moment tensors of the ellipsoidal cavities using eq. (3.5). Then, using eq. (3.7), we derive the potency and aspect ratios of the corresponding CDM uniquely. However, similar to other finite source models in the far field, there is a trade-off between the CDM dimensions and opening. Therefore, using the known potency and aspect ratios of the CDM from the previous step, we determine the optimized CDM dimensions and opening that provide the best fit to the BEM displacements. However, because the point CDM is dimensionless, the displacements associated with it can be directly calculated from the potency and aspect ratios. Following this approach for the comparisons minimizes the optimization-related uncertainties and guarantees that any deviation from the accurate BEM calculations is due to the mathematical and geometrical structures of the CDM and point CDM.

We conduct the comparisons for various prolate, equidimensional and oblate cavities in the near field. Here, we only detail three cases, which represent all of the three geometrical categories of ellipsoidal cavities. However, utilizing triaxial ellipsoidal cavities and considering the model performance along the X and Y axes simultaneously, we cover a wider spectrum of cavity aspect ratios. In the following comparisons, the Lamé coefficients are $\mu = \lambda = 33\,\mathrm{GPa}$, the depth to the centre of the cavity is $d = 3\,\mathrm{km}$, and the uniform pressure on the cavity walls is $P = 10\,\mathrm{MPa}$. We summarize the results of the comparisons in Figs 3.5-3.7), in which profiles of the BEM, CDM and point CDM horizontal and vertical surface displacements along the X and Y axes are presented. In each case, the distances are normalized by the depth to the centre of the cavity and the horizontal and vertical displacements are normalized by the maximum vertical displacement of each method.

For the first comparison, we use an ellipsoidal cavity with semi-axes of 0.75, 0.5 and 1.5 km along the X, Y and Z axes, respectively. In this case, the point CDM and CDM displacements are equivalent, and both are in reasonable agreement with the BEM displacements (Fig. 3.5). The fit to the BEM displacements along the X and Y axes of the model are very similar; however, the quality of the fit for the horizontal displacements along the longest horizontal axis of the cavity, that is, along the X axis, is slightly better (Fig. 3.5, left). As the second case, we consider an ellipsoidal cavity with semi-axes of 1, 2 and 0.75 km along the X, Y and Z axes, respectively. In this comparison, the CDM displacements are in very good agreement with the BEM displacements, and in general, the CDM performs better than the point CDM (Fig. 3.6). In particular, along the major axis of the ellipsoid, which aligns with the Y axis, the CDM clearly shows a better fit to the BEM displacements than the point CDM does (Fig. 3.6, right). In the third comparison, we consider an ellipsoidal cavity with semi-axes of 2, 3 and 0.25 km along the X, Y and Z axes, respectively. Fig. 3.7 clearly shows that the CDM and BEM displacements match perfectly, whereas the point CDM overestimates the near-field displacements and underestimates the far-field displacements. This case shows that in the near field, the CDM can be used as an appropriate source model for rather thin magma bodies, particularly those that resemble planar intrusions such as dikes and sills.

The first ellipsoidal cavity in our comparisons resembles a prolate ellipsoidal source. For this cavity, the ratio of the semi-major axis to the depth to the centre, which we refer to as the characteristic ratio, is equal to 0.5. Prolate cavities in the near field can be approximated by a point source if their characteristic ratio is smaller than 0.5 (Yang et al., 1988). This explains the rather good agreement between the BEM displacements and those of the CDM and point

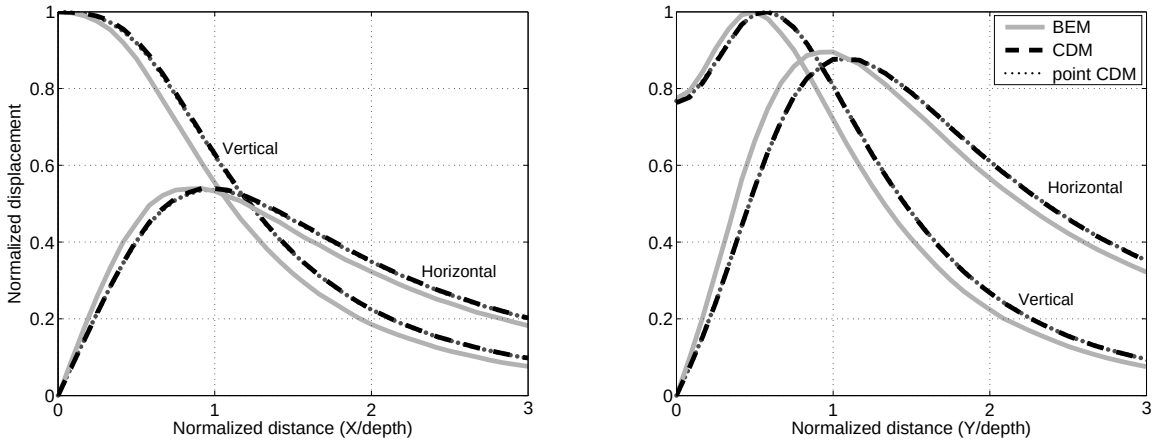

Figure 3.5: Comparison of the BEM (solid line), CDM (dashed line) and point CDM (dotted line) normalized displacements along the X axis (left) and the Y axis (right) for the first ellipsoidal cavity with 0.75, 0.5 and 1.5 km semi-axes along the X, Y and Z axes, respectively.

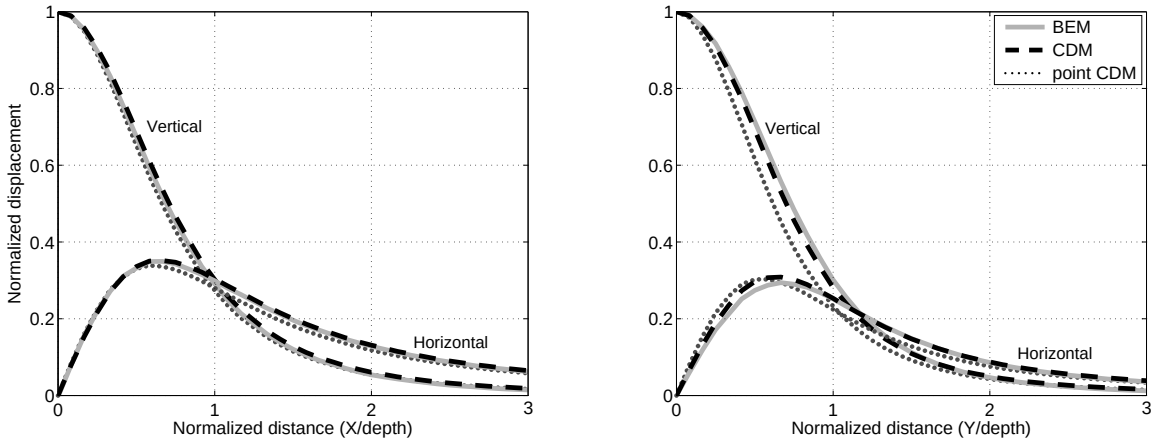

Figure 3.6: Comparison of the BEM (solid line), CDM (dashed line) and point CDM (dotted line) normalized displacements along the X axis (left) and the Y axis (right) for the second ellipsoidal cavity with 1, 2 and 0.75 km semi-axes along the X, Y and Z axes, respectively.

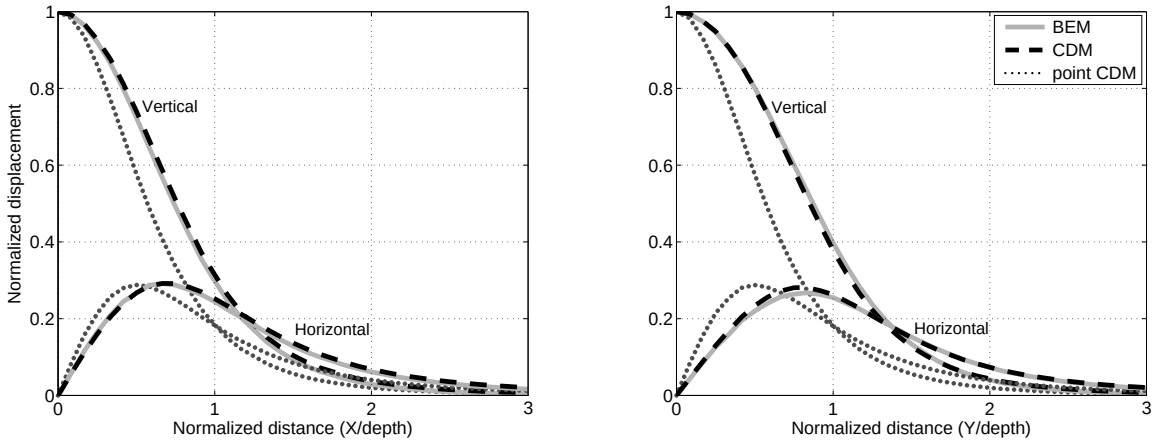

Figure 3.7: Comparison of the BEM (solid line), CDM (dashed line) and point CDM (dotted line) normalized displacements along the X axis (left) and the Y axis (right) for the third ellipsoidal cavity with 2, 3 and 0.25 km semi-axes along the X, Y and Z axes, respectively.

CDM (Fig. 3.5). However, the equivalence of the CDM and point CDM displacements shows that for prolate ellipsoidal sources of pressurization, the point CDM can perfectly replace the CDM.

The second ellipsoidal cavity, however, represents a near equidimensional volumetric source. For a spherical cavity, the point-source approximation (Mogi, 1958) is appropriate if the characteristic ratio of the cavity is smaller than 0.5 (McTigue, 1987). The characteristic ratio of the second cavity in the XZ-plane is equal to 0.3, and as mentioned earlier, both the CDM and point CDM perform very good in this cross-section (Fig. 3.6, left). Additionally, the characteristic ratio of the cavity in the YZ plane is equal to 0.7. Therefore, in this plane, the point CDM does not perform as well as in the XZ plane. However, the CDM, due to its finite spatial extent, performs considerably better than the point CDM (Fig. 3.6, right).

The third ellipsoidal cavity resembles a horizontal sill. The point-source approximation of a horizontal penny-shaped crack (Fialko et al., 2001) is fully adequate for characteristic ratios smaller than 0.2 (Segall, 2010). Therefore, in this case, the characteristic ratios of 0.7 and 1 completely explain the poor performance of the point CDM in the XZ and YZ planes, respectively (Fig. 3.7). However, again due to the finite spatial extent of the CDM as in the second test and also because of the aspect ratios of the third cavity, the performance of the CDM is excellent (Fig. 3.7).

We performed other tests using dipping cavities with arbitrary orientations in space. Similar to the three cases above, the results of these tests show that the performance of the CDM is a function of the depth and aspect ratios of the cavity and that the cavity orientation does not significantly alter the performance. According to the results of the evaluation tests that we discussed here, in the near field, the CDM and point CDM perform equivalently only for prolate ellipsoidal sources. However, in all the other tests, the performance of the CDM is better than the performance of the point CDM. In the following, we will apply the CDM to explain the deformation data measured at a real volcano.

3.4 The 2015 Calbuco co-eruptive deformation modelling

After more than four decades of being dormant, Calbuco volcano (72.614°W, 41.326°S) in the southern volcanic zone in Chile erupted on 2015 April 22. The summit of the Calbuco volcano is approximately two kilometres above the mean sea level. This dome building volcano is an andesitic stratocone that produces pyroclastic and blocky lava flows (López-Escobar et al., 1995).

We estimate the surface displacements due to the 2015 eruption from the Sentinel-1A satellite ascending acquisitions of April 14th and April 26th and descending acquisitions of April 21st and May 3rd. We process the data following the Prats-Iraola et al. (2012) interferometric approach. For this purpose, we use the satellite state vectors and the 90 m resolution topographic data generated from NASA's Shuttle Radar Topography Mission (SRTM) to align the radar images and to remove the topographic component from the interferometric phase. By applying this method to the two Sentinel-1A pairs, we retrieve the two ascending and descending differential InSAR interferograms shown in Fig. 3.8. Due to the small perpendicular baselines of 43 m and 96 m for the Sentinel-1A ascending and descending track pairs, respectively, topographic errors would be minimal. Therefore, the phases observed in the differential interferograms are primarily attributed to deformation and minor atmospheric artefacts. However, in both cases, the topography correlated atmosphere has minimal effect on the Calbuco deformation because the main deformation fringes, which are coherent, fall in rather flat areas that have minor atmospheric noise (see Fig. 3.8).

The broad range of the observed surface deformation with a radius exceeding a few tens of kilometres about the summit implies that the deformation source is rather deep or horizontally elongated. In either case, considering the tests in Section 3.3, the CDM can be applied to the 2015 Calbuco co-eruptive displacements as a first source model.

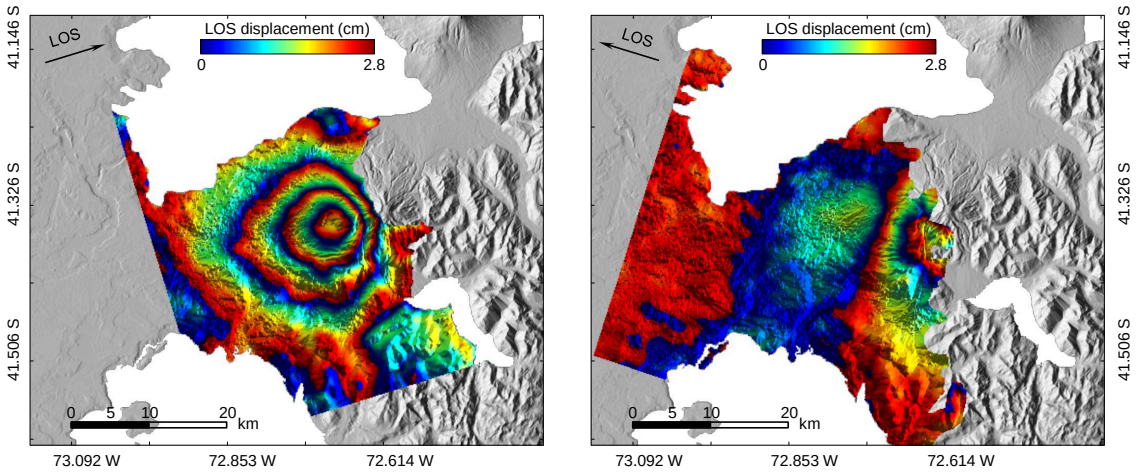

Figure 3.8: Sentine1-1A ascending (left) and descending (right) interferograms representing the ground deformation due to the 2015 April 22 eruption of the Calbuco volcano in Chile. The ascending images are acquired on April 14th and April 26th, and the descending images are acquired on April 21st and May 3rd.

We invert the subsampled Sentinel-1A ascending and descending line-of-sight (LOS) displacements (see Fig. 3.A.1) to infer the unknown parameters of the deformation source. For this purpose, we implement the CDM in a non-linear inversion scheme based on the genetic algorithm (GA; Haupt and Haupt, 2004). The objective function that is minimized in the inversion is the L1-norm of the model residuals. We use the reciprocal of the observation variances as the observation weights in the inversion. Due to a better data quality and coherence, the standard deviation of the ascending data is on average half the standard deviation of the descending data. Therefore, the influence of the ascending data on the modelling outcomes is four times greater than the influence of the descending data. In addition to the unknown CDM parameters in the inversion, we also account for two more parameters, which represent the phase biases of the ascending and descending interferograms. We introduce these biases to the simulated ascending and descending LOS displacements as independent constant shifts. Consequently, these biases in the interferograms, which may exist due to atmospheric noise, unwrapping errors or local site effects, cannot significantly alter the modelling results. In the inversion procedure that we follow, the solution space is chosen to be very wide initially in order to span the likely parameter solution space and find the global minimum residual solution. We then restrict the solution space boundaries based on the preliminary inversion results. To estimate the uncertainties associated with the parameters of the optimal solution, we repeat the inversion 5000 times. We use a population size of $N_{pop} = 60$ chromosomes, a mutation rate of $m_r = 0.25$ and $N_{itr} = 55$ iterations in the GA (see Haupt and Haupt, 2004). The Poisson ratio in the model is 0.25. We show the ascending and descending observations and predicted displacements and residuals from the best-fitting CDM in Fig. 3.9 (see also Fig. 3.A.1). The largest absolute value of the residuals for both the ascending and descending cases is about 1 cm. Additionally, the 1-D and 2-D marginal distributions of the estimated CDM parameters from the inversions, and also the geometry of the best-fitting CDM are illustrated in Fig. 3.10. The marginal distributions show that, in the restricted solution space, any trade-off between the estimated CDM parameters in the inversions are fairly well controlled. The best-fitting CDM parameters and their 95 per cent confidence bounds are summarized in Table 3.1. Using the estimated CDM dimensions and opening from Table 3.1 in $\Delta V = 4u\,(ab + ac + bc)$ (see Section 3.2.2), we estimate a potency of $\widehat{\Delta \mathrm{V}} = -0.099\,\mathrm{km}^3$ for the best-fitting CDM. The 95 per cent confidence bounds for the estimated potency are $(-0.114, -0.057)$. The minimum axis to maximum axis and intermediate axis to maximum axis ratios for the best-fitting CDM are $\frac{a}{c} = 0.171$ and $\frac{b}{c} = 0.693$, respectively.

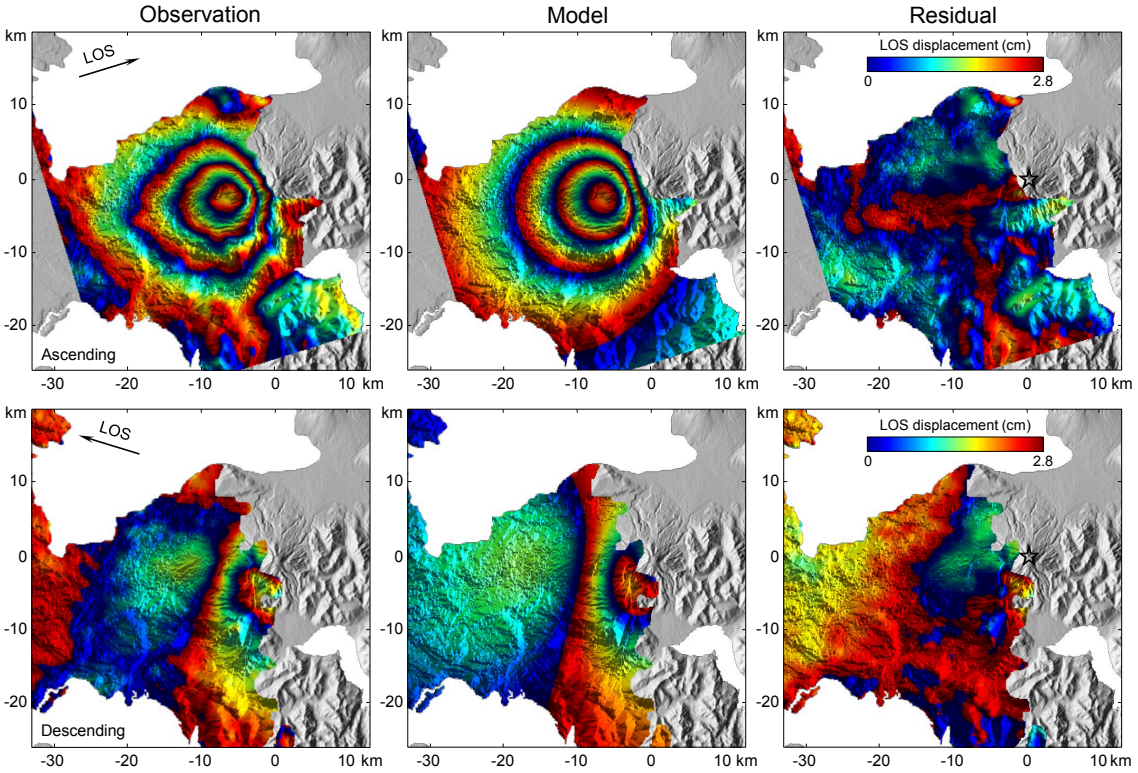

Figure 3.9: The results of the best-fitting CDM for the 2015 Calbuco eruption. The first row shows the InSAR line-of-sight (LOS) displacements, the CDM displacements and the residuals for the ascending acquisition. The second row corresponds to the descending acquisition. The stars in the residual panels indicate the centroid of the best-fitting CDM. The summit of Calbuco is located on the origin of the coordinate system.

Table 3.1: The parameter values and 95 per cent confidence bounds of the best-fitting CDM associated with the 2015 Calbuco eruption. The λ_0 and ϕ_0 are the geodetic longitude and latitude of the CDM centroid, respectively, and d is the depth to the CDM centroid from the free surface in the model. The ω_X, ω_Y and ω_Z are the angles of rotation about the X, Y and Z axes, respectively. The a, b and c are the semi-axes of the CDM that, before applying the rotations, align with the X, Y and Z axes, respectively. The $bias_{asc}$ and $bias_{dsc}$ are the ascending and descending bias terms. The coordinates of the best-fitting CDM centroid in the local coordinate system in Fig. 3.9 are $(0.263, -0.161)$ km. The 95 per cent confidence bounds for these local coordinates from the inversions are $(-2.445, 1.337)$ and $(-2.710, 1.070)$, respectively.

Parameter	Value	95 per cent confidence bounds	Parameter	Value	95 per cent confidence bounds
λ_0 (°)	−72.611	(−72.643, −72.598)	a (km)	0.409	(0.200, 0.731)
ϕ_0 (°)	−41.327	(−41.350, −41.316)	b (km)	1.660	(0.936, 1.844)
d (km)	8.206	(6.557, 9.534)	c (km)	2.395	(1.805, 3.305)
ω_X (°)	1.316	(−12.494, 12.669)	u (m)	−4.398	(−6.307, −2.591)
ω_Y (°)	−4.023	(−8.653, 11.631)	$bias_{asc}$ (cm)	−0.100	(−0.974, 0.340)
ω_Z (°)	159.500	(144.886, 178.928)	$bias_{dsc}$ (cm)	1.163	(0.542, 1.698)

In our second modelling attempt, we utilize the point CDM as the source model and follow the same inversion procedure that we mentioned above. The predicted displacements and residuals from the best-fitting point CDM are almost the same as those of the CDM (see Fig. 3.A.2). The marginal distributions of the estimated point CDM parameters from the inversions, and also the force dipoles that form the best-fitting point CDM are depicted in Fig. 3.11. The corresponding estimated parameters and 95 per cent confidence bounds are summarized in Table 3.2. We use the estimated potencies for the individual point dislocations in $\Delta V = \Delta V_A + \Delta V_B + \Delta V_C$ and calculate the total point CDM potency of $\widehat{\Delta \mathrm{V}} = -0.091\,\mathrm{km}^3$ with $(-0.176, -0.087)$ as its 95 per cent confidence bounds. We also calculate $\frac{da}{dc} = \frac{\Delta V_C}{\Delta V_A} = 0.151$ and $\frac{db}{dc} = \frac{\Delta V_C}{\Delta V_B} = 0.706$, where the da, db and dc are the differential axes of the point CDM (see Section 3.2.2), and $\frac{da}{dc}$ and $\frac{db}{dc}$ are the ratios of minor axis to major axis and intermediate axis to major axis, respectively.

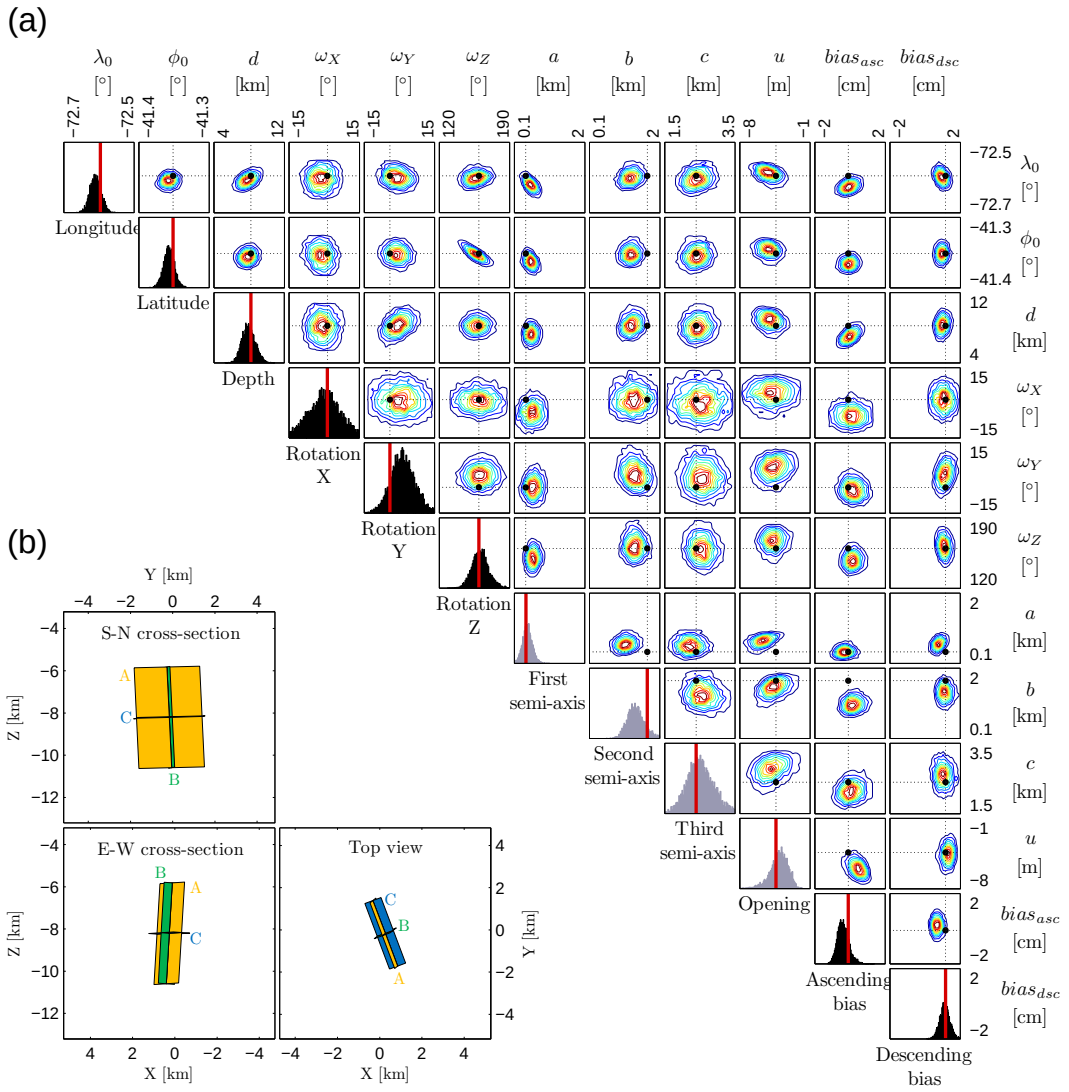

Figure 3.10: Results from the 5000 genetic algorithm inversions of the InSAR data using the compound dislocation model (CDM). (a) The 1-D and 2-D marginal distributions for estimated parameters of the CDM as well as the two phase bias terms (see Section 3.4) are shown on the diagonal and off-diagonal panels, respectively. The black distributions represent the parameters that the CDM and point CDM have in common. The grey distributions represent the parameters that determine the source shape and potency. Vertical red lines and black points indicate parameter values for the best-fitting CDM, respectively. The exact numerical values of the estimated parameters and their 95 per cent confidence bounds are given in Table 3.1. (b) Illustration of the south-north and east-west cross-sections and the top view of the best-fitting CDM in the local coordinate system as introduced in Fig. 3.9. Geodetic coordinates are provided in Table 3.1. The colours and labelling of the RDs are the same as in Fig. 3.3.

3.4.1 Implications of the 2015 Calbuco eruption modelling

The inversions of the 2015 Calbuco co-eruptive displacements that we detailed in the previous section, do not rely on any *a priori* information or constraints on the deformation source geometry and mechanism. This is a major advantage, particularly because no prior knowledge was available regarding the depth and type of the magma source. The parameters of the best-fitting CDM in Table 3.1 clearly show that the deformation source is a rather thin, vertically-elongated source that may somewhat resemble a dike. From the best-fitting CDM parameters, a characteristic ratio of 0.3 can be estimated for the deformation source. Given this small characteristic ratio, one can reasonably deduce that the far-field approximation can be applied to the deformation source, implying that the point CDM can replace the CDM in this case. We tested this by repeating the inversion procedure using the point CDM as the source model. As

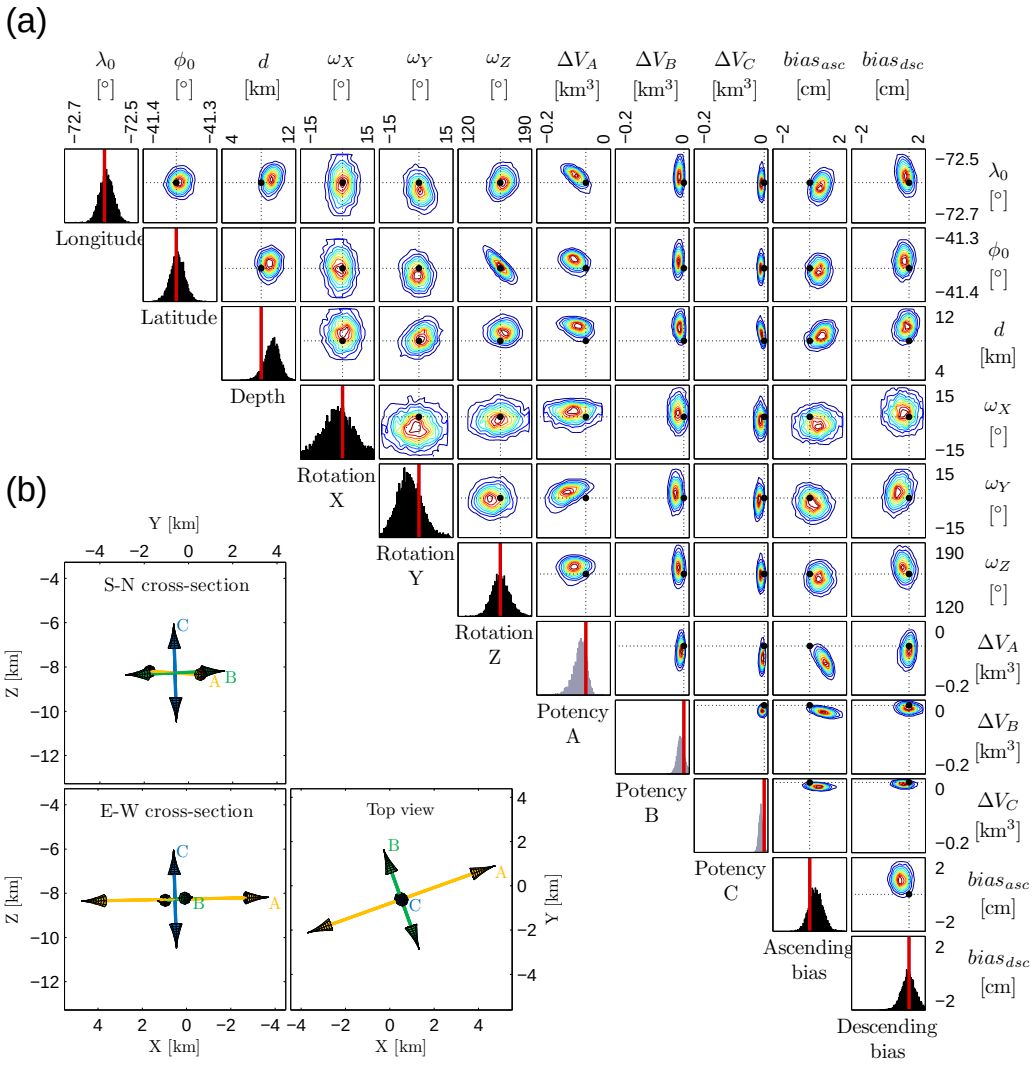

Figure 3.11: Results from the 5000 genetic algorithm inversions of the InSAR data using the point CDM. (a) The 1-D and 2-D marginal distributions for estimated parameters of the point CDM and the two phase bias terms (see Section 3.4). The grey distributions represent parameters that determine the source potency. Vertical red lines and black circles indicate parameter values for the best-fitting point CDM. The exact numerical values of the estimated parameters and their 95 per cent confidence bounds are given in Table 3.2. (b) Cross-sections and the top view of force dipoles of the best-fitting point CDM. The dipole magnitudes are calculated from eq. (3.3). The orientation of each dipole shows the opening direction of a point dislocation. The colour and labelling allow for comparison to the RDs in Figs 3.3 and 3.10. Note that the dipole with the largest magnitude corresponds to the dislocation with the largest potency, which in case of a CDM is the RD with the largest area.

Table 3.2: The parameter values and 95 per cent confidence bounds of the best-fitting point CDM associated with the 2015 Calbuco eruption. The ΔV_A, ΔV_B and ΔV_C are the potencies of the point dislocations that, before applying the rotations, are normal to the X, Y and Z axes, respectively. The other parameters are the same as the CDM (see Table 3.1). The coordinates of the best-fitting point CDM in the local coordinate system in Fig. 3.9 are $(0.521, -0.607)$ km. The 95 per cent confidence bounds for these local coordinates from the inversions are $(-2.445, 1.337)$ and $(-2.710, 1.070)$, respectively.

Parameter	Value	95 per cent confidence bounds	Parameter	Value	95 per cent confidence bounds
λ_0 (°)	−72.608	(−72.630, −72.576)	ΔV_A (km^3)	−0.067	(−0.124, −0.055)
ϕ_0 (°)	−41.332	(−41.351, −41.309)	ΔV_B (km^3)	−0.014	(−0.040, −0.005)
d (km)	8.271	(7.732, 10.953)	ΔV_C (km^3)	−0.010	(−0.030, −0.007)
ω_X (°)	2.086	(−12.632, 13.110)	$bias_{asc}$ (cm)	0.009	(−0.383, 1.087)
ω_Y (°)	1.115	(−11.732, 8.229)	$bias_{dsc}$ (cm)	1.119	(0.340, 1.808)
ω_Z (°)	160.259	(144.930, 178.616)			

expected, the depth and potency, as well as the aspect ratios and the surface displacement field associated with the best-fitting point CDM, are equivalent to those of the best-fitting CDM (see Section 3.4).

The potency of the largest RD of the best-fitting CDM, however, is only 71 per cent of the total CDM potency. This result shows that the deviation of the deformation source from a planar tensile dislocation is significant. The large differences between the estimated aspect ratios of the optimal CDM in Section 3.4 show that the deformation source is also different from the McTigue (1987) and Mogi (1958) isotropic source models. Using eq. (3.2), we calculated M_1, M_2 and M_3, which are the eigenvalues of the optimal CDM moment tensor. The eigenvalue ratios $M_2/M_1 = 0.559$ and $M_3/M_1 = 0.515$ correspond to a point near the lower boundary of the domain of ellipsoids in Fig. 3.4, again showing that the deformation source has a lens-shaped geometry, different from a plane and substantially different from a sphere. To check this result numerically, we performed other inversions using the Mogi (1958) and Okada (1985) models (see Appendix 3.A). The best-fitting Mogi model is located at 4.5 km to the west and 2.9 km to the south of the volcano at a depth of 8.3 km, and its potency is $-0.058\,\mathrm{km}^3$. The estimated depth is comparable to that of the best-fitting CDM in Section 3.4; however, the potency is approximately 41 per cent smaller. Although the model fit to the ascending data in this case is good, the Mogi model completely fails to model the descending data (see Fig. 3.A.4). The centre of the best-fitting Okada (1985) model, however, is located at 1.5 km to the east and 0.4 km to the north of the volcano at a depth of 8.1 km. The strike and dip angles of the best-fitting Okada (1985) model are 157° and 88°, respectively. The horizontal and along-dip dimensions of this best-fitting RD are 3.8 km and 2.7 km, and its potency is $-0.066\,\mathrm{km}^3$. In this case, the depth to the centre also compares well to the CDM depth, but the potency is approximately 33 per cent smaller than the best-fitting CDM potency. As expected from the moment tensor ratios of the optimal CDM, the Okada (1985) model performs better than the Mogi (1958) model. However, the Okada (1985) model residuals are greater than those of the best-fitting CDM (see Fig. 3.A.3), and given that the best-fitting Okada (1985) model is almost vertical, the deviation of its centre from the volcano centre cannot be realistic.

Considering the results of the 2015 Calbuco co-eruptive displacement modelling in Figs 3.9 and 3.A.1, the CDM displacements show a very good agreement with both sets of the ascending and descending observations with residuals that are generally smaller than 1 cm. The residuals may partly be due to atmospheric artefacts in the InSAR data. The small systematic residuals near the summit area, however, can be related to the shallow part of the plumbing system, which became active during the eruption. Given the very small magnitude of the residuals, we speculate that any contribution from other shallow processes cannot be significant. We note that each InSAR interferogram reflects the total displacements over the period of time spanned by the two master and slave images. However, these periods for the ascending and descending acquisitions are not the same (see Section 3.4). The possible differences between the temporal variations of the displacements in the ascending and descending interferograms might be reflected in the results as the systematic residuals. Because both ascending and descending InSAR data can be well explained by a single model, we conjecture that the deformation episode was fully covered by the data.

3.5 Discussion

The CDM that we presented in this paper is a generalization of the Bonafede and Ferrari (2009) dislocation model. Under the far-field approximation, the CDM represents a pressurized 'rectangular box' of arbitrary aspect ratios and orientation (Bonafede and Ferrari, 2009; Ferrari et al., 2015), which in some cases is equivalent to the Davis (1986) point ellipsoidal cavity in a half-space (see Fig. 3.4). The aspect ratios and the pressure boundary condition of the latter

case can be determined through the Eshelby (1957) theory. However, in the near-field case, the CDM can represent finite planar intrusions, namely, dikes and sills, and more volumetric variations thereof. In either case, given the simple configuration of the CDM as a kinematic model (see Section 3.2.2), the potency associated with the underlying deformation source can be easily estimated through simple arithmetic operations, which utilize the CDM dimensions and opening as well as the Lamé parameters. Central to the implementation of the CDM are the new solutions for the displacement and stress fields of the RDs that we developed in Section 3.2.1.

3.5.1 The limitations of the CDM

Like all other analytical solutions used for volcano deformation modelling, the CDM assumes that the Earth's crust is an isotropic, uniform elastic half-space. Therefore, to apply the CDM to case studies that involve a rough topography or substantial layering and material heterogeneity, one would need to be very careful about possible contributions of these factors. Moreover, the CDM can only represent the geometry of the deformation that a subsurface fluid reservoir may undergo. In the absence of further physical and geological evidences the inferred deformation geometry does not necessarily represent the real shape of the reservoir.

Regarding the results of the evaluation tests in the near field (see Section 3.3), for pressurized cigar-shaped cavities, the CDM and the point CDM perform alike. However, for the other cases in the near field, the more oblate the cavities are, the better the CDM performs over the point source models. This is very distinctive particularly for sheet-like intrusions such as dikes and sills in the near field (see Fig. 3.7). Considering the geometrical structure of the CDM in Fig. 3.3, it is clear that in the vicinity of pressurized cavities, the CDM cannot accurately simulate the stress field. In such cases and for more detailed modelling of the displacement and stress fields associated with the deformation sources, numerical models provide considerably better results.

In contrast to the source potency, the pressure that a deformation source applies to the surrounding medium does not appear in the CDM formulation. Therefore, the problems that require pressure boundary conditions associated with the cavities cannot be investigated through applying the CDM only. In such cases and for estimating the pressure associated with deformation sources, the CDM relies on the Eshelby (1957) solution. However, because of this simple geometrical and mathematical structure, the CDM and point CDM are versatile models for kinematic source modelling purposes.

3.5.2 Method improvements and comparison to earlier works

The Okada (1985, 1992) solutions for RDs in a half-space have the limitation that the upper edge of the RDs is constrained to be parallel to the free surface. We addressed this issue by adding the 'plunge angle' to the new RD solutions, which have full rotational degrees of freedom (see Figs 3.2 and 3.3b). Note that such an RD solution can also be formed as a superposition of two triangular dislocations (TDs), as detailed in Nikkhoo and Walter (2015). However, such an approach is not only computationally more expensive but also due to the diagonal dislocation line in its configuration, it does not allow for calculations at the centroid of the RD. The latter in particular is an important drawback for implementing the RD solutions in computer routines based on the boundary element method (BEM).

Another problem in the Okada (1985, 1992) solutions is the imperfection in dealing with the artefact singularities and numerical instabilities along the edges and underneath and above the vertices of the RDs. For the calculation points within a predefined neighbourhood of the artefact singularities, Okada (1992) replaced the singular and numerically instable terms by

their mathematical limits. This approximative approach, however, makes the Okada (1992) solution scale dependent, meaning that depending on how small the RDs in a model are or how close the calculation points to the artefact singularities are, the accuracy of the results may be degraded. Bradley and Segall (2012) considered this problem in a high-resolution BEM simulation based on RDs and addressed the instabilities along the RD edges. However, the Bradley and Segall (2012) work does not remark on the other artefacts and instabilities associated with the Okada (1992) solution. Following the Nikkhoo and Walter (2015) approach, we addressed the problem of the artefact singularities in the RD solutions in both full-space and half-space (Fig. 3.1).

Bonafede and Ferrari (2009) showed the analogy between the Mogi model and a dislocation model composed of three mutually orthogonal square tensile dislocations. They interpreted the dislocation model as a pressurized box in the far field and detailed its implications in the internal and external volume changes associated with a magma chamber. A generalization of the Bonafede and Ferrari (2009) model in its primary form that is based on the Okada (1985, 1992) solutions could only simulate pressurized horizontal and vertical 'boxes'. This is because of the geometrical limitation of the Okada (1985, 1992) RD solutions. Thanks to the new RD solutions that we discussed above, the CDM can take any arbitrary orientation in the space.

Ferrari et al. (2015) developed a numerical model for pressurized rectangular 'boxes' by using the Okada (1992) solution in a BEM scheme. Each side of the rectangular box in this model can be composed of any number of RDs. A uniform traction boundary condition is fulfilled at the centroid of the RDs that form the box. This numerical model is a good approximation of rectangular boxes in both the far field and near field. The moment tensor representation of the Ferrari et al. (2015) model and the CDM are identical, and their corresponding eigenvalue ratios cover the same area in the moment tensor spectrum (see Fig. 3.4). Nevertheless, due to the same geometrical limitation in the Okada (1992) RD solution, the Ferrari et al. (2015) model can only simulate pressurized horizontal and vertical rectangular 'boxes'. Clearly, this issue can be addressed by using the RD solutions that we developed in Section 3.2.1.

Under the far-field approximation, a second-order moment tensor that corresponds to a system of force couples located at a point can represent generalized point sources, including uniformly pressurized cavities (Aki and Richards, 2002). Although the inversion of geodetic datasets for the location and components of a moment tensor does not require any *a priori* information about the geometry of the deformation source, the interpretation of the source geometry and mechanism through the inferred moment tensor is not unique (Trasatti et al., 2009).

The point CDM, as a special case of a moment tensor (see Section 3.1 and 3.3.1), can only represent volumetric changes due to expansion or contraction in all directions in space. This is because in the point CDM formulation, potencies of the point dislocations that form the point CDM are constrained to have the same sign. As a result, the point CDM does not cover the whole domain of universal moment tensors as illustrated in Fig. 3.4. Including arbitrary positive and negative potencies for the point dislocations in the point CDM formulation allows for modelling of sources that randomly expand or contract in any of the three main directions. However, in the present paper we do not consider this case.

Based on the moment tensor inversion concept, Davis (1986) developed a multi-stage inversion scheme for estimating the unknown parameters of a generalized point ellipsoidal cavity in the far field. After inverting the surface displacements for the components of a generic moment tensor, Davis (1986) estimated the source parameters by using the moment tensor eigenvalues and eigenvectors as well as the Eshelby (1957) tensor. However, the estimated moment tensor in the first step of the Davis (1986) method might not represent a pressurized ellipsoidal cavity (Trasatti et al., 2009). Consequently, for some cases, the Davis (1986) inversion scheme does not converge to an optimal solution. As another disadvantage, the Davis (1986) method,

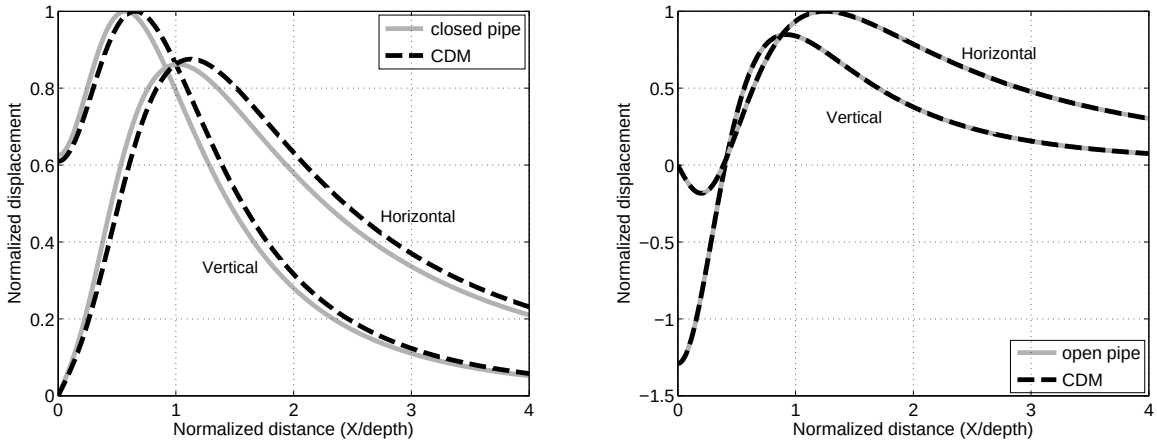

Figure 3.12: Comparison of the CDM and the Bonaccorso and Davis (1999) pipe models. In both cases, the conduit is a vertical cylinder with a height of 1 km, a radius of 0.1 km and a centroid depth of 1.5 km. The horizontal and vertical surface displacements of the closed pipe model (left) and the open pipe model (right) are normalized by the maximum vertical displacement and maximum horizontal displacement, respectively. The solid and dashed lines represent the pipe and the CDM, respectively.

because of its special multi-stage inversion scheme, cannot be implemented in computer codes that use forward-model-based heuristic search algorithms, such as genetic algorithm (GA) or Markov chain Monte Carlo (MCMC) methods. These problems have kept the Davis (1986) generalized point ellipsoidal cavity model from replacing its isotropic counterpart, that is, the Mogi model. Considering the details in Section 3.2.2, it is clear that these issues do not apply to the CDM. Using the relationship between the point CDM and point ellipsoidal cavity in Section 3.3, one can easily perform the forward modelling of the point ellipsoidal cavity. In this way, the convergence issue can be avoided. The point CDM covers the entire domain of pressurized cavities in the far field (see Fig. 3.4), while its application in practice is as convenient as the Mogi model. The latter is because the point CDM does not rely on the Eshelby (1957) method for calculating the displacement and stress fields and the source volume change. Moreover, similar to other dislocation models, the point CDM directly allows for the forward model calculations, and it is straightforward to integrate this source model in various inversion routines. Therefore, the point CDM is an appropriate alternative for generalized point-source cavity models in the far field.

In addition to the planar and ellipsoidal deformation sources, the CDM can also be used to represent other source geometries. Bonaccorso and Davis (1999) presented approximate analytical models for closed and open vertical volcanic conduits or pipes. The closed pipe model is the limiting case of a pressurized prolate ellipsoid with a negligible short axis. The open pipe model is the limiting case of a tensile cylindrical dislocation with a negligible radius. Both models are effectively uniform distributions of moment tensors along their vertical axis. The moment tensors in the closed pipe model generate lateral and upward pressure, but in the open pipe model, they only exert lateral pressure to the surrounding medium. A narrow vertical CDM has a similar configuration to the open pipe model. However, the CDM generally cannot produce the same amount of upward push that exists in the closed pipe model. The characteristic ratio of the closed pipe in Fig. 3.12 is 0.5, but the CDM approximation is not perfect. Therefore, the CDM is not an ideal substitute for the closed pipe model, except for considerably smaller characteristic ratios, which may not be realistic. However, the limiting case of a very narrow CDM, which coincides with the pipe's vertical axis, can perfectly simulate the open pipe model (see Fig. 3.12). Moreover, the CDM in this case can be applied to more general non-vertical conduit models with a non-circular base.

In the near field, the finite size of a deformation source must be included in the source model,

and rather than a point-source model, a finite source or a multipole point-source model should be used (Davis, 1986). In fact, the explicit equations in the Eshelby (1957) theory first showed that the displacement field of a pressurized ellipsoidal cavity in a full-space is exactly equivalent to that of a uniform distribution of three orthogonal force dipoles inside the ellipsoid (Segall, 2010). The full-space Green's functions (Kelvin, 1848) associated with these force dipoles can be replaced by the half-space Green's functions (Mindlin, 1936) to achieve an approximate solution in the half-space (Segall, 2010). These latter points better explain the performance of the CDM in modelling the finite cavities in the near field that we discussed in Section 3.3.2. Each of the RDs that form the CDM has a uniform distribution of orthogonal force dipoles with a moment tensor proportional to those in eq. (3.1). Therefore, in contrast to point-source models, the CDM can represent a portion of the uniform distribution of some force dipoles in a cavity. This property of the CDM can generally improve the performance of the CDM compared to the point-source models (see Fig. 3.6). However, this improvement for planar intrusions and thin oblate cavities in the near field can be significant (see Fig. 3.7). Clearly, when the length of one of the CDM edges tends to zero, the CDM will be reduced to a single RD (see Fig. 3.3). Therefore, similar to finite dislocation models that in many cases are good source models for dikes and sills (Davis, 1983; Segall, 2010), the CDM can also adequately model the planar intrusions in the near field.

3.6 Conclusion

In this paper, we developed analytical artefact-free solutions for RDs in the full-space and half-space. These RD solutions possess full rotational degrees of freedom, meaning that their upper edge is not constrained to be parallel to the free surface. Using these RD solutions, we constructed a CDM in terms of three mutually orthogonal tensile RDs. Under the far-field approximation, that is, for small source dimension to depth ratios, the CDM can represent any triaxial ellipsoidal or planar sources. The point CDM is a generalized point source that covers a wider spectrum of moment tensors compared to the Davis (1986) point ellipsoidal cavity. In the near field, however, the CDM can simulate planar intrusions, namely, dikes and sills, as well as thin oblate ellipsoidal sources. The potency of the CDM is the sum of the potencies of the individual RDs that it comprises. Regardless of the shape of the deformation sources, their potency can be uniquely determined by using the CDM.

The convenience of integrating the CDM and point CDM in various optimization schemes compares to the Mogi model as the simplest analytical point-source model. Therefore, the CDM can be used as a first model for rapid co-eruptive displacement modelling. This is particularly of great relevance for early warning and rapid response systems, which shortly after or during a crisis require the volcanic source parameters without any preliminary information on the shape and depth of the source. As the first option in these cases, using the point CDM can provide an even higher performance. If this model could not succeed in simulating the ground deformation, it implies that most probably a finite source in the near field is causing the deformation. As the second option, the CDM can then be used.

We applied the CDM to the 2015 Calbuco co-eruptive ground deformation observed by the Sentinel-1A InSAR satellite. The inferred deformation source is a vertically extended lens-shaped magma body at a depth of 8.2 km. The estimated potency of the source is $-0.1\,\mathrm{km}^3$. We showed that applying the isotropic Mogi (1958) model or the Okada (1985) model to this case study produces erroneous estimations of the deformation source parameters.

We provide the 2015 Calbuco co-eruptive subsampled InSAR data. The MATLAB functions that accompany this paper allow for easy calculations using the new RD solutions, as well as the CDM and the point CDM.

Appendix

3.A Comparison of results from inversions of the 2015 Calbuco co-eruptive displacements using various source models

The Mogi (1958) and Okada (1985) models are the most well-known and widely used analytical models in volcano deformation studies. Due to the simplicity of the mathematical formulation of the Mogi (1958) model in particular, using it in practice is very convenient. However, as also shown by Davis (1986), the application of the Mogi model may result in large errors in some of the estimated source parameters. To determine how this is relevant in the 2015 Calbuco co-eruptive deformation, in addition to the CDM and point CDM, we also perform separate inversions using the Mogi model and Okada (1985) model, respectively. In the following figures, we show the subsampled InSAR data that we used in the inversions. We use the local XY coordinate system that we introduced in Fig. 3.9. We show the results associated with the CDM in Fig. 3.A.1. In this case study, the CDM results are almost equivalent to those of the point CDM that are shown in Fig. 3.A.2. We also show the results of the modelling for the Okada (1985) model and the Mogi model in Figs 3.A.3 and 3.A.4, respectively. In this case, the Mogi model can simulate the ascending data very well, but it completely fails to simulate the descending data (see Fig. 3.A.4). The inferred deformation source derived using the Mogi model is 5.4 km off-centred (see Section 3.4.1). The deviation of the best-fitting Okada (1985) model from the Calbuco centre is 1.5 km. The Okada (1985) model simulates the general pattern of the ascending and descending displacements better than the Mogi model. Nevertheless, neither of these two models performs as well as the CDM and point CDM. This can be better seen in the root mean square error (RMSE) values of the residuals of the four models in Table 3.A.1. It should be noted that the Mogi model can be considered as the special case of a CDM that has three equal axes. Also, the Okada (1985) model is the special case of a CDM that has only two non-zero axes. Therefore, in general the CDM performs better than the Mogi (1958) and Okada (1985) models and in special cases performs the same as these two models.

Table 3.A.1: Quantitative comparison of the residuals of the CDM, the point CDM, the Okada (1985) model and the Mogi model for the 2015 Calbuco eruption. The min, max and RMSE in the table stand for the minimum residual, maximum residual and the root mean square error of the residuals, respectively. All the numerical values are given in (mm).

	Asc. data			Desc. data			Asc. & Desc. data		
Model	Min	Max	RMSE	Min	Max	RMSE	Min	Max	RMSE
CDM	−9.8	9.2	3.5	−12.5	12.4	5.2	−12.5	12.4	3.9
point CDM	−10.9	8.7	3.6	−11.9	13.3	5.4	−11.9	13.3	4.0
Okada (1985)	−19.2	10.9	4.6	−15.4	12.9	4.4	−19.2	12.9	4.6
Mogi (1958)	−13.2	18.6	5.5	−14.2	53.4	15.2	−14.2	53.4	8.2

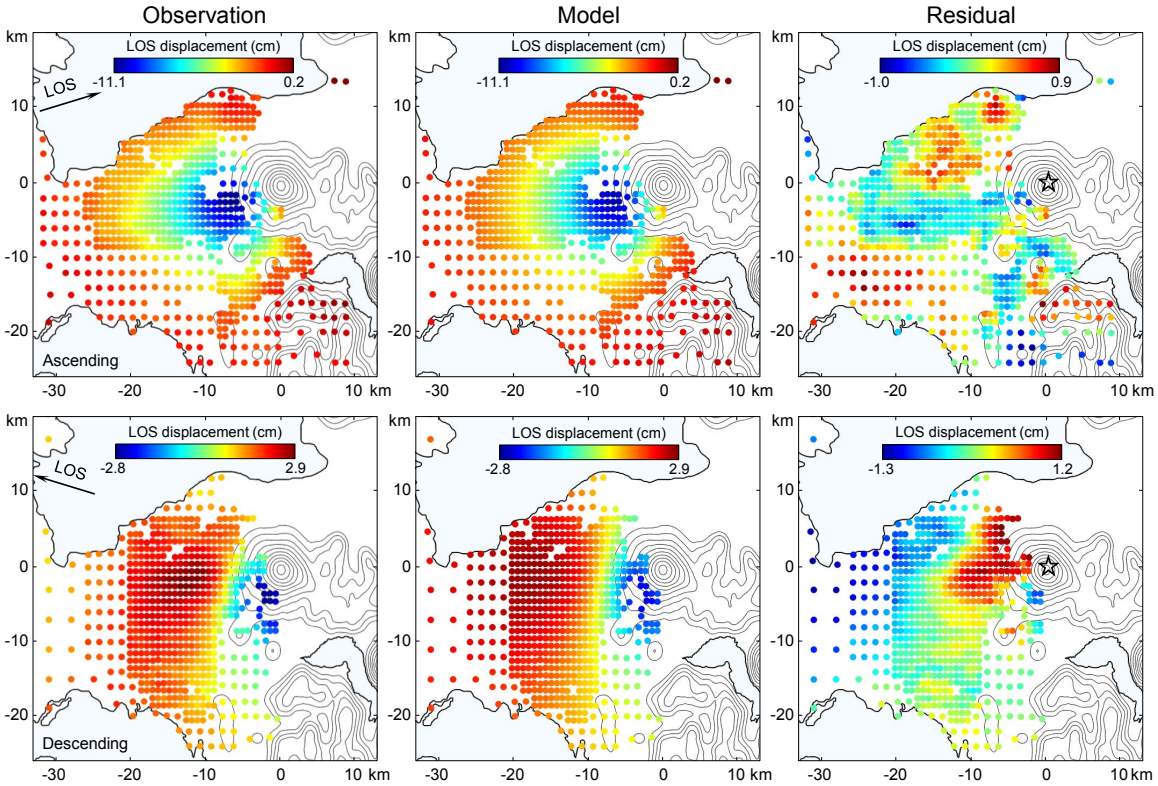

Figure 3.A.1: The results of the CDM for the 2015 Calbuco eruption. The first row shows the subsampled InSAR observations, the CDM displacements and the residuals for the ascending acquisition. The second row corresponds to the descending interferogram. The summit of Calbuco is located on the origin of the coordinate system. The stars in the residual panels indicate the centroid of the best fitting CDM.

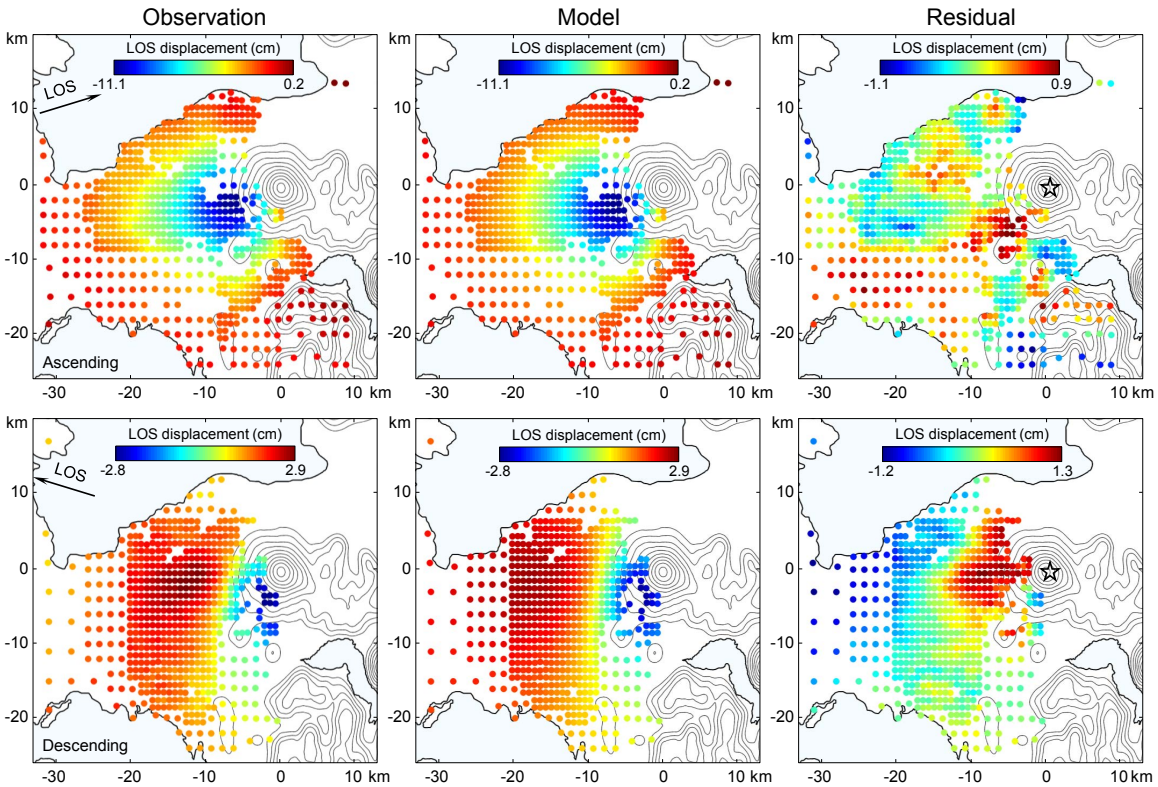

Figure 3.A.2: The results of the point CDM for the 2015 Calbuco eruption. The first row shows the subsampled InSAR observations, the point CDM displacements and the residuals for the ascending acquisition. The second row corresponds to the descending interferogram. The summit of Calbuco is located on the origin of the coordinate system. The stars in the residual panels indicate the centroid of the best fitting point CDM.

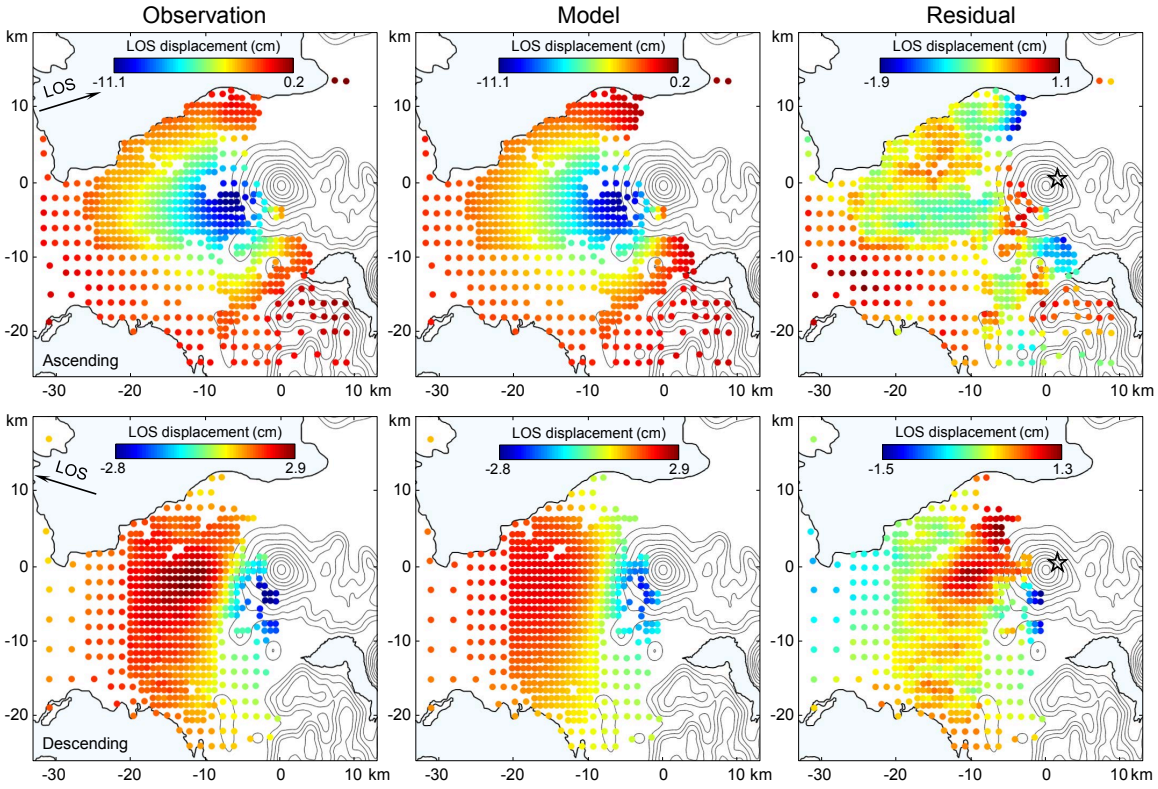

Figure 3.A.3: The results of the Okada (1985) model for the 2015 Calbuco eruption. The first row shows the subsampled InSAR observations, the Okada (1985) model displacements and the residuals for the ascending acquisition. The second row corresponds to the descending interferogram. The summit of Calbuco is located on the origin of the coordinate system. The stars in the residual panels indicate the centroid of the best-fitting Okada (1985) model.

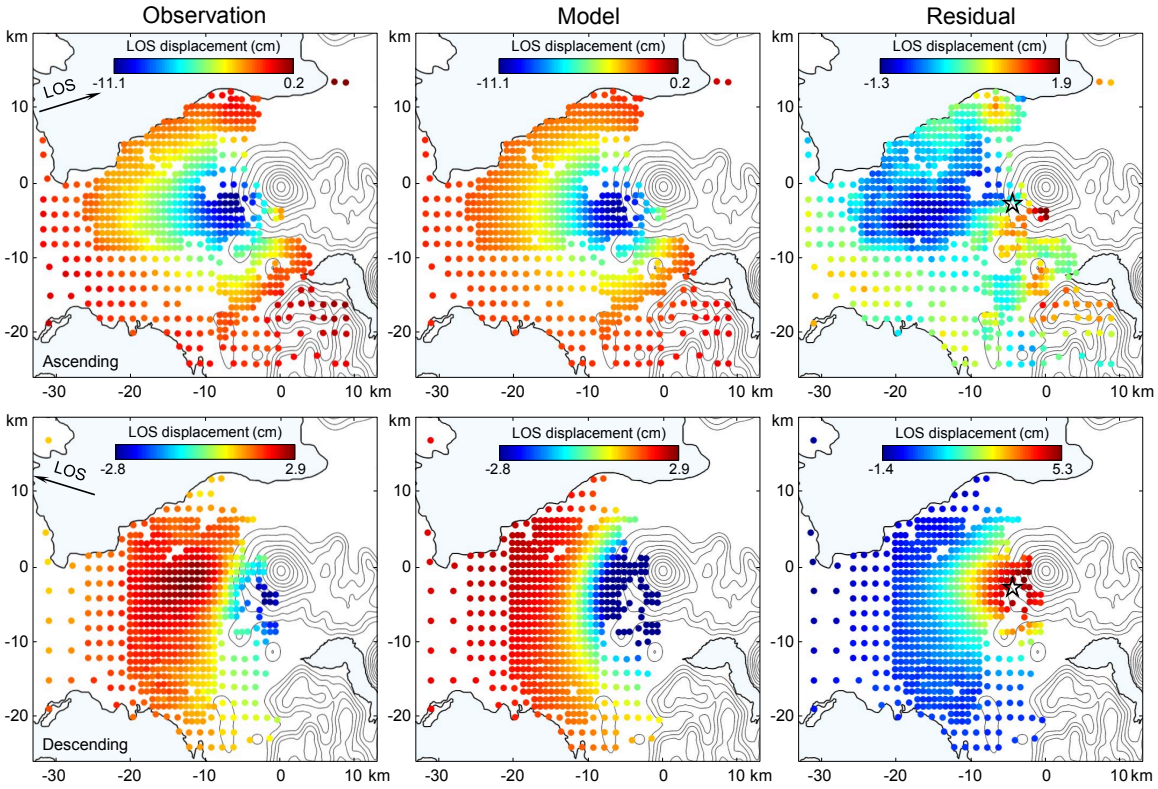

Figure 3.A.4: The results of the Mogi model for the 2015 Calbuco eruption. The first row shows the subsampled InSAR observations, the Mogi model displacements and the residuals for the ascending acquisition. The second row corresponds to the descending interferogram. The summit of Calbuco is located on the origin of the coordinate system. The stars in the residual panels indicate the location of the best-fitting Mogi model.

Part II

Applications

Chapter 4

Source model for the Copahue volcano magma plumbing system constrained by InSAR surface deformation observations

Abstract

Copahue volcano straddling the edge of the Agrio-Caviahue caldera along the Chile-Argentina border in the southern Andes has been in unrest since inflation began in late 2011. We constrain Copahue's source models with satellite and airborne interferometric synthetic aperture radar (InSAR) deformation observations. InSAR time series from descending track RADARSAT-2 and COSMO-SkyMed data span the entire inflation period from 2011 to 2016, with their initially high rates of 12 and 15 cm/yr, respectively, slowing only slightly despite ongoing small eruptions through 2016. InSAR ascending and descending track time series for the 2013–2016 time period constrain a two-source compound dislocation model, with a rate of volume increase of 13×10^6 m^3/yr. They consist of a shallow, near-vertical, elongated source centred at 2.5 km beneath the summit and a deeper, shallowly plunging source centred at 7 km depth connecting the shallow source to the deeper caldera. The deeper source is located directly beneath the volcano tectonic seismicity with the lower bounds of the seismicity parallel to the plunge of the deep source. InSAR time series also show normal fault offsets on the NE flank Copahue faults. Coulomb stress change calculations for right-lateral strike slip (RLSS), thrust, and normal receiver faults show positive values in the north caldera for both RLSS and normal faults, suggesting that northward trending seismicity and Copahue fault motion within the caldera are caused by the modelled sources. Together, the InSAR-constrained source model and the seismicity suggest a deep conduit or transfer zone where magma moves from the central caldera to Copahue's upper edifice.[1]

[1]Originally published as: Lundgren, P., Nikkhoo M., Samsonov S. V., Milillo P., Gil-Cruz F., Lazo J. (2017): Source model for the Copahue volcano magma plumbing system constrained by InSAR surface deformation observations. - Journal of Geophysical Research. Solid Earth, 122, 5729-5747. 10.1002/2017JB014368

4.1 Introduction

Our understanding of volcanic systems and their future behaviour depends on interpreting the changes within the volcano's plumbing system as expressed through seismicity, surface deformation, gas, and eruptive emissions. Surface deformation remains one of the major observational controls toward developing numerical physical models of these systems through its constraint on source shape and dimensions, location, depth, and temporal behaviour. Over the past two decades interferometric synthetic aperture radar (InSAR), primarily from satellites, has been of fundamental importance for constraining volcano processes with its ability to image surface deformation at meter-scale sampling resolution and subcentimeter precision over broad areas. This has led to numerous insights into hydrothermal activity (Wicks et al., 1998; Lundgren et al., 2001; Lundgren and Lu, 2006; Chang et al., 2010), highly dynamic calderas (Amelung et al., 2000; Yun et al., 2006; Chang et al., 2010; Le Mével et al., 2015), and discoveries of previously unknown magma influx into the crust at locations offset from the nearby active volcano (Lu et al., 2002; Pritchard and Simons, 2002; Wicks et al., 2002; Fialko and Pearse, 2012; Lundgren et al., 2015). It is this detailed, yet synoptic view of surface deformation, coupled with satellite InSAR's potential for global reach that has provided important insights into complex volcano source processes beyond simple point sources.

Copahue volcano (Fig. 4.1) (71.16°W, 37.85°S) is a basaltic-andesitic volcano on the Chile-Argentina border in the southern Andes, situated between the intra-arc Liquiñe-Ofqui fault zone (LOFZ) and the Antiñir-Copahue fault zone (ACFZ) (Folguera et al., 2004; Melnick et al., 2006; Folguera et al., 2016). Copahue lies within the Callaqui-Copahue-Mandolegüe (CCM) volcanic lineament (Melnick et al., 2006; Folguera et al., 2016), with the NE alignment of Copahue's edifice and summit vents parallel to the direction of maximum compressive stress within the CCM (Bonali, 2013). Its northeast flank is characterized by an alignment of vents and hot springs related to a shallow, seismically active hydrothermal system (Ibáñez et al., 2008). Copahue's high $^{3}He/^{4}He$ and $CO_2/^{3}He$ ratios suggest that it is influenced by its extensional setting, with magmas reflecting mantle asthenospheric upwelling and subducted sediments (Agusto et al., 2013). The high fumarolic gas flux beneath the NE flank of Copahue and the broad area affected are compatible with a large magmatic source beneath this area (Chiodini et al., 2015). This activity has led to extensive hydrothermal alteration, suggesting that edifice flank instability is a potential hazard (Varekamp et al., 2001).

During the past 260 years there have been 11 phreatic/phreatomagmatic eruptions, with the most recent ones in 2000 and December 2012–2016 during the current unrest period (Naranjo and Polanco, 2004; Caselli et al., 2016a,b). The December 2012 phreatomagmatic-magmatic eruptions ($\leq$VEI 2) were similar to the one in 2000, erupting from the same easternmost summit crater after a period of increasing seismic activity following the 2010 Maule earthquake (Caselli et al., 2016a). Since the 2012 eruptive events, Copahue volcano has developed several episodes of similar phreatomagmatic and magmatic eruptions, with hydrothermal and magmatic systems alternating in dominance, with the most significant occurring during the period between October 2015 and December 2016, when a quasi-continuous Strombolian activity was observed. Numerical modeling of the 2010 Maule earthquake found unclamping of vertical faults that would favor the migration of fluids resulting in the 2011 to present unrest period (Bonali, 2013; Bonali et al., 2015). Analysis of pyroclastic density current deposits shows phreatomagmatic vesiculation occurred at 400 m depth with fragmentation occurring through the interaction of magma with a summit hydrothermal system at 1500 m depth beneath the summit (Balbis et al., 2016).

In this study, we characterize the sources of inflation at Copahue volcano during an extended period of volcano unrest. We measure surface deformation using synthetic aperture radar (SAR) data from 2011 to 2016. InSAR surface deformation time series velocities are analysed from

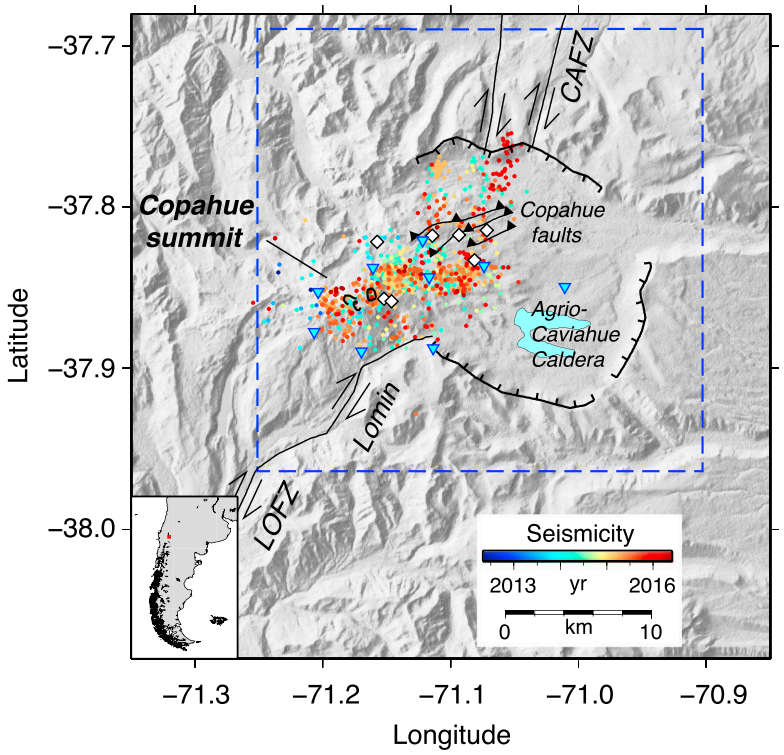

Figure 4.1: Shaded relief map of Copahue volcano and the adjacent Agrio-Caviahue caldera. Bold lines outline summit craters and lines with tick marks indicate the caldera rim. The right-lateral Liquiñe-Ofqui fault zone (LOFZ), Lomin fault, and the Copahue-Antiñir fault zone (CAFZ) are shown as solid thin lines (Melnick et al., 2006; Bonali et al., 2016; Folguera et al., 2016). The Copahue faults are shown as solid lines with solid triangular barbs on the hanging walls, considered thrust faults, which in this study we find exhibited normal motion. Volcano tectonic (VT) seismicity for events with location quality ratings of A and B according to the HYPO-71 algorithm (Lee and Valdes, 1985) is coloured by time. White filled diamonds show the locations of geothermal areas (near the Copahue faults) and hot springs (near Copahue volcano summit) (after Velez et al., 2011). Cyan-filled inverted triangles show locations of seismic stations used in b value analysis. Blue dashed box outlines the data area used for modelling.

ascending and descending track COSMO-SkyMed data and descending track RADARSAT-2 data. We also include, for comparison, airborne UAVSAR data, which provides improved viewing diversity, over a subportion of the unrest period. We apply a new type of analytical solution, the compound dislocation model (CDM) and its point-source version (Nikkhoo et al., 2017), to solve for the complex sources constrained by the asymmetric deformation patterns revealed by the InSAR data. We discuss the implications of the source solutions in terms of the volcano plumbing system and eruption processes of the Copahue volcano caldera system.

4.2 Data analysis

We used synthetic aperture radar (SAR) data from two satellites and one airborne system: the Canadian Space Agency (CSA) RADARSAT-2 (RSAT2) C-band (5.6 cm wavelength) satellite, the Italian Space Agency (ASI) COSMO-SkyMed (CSK) X-band (3.1 cm wavelength) four-satellite constellation, and the National Aeronautics and Space Administration (NASA) UAVSAR airborne repeat pass interferometry L-band (23.8 cm wavelength) system. For each sensor we compute InSAR maps of relative ground surface deformation projected into the radar line-of-sight (LOS) direction (Rosen et al., 2000).

Each sensor's data were processed into differential interferograms, after removal of Earth curvature and topographic effects, with different processing software. For RSAT2 only descending track data were available and were processed at the Canada Centre for Remote Sensing using

the Gamma processing package (Wegmüller and Werner, 1997). CSK data were available from both ascending and descending tracks; however, like RSAT2, the CSK background volcano acquisitions are only for descending tracks. Ascending track CSK data were requested beginning in June 2013 once deformation from RSAT2 indicated ongoing inflation. CSK data were processed using the InSAR Scientific Computing Environment (ISCE) package developed at the Jet Propulsion Laboratory (JPL), Caltech, and Stanford University (Rosen et al., 2015). ISCE processing used the SRTM 30 m digital elevation model (Farr et al., 2007) to correct for topography. For interferogram unwrapping we used the SNAPHU unwrapper (Chen and Zebker, 2000) implemented in ISCE. Lists of interferograms used in the analysis are given in the supporting information. Baselines for the CSK data were generally constrained to be within 150 m and 3 months in orbital (perpendicular baselines, $B_\perp$) and temporal separation, respectively, but with longer (up to 1.5 years) summer-to-summer pairs required to span winter incoherence. The criteria were similar for the RSAT2 interferograms with $B_\perp$ less than 250 m and temporal baselines up to 500 days.

For each satellite data set we compute InSAR time series from sets of interconnected interferograms using the GIAnT software package (Agram et al., 2013) in the NSBAS mode. Atmospheric corrections were not applied; instead, to smooth out atmospheric scatter, we used temporal Gaussian filters with lengths of 0.20, 0.05 and 0.10 years for the RSAT2, CSK descending, and CSK ascending solutions, respectively. The filter length depended largely on the temporal sampling, which was sparsest for RSAT2 (with its 24 day repeat orbit) and densest for the CSK descending track (CSK 4 acquisitions possible per 16 days), which had more acquisitions than for the ascending track. The scatter of the raw unfiltered solution (red dots) compared to the filtered solution (blue dots) gives a sense of the time series uncertainty (Fig. 4.2). The InSAR time series show inflation started in late 2011, which was fastest during the initial 3 years, with a slightly lower rate through mid-2016. The start of inflation in late 2011 is also inferred from Envisat time series analysis for the time period 2011.1–2012.25 (Velez et al., 2016). Due to snow during the austral winter (June through September or October) gaps occur in the time series. The linear (or mean) LOS velocity inflation pattern we find is very distinct, with the descending tracks showing a very similar, elliptical pattern, extending from the summit of Copahue volcano at the SW edge of the caldera toward the ENE interior of the caldera (Fig. 4.2). The descending track data sets provided our initial imaging of the LOS displacements and suggested an asymmetric source directed toward the caldera interior. The ascending track CSK time series show a completely different, roughly circular, pattern centered slightly north of the summit. Together, the two deformation patterns illustrate the need for both viewing geometries to constrain the source or sources and the importance of having at least two viewing directions (that is, if you only had the ascending track data its roughly circular pattern might suggest that only a simple Mogi point source solution was required to fit the data).

The UAVSAR interferograms and the satellite InSAR time series linear LOS velocities for the 2013–2014 interval (Table S1) are shown in Fig. S1. We show these interferograms along with the time series velocities at a wrap rate of 3 cm/yr. As evident in the UAVSAR interferograms, there is a fair amount of atmospheric or aircraft residual baseline-induced phase noise. In the case of Fig. S1e, there was significant topographically correlated noise that we reduced by using a tropospheric phase correction based on the European Centre for Medium-Range Weather Forecasts weather model (Agram et al., 2013).

In order to reduce the number of data points to a reasonable number for our Bayesian modelling approach, we downsample interferograms using a model-based quadtree method from Lohman and Simons (2005). A horizontal tensile dislocation model is used to downsample the data to ∼500 data points retained, slightly varying for each UAVSAR interferogram or time series linear velocity map. Each downsampled point is computed from the mean value of the original coherent unwrapped phase within each quadtree square area of pixels. Stan-

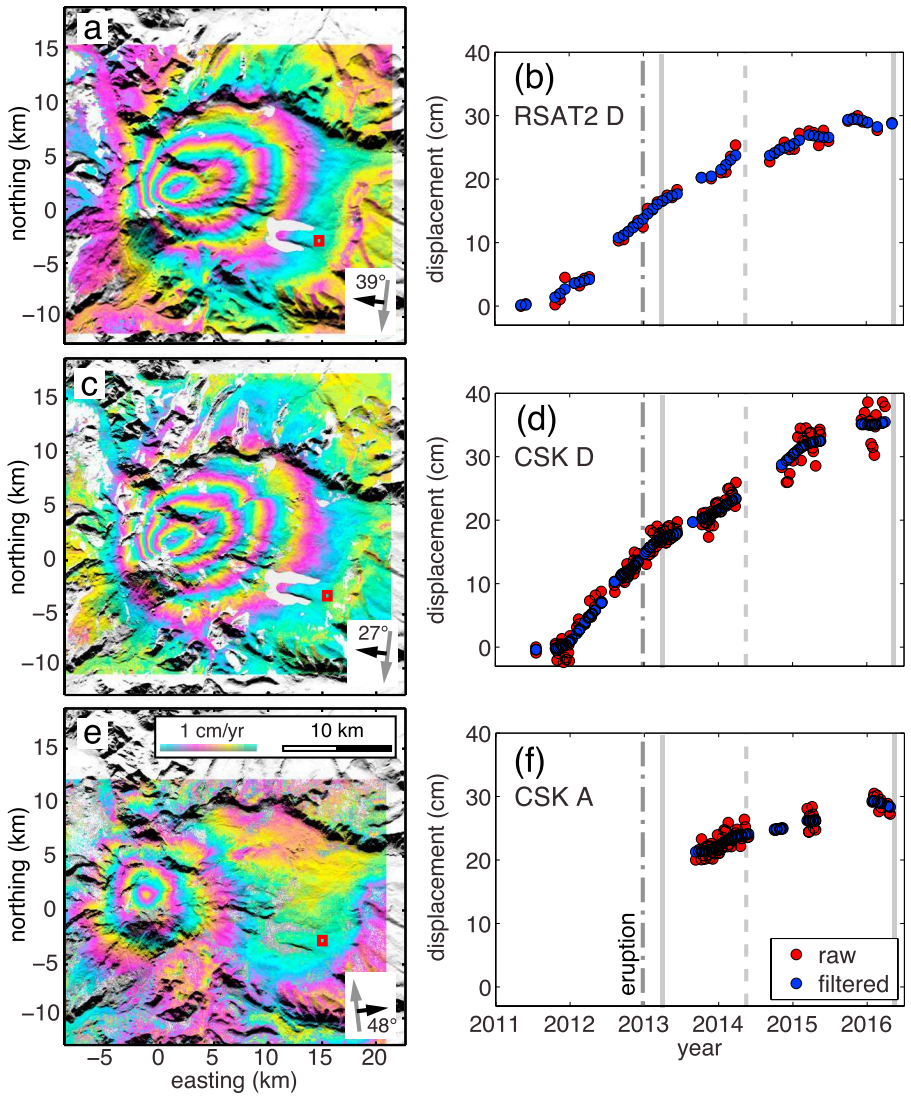

Figure 4.2: InSAR time series LOS linear velocity maps and peak inflation time series. (a, c, and e) Maps give the linear velocities for the 2013.25–2016.4 interval. The box in the lower right corner of each plot gives the satellite heading direction (grey arrow), the radar look direction (black arrow), and the incidence angle from vertical in degrees. The small red square in each map is the time series reference box (10 × 10 pixels). (b, d, and f) Time series of peak LOS inflation, each corresponding to the map to its left. The scatter of the raw unfiltered solution (red dots) compared to the filtered solution (blue dots) gives a sense of the time series uncertainty. The dark grey dash-dotted line marks the dates of the late phreatomagmatic eruptive period starting in December 2012. The solid grey lines 2013.25–2016.4 mark the limits of the 2013.25–2016.4 linear velocity time window. The solid grey to dashed lines (2013.25–2014.3) mark the dates spanned by the UAVSAR data (and corresponding time series linear velocities).

dard deviations (σ) for the points are computed and are generally in the range from 0.1 to 0.3 mm/yr for the linear velocity and 1–2 mm for the interferograms. In our modelling we used the data variances rather than the full data covariances (see Section 4.3) due to computational limitations.

Due to the heterogeneity of the different data sets, we explore two time intervals: the mean velocities from the satellite data for the 2013 through May 2016 period, which gives the longest time series with both descending and ascending data, and the 2013–2014 interval in which we have relatively clean UAVSAR interferograms from three different viewing directions. UAVSAR data were also collected in 2015; however, the quality of the set of three interferograms was poorer than the 2013–2014 interferogram set.

4.3 Modelling

We use a Bayesian inference approach based on a Markov chain Monte Carlo (MCMC) sampling (Fukuda and Johnson, 2010) to estimate posterior probability density functions (PDFs) of model parameters. In our implementation of the MCMC code we run the inversion through one million kept solutions (Malinverno, 2002), throwing out the first 100 000 solutions during the 'burn-in' phase (Lundgren et al., 2015).

Analysis of the InSAR time series from the satellite data shows that over time the pattern of deformation did not change, although there was some reduction in rate, the reason we model time series and interferograms for comparable time intervals. We consider the data from 2013 to the end of summer 2016 (May) to represent the highest-quality data set for modelling. In the supporting information we also show the results for the 2013–2014 interval covered by the UAVSAR data as a basis of comparison to the 2013–2016 time series results.

In initial analyses of the modelled source(s) we used point (Mogi, 1958), spheroid (Yang et al., 1988), and tensile dislocations (Okada, 1985) either alone or in combination. In general, these initial analyses required two sources, one shallower to fit the more acutely shaped deformation source nearer the summit, with a deeper dipping elongated spheroidal and dislocation source required to fit the extended positive line-of-sight (LOS) displacements to the ENE (evident in the descending track while mostly cancelling in the ascending track). However, in the case of the spheroidal sources, the large radius of curvature of the deeper source with respect to its depth meant that the Green's functions were inaccurate (Yang et al., 1988).

We resolved these previous analytic source limitations by using a new type of analytical source, the compound dislocation model (CDM) and its point-source version, the point CDM (pCDM) (Nikkhoo et al., 2017). The CDM is composed of three orthogonal tensile dislocations, each with the same opening (or closing) magnitude, giving a total potency, or influx volume ΔV. The CDM has 10 parameters: three for location (x, y, z), three semiaxes lengths (a, b, c), three axial rotations $(\omega_x, \omega_y, \omega_z)$, allowing for arbitrary orientation and axes lengths, and uniform opening u. The CDM can approximate shapes ranging from equidimensional, to pancake shaped, to cigar shaped, to pipe like. In the case of the pCDM its computation time is faster and it has three potencies in place of the axes and uniform opening. For extended sources the pCDM is less accurate than the CDM, but we present it here (and in the supporting information) for comparison and to compare one versus two sources.

The solution for the two CDM source model constrained by the 2013–2016 data set (Figs 4.3-4.5 and Table 4.1) is a very long, thin source located slightly north and several kilometres east of the summit, centered at 7 km depth and plunging shallowly to the ENE. The second source is shallower (2.5 km depth), located above the upper portion of the deep source and elongated steeply toward the summit craters. The rate of influx volume increase (ΔV/yr), or potency rate, is $\sim 13 \times 10^6\,\mathrm{m}^3$/yr, where $\Delta V = 4u\,(ab + ac + bc)$ and a, b, and c are the semiaxes of the CDM and u is the opening.

We also computed source models using the pCDM solutions for one or two sources (Table 4.1). The one-source solution results are shown in Figs S2-S4. Results for the two-pCDM solution are shown in Figs S5-S8. The synthetic displacements for the single pCDM appear significantly worse than that for the two-source synthetic, especially for descending track data. We performed an F test of significance (see Lundgren et al., 2015, for equation and description). For the pCDM solutions $F = 199$, which for the large number of data points and the nine additional parameters for the second source, is significant at the 99 per cent confidence level. The pCDM source maps (Figs S4 and S8) show locations and orientations of the three force dipoles for each source that are similar to the potencies or ΔV for the CDM (see Nikkhoo et al., 2017, for details). For the pCDMs the potency, ΔV, is simply the sum of the potencies for each axis. The single-source pCDM solution is intermediate in location and mechanism between the

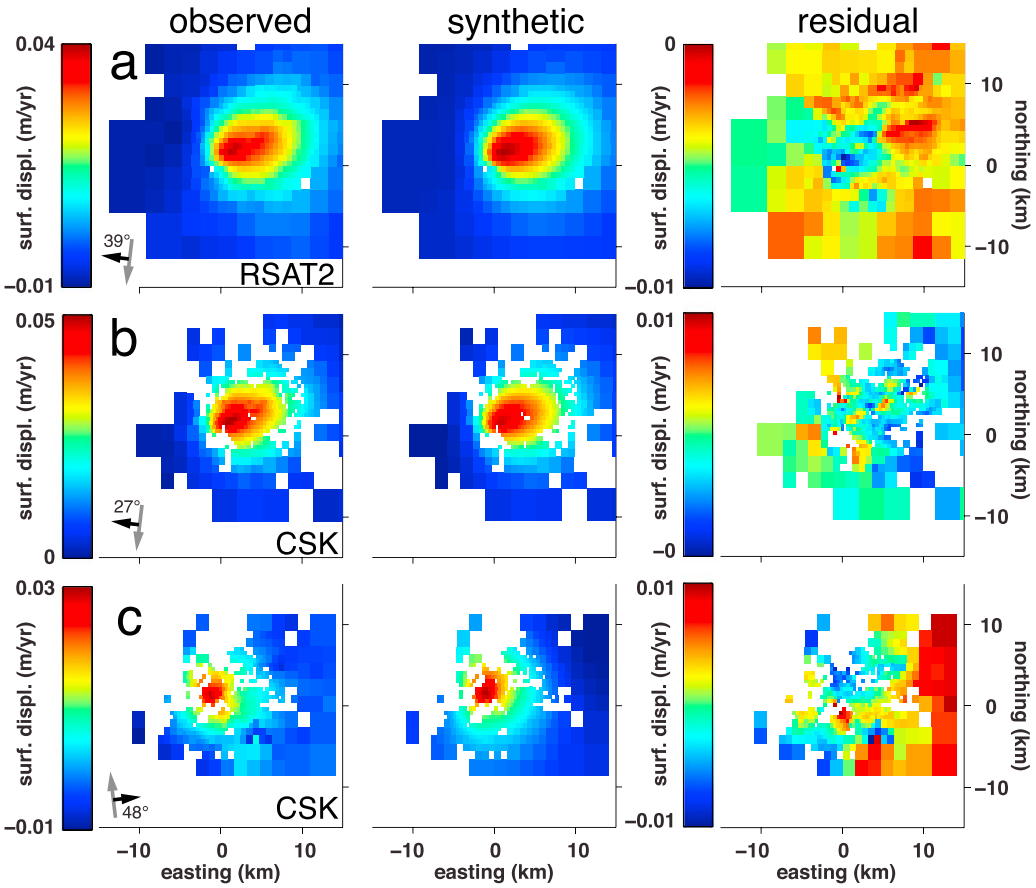

Figure 4.3: Two source CDM solution modeled InSAR line-of-sight (LOS) surface displacement rates for the 2013.25–2016.4 time interval. For each (left column) observed InSAR time series linear velocity we show the (middle column) synthetic displacements given by the source model and (right column) the residual. For each data set: (a) RSAT2 descending, (b) CSK descending, and (c) CSK ascending track, the satellite heading (grey arrow), look direction (black arrow), and incidence angle are indicated in the lower left corner.

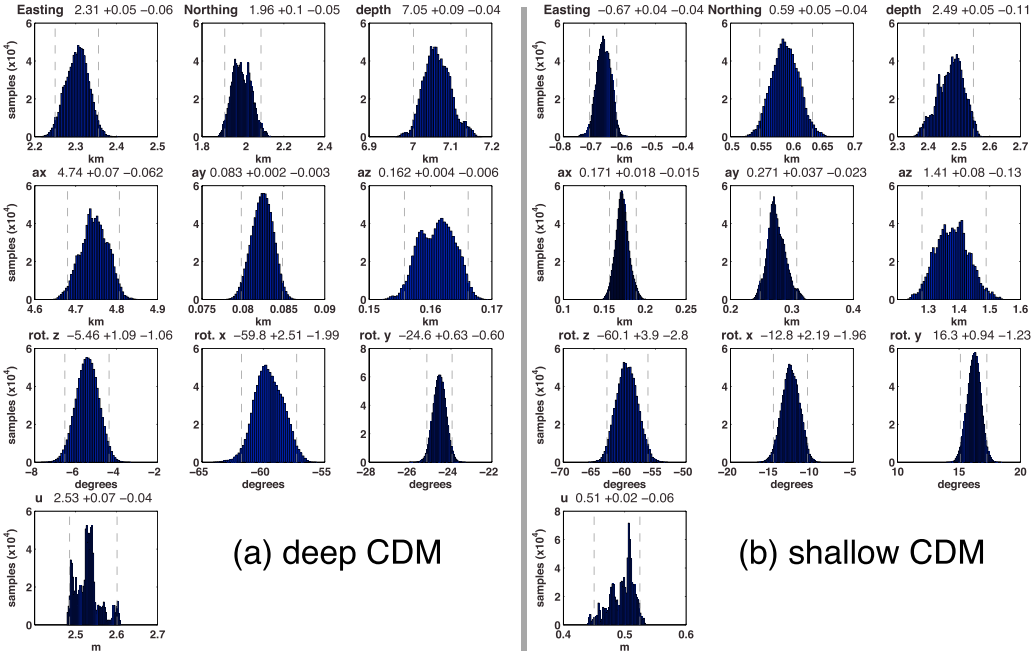

Figure 4.4: Two source CDM solution posterior probability density functions (PDFs) for each parameter. (a) Deep CDM source. (b) Shallow CDM source. The label for each parameter is given above each subplot. The number adjacent parameter label gives the mode value, and the plus and minus 95 per cent confidence bounds are indicated in the PDF plots by dashed grey lines.

Table 4.1: Source Model Inversion Results[a]

Model (Type, N Src Year-Range)	x (km)	y (km)	Depth (km)	a (km) / ΔV_x (10^6m^3/yr)	b (km) / ΔV_y (10^6m^3/yr)	c (km) / ΔV_z (10^6m^3/yr)	ω_x (deg)	ω_y (deg)	ω_z (deg)	u (m/yr)	ΔV (10^6m^3/yr)	RMS (mm/yr)
CDM 2 src 2013–2016	2.31	1.96	7.05	4.74	0.08	0.16	-59.8	-24.6	-5.5	2.53	11.8	1.9
	-0.67	0.59	2.49	0.17	0.27	1.41	-12.8	16.3	-60.1	0.51	1.4	
pCDM 2 src 2013–2016	3.47	2.97	8.44	0.44	2.45	4.71	5.9	-23.4	-16.0		7.6	2.0
	-0.90	0.81	4.57	3.64	1.50	0.83	38.7	33.2	-57.6		6.0	
pCDM 1 src 2013–2016	-0.85	1.93	7.64	1.43	0.18	9.55	-8.0	-46.6	-27.2		11.0	2.9
pCDM 2 src 2013–2014	2.06	0.77	9.0	3.11	3.97	18.1	22.9	-43.1	-32.8		25.2	6.0
	-0.36	1.23	2.39	1.34	1.97	0.69	-11.9	-10.5	25.4		4.0	

[a] See Nikkhoo et al. (2017) for CDM and pCDM definitions.

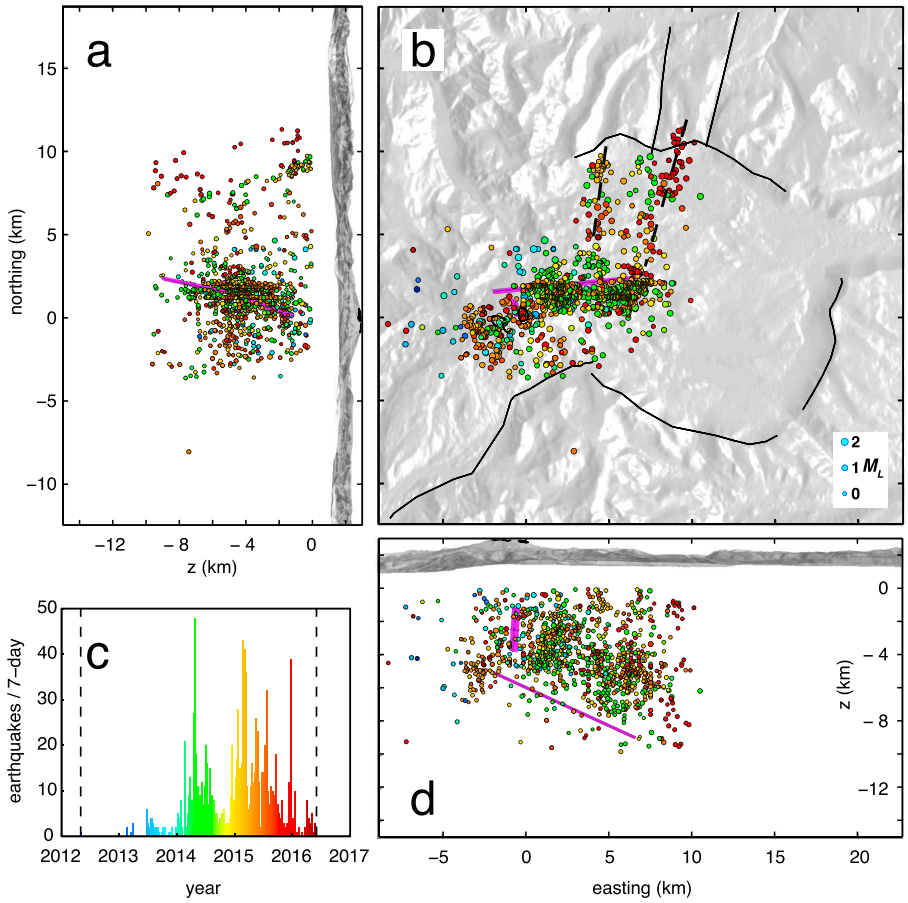

Figure 4.5: Two-source CDM solutions (magenta) and volcano tectonic (VT) seismicity from the OVDAS catalogue for events with location quality A and B. (a) Side view from the west. (b) Map view, area corresponds to box shown in Fig. 4.1. Dashed black lines north of the sources roughly parallel the two bands of seismicity in the northwest portion of the caldera, similar to the mapped faults (Fig. 4.1) extending to the north of the caldera. (c) Histogram of the number of volcano tectonic (VT) events per week. Color in the histogram and Figs 4.5a, 4.5b, and 4.5d correspond to the date of the earthquake. Seismicity circle size scales with local magnitude (M_L), legend given in Fig. 4.5b.

two-source solution. As such, it is less able to fit both the shape and extent of the observed LOS displacements. In the case of the two-pCDM source model we can also look at the model parameter covariances in addition to the PDFs (Fig. S7). In general, significant covariance occurs between the ΔVs and the source locations and depths, both within the same source and between sources. Some of these coupled variations in parameters for influx volume and depth are easily understood—the deeper the source the greater the influx volume required to maintain a given magnitude in surface displacement. The coupling between sources is strongest in depth, with opposing covariance in depth—as the deep source moves slightly deeper the shallower one moves toward the surface in compensation. However, it should be noted that the inferred uncertainties in these location parameters are relatively small (0.1–0.2 km in depth and <0.1 km in easting and northing; Fig. S6).

The root-mean-square (RMS) solution errors are 0.0029, 0.002 and 0.0019 m for the single pCDM, two-source pCDM, two-source CDM solutions, respectively (Table 4.1). This shows that the CDM solution is about 5 per cent better than the two-source pCDM solution, with the single-source pCDM about 50 per cent poorer in fitting the data. The finite CDM is better able to fit the extended deformation relative to its source depth and the length and orientation of the CDM, not surprising considering the improved fidelity of the CDM solution relative to the pCDM for finite, laterally extended sources (Nikkhoo et al., 2017).

We also compare the pCDM results for the UAVSAR data and the InSAR time series for the

2013 to 2014 time interval. We use two pCDMs and find similar results to those for the 2013–2016 InSAR time series linear LOS rates. The model fit to the six InSAR data sets (Fig. S9), the PDF distributions (Fig. S10), and solution force dipoles (Fig. S11) differ mainly in source depths, with the 2013–2014 depths both deeper and shallower compared to the deep and shallow pCDM solutions for the 2013–2016 interval. Because of these shifts, the size for each source in the 2013–2014 interval is larger and smaller for the deep and shallow sources, respectively. These model differences lie beyond their formal uncertainties shown for their distributions (Figs S6 and S10). We interpret these source differences as most likely reflecting data noise due to residual atmospheric effects, rather than true variations in the source locations. Atmospheric effects are particularly significant for the UAVSAR interferograms and can also affect InSAR time series, especially over shorter time intervals. UAVSAR interferograms can also suffer from residual aircraft motion effects.

4.4 Discussion

There are three interesting aspects to the Copahue source solution that warrant further discussion: (1) the interpretation of the solutions themselves, (2) the comparison of these solutions to other observations from the volcano since the onset of unrest in late 2011, and (3) the relationship of the source to seismicity and eruptive activity.

4.4.1 Deformation source implications

First, the asymmetry in the surface deformation indicates the need for a source extending from the Copahue edifice toward the caldera interior. Given the different viewing geometries of the satellite InSAR data and the apparent asymmetry between the ascending and descending time series linear velocity maps, we consider inverting for the three-dimensional displacements. We performed a least squares inversion of the three InSAR time series for the 2013.25–2016.4 interval up (U), northing (N), and easting (E) components (Fig. 4.6) using the method of Hu et al. (2010). As expected, the N component has very noisy values reflecting the poor constraint on it due to the mostly E-W viewing directions of the SAR satellites, which normally allows for the inversion of only the mostly U + N and E components (e.g., Lundgren et al., 2004; Milillo et al., 2016). Nonetheless, the U and E components show that there is a significant asymmetry from west to east, with both profiles extending more to the east than to the west of the summit, as expected for an asymmetric source plunging into the caldera to the east (Fig. 4.7a).

It is worth noting that the highly elongated shapes of the two CDMs are outside the moment ratio regimes for pressurized ellipsoidal cavities (from pancakes to cigar-like ellipsoids) as shown in Fig. S12 (see Nikkhoo et al., 2017). A more apt comparison might be to the open and closed conduit models of Bonaccorso and Davis (1999). If we compute a very elongated CDM source (Fig. S13a), we find that the central dimple in the peak vertical uplift, as well as the horizontal radial displacements, becomes more extreme, more similar to the open conduit model (Fig. S13b) than to the closed conduit model (Fig. S13c). As the radius of the conduit in Figs S12 and S13 is reduced, the CDM is exactly equivalent to the open conduit case. In our case the deep highly elongated source is shallowly plunging to the ENE, such that the effects of being open or closed may be muted. Nonetheless, the numerical implications of the very elongated source's displacements are that there would be minimal 'push' at the 'ends' of the source as expected for the closed pipe, but instead, it behaves more like the open pipe solution. Numerically, the very elongated CDM is unable to produce a very elongated closed pipe solution, though as the CDM becomes less extreme it plots in the ellipsoidal regime in Fig. S12. In the case of the shallow CDM, assuming its near-vertical orientation as vertical, we find that its vertical and

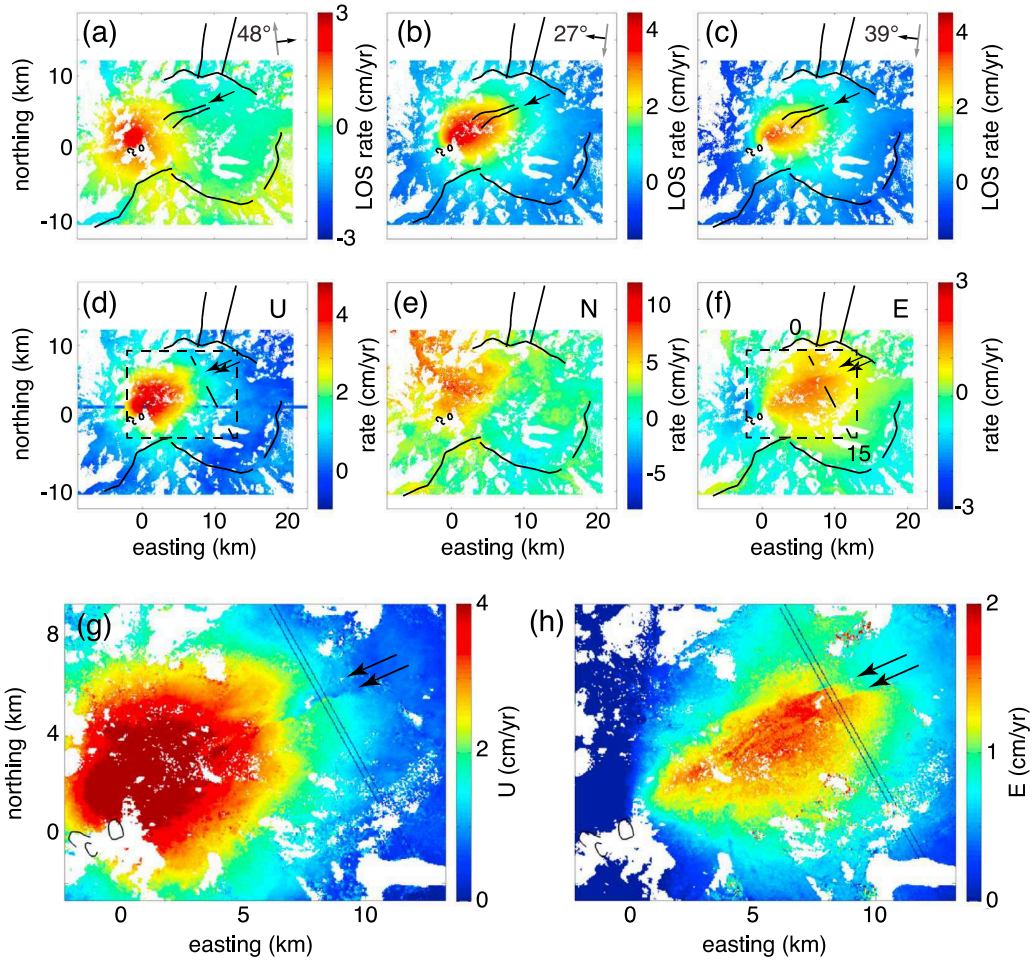

Figure 4.6: Inversion of InSAR time series linear LOS displacement rates into three-component displacement fields for the 2013–2016 interval. Bold black lines mark faults and caldera boundary, with the summit craters located near the origin. The COSMO-SkyMed (a) (CSK) ascending, the (b) CSK descending, and (c) RADARSAT-2 (RSAT2) descending track data are inverted into the (d) up, (e) north, and (f) east components using the approach of Hu et al. (2010). The blue horizontal 11 pixel-wide stripe in Fig. 4.6d is centered on the profile location shown in Fig. 4.7a. The black arrows in Figs 4.6d and 4.6f point to normal faulting discontinuities with the long dashed line marking the profile shown in Fig. 4.7b, and the short dashed box outlines the zoomed in areas shown in Figs 4.6g and 4.6h for the up and east rates, respectively. In Figs 4.6g and 4.6h the arrows point to the graben-bounding Copahue fault, the two thin parallel lines mark the bounds for the profiles in Fig. 4.7. The two NNW-SSE parallel lines in Figs 4.6g and 4.6h show the actual width of the profile (dashed line in Figs 4.6d and 4.6f) whose average values along the profile are shown in Fig. 4.7b.

horizontal displacements (Fig. S14) lie between those of an open and closed pipe for the same dimensions and depth range.

The deformation data alone cannot provide a unique interpretation of the source model. However, our deformation modelling suggests a few options:

1. Both CDMs represent conduits.

2. For the deep CDM: a network of intersecting dikes and sills, subjected to opening. In this case, they would still have to occupy a rather narrow zone that follows the shallow plunge of the deep CDM. For the shallow CDM: a shallow magma chamber.

3. The deep CDM represents the uppermost part of a large magma body. In this case only the top would yield the observed deformation due to properties of the magma body, such as composition or fluid zonation (Kazahaya et al., 2002). In contrast, a narrow

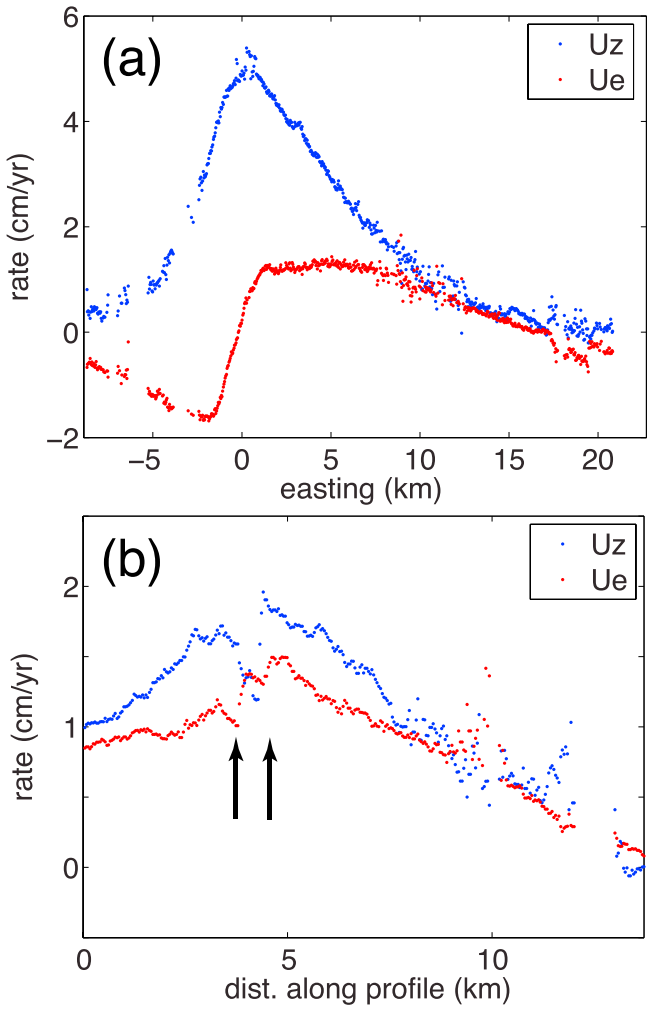

Figure 4.7: (a) Up (blue) and east (red) component relative motion profiles for the E-W profile location shown in Fig. 4.6d. The asymmetry in both profiles reflects both the two sources and their relative locations and geometries. (b) Up and east displacements along the profile crossing the NE trending faults shown in Figs 4.6d and 4.6f by the dashed line.

topped, deeply rooted body under constant change in overpressure would give a distinct deformation signature related to its depth extent that is not evident in the Copahue data, unlike for the case of a broad, shallow sill with a conical deep root (Yun et al., 2006).

4.4.2 Comparison with seismicity

It is important to compare the InSAR-constrained solution with observed volcano tectonic (VT) seismicity and volcano activity. We consider unrelocated seismicity from the Southern Andes Volcano Observatory (OVDAS). The OVDAS locations in the catalogue have depths relative to zero elevation; however, OVDAS considers the reference elevation at over 3600 m, but this is clearly too high for Copahue, which barely reaches 3000 m, with the low elevation portion of the Agrio-Caviahue caldera below 2000 m. The mean elevation of our InSAR data is 2009 m. In lieu of estimating an exact elevation shift for the solution and the seismicity we simply leave them referenced to zero elevation. We compare the VT OVDAS seismicity with high location quality (A and B) rankings to the CDM two-source model (Fig. 4.5). Comparison of the CDM solutions with the VT seismicity shows an interesting correlation. In map view we see that the seismicity roughly trends along with the deep shallowly plunging source. Viewed from the south, we see that the deep source lies just below and at a similar plunge as the lower bound of the main seismicity cloud. We also find that the shallower source cuts up through the near

summit seismicity, although a gap in the seismicity there is unclear. In map view there are two roughly parallel bands of seismicity that extend to the north from roughly the middle and eastern end of the source, likely linked to the Copahue-Antiñir fault zone (CAFZ) (Melnick et al., 2006; Folguera et al., 2016). It is worth noting that the eastern extent of the seismicity is within about 2 km of the eastern extent of the deep source. Together, these observations suggest that (1) there is a good correspondence between the VT seismicity and the deformation source and (2) the depth and extent of the source and VT seismicity are complementary. For (2) the implication on the depth and trend in depth of the deeper extent of the main VT seismicity cloud is that the deep source lies directly beneath this seismicity. This fits with observations from other volcanoes, such as Mount Etna, where the volcano source forms a 'hole' in the VT seismicity, which is concentrated above or to the sides of the source due to higher stress changes surrounding the source (Patanè et al., 2003). We do not plot the error bars for the seismicity locations; however, the mean standard deviations in the horizontal (1.2 km) and vertical (0.6 km) locations do not significantly affect our inferences regarding their locations relative to the sources.

Also, it is interesting to note that our model matches reasonably well with results on the spatial distribution of the seismicity magnitude-frequency b value (Lazo et al., 2015). Updated b value analysis, based on the VT seismic event catalogue from OVDAS for the period December 2012 through September 2016, shows two high b value volumes similar to the two CDM sources as well as the locations of active seismic and hydrothermal activity (Fig. 4.8). The spatial b value was calculated by means of the Ishimoto and Lida (1939) and Gutenberg and Richter (1944) methods for magnitude frequency distribution. Using 6172 well-located earthquakes, their spatial distribution was determined with a grid spacing of 100×100 m, taking a radius of 1.5 km and a minimum number of 80 events per calculation. Both of the high b value regions are related to a production of low magnitude VT events, evidence of regions with more fragile and heterogeneous characteristics like hydrothermal and magmatic zones. Analyzing the 3-D distribution, it is possible to observe two possible structures delimited by the high b values, one sketching a vertical conduit below the active crater to more than 6 km depth and the other one extending quasi-perpendicular to the first zone below 2 km depth (Fig. 4.8b). Together, they define an L-shaped structure, reflecting a possible conduit and magmatic reservoir below Copahue volcano. However, there are differences between the spatial distribution of high b values and our solutions for two CDMs: (1) the high b value structure trending NE from the central conduit below 2 km depth is more aligned with the Copahue faults and the NE flank hydrothermal system, suggesting that it does not reflect the deep deformation source in our model. (2) The high b values extending directly beneath the summit craters through at least 6 km depth does coincide roughly with our shallow source. However, it extends deeper than our geodetically determined source, which likely reflects (1) the resolutions of both the geodetic inversion and the b value technique in resolving the actual spatial dimensions and (2) that each observation does not correspond to the same process (e.g., the surface deformation is only sensitive to the location of the volume change, whereas the b value reflects the broader changes to mechanical properties of the continuum surrounding the sources). This highlights the multiple interpretations for high b values, which suggests that some of the higher b values to the NE of Copahue's summit may reflect fluid processes in the NE trending Copahue fault zone.

The two parallel bands of VT seismicity to the north of the deep source lie mostly within the caldera, with some events lying north of the caldera between the two main, right-lateral strike-slip faults of the southern CAFZ (Melnick et al., 2006; Folguera et al., 2016). Crosscutting this area of the NW caldera is the Copahue fault, a zone of N60°E trending, NW verging thrusts related to the Chancho-Co anticline (Melnick et al., 2006; Bonali et al., 2016; Folguera et al., 2016). Given the fault complexity within this area of the NW caldera and the apparent

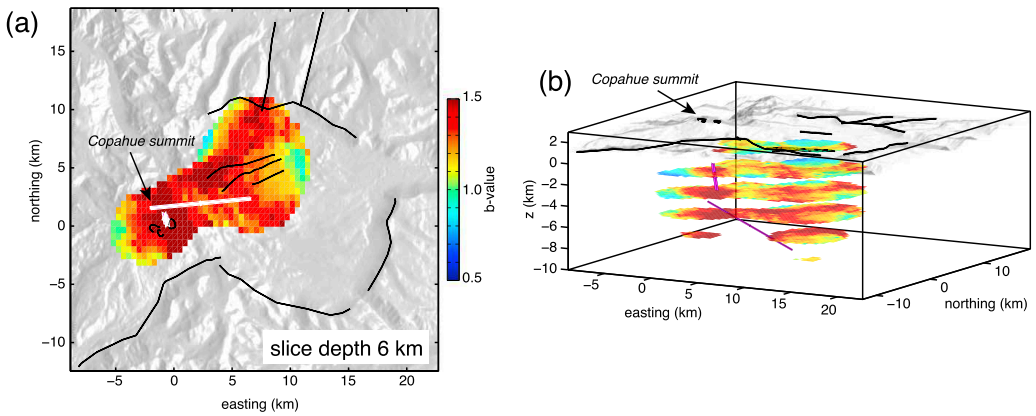

Figure 4.8: Spatial b value variations based on the VT seismic event catalogue from OVDAS for the period December 2012 through September 2016. For reference, we also plot the two-source CDM solution. (a) Plan view for a slice at 6 km depth. Results reveal two high b value anomaly zones, one extended zone extending up to 10 km NE from the active crater and a second zone around the active crater (map view). CDM outlines are in white; portion of CDMs shallower than the 6 km slice is colored magenta. (b) 3-D perspective view, from S30°E and 10° elevation angle, of b value horizontal slices from 0 to 10 km depth at 2 km intervals. Here we observe the first high b value zone (reddish colors) to the NE of the summit spans a depth between 2 and 8 km, while the zone around the crater extends from the surface to 8 km depth. Two-source CDMs are coloured magenta with black outlines.

northern trends to the seismicity pattern, we compute the Coulomb stress change (Stein et al., 1992; King et al., 1994; Toda and Stein, 2003) for both vertical, N10°E striking, right-lateral strike slip (RLSS) and 60° dipping (to the NW) S60W striking thrust and normal faults (Fig. 4.9). We show the Coulomb stress change (ΔCFS) for depth slices at the near surface (0.25 km depth) and at 5 km depth. For each we show the OVDAS VT seismicity for depth ranges of 0–2.5 km and 2.5–7.5 km. For the RLSS case we see that the north trending bands of seismicity fall within the zone of positive ΔCFS, suggesting promotion of these events within both depth slices (Figs 4.9a and 4.9b). The thrust motion on the Copahue fault system would not be promoted at either depth (Figs 4.9c and 4.9d). Instead, we see that normal motion would be promoted, although some variation in the pattern would occur with changes in dip angle (Figs 4.9e and 4.9f). Regarding the RLSS events, it is also worth noting that the north trending seismicity has only a few events that occur outside the caldera to the north and that these events occur beyond the area with positive ΔCFS, suggesting the extent of positive ΔCFS controls the northern limit to these events. It should also be noted that these ΔCFS computations were carried out assuming a particular effective friction ($\mu' = 0.5$), receiver fault geometry, and without considering regional stresses, all of which will affect the ΔCFS pattern (King et al., 1994).

The case for normal fault motion derives from the observation in the 3-D surface displacement rate inversion of fault motion trending to the NE along the NE flank of Copahue (Fig. 4.6). This feature is quite evident in the InSAR time series mean velocities (Fig. 4.2), but it is the decomposition into the 3-D displacements, effectively up and east since the north component is unconstrained that allows us to see there are two parallel faults. These two faults are most evident in the east component (Fig. 4.6f) where the north side moves to the west relative to the south side of each fault. Instead, if we look at the up component (Fig. 4.6d), we see that they constitute a graben, with the area between the two faults subsiding relative to the flanks. In profiles across the structures (black arrows in Fig. 4.7b) we see the downward displaced axial graben and horizontal motion reflecting extension. This fits with the Coulomb stress change calculations (Figs 4.9e and 4.9f) showing promotion of normal fault motion. Essentially, this is not surprising since the crust above an inflating body, composed of both vertical and radial horizontal displacements, would promote graben formation and are very similar to structures

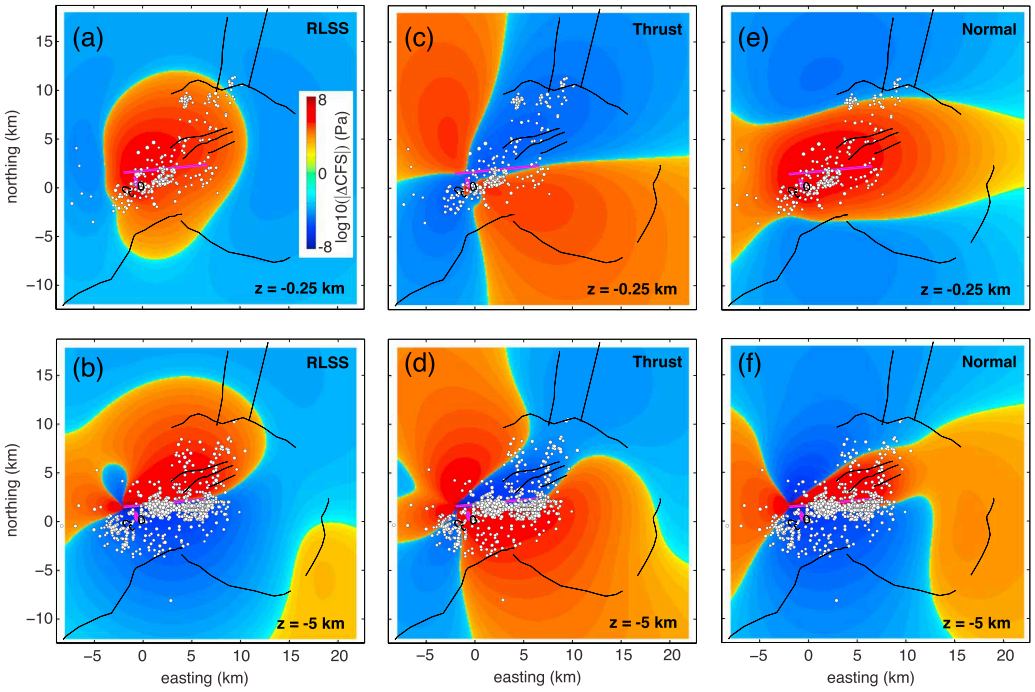

Figure 4.9: Change in Coulomb fault stress (ΔCFS) for the CDM model (shown in Fig. 4.5) for (a, b) right-lateral vertical strike-slip (RLSS) striking N10°E, for (c, d) S60W striking, 60° dipping thrust faults, and for (e, f) S60W striking, 60° dipping normal faults. VT seismicity is from the OVDAS catalogue for events with location quality A and B. For plots Figs 4.9a, 4.9c, and 4.9e the ΔCFS is shown at a depth of 0.25 km with seismicity in the depth range from 0 to 2.5 km. For Figs 4.9b, 4.9d, and 4.9f the ΔCFS is for a depth of 5 km with seismicity in the depth range from 2.5 to 7.5 km. The two CDM sources are shown in magenta. For all ΔCFS solutions we use the calc_coulomb function from the Coulomb34 package by S. Toda (toda@rcep.dpri.kyoto-u.ac.jp; https://earthquake.usgs.gov/research/software/coulomb/). We use an effective friction of 0.5 and equal Lamé coefficients of 30 GPa.

seen in laboratory experiments for volcano inflation and caldera formation (Acocella, 2007).

It is useful to compare our CDM modeling results (Fig. 4.5) to prior InSAR modeling results. Velez et al. (2011) studied a period of subsidence from 2002 to 2007 using Envisat SAR data, computing time series LOS mean velocities from both ascending and descending tracks. During this time period they found maximum subsidence rates of nearly 2 cm/yr. Similar to the current episode, the ascending and descending tracks had similar patterns. Velez et al. (2011) modeled a single source, comparing solutions for either a Mogi or spheroidal source. Both solutions were located at 4 km depth, with the spheroidal source the preferred solution. Velez et al. (2011) interpreted the subsidence and source solution in terms of the release of briny fluids through a sealed carapace, some 3–4 km beneath the summit, at the brittle-plastic transition above a deeper magma body. The depth of the Velez et al. (2011) subsidence source is intermediate between our solutions. Since they only modelled a single source in this paper, it is possible there were two sources involved and that their single-source model solution found a depth intermediate between those for a two-source model. Under that scenario the interpretation might be that both the deep and shallow sources deflated together, thus undermining the sealed carapace interpretation.

More recently, Velez et al. (2016) modelled both the 2002–2007 km and the 2011–2012 km portion of the current unrest, comparing the results for point, spheroidal, and tensile dislocation sources. They found solutions located between 7.5 km and 9 km beneath the surface for the current unrest, with the shallower depth found for the point and spheroid sources and the deeper one found for the tensile dislocation (sill) source. Velez et al. (2016) preferred the spheroidal source solution since the sill-like dislocation source extended beyond the edifice into the caldera. In order to reduce a positive residual on the volcano's northern flank, Velez et al. (2016) added

a conduit that they approximated by a high aspect ratio, prolate, inclined spheroid. Their best fit conduit solution was located at 2 km depth beneath the edifice. Conceptually, their two-model solution has similarities with our own: a shallow conduit lying above a deeper source. The main difference between the Velez et al. (2016) solution and ours lies in the inclined orientation of our deeper source and the greater depth separation between their sources. It is also worth noting that their volume change (δV), the amount the surrounding medium deforms for a change in pressure within their source volume (see Nikkhoo et al., 2017, and eq. 3.10), for the 2011.75–2012.25 (half-year) interval for their two-source solution ($\delta V = 0.050\,\mathrm{km^3\,yr^{-1}}$ if assumed a rate) is considerably larger than our two-source pCDM potency change (ΔV) solution (Table S1) for the 2013–2014 interval ($\Delta V = 0.029\,\mathrm{km^3\,yr^{-1}}$), even though the LOS rates in the ascending tracks were similar (∼8 cm/yr). The potency ΔV^E and volume change δV^E of an ellipsoidal cavity are related through $\Delta V^E = \delta V^E + pV/K$, where p is the pressure change and K is the bulk modulus (Nikkhoo et al., 2017). In the case of a Mogi source in a Poisson solid $\Delta V^{Mogi} = 1.8\delta V^{Mogi}$, and in the limit of a planar crack $\Delta V^{Mogi} = \delta V^{Mogi}$ since there is no initial cavity volume V. Therefore, for the same observed deformation the potency of a CDM solution equivalent to a point sphere (Mogi source) should be 1.8 times larger than the volume change derived for the Mogi source. Our problem is the reverse, with $\Delta V < \delta V$, requiring a more fundamental reason for this discrepancy. Some of the differences between their models and ours may be due to their more restricted time interval and having only ascending track data, which likely restricts their model resolution. We also point out that during 2012 we find LOS rates for the descending track time series of approximately 12 and 15 cm/yr for RSAT2 and CSK, respectively. This would imply higher rates of volume change prior to the December 2012 eruptions, which would likely reduce this discrepancy.

Our modelling of the current inflation episode involves both a shallow conduit-like source and a second deeper source. The VT seismicity, despite limitations in location precision (standard deviations of 1.2 km in horizontal and 0.6 km in depth locations) and accuracy due to uncertainties in the velocity structure and reference depth, suggests that the hypocenters are located in close proximity above the modelled sources. Taken at face value, the dimensions and aspect ratio of the deep CDM are unexpected. Numerically, the MCMC solution is allowed to blindly find the best fitting set of two sources to fit the data. In its most literal interpretation the modelled deep source would represent an open pipe, although the CDM solution does not produce a very elongated closed pipe model, and its shallowly reclined orientation means that the deformation is relatively insensitive to it being open. It would represent an inclined conduit, some 160–320 m in diameter and 9 km long. This source appears to connect the shallow near-summit magma body with a deeper source that did not produce resolvable deformation during the study period. However, as mentioned at the end of Section 4.4.1, there are other plausible interpretations either in terms of an inclined plexus of intersecting dikes and sills or the upper extent of a deeper magma reservoir whose primary body does not produce resolvable deformation (Fig. 4.10). It is worth noting at this point that although our interpretation is but one scenario (Fig. 4.10) the highly elongated shape and orientation of the deeper source, pointing from beneath the shallower source toward the center of the caldera, favours a zone of magma transfer (and volume change) from a central caldera source. The lack of a detectable geodetic signature from this deeper caldera source implies that its volume change during this time interval was insignificant relative to its depth, although other volcanoes in the central and northern Andes have produced detectable deformation from deeper sources (Pritchard and Simons, 2002; Fialko and Pearse, 2012; Pearse and Lundgren, 2013; Remy et al., 2014; Lundgren et al., 2015).

The shallower source, though less elongated, falls outside the ellipsoidal cavity regime in the moment ratio plot (Fig. S12). We model the deformation as resulting from two sources; however, the proximity of the lower end of the shallow source with the shallower portion of the

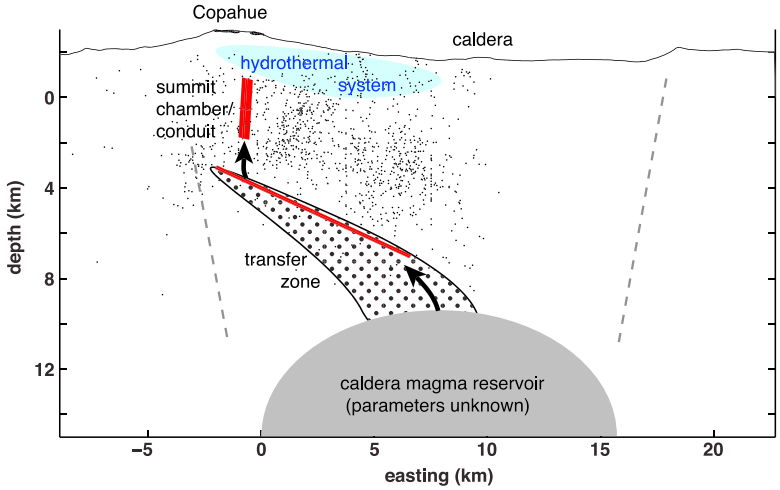

Figure 4.10: Conceptual diagram for the Copahue volcano-Agrio-Caviahue caldera system. The view is from the south. In red are the modelled CDM solutions; black dots are the OVDAS VT seismicity. Topography profile crosses the summit of Copahue. Dashed lines mark nominal caldera bounding faults; locations and dips are speculative. The eastern end of the deep CDM source suggests that it acts as a zone of magma transfer from a source beneath the center of the caldera, whose depth and size are unknown (grey semiellipse). At shallower depths from the summit of Copahue to the NE lies a hydrothermal system. The stippled region extending from the deep source to beneath the deep CDM source represents the transfer zone of uncertain dimensions.

deeper source suggests that they might represent a single source with a more complex geometry or, at least, two sources that are well connected. This high connectivity is supported by the constant shape of the surface deformation with time.

The rate of influx volume for the CDM and pCDM sources is fairly similar. For the 2013–2016 time interval the influx volume rates are 13.2, 13.2 and $11.0 \times 10^6\,\mathrm{m}^3/\mathrm{yr}$ for the CDM two-source, pCDM two-source, and pCDM one-source, respectively. The somewhat smaller ΔV for the single pCDM solution reflects its inability to fit well all the observations and the resultant higher misfit. For the 2013–2014 interval the rate of influx volume ($29.3 \times 10^6\,\mathrm{m}^3/\mathrm{yr}$) is more than double that for the 2013–2016 interval, which reflects the higher deformation rate in the first 2 years of unrest.

Although no quantitative assessments of erupted volume are found for the 2012–2016 eruptions, the assessment of volcanic explosivity index (VEI) 2 eruptions in late December 2012 (Caselli et al., 2016a) corresponds to ejecta volumes greater than $1–10 \times 10^6\,\mathrm{m}^3$, based on the scaling relationship built into the VEI scale (Newhall and Self, 1982). Following the 2012 eruptions, we see only a slight reduction in the inflation rate, suggesting that these small eruptions did not significantly reduce the accumulated pressure increase within Copahue's magmatic system. In fact, as mentioned before, more eruptive episodes occurred through 2016 (OVDAS reports).

4.4.3 Comparison with summit activity

Copahue volcano is an interesting case of ongoing inflation accompanied by eruptive activity. As we have already seen for the VT seismicity (Fig. 4.5c), it starts soon after the start of inflation, with increasing numbers of events through 2015–2016. Previous studies have associated the activity to a delayed response following the 2010 Maule (Mw 8.8) earthquake that would have caused unclamping of the main north and NE oriented vertical faults at Copahue and promoted fluid migration into the volcano from depth (Bonali, 2013). High-quality location VT seismicity at Copahue is not at resolvable numbers in Fig. 4.5c until 2013, after the December 2012 eruption, with the largest numbers of earthquakes reaching maxima in 2014 and 2015, before starting the longest and last eruptive episode characterized by quasi-continuous strombolian

activity. Since roughly half of the surface deformation occurred after 2012, this might suggest that VT events were stimulated by increasing Coulomb stress changes due to movement of new magma toward the surface.

The inflation time series, which is characterized either as piecewise linear or as an exponential decay (Fig. 4.2), might result from different mechanisms (Dzurisin et al., 2009). In the absence of eruptive activity (that is, pressure release), exponentially decreasing inflation rates can be explained conceptually by (1) a hydraulically coupled system of deep and shallow magma reservoirs connected by a conduit (Reverso et al., 2014) or (2) viscoelastic relaxation following pressurization of a magma reservoir with a viscoelastic shell (Dragoni and Magnanensi, 1989; Newman et al., 2001, 2006). Hydrothermal system models can also exhibit time-dependent behaviour due to a pulse of heating at the base of the system, possibly leading to very large displacements for caldera systems such as Campi Flegrei, Italy (Gaeta et al., 1998). However, the hydrothermal system at Copahue is likely restricted to within 1 km–2 km depth (Varekamp et al., 2009; Agusto et al., 2013; Varekamp et al., 2016) and would not explain the deformation time series that is dominated by the signal from the deeper source.

Distinguishing between these various mechanisms might be accomplished with microgravity observations, assuming that the deformation source is adequately constrained and that corrections to topography, vertical deformation, groundwater, and magma compressibility (Rivalta and Segall, 2008) can be made to estimate mass changes that combined with volume change estimates infer the density of the intrusion (Battaglia et al., 1999; Battaglia and Segall, 2004; Battaglia et al., 2008). With regard to the hydraulically coupled system (1), there is no geodetically resolved deformation signature for a deeper source. The two-chamber model (Dvorak and Okamura, 1987), typically invoked to explain exponentially decreasing inflation following an eruption, (Lu et al., 2003), involves pressure balance between the shallow and deep reservoir with consideration of the magma flux into the deep chamber as well as the conduit connecting the deep to shallow chambers (Reverso et al., 2014). In the case of Copahue this could mean that the chamber volume change is either too deep or too low in volume change to produce resolvable deformation with InSAR. It is instructive to look at other systems that might place constraints on the magnitude of volume change and depth permitted. For example, Nevado del Ruiz volcano (NRV) recently experienced inflation from a source located 14 km beneath the surface with a volume change rate of $\sim 40 \times 10^6\,\mathrm{m}^3/\mathrm{yr}$, which produced an LOS uplift rate of 3 cm/yr. Our estimate for the Copahue volume change rate is around one third to two thirds that of NRV. Such a LOS rate might be evident in the Agrio-Caviahue caldera; however, at NRV the deformation signal spanned some 30 km, roughly the size of the map area in Fig. 4.2. The lack of any such signal suggests that a more likely interpretation would be that any flux of magma from the deeper to shallower chamber (where shallower means both our modelled sources) would be compensated by influx from below into the deep caldera chamber, a hypothesis we cannot test with the geodetic data alone.

The existence of eruptions in 2012 and continual eruptive episodes, as well as gas emission over the period of this study, implies that Copahue is a partially open system. It is interesting, however, that the VT seismicity rates increased and gas flux remained high (Carn et al., 2017) since the phreatomagmatic eruption in December 2012 (Caselli et al., 2016a,b). This might suggest that these processes are related to stress increases as volume changes increased at depth and the movement of new magma batches to the surface, giving rise to increased numbers of VT events, possibly facilitating increased gas flux and new magmatic eruptive episodes.

4.5 Conclusions

InSAR time series from RSAT2 descending and CSK ascending and descending track data for the 2011–2016 unrest period show an asymmetric inflation pattern that started abruptly in late

2011, grew at roughly constant rate (approximately 12 and 15 cm/yr LOS on the RSAT2 and CSK descending track time series) through the main eruptions in December 2012, followed by slightly lower rates of inflation since. Total accumulated RSAT2 and CSK descending track LOS displacements were ∼30 and 36 cm, respectively, over 4 years (2012–2016). During the final year of this study (2016) it is unclear whether inflation slowed or possibly stopped, given the uncertainty in the InSAR time series; however, additional RSAT2 data through early 2017 show that inflation continues. We also examined repeat-pass UAVSAR airborne data in 2013–2015. The best set of interferograms for modelling were for 2013–2014 and show inflation consistent with the satellite time series observations.

We modelled the InSAR time series linear velocity deformation maps from 2013 to 2016 using the compound dislocation model (CDM) and, for comparison, the point CDM (pCDM) of Nikkhoo et al. (2017). This time interval allowed us to use time series mean LOS velocities from three satellite tracks (two descending and one ascending) in order to provide the best constraint on the sources. We found that a two-source model was required for Copahue and that the CDM gives a slightly improved fit to the data compared to the pCDM two-source solution, with the latter solution giving a significantly better fit to the data compared to the single-source pCDM based on an F test. Models using the pCDMs give results with a similar interpretation as the CDM solution. Models for the six InSAR data sets (three satellite and three UAVSAR) that covered the 2013–2014 time interval were computed for the two pCDMs. The results are similar to the two pCDM solution for the 2013–2016 InSAR time series satellite data sets.

The preferred two-source CDM gives an interesting, and somewhat surprising solution. The shallow source is elongated, steeply plunging, and centered at 2.5 km beneath the surface, which can be considered to be the 2000 m average elevation of the InSAR data, as shown in Fig. 4.10, thus placing the shallow source roughly at sea level. The second source is much deeper, centered at 7 km below the surface (5 km below sea level), but with a highly elongated, pipe-like shape plunging 25° to the east, whose shallow end lies beneath the shallow summit source and whose deeper end extends into the center of the caldera. The location and orientation of the deep CDM source fits well with the deeper extent of VT seismicity, suggesting that the seismicity is related to stress changes due to the deep source's volume change, whereas the spatial variation in b values are sensitive to both the central conduit as well as processes linked to the NE flank fault and hydrothermal systems. While a literal interpretation of the deep CDM source as a narrow (∼160 × 320 m cross section) conduit does not fit with typical geodetically constrained volcano sources, it does suggest that much of the surface deformation during the most recent inflation of Copahue volcano occurred in a narrow transfer region between a deeper, unresolved source beneath the caldera and a shallow reservoir beneath Copahue's summit.

Chapter 5

Satellite radar data reveal short-term pre-explosive displacements and a complex conduit system at Volcán de Colima, Mexico

Abstract

The geometry of the volcanic conduit is a main parameter controlling the dynamics and the style of volcanic eruptions and their precursors, but also one of the main unknowns. Pre-eruptive signals that originate in the upper conduit region include seismicity and deformation of different types and scales. However, the locality of the source of these signals and thus the conduit geometry often remain unconstrained at steep sloped and explosive volcanoes due to the sparse instrumental coverage in the summit region and difficult access. Here we infer the shallow conduit system geometry of Volcán de Colima, Mexico, based on ground displacements detected in high resolution satellite radar data up to 7 h prior to an explosion in January 2013. We use the boundary element method (BEM) to reproduce the data synthetically and constrain the parameters of the deformation source, in combination with an analysis of photographs of the summit. We favour a two-source model, indicative of distinct regions of pressurization at very shallow levels. The horizontal location of the upper pressurization source coincides with that of post-explosive extrusion. The pattern and degree of deformation reverses again during the eruption; we therefore attribute the displacements to transient (elastic) pre-explosive pressurization of the conduit system. Our results highlight the geometrical complexity of shallow conduit systems at explosive volcanoes and its effect on the distribution of pre-eruptive deformation signals. An apparent absence of such signals at many explosive volcanoes may relate to its small temporal and spatial extent, partly controlled by upper conduit structures. Modern satellite radar instruments allow observations at high spatial and temporal resolution that may be the key for detecting and improving our understanding of the generation of precursors at explosive volcanoes.[1]

[1] Originally published as: Salzer, J. T., Nikkhoo, M., Walter, T. R., Sudhaus, H., Reyes-Davila, G., Breton, M., Arambula, R. (2014): Satellite radar data reveal short-term pre-explosive displacements and a complex conduit system at Volcán de Colima, Mexico. - Frontiers in Earth Science, 2, p. 1-11. doi:10.3389/feart.2014.00012

5.1 Introduction

The conduit systems feeding dome-building eruptions can be highly dynamic, with irregular changes in the location and style of magma extrusion (Bernstein et al., 2013). At some volcanoes, the timing and dimension of extrusive activity may be forecasted based on precursory signals such as earthquakes, tremors and long periodic seismicity (Kilburn and Voight, 1998; Neuberg, 2000; Bean et al., 2014), as well as ground displacements on different scales (Surono et al., 2012; Di Traglia et al., 2013) that can be readily identified and have been successfully used for timely evacuation. A large variety of conduit processes may generate precursory signals, including gas accumulation beneath a volcanic dome (Johnson et al., 2008), episodic slip on the conduit margins (Anderson et al., 2010), changes in a dynamic plumbing system (Kahl et al., 2011) or the accumulation of magmatic material at shallow levels (Ratdomopurbo et al., 2013).

However, identifying which periods of unrest will lead to an eruption still remains a challenge (Sparks et al., 2012). Improving our understanding of the processes generating short-term pre-eruptive geophysical signals and ultimately avoiding false alarms require close observations of the dome feeding system and positioning of instrumentation in proximity of the vent. Such observations are rare at explosive volcanoes due to the vulnerability of near summit stations. Therefore, detailed observations of processes in a volcano feeding system are mostly obtained at non-explosive volcanoes, or where complete seismic and geodetic monitoring was achieved. A constrained path the magma propagates through could only be described in a few of those cases, such as Stromboli (Chouet et al., 2008; Di Traglia et al., 2013), Mount Etna (Kahl et al., 2011), Piton de la Fournaise (Massin et al., 2011) or Hawaii (Chouet and Dawson, 2011). At explosive dome-building volcanoes, the location of the conduit is more difficult to constrain. In some cases, we can observe summit deformation caused by the pre-eruptive intrusion of magma to very shallow levels of the volcano (Dzurisin et al., 2008; Saepuloh et al., 2013). Since the newly injected material remains there, this deformation is static and lacks co-explosive subsidence (Ratdomopurbo et al., 2013). However, short term pre-eruptive deformation originating from conduit processes of smaller magnitude are rarely detected with geodetic instrumentation, yet may be related to a considerable proportion of pre-eruptive seismic signals.

We present a model of the uppermost conduit system of Volcán de Colima (Fig. 5.1), a dome building volcano located in Western Mexico, based on geodetic data acquired shortly prior to an explosion. The eruptive history indicates that Volcán de Colima may experience Plinian eruptions with VEI (volcanic explosivity index) > 4 approximately every 100 years, the last of which occurred in 1913 (Bretón González et al., 2002). Between 2007 and June 2011, the activity at Volcán de Colima was characterized by periods of dome extrusion, as well as pyroclastic flows and explosions. After the last explosive event in June 2011, Colima entered a period of quiescence, until a new period of eruptive activity was initiated by a vulcanian explosion on January 6th, 2013, preceded only by 3 days of increased seismicity (Fig. 5.2). Smaller explosions occurred on January 11th and 13th and were preceded by smaller increases in seismicity. The explosions were followed by relatively low seismicity rates. The pre-explosive seismic activity was observed at the nearest seismic station (EZV4), located at 1.5 km from the summit (Figs 5.1 and 5.2). A similar type of seismicity has previously been observed at Volcán de Colima (Arámbula-Mendoza et al., 2011) and is possibly related to fluid movement and rock fracturing in the conduit (Bean et al., 2014).

We use a satellite radar dataset at unprecedented resolution to measure the surface displacements prior to the first explosion at thousands of points on the volcano summit and crater region. The timing of the satellite imagery precedes the 6th January 2013 explosion by hours only (Fig. 5.2). We exploit the radar data interferometrically (InSAR), a method now used routinely to analyse large scale deformation at many volcanoes (Fournier et al., 2010; Ebmeier

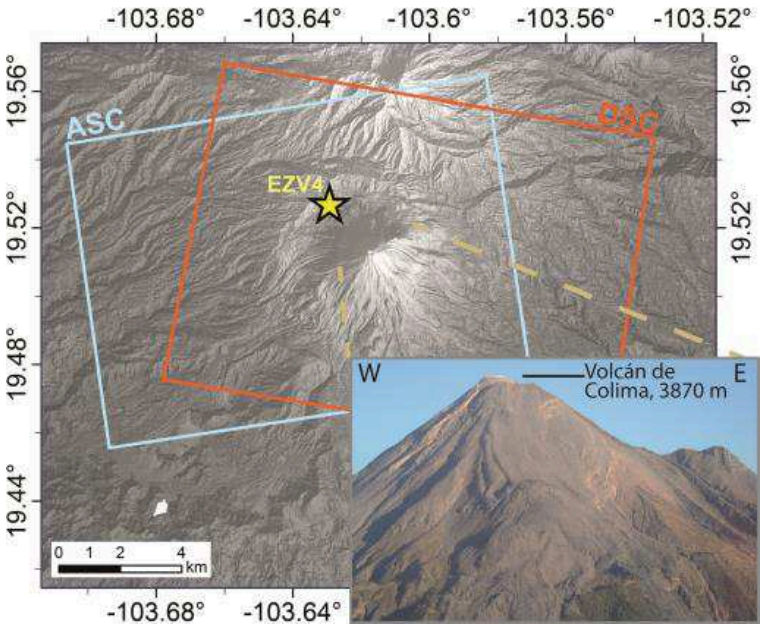

Figure 5.1: Location map and overflight photograph of Volcán de Colima. The steep-sloped volcanic cone is approximately 4–6 km wide, and completely covered by both the ascending and descending TerraSAR-X satellite data (blue and red boxes in map view). The yellow star marks the seismic station EZV4 described in this paper.

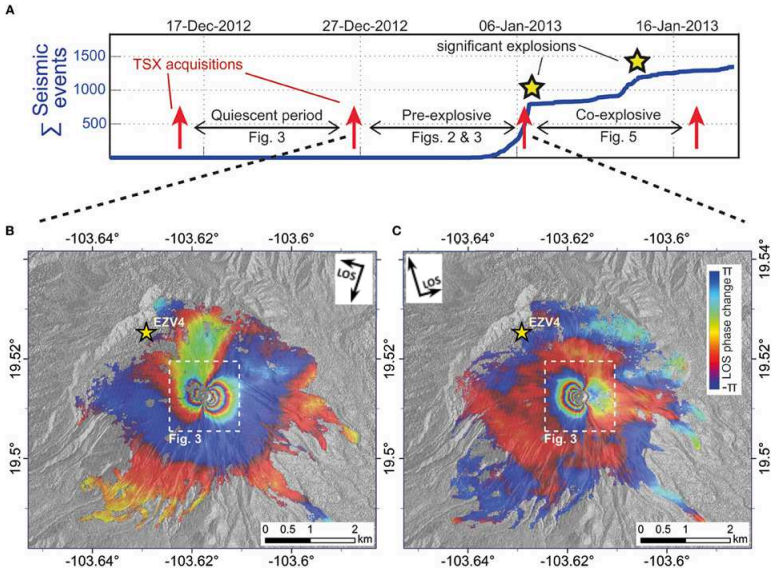

Figure 5.2: Seismicity increase in January 2013 and TerraSAR-X interferograms. (A) Time plot with cumulative number of seismic events recorded at EZV4 (blue), timing of TerraSAR-X satellite acquisitions (red arrows) and timing of significant explosions (yellow stars). The interferograms cover the quiescent period, the pre-explosive period and the co-explosive period. (B,C) The re-wrapped pre-explosive interferograms (December 26th-January 6th) show strong deformation affecting the summit area and are used in our modelling study. The descending data (B) were acquired on track number 128, the ascending data (C) on track 121. Each colour cycle corresponds to 1.55 cm of line-of sight (LOS) displacement. The arrows indicate the horizontal projection of the LOS and the radar azimuth direction. The seismic station EZV4 lies outside the deforming region.

et al., 2013), and allowing the identification of the depths and geometries of volcanic magma chambers (Dzurisin, 2007). Recent studies have also revealed the importance of both timeliness and spatial resolution when identifying processes associated with basaltic eruptions (Bagnardi et al., 2013; Richter et al., 2013). However, this is the first time that transient plumbing of a dome feeding system was detected as a pre-explosive inflation episode using InSAR. This allows the modelling of the conduit associated with an explosion, linking the deformation to the

pattern of pre-explosive seismicity and drawing conclusions on the processes generating these signals.

5.2 Methods

5.2.1 Data Processing and Generation of Displacement Maps

Interferometric Synthetic Aperture Radar (InSAR) is a method used to measure ground displacements in the line of sight (LOS) of the satellite that occurred between two SAR acquisitions. We consider SAR images on ascending and descending tracks acquired every 11 days by the German radar satellite TerraSAR-X (TSX) in spotlight mode. This type of acquisition yields a spatial resolution of over 2 m, which is unprecedented at Volcán de Colima and most other volcanoes worldwide. We focus our study on images taken on December 15th, December 26th, January 6th, the day of the first explosion, and January 17th, following another explosion (Fig. 5.2). The acquisitions on January 6th fall into the period of increasing seismicity and precede the explosion by 19 and 7 h on the ascending and descending track, respectively. This imagery therefore allows us to analyse the deformation during the quiescent period during which no seismicity was detected, during the pre-explosive seismicity increase, as well as the time frame covering the explosions. Our data extends further back into the quiescent period in 2012, for simplification we only show the last interferogram.

In order to quantify the surface displacements, we used the processing chain implemented in the ROI_PAC software (Rosen et al., 2004). The Digital Elevation Model (DEM) used for correction of topographic effects was kindly provided by the Universidad Nacional Autonoma de Mexico, based on airborne LIDAR data acquired in 2005, with a horizontal resolution of 5 m. We superimposed a photogrammetric DEM of the volcano summit from December 2011 on the LIDAR data, in order for our DEM to contain the dome built in the years 2007 to 2011 (James and Varley, 2012).

5.2.2 Source modelling

We use the boundary element method (BEM) to simulate the observed surface displacement and herewith to quantify parameters such as the pressurization and the geometry of the source. This modelling method is based on the analytical solution of a triangular dislocation (TD) in an elastic full-space (Yoffe, 1960). The TDs allow us to discretize any curved surface, such as topography and the geometry of complex sources without any discontinuity (Kuriyama and Mizuta, 1993; Maerten et al., 2005). In our model, we simulate the pressurization of the source by defining traction boundary conditions at the centroids of the TDs. The topography on the other hand is simulated as a traction-free surface, that is, the traction at the centroids of all surface TDs is zero (Walter et al., 2005). By computation of the stress influence coefficient matrix of our model and considering the imposed boundary conditions we are able to solve for the unknown slip and opening components at the TDs (Jeyakumaran et al., 1992), which allows the calculation of the displacements at any point in the model. We have chosen this modelling method because it considers topographic effects (Cayol and Cornet, 1998a) and also the interaction of multiple sources of pressure.

Through a combination of forward modelling and optimizations we minimize the misfit between the modelled displacements and the data. Forward models first aim at investigating the effect of the source type on the modelled surface displacements and confine the solution space. We use these search parameter ranges to find the solution with minimum misfit by performing a non-linear optimization using a genetic algorithm (Haupt and Haupt, 2004). In our optimization we use a population size of 40–50, mutation rate of 0.2, selection rate of 0.5

and a maximum iteration of 50, which lead to stable convergence of the results. We ran up to 5 optimizations for each model set-up, each run taking approximately 20 h on a standard PC.

To prepare the data set for the model optimization we reduce the number of data points in the InSAR displacement maps from several million pixels to 6000 data points using a Quadtree subsampling approach (Jónsson et al., 2002). Quadtree subsampling is an irregular subsampling approach assigning higher point densities in areas of larger displacement gradients. In our subsampled data, the summit region of strong deformation is represented by a higher number of points than the far-field; and by weighting the points equally, we assign a more relevant role to the summit data during the optimization. This irregular subsampling is essential, since the deforming region only covers a fraction of the full dataset. It also allows us to limit the impact of far-field data, which are not relevant for our model, on the optimization results.

The topographic mesh consisted of 3250 TDs and was constructed based on the same DEM as used for the InSAR data processing (Persson and Strang, 2004). We used a mesh spanning a radial distance of 1 km to the summit crater, and reaching a resolution of 5 m in the center, corresponding to the summit of the volcano and region of highest displacements.

We chose a shear modulus of 1 GPa and a Poisson's Ratio of 0.25 for our model. The low shear modulus reflects the fragmented, uncompacted lava and ash matrix, which commonly composes the summit structure at dome-building volcanoes. Similar values have been constrained at Montserrat (Voight et al., 1999) and at Merapi Volcano (Beauducel et al., 2000).

5.3 Results

The pre-explosive ascending and descending interferograms (December 26th-January 6th) both reveal significant deformation that is focused around the upper edifice of Volcán de Colima (Fig. 5.2). Coherent interferometric phase is found at pixels almost throughout the volcano edifice, except for some parts of the dome summit and of the flank areas. Loss of coherence is possibly due to the high displacement gradients and partial snow cover near the summit, and vegetation on the lower flanks. The seismic station EZV4 lies outside the strongly deforming area.

The unwrapped interferograms covering the quiescent period (December 15th to December 26th) show that no major deformation took place during the 11 and 22 days prior to the January 6th explosion, which is in strong contrast with the pre-explosive interferograms described above (Fig. 5.3). This change in detectable surface displacements is confirmed in both ascending and descending tracks. The descending interferogram shows a butterfly pattern, with oppositely directed displacements approaching 6 cm in the satellites line of sight (LOS) on either flank of the volcano. The displacements in the ascending interferogram are, however, more asymmetric, with strong movements also approaching 6 cm in LOS on the western flank, yet little LOS displacements are observed on the eastern flank. In both datasets, the deformation is confined to the summit area. The displacement patterns on the ascending and descending interferograms are found to be consistent, suggesting a complex source of deformation likely to be related to the explosion that removed a part of the dome only few hours later.

The co-explosive interferograms (January 6th-January 17th) are strongly decorrelated in contrast to the pre-explosive interferograms due to the deposition of ash and other material. We can however still identify fringes locally in the summit area in both satellite look directions (Fig. 5.4). The spacing of the fringes in the co-explosive interferogram is found to be almost identical with that of the 'pre-explosive' fringes, but opposite in sign. Also, the asymmetry of the pre-explosive deformation is visible in the co-explosive interferograms: the descending interferogram exhibits two lobes of displacements with opposite signs, while only a single displacement lobe is visible in the ascending interferogram. The co-explosive displacements therefore appear to be the evidence for the reversing of the process producing the pre-explosive displacements. The

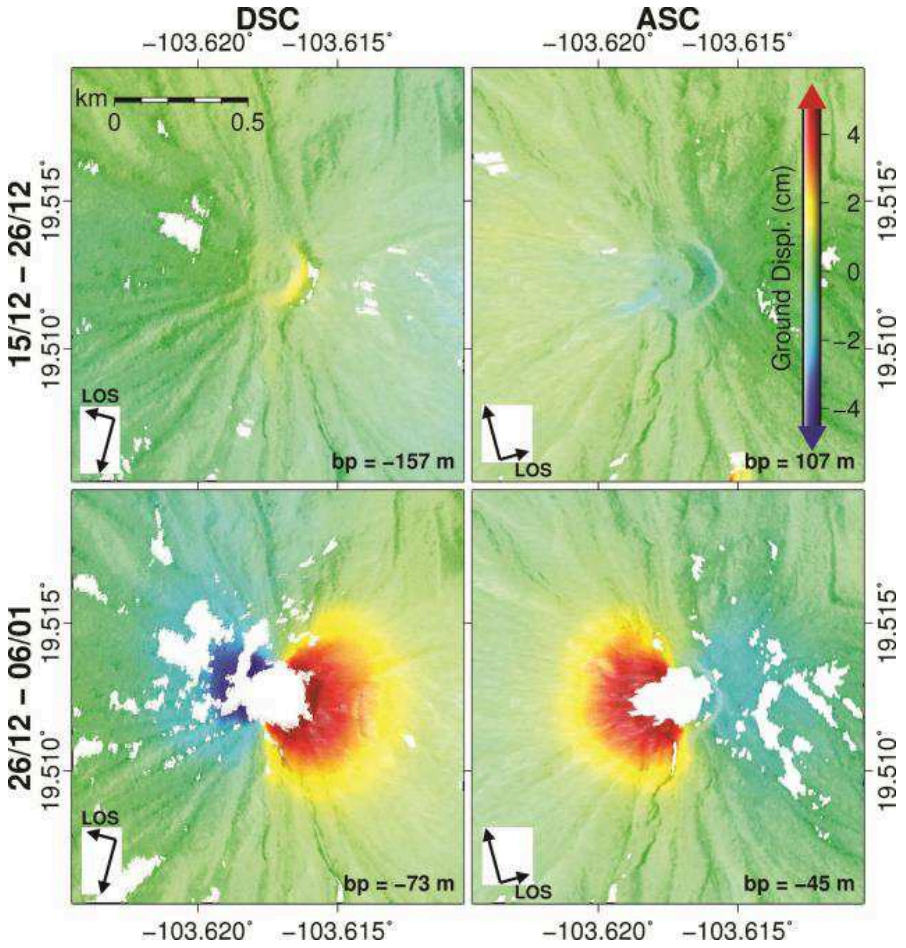

Figure 5.3: InSAR data shows deformation shortly prior to the January 2013 eruption. Top panels: no significant displacements are observed at the summit during the quiescent period (15th December-26th December). Bottom panels: pre-explosive deformation (26th December-6th January, 11–1 days prior to the explosion). The arrows indicate the satellite LOS and azimuth direction.

deformation is hence considered elastic, and no significant amount of magma has intruded and arrested within the volcano summit.

5.3.1 Source modelling

Our modelling efforts are focused on explaining the pre-explosive displacements. We first attempted to model these by using single pressurized sources of various shapes, that is, volumetric bodies and planar (sill- or dike-like) sources (Dzurisin, 2007). The better fit to the data was achieved using pressurized cylindrical and ellipsoidal sources, the inversion results of which are shown in Fig. 5.5. We assess the ability of the models to explain the observations by investigating the patterns of the simulated surface displacements, residuals as well as plots showing the data and modelled displacements along an E-W profile crossing the summit.

The overall results for a single ellipsoid or cylinder are quite similar in the modelled displacement range, patterns and fit to the data, however the source parameters are slightly different in terms of size and depth. The distribution of the residuals suggests that the cylindrical source provides a slightly better fit to the data; however, neither source can explain the characteristic asymmetric patterns observed in the displacements. The E-W profiles in particular reveal the inconsistent shapes of the two curves: while the observations show an exponential pattern on both the eastern and western segments of the descending data, the modelled displacement curves are bell-shaped and often divergent when approaching the summit (Fig. 5.5, profiles

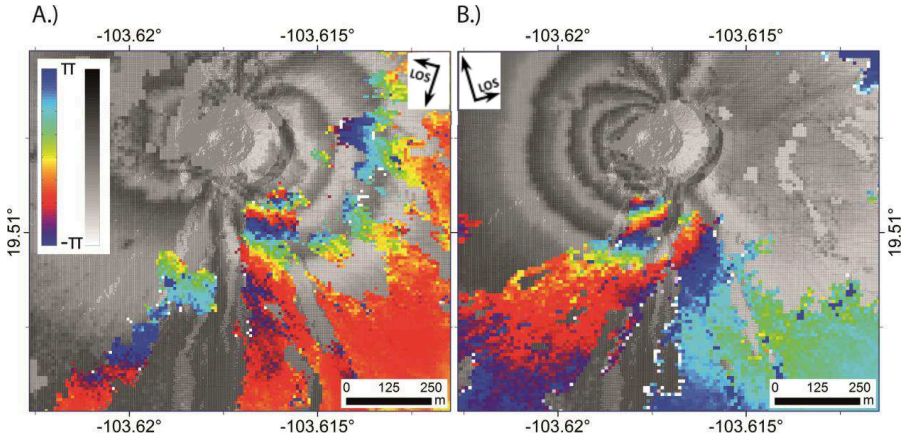

Figure 5.4: InSAR data prior to and covering the January explosion. The co-explosive deformation in LOS (in colour) is shown overlying the pre-explosive inflation fringes (greyscale) in the descending and ascending interferograms (A and B, respectively). The shaded relief of the summit dome can be seen in the center, not covered by data.

P-P', labels a-f). The lack of displacements in the ascending data up to the immediate summit proximity could not be reproduced by any of the single-source models (Fig. 5.5, profiles P-P', labels c, f), without significantly compromising the fit to the data elsewhere. The displacement pattern could therefore not universally be explained by any of the single sources investigated. We attributed this to the real source geometry being more complex in shape than our simple single-source models. Furthermore, the explosion left an almost circular shallow crater in the summit dome (see Fig. S16), which indicates pressurization at levels which are more shallow than those suggested by our single-source optimization results. Therefore, we approximate a more complex source geometry by using a combination of two sources.

In order to stabilize our results in the two-source model optimization, we narrow down the solution space by first modelling the data on the volcano flanks (excluding a radius of 350 m about the summit), using an ellipsoidal source, through an inversion (Fig. S15). The residuals for this source were in the mm-range everywhere outside the 350 m radius, however, as expected, very high within. We kept this source model and added a second, shallow triaxial ellipsoid to simulate the displacements within the near field of the summit. In the following optimization we constrain the search ranges for the deep source parameters based on the result of the previous inversion. The limits for the geometrical parameters for the shallow ellipsoid were given by the summit topography, which it may not intersect. We also found that the E-W profiles of the displacements are very sensitive to the position, E-W extension and pressurization of the shallow source; hence these parameters appear well constrained in our set-up. Including the data within the 350 m radius again, we initialize the inversion with two sources, the result of which is shown in Fig. 5.5C.

The best-fitting two-source model is made up by a deep, vertically elongated source located 150 m–300 m depth below the summit, and a shallow, horizontally elongated source, located just a few tens of meters below the summit and inside the dome. The deep source has a near circular horizontal aspect ratio, and is located within the volcanic cone at a centered position with respect to the main edifice. The distinct shallow source, on the other hand, is significantly offset to the West, extended in North-South direction and almost perfectly centered beneath the active dome. Although location and geometry of these two sources are distinct, a similar amount of pressurization (22 and 25 MPa for the shallow and deep sources, respectively) was estimated in our optimization. The similar degree of pressurization of the two sources suggests a physical connection between them.

The residual displacements are reduced overall in the two-source model, and distributed more equally over the ascending and descending datasets. However, from the root-mean-square error

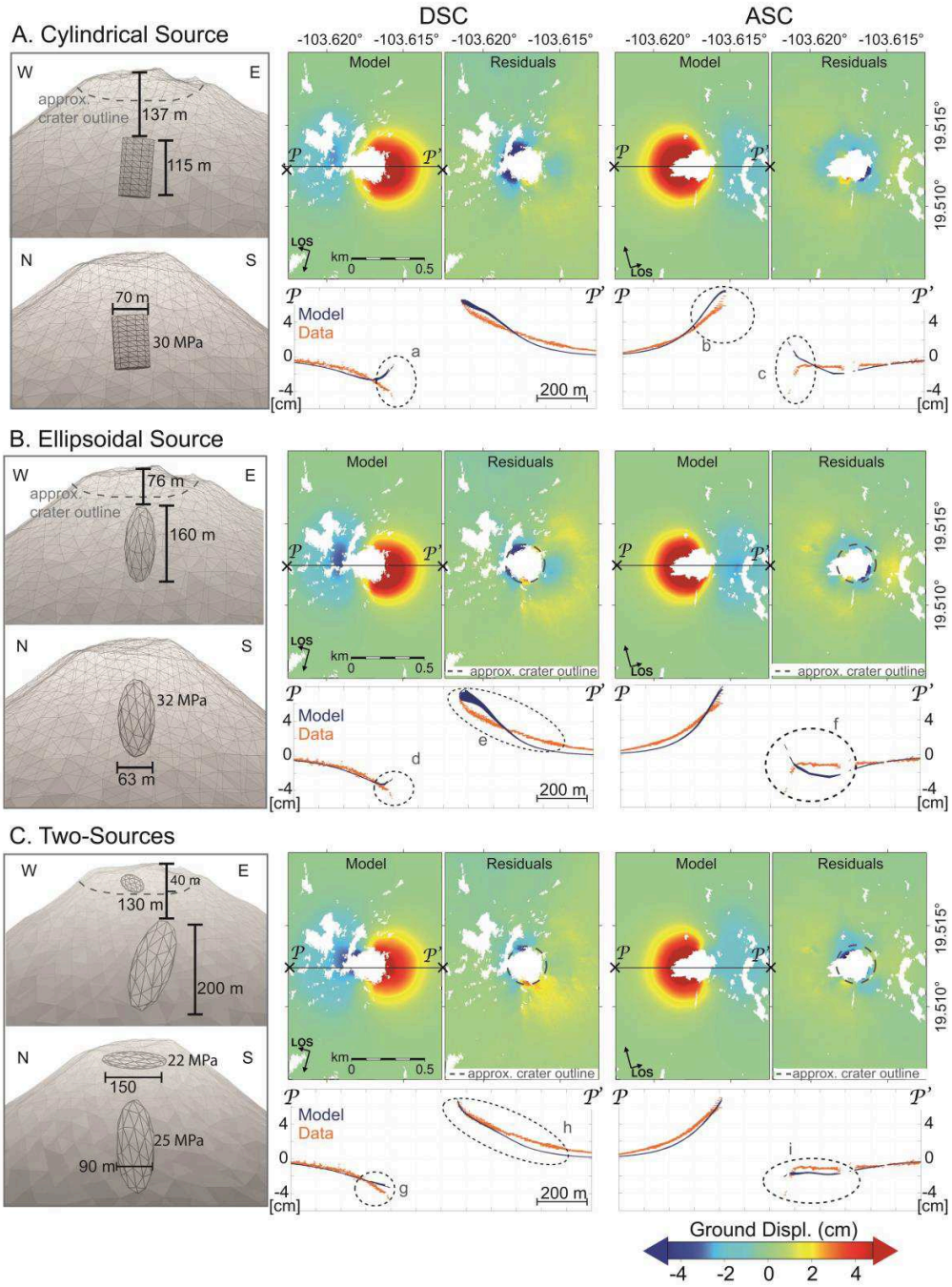

Figure 5.5: The modelling results. Three different model set-ups are shown: a cylindrical source (A), an ellipsoidal source (B) and a combination of two ellipsoids (C). For each, we present the best-fitting source geometry and its parameters. In addition, we provide maps showing the modelled displacements and residuals in both look directions for each set-up. Under each map are profiles (P-P') of the data (red) and the modelled displacements (blue). These profiles comprise a projection of all values within a 40 m-wide strip centered on the line of profile. The marked regions in the profiles (a-i) are referred to in the main text.

(RMSE) values alone, the improvement of the data fit is not significant enough to justify the two-source model over the single-source models. We still favour the two-source model since it can better reproduce the complexities in the observed displacement gradients, such as the increase toward the summit and the existence of both long and short-wavelength signals. The modelled displacement patterns of the two-source model follow the observations more closely, in particular the lack of displacements in the eastern ascending data (Fig. 5.5C-i), as well as the exponential trend in the other segments (Figs 5.5C-g and 5.5C-h). Also, short-wavelength changes in the observed displacements can now be reproduced (Fig. 5.5C-i).

5.4 Discussion

Our results indicate that the summit area of Volcán de Colima was first at rest, and then unexpectedly underwent strong deformation just during a few days prior to the January 6th explosion. This we attribute to shallow sources of pressurization located within the shallow volcanic conduit. Source complexities are found concerning the location and orientation of the two sources, determined from a lateral shift from the centralized deeper source to an off-centered shallow source, and from a change of a vertically extended radial symmetric geometry at depth to a horizontally extended, fracture-like geometry near the surface. The pre-explosive pressure increase lies in the order of 22 to 25 MPa, values that are realistic for plumbing systems of this setting (Voight et al., 2010; Lavallée et al., 2012). During the period covering the explosion, the summit area subsided again, and did so by an amount and in a spatial pattern similar to the pre-explosive inflation. Our study therefore shows, for the first time, on a very small spatial and temporal scale, the transient pre-explosive pressure increase in the uppermost conduit system of Volcán de Colima.

Observations of precursory deformation with InSAR are relatively rare at explosive volcanoes, which has been attributed to the characteristics of the magma reservoir (Chaussard and Amelung, 2012; Ebmeier et al., 2013), a lack of pressurization (Chaussard et al., 2013), the steep topography (Pinel et al., 2011) or temporal aliasing (Fournier et al., 2010). The short temporal baseline and high resolution of our satellite imagery, in combination with a high quality DEM, reduces errors typically associated when using standard resolution InSAR in this type of terrain (Pinel et al., 2011). In the case of Colima, the timing of the satellite acquisitions was critical for detecting the deformation.

Pre-explosive pressurization previously observed at the conduit of Montserrat (Voight et al., 2010) may resemble the situation observed at Volcán de Colima, as in both cases pressurization has occurred within the edifice, very close to the actual eruption center, but the case presented here stands out for two reasons: firstly, because of the short period during which the pressurization developed, and secondly, because the high spatial resolution of the displacement data in the summit area allowed resolving the summit deformation and modelling the underlying sources. The first point implies that the conduit system feeding dome explosions at Volcán de Colima was temporally plugged, leading to the January 2013 volcano explosion; the second point allows us to draw conclusions on the geometry of the conduit system and its effect on the generated displacements.

Before discussing the broader implications of these findings, we address the limitations of our study.

5.4.1 Limitations

5.4.1.1 Data limitations

The number of seismic events at Volcán de Colima began increasing exponentially 3 days prior to the eruption. Similarly, the rate of pre-eruptive deformation can increase toward the explosion (Sigmundsson et al., 2010), therefore, the 12 h time difference lying between the ascending and the descending slave images may have caused a certain amount of additional displacements in the descending interferogram. We cannot account for such a possible mismatch, as any model based solely on one data set would be poorly defined. However, due to the similar spatial extent and maximum amounts of displacements in both look directions we believe that the effect may be neglected in this study. Other instrumentation, such as GPS, tiltmeters or EDM, could have provided a higher time resolution and hence allowed the consideration of the 12-h gap between our TerraSAR-X datasets. However, given the complexity of the deformation and the positioning of other instrumentation at greater distance from the summit, any such point-wise

measurements would not have allowed constraining the two-source model as we have done here.

5.4.1.2 Model limitations

The main limitations of our modelling are the assumptions of elastic deformation and a homogeneous medium. Material heterogeneities, such vertical and lateral changes in the elastic parameters, are known to strongly affect the source evolution, that is, by arresting the ascent of magmatic material when it enters a stiffer medium (Maccaferri et al., 2011) but also the displacement pattern at the surface (Manconi et al., 2007). At Volcán de Colima, changes in the material properties may be found for instance at the contact between the dome and the pre-existing crater, but are also produced by the thermal, structural and compositional changes relating to the conduit and the volcanic cone itself. This may lead to distinct zones of pressurization, such as in the dome interior. Whether the models' complexity is an artefact of the homogeneous material assumption, or whether the distinct two zones of pressurization result from mechanical contrasts in the dome and edifice itself, cannot be assessed using the available surface deformation data alone, and necessitates additional information on the mechanical heterogeneities.

The near summit region may also experience non-elastic deformation. The very near field of the summit dome in particular (<50 m away from the dome) may have responded in a brittle fashion, which would explain the high displacement residuals in this region. However, brittle deformation did not have a strong influence on the pre-explosive displacements at Volcán de Colima. This is evidenced by, firstly, the continuity of the signal in the InSAR data suggesting no faulting near the surface. Secondly, the explosion itself reflects the failure of the dome material occurring after the observed deformation. Thirdly, the co-explosive interferograms (Fig. 5.4) show displacements in opposite sign and similar spatial wavelength to the pre-explosive deformation up to very close to the summit, the process leading to the displacements therefore needs to be reversible. We conclude that our elastic model assumption is well justified.

The pressure changes suggested by our models are on the order of 20 MPa, which might appear rather high if compared to the rock mass strength values of below 10 MPa as determined at similar settings (Sparks, 1997; Lavallée et al., 2012). However, the required pressurization in geodetic models is dependent on the values used to describe the material properties in the model, which, at Volcán de Colima, are difficult to constrain. Also, in this particular case, the presence of a solidified plug and a cooled dome may lead to strength values which are considerably larger than 20 MPa (Schultz, 1995). Additionally, shear along the conduit walls may also contribute to the deformation during dome-building eruptions (Beauducel et al., 2000; Green et al., 2006). Mechanical testing of the material properties is therefore a prerequisite to further improve models and understand the nature of precursory deformation.

Due to the long computation time, our optimization does not allow to constrain true confidence bounds of our model results based on multiple optimizations. However, we investigated the development of the individual model parameters during the inversion and analysed the range in which the parameters converge. While this does not provide model uncertainties, it allows estimating the stability of the model results and how well the parameters are constrained. We conclude that the main features of the source model on which we base our interpretations are robust.

5.4.2 Implications

In order to corroborate our modelling results and put them into relation with the volcano's activity, we analyse a set of photographs taken during an airplane overflight on January 10th, only 4 days after the explosion (Fig. 5.6). We geocoded the photograph showing the western

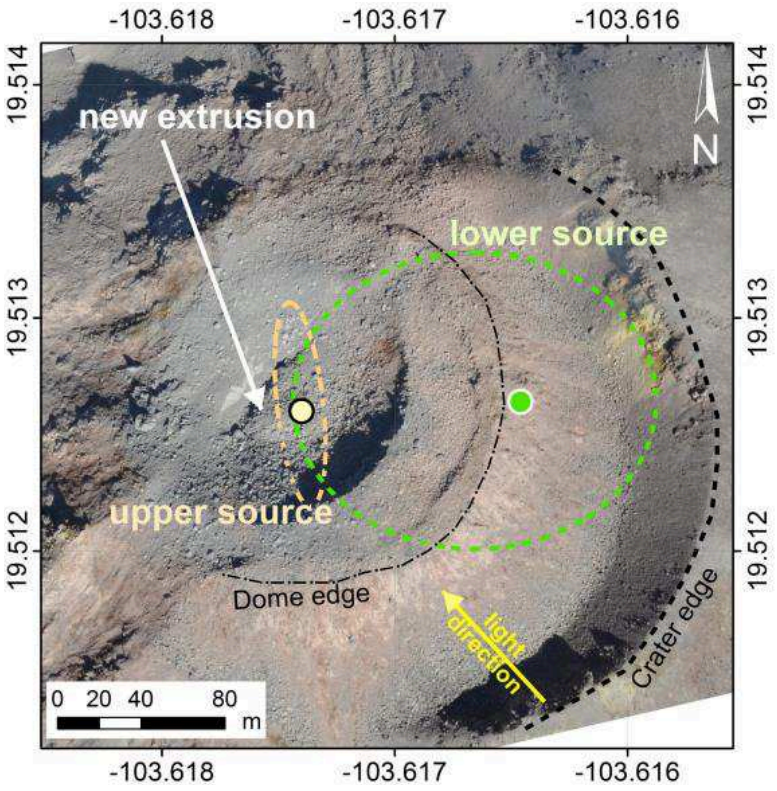

Figure 5.6: Geocoded photograph of the summit taken on January 10th during an airplane overflight. The circular markers show the approximate projected locations of the upper source (in orange) and the lower source (in green), as well as their approximate extents. The white arrow points to the location of the new extrusion, located at the center of the crater left by the January 6th explosion. This extrusion was removed by the following explosion on January 11th.

summit and the January 6th explosion crater using distinct features visible both in the photograph and in the high-resolution DEM of the volcano summit. The extrusion of the uppermost part of the conduit material can be identified within the explosion crater. This location almost perfectly agrees with the position of the shallow pressurization source, which lies just beneath the dome. The figure also provides the projected location and approximate extension of the deep spheroid, positioned central to the edifice and offset with respect to the dome, which has important implications for the plumbing system and magma pathway.

The good spatial agreement found between the locations of the shallow source and renewed dome extrusion as seen in aerial photographs suggests that the region was first blocked and pressurized, therefore detectable as a precursory signal by InSAR data, and began serving as a feeding system within less than 4 days following the explosion.

Pressurized regions along a volcanic conduit system may develop at geometric bends or changes in the conduit (Hautmann et al., 2009). It has been proposed that the upper conduit at Volcán de Colima may curve away from the center due to a strong plug of degassed material located beneath the summit crater (Lavallée et al., 2012). In this view, the feeder is centralized under the edifice, but bending westward toward the active dome close to the surface. Our InSAR data and model results agree with this conceptual model derived from independent data by Lavallée et al. (2012), and adds additional constraints on the localization of this postulated curvature. We postulate that our deeper source, centered at a depth of around 220 m below the summit, is the result of a geometrical change produced by the plug. The shallow source in turn reflects the transition into the summit dome.

Possibly, a larger scale structural trend may also play a role in defining the geometry of the sources. Volcán de Colima is located in an extensional regional stress field directed N-S, and in

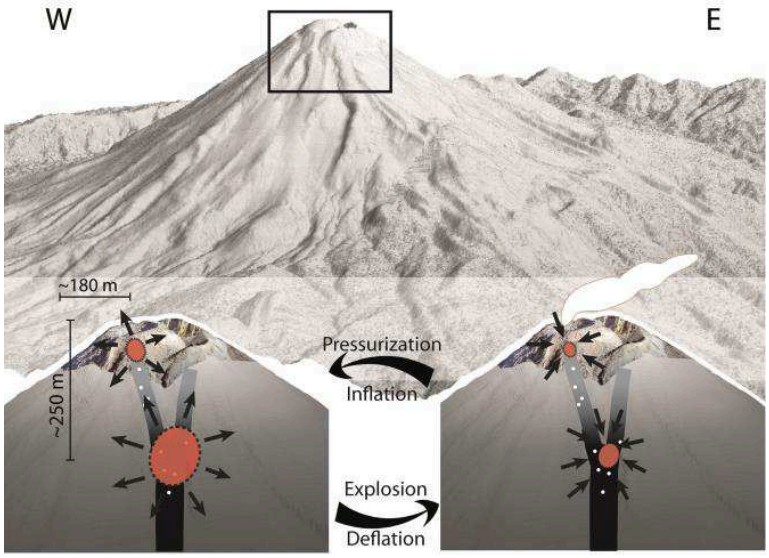

Figure 5.7: Conceptual model. Transient pressurization at distinct locations of the conduit at Volcán de Colima. The sources are located in the uppermost region of the edifice. The depth of the lower source reflects the bifurcation of the conduit and presence of a plug, the upper source is located at the transition between the crater floor and the volcanic dome.

an E-W trending volcanic graben, leading to gravitational spreading of the volcanic complex toward the south (Norini et al., 2010). It has been suggested that these trends may also be reflected in dome structures (James and Varley, 2012). However, the axial symmetry of the deeper source suggests that the shape of the edifice plays a stronger role than regional trends in controlling the geometry of the shallow conduit system at Volcán de Colima. The N-S extension of the shallow source is more likely to be controlled by the shape and local stress field of the dome, overflowing to the West (Walter et al., 2013), which in turn is a consequence of the off-centered position of the vent. The N-S structures visible in the 2007–2011 Colima dome are therefore likely to be dominantly controlled by the local rather than the regional stress field.

We therefore describe the current system feeding dome-building eruptions at Colima by a conduit-like source within the main edifice, overlain (with a lateral offset) by a horizontally extended source. Two shallow but distinguished zones of pressure buildup have also been localized at other volcanoes, one located within or just beneath a dome with a visco-elastic dome cap (Johnson et al., 2008), and one located few hundred meters below, within the edifice (Holland et al., 2011). Our results suggest that a combination of processes was taking place at Colima prior to the January 6th explosion. A physical connection, such as a fracture network, could have developed between the shallow and the deeper source, accompanied by pre-explosive seismicity, until the pressure overcame the strength of the dome cap. The explosions released the pressure built up in the conduit, leading to co-explosive summit subsidence (Fig. 5.7). The prolonged low rates of seismic events following the explosions suggest that the pressure release was not followed by immediate re-pressurization. Possibly, the increase in seismicity visible prior to the January 14 explosion suggests another pressurization cycle, smaller in magnitude, took place then. However, due to temporal aliasing, this deformation would not be visible in our interferograms.

Our study differs to other investigations of pre-eruptive inflation (Fournier et al., 2010; Lu et al., 2010; Chaussard and Amelung, 2012) in that there are no significant amounts of new deeply sourced material detected in our InSAR data, but the bulk of the deformation was caused at very shallow levels. We do not attribute the deformation to the inflation of a deep magma reservoir, but to transient pressurization of the dome feeding system, possibly only lasting a few days. The ultimate trigger for this pressurization however still remains unclear.

Camera observations show significant snowfall beginning around 4 days prior to the explosion, associated with increased fumarolic activity, suggesting that precipitation may have percolated into the edifice leading to a pore pressure buildup at depth.

The time span over which displacements were observed as well as the proximity of the deformation sources to the summit underline the need for a configuration of the monitoring instruments that allows the detection of such short term pre-explosive changes. The spatial pattern of the pre-explosive surface displacements at Volcán de Colima was mainly controlled by the internal structure of the summit, with the size and position of the conduit, the presence of a plug and the shape of the edifice all playing a role. Therefore, these factors may also affect the distribution of pre-explosive signals generated by conduit pressurization at other volcanoes, that is, the shallow pressurization of a geometrically simple conduit system may lead to signals smaller in magnitude and spatial amplitude, and hence even more difficult to detect. This type of precursors may be detected and early warning measures implemented only when monitoring systems operate at a sufficiently high spatial and temporal resolution.

5.5 Conclusions

The January 6th 2013 Colima explosion is a rare example where satellite radar interferometry allowed the quantification of activity changes only few hours prior to an explosive volcanic eruption. The geometry of the reactivated conduit and the location of renewed activity can be constrained using high-resolution InSAR data. Ground displacement on the volcano flanks are best explained by a cigar-shaped source centered within the main edifice and subject to pressurization. The displacements at the volcano summit, in turn, can only be explained by an additional source located inside the dome.

The two-source model is supported by independent observations, such as the characteristics and location of the explosion crater as evidenced by photographs of the summit. It is also in agreement with the conceptual model presented by Lavallée et al. (2012), based on geological data. Our results support the existence of a plug beneath the crater floor at Volcán de Colima, implying the presence of a curved ascent path leading to off-centered extrusion sites at the surface. We associate the lower source with the depth of the plug, which we now speculate to reach a depth of around 200 m–250 m. The geometry of the upper source appears to be controlled by the local stress field of the dome, while the geometry of the lower source may be an approximation of more complex flow patterns, or imposed by the presence of the plug. These conduit complexities are directly reflected in the distribution of the observed displacements, suggesting that the spatial dimension of pre-explosive signals at other volcanoes may also depend on the properties of the conduit system.

The spatiotemporal characteristics of the signals shown here suggest that the occurrence of explosive eruptions lacking deformation precursors may be due to the poor spatial and/or temporal resolution of geodetic monitoring data in the summit area. In our study, the timing of the satellite acquisitions was crucial for detecting the deformation. The transient nature of the process generating them suggests that temporal aliasing, rather than a lack of pressurization, limits our ability to detect pre-explosive deformation by InSAR.

We therefore believe future satellite missions with a high revisiting frequency, as well as the installation of near-summit monitoring stations, will reveal more details about the upper conduit system at other volcanoes. The combined analysis of short-term pre-explosive seismic and geodetic data of high resolution will improve our understanding of the generation of these signals their relevance for eruption forecasts.

Chapter 6

Insights into the 3-D architecture of an active caldera ring-fault at Tendürek volcano through modelling of geodetic data

Abstract

The three-dimensional assessment of ring-fault geometries and kinematics at active caldera volcanoes is typically limited by sparse field, geodetic or seismological data, or by only partial ring-fault rupture or slip. Here we use a novel combination of spatially dense InSAR time-series data, numerical models and sand-box experiments to determine the three-dimensional geometry and kinematics of a sub-surface ring-fault at Tendürek volcano in Turkey. The InSAR data reveal that the area within the ring-fault not only subsides, but also shows substantial westward-directed lateral movement. The models and experiments explain this as a consequence of a 'sliding-trapdoor' ring-fault architecture that is mostly composed of outward-inclined reverse segments, most markedly so on the volcano's western flanks but includes inward-inclined normal segments on its eastern flanks. Furthermore, the model ring-fault exhibits dextral and sinistral strike-slip components that are roughly bilaterally distributed onto its northern and southern segments, respectively. Our more complex numerical model describes the deformation at Tendürek better than an analytical solution for a single rectangular dislocation in a half-space. Comparison to ring-faults defined at Glen Coe, Fernandina and Bárðarbunga calderas suggests that 'sliding-trapdoor' ring-fault geometries may be common in nature and should therefore be considered in geological and geophysical interpretations of ring-faults at different scales worldwide.[1]

[1]Originally published as: Bathke, H., Nikkhoo, M., Holohan, E., Walter, T. R. (2015): Insights into the 3D architecture of an active caldera ring-fault at Tendürek volcano through modeling of geodetic data. - Earth and Planetary Science Letters, 422, p. 157-168; doi:10.1016/j.epsl.2015.03.041

6.1 Introduction

Sources of deformation at active volcanoes may comprise magma bodies (e.g., chambers, sills, dikes or conduits) (Dzurisin, 2007) or hydrothermal systems undergoing growth or pressure changes (Fournier, 1999), or may also include fracture systems undergoing opening-mode or shear displacement, that is, fissures or faults (Peltier et al., 2009). Arcuate or ring-shaped fracture systems are commonly inferred or observed at modern and ancient volcanoes, and are generally related to local stress fields resulting from inflation or deflation of underlying magma bodies (Anderson, 1936). Ascertaining the 3-D geometry and kinematics of ring-faults is notoriously difficult, however, especially at active volcanic systems where they are ill-exposed or rapidly obscured (Geshi et al., 2002; Howard, 2010). Past approaches to this problem have relied on (1) rare and fragmentary field exposures, e.g. Glen Coe (Clough et al., 1909), (2) earthquake hypocenter distributions, e.g. Rabaul (Jones and Stewart, 1997), (3) seismic source inversions, e.g. Bárðarbunga (Fichtner and Tkalčić, 2010) or (4) inversion of gravimetric and sparse levelling data, e.g. Campi Flegrei (Beauducel et al., 2004). In addition, dense geodetic observations are made worldwide now by modern satellite radar techniques (Ebmeier et al., 2013) and provide an alternative way to determine the 3-D complexity of sub-surface deformation sources at volcanoes (e.g., Bathke et al., 2011; Bagnardi and Amelung, 2012; Jónsson, 2009; Shirzaei et al., 2013).

In this paper, we aim to infer the 3-D geometry and kinematics of an active ring-fault. We do this by modelling spatially dense geodetic data with a combined numerical and analogue approach. Analysis of recently detected deformation at Tendürek volcano during 2003–2010 has shown that, after removing the contribution of a contracting sill-like source, the residual deformation contains strong evidence for an active sub-surface ring-fault (Bathke et al., 2013). Although the sill-like source could account for most of the deformation signal, effects of the suspected ring-fault on the signal were not directly modelled. To do this, we use the boundary element method (BEM) to construct an improved model that accounts for the effect of topography and the interaction of ring-fault and sill-like sources. Such a model better explains the geodetic data. Upon inverting for the unknown parameters of the sources, we resolved a 'sliding-trapdoor' architecture (Holohan et al., 2013) to the ring-fault in three dimensions. This means that area within the ring-fault is not just subsiding, but is also subject to considerable lateral motion. The plausibility of the inferred ring-fault architecture is supported by our analogue subsidence models, which additionally reveal that such a geometry may be favoured by off-centered depletion of a magma-reservoir. Comparing the geodetically-determined ring-fault geometry at Tendürek volcano to those inferred via other approaches at other volcanoes, we hypothesize that an asymmetric 'sliding-trapdoor' geometry to ring-faults at active volcanoes might be the rule rather than the exception.

6.2 Tendürek volcano

Tendürek is a shield-volcano of mainly basaltic-trachytic magma composition in Eastern Anatolia (Fig. 6.1). Volcanism in Eastern Anatolia is related to the N-S directed collision of the Arabian and Eurasian tectonic plates (Pearce et al., 1990), whereby westward movement of the laterally-escaping Anatolian plate (Fig. 6.1) results in partial melting of the lower lithosphere (Pearce et al., 1990; Reilinger et al., 2006). Tendürek volcano sits in a basin between two active, dextral, north-west or west-north-west oriented, strike-slip faults (the Balık Gölü and Çaldıran Faults) that partially accommodate the continental collision.

The volcano has an elongated edifice with gentle slopes (average $\sim 7°$) and two main summit craters aligned east-west. The earliest dated eruptive products at Tendürek are basaltic rocks with an age of 700 kyr. While the youngest erupted products are dated to 2500 yr ago, still

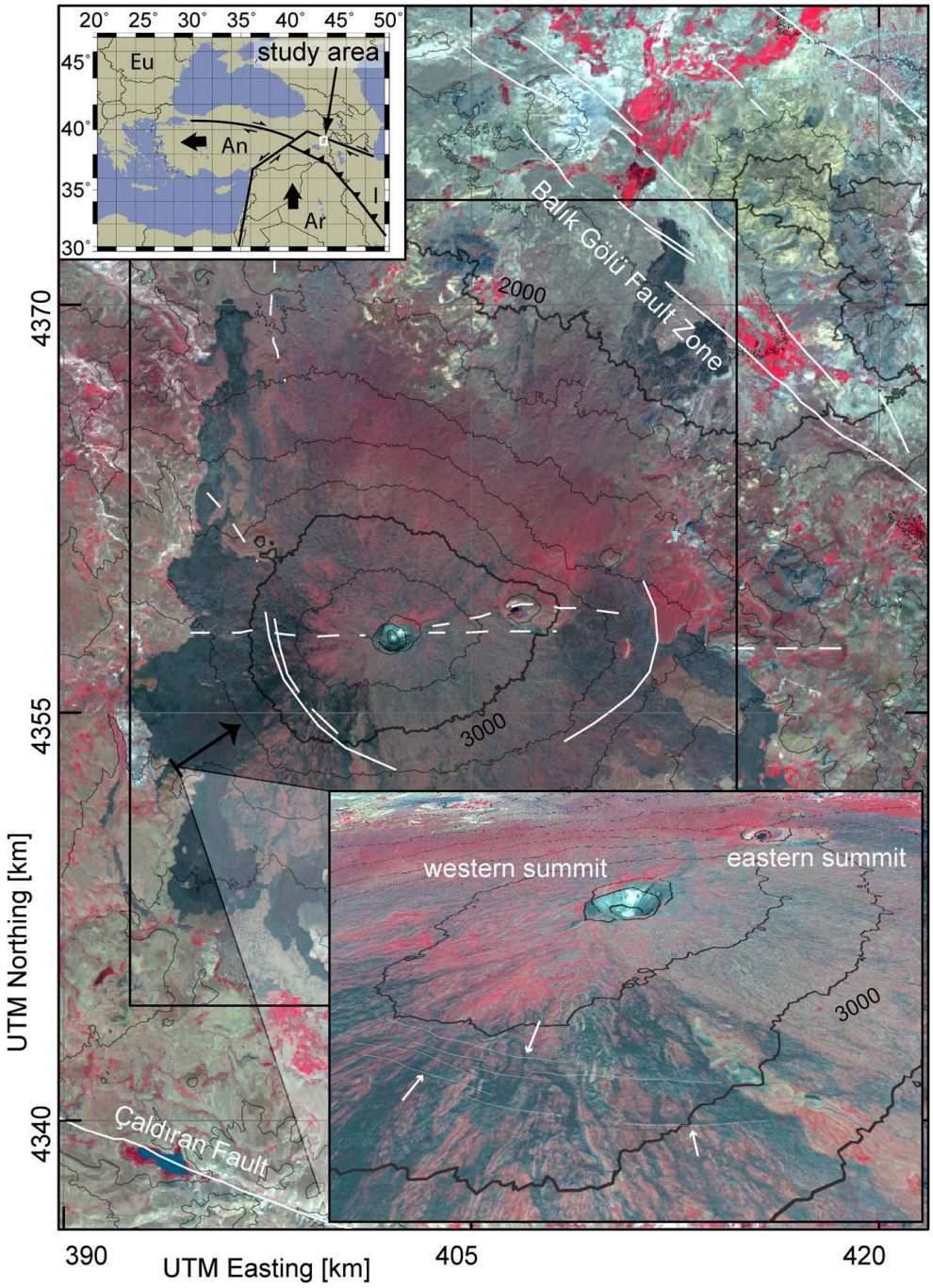

Figure 6.1: Study area, Tendürek volcano: Rapideye image from 30th August 2011 in false color (red, green, blue channels are bands 5, 3 and 2, respectively) of Tendürek volcano, modified after Bathke et al. (2013). White dashed and continuous lines mark faults inferred or observed by Yılmaz et al. (1998). The black box marks the extent of the Envisat data that has been used in the modelling (Bathke et al., 2013). The inset map shows the major plate movement directions, modified after Reilinger et al. (2006). The study area (UTM zone S38) is marked with the white rectangle. The inset figure in the bottom right corner is a 3-D perspective view of the western volcano flank (elevation contour lines in 200 m increments). Shown are the two summit craters of Tendürek and the arcuate fractures on the western flank system (white arrows).

more recent activity is suspected (Yılmaz et al., 1998). On the volcano's western flanks, there is an arcuate fracture system that has been interpreted as the surface expression of a ring-fault that might have been created during a historic collapse event (Yılmaz et al., 1998) (inset Fig. 6.1). On the eastern flanks, blockage of old lava flows (>13 000 yr) by fractures of this system gives a minimum age for it (Bathke et al., 2013). More detailed overviews of the geology and regional setting of the volcano are given by Yılmaz et al. (1998) and Bathke et al. (2013).

6.3 Methods

6.3.1 InSAR data and time series analysis

Here we provide a short summary of the InSAR data processing, since this is described in detail in our previous article on Tendürek volcano (Bathke et al., 2013). We generated two time series of the surface displacement fields at Tendürek volcano, from Envisat data of the ascending (19 images, I2 track 500) and descending (22 images, I2 track 135) satellite tracks, by using the small baseline subset module of the StaMPS software (Hooper et al., 2012). Time series methods increase the signal-to-noise ratio of the data by reducing for example the atmospheric phase components and, therefore, increase the ability to detect very subtle deformation signals. The data span the periods 2004–2009 and 2003–2010, and they comprise 47 and 52 interferograms from the ascending and descending tracks, respectively. We used a 90 m resolution SRTM digital elevation model to reduce the phase component caused by topography (Farr et al., 2007).

6.3.2 Boundary element method (BEM) modelling

Surface displacements can be used to investigate the underlying sub-surface processes through modelling. To do so, some assumptions about the properties of the sub-surface medium and the source(s) of deformation have to be made. Due to the lack of further information, we assume the sub-surface medium to be homogeneous, isotropic and linearly-elastic with Young's modulus of 33 GPa and Poisson's ratio of 0.25 (Cayol and Cornet, 1998b; Segall, 2010).

The boundary element method (BEM) is a numerical approach to solve linear partial differential equations, such as those in the theory of linear elasticity. An advantage of the BEM is that only the boundaries of the different sources in the problem need to be discretized (Scavia, 1991). This reduces the amount of necessary computations significantly. Boundaries of sources that may have complex or irregular geometries, such as faults or magma bodies, can be represented by meshes of triangular dislocations (TDs). Here we use the new artefact-free formulation of a TD by Nikkhoo and Walter (2015). By introducing appropriate (traction) boundary conditions for each dislocation, we solve for the slip components of all of the TDs simultaneously. This way, the interaction of the TDs, which compose the sources and the topography, is taken into account (Salzer et al., 2014). We then calculate the stress and the displacement field for the whole model.

On the basis of previous results (Bathke et al., 2013), we chose a model set-up consisting of two sources: a contracting sill and a ring-fault. The sill is represented as an ellipse composed of 24 TDs and the ring-fault is simulated as a truncated cone or a cylinder composed of 224 TDs. We also accounted for the effect of topography in the model, by simulating the Earth's surface as a traction-free crack (Cayol and Cornet, 1997, 1998b). To mimic the real surface topography at Tendürek, we constructed a mesh of 3881 TDs from the SRTM digital elevation model (Farr et al., 2007).

We defined the model ring-fault by starting with two ellipses, one above the other. These ellipses represent the upper and lower edges (that is tip lines) of the ring-fault. The surface of the ring-fault was then linearly interpolated between these two ellipses. Therefore, the geometry of the ring-fault surface only depends on the parameters of the two ellipses, variation of which allows for variable dip-angles around the fault's circumference. To determine the general source geometry of the sill and the ring-fault, we used a uniform traction constraint as the boundary condition in the dip direction of the ring-fault and in the direction normal to the sill (Fig. 6.2a).

By systematically changing the parameters of the simulated sill and the ring-fault, we solved for the optimum model parameters that best explain the mean surface displacement velocities observed in radar line-of-sight (LOS) from the ascending and descending tracks. However, due to the geophysical ambiguity of the problem, there might be various combinations of model

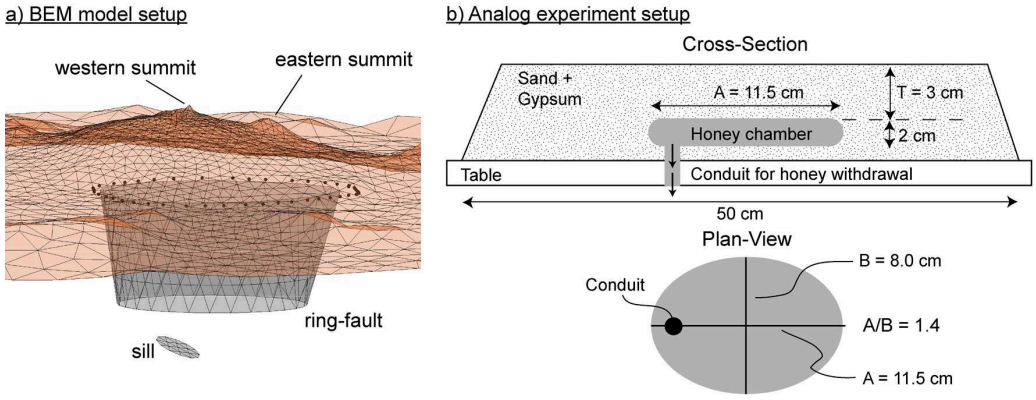

Figure 6.2: Model and experiment set-ups: (a) Boundary element method (BEM) model set-up in perspective view, showing the meshes of the topography (transparent), the ring-fault and the sill-like source. Black dots mark the surface trace of the 'ring-like residual' (see main text for details). (b) Set-up of the analogue subsidence experiment in cross-section and plan-view. Note the off-centered point of depletion (conduit) of the elliptical honey reservoir.

parameters that similarly well explain the data. Consequently, it is important to repeat the search for the model parameters numerous times to estimate a volume, rather than a single point, of the potential solution space. To address this optimization problem, we used the genetic algorithm (Holland, 1975) with the following parameters: 40 starting models (chromosomes), 50 iterations, a selection value of 0.5 and a mutation rate (Haupt and Haupt, 2004) of 0.22. This algorithm approaches the optimum solution by selecting the models that best explain the observed signal. Consecutive combination and random changes (mutation) of these models' parameters then create a new set (generation) of models that are evaluated again. This process is iterated until the model parameters converge to a narrow range of values. We undertook twenty repetitions of the search for the optimum model set-up, which in total consists of eighteen parameters (Table 6.1). We estimated model uncertainties of the final source geometries by calculating an envelope that is defined by the meshes of optimum sill and ring-fault models within the 95 per cent confidence bounds of all twenty optimizations.

Table 6.1: Source parameters of the optimum sill and ring-fault combination with respect to an XYZ coordinate system, where positive $X-$, $Y-$ and $Z-$axes point to the east, north and up, respectively. The origin of the XYZ coordinate system is located at the mean sea level and has a latitude and longitude of 39°21′16″ and 43°51′59″, respectively. The ω_X, ω_Y and ω_Z are the angles of rotation about the X, Y and Z axes, respectively. The a and b represent the elliptic semi-axes of the sill (a_{sill} and b_{sill}) and upper (a_{upper} and b_{upper}) and lower (a_{lower} and b_{loewr}) rims of the ring-fault, respectively. Before applying the rotations, a_{sill} and b_{sill} align with the X and Y, respectively. In each case, X_0, Y_0 and Z_0 are the coordinates of the ellipse center. The scale factors applied to the a_{upper} and b_{upper} and their 95 per cent confidence bounds are 0.8 $(0.70, 1.00)$ and 0.96 $(0.86, 1.03)$, respectively.

Sill parameters	Optimal solutions	95 per cent confidence bounds	Ring-fault parameters	Optimal solutions	95 per cent confidence bounds
a_{sill} (km)	1.36	$(0.80, 1.4)$	a_{upper} (km)	7.0	–
b_{sill} (km)	0.9	$(0.87, 1.4)$	b_{upper} (km)	4.9	–
X_0 (km)	0.35	$(0.0, 0.76)$	Z_{upper} (km)	1.75	$(1.5, 1.9)$
Y_0 (km)	0.27	$(-0.5, 1.1)$	X_{lower} (km)	0.45	$(-0.39, 1.57)$
Z_0 (km)	-2.5	$(-2.2, -3.3)$	Y_{lower} (km)	-0.45	$(-1.81, -0.1)$
ω_X (°)	18	$(-15, 25)$	Z_{lower} (km)	0.25	$(-0.1, 0.9)$
ω_Y (°)	2	$(-3, 22)$	a_{lower} (km)	5.9	$(5.1, 7.0)$
ω_Z (°)	97	$(97, 333)$	b_{lower} (km)	5.1	$(4.2, 5.3)$
Traction (MPa)	-10.1	$(-12.3, -8.3)$	Traction (MPa)	-0.09	$(-0.05, -0.18)$

6.3.3 Analogue experiments

Analogue experiments of caldera subsidence are here used in complementary fashion to test the plausibility of the ring-fault architecture that is resolved by the BEM model and to gain insights into the fault's development. In particular, quantification of surface displacements and structural kinematics during an experiment enables a detailed comparison to similar observations in the BEM model and in nature (Holohan et al., 2013; Le Corvec et al., 2014).

The analogue experiment set-up consisted of a sand/gypsum pack that lay on top of a table and enclosed a sill-like honey reservoir (Fig. 6.2b). The reservoir could be drained via a honey conduit (diameter 0.8 cm) by unplugging a pipe passing through the bottom of the table. Although this set-up is typical of many previous works (Roche et al., 2000; Holohan et al., 2008, 2013), we here include an off-centered conduit – a factor not previously tested in the literature. As discussed later, an off-centered conduit or depletion source may be a contributory factor to the pattern of ring-faulting at Tendürek, although not an essential one.

In total we ran twelve experiments. These have been scaled geometrically such that 1 cm in the experiment was approximately 1 km in nature (see Holohan et al., 2008, for details). The 2 cm thick, elliptical reservoir lay at a depth of 3 cm with major axis of $A = 11.5$ cm and minor axis of $B = 8$ cm. The reservoir depth to diameter ratio in the experiment hence varied circumferentially between $T/A = 0.26$ and $T/B = 0.38$. The geometry of the reservoir and its depth at Tendürek before formation of the ring-fault are unknown. Therefore, we assume firstly that the magma body lateral dimensions are 14×10 km ($A/B = 1.4$), which is similar to the area encompassed by the arcuate fracture system and which is approximated by an experimental $A/B = 1.4$. We assume secondly that this body was emplaced in the brittle upper crust at a depth between 2 and 15 km (Watts and Burov, 2003), from which one arrives at a possible reservoir depth to diameter range of 0.14–2.0. Our experiments are thus limited to considering the lower (that is, shallower) end of this range.

Horizontal displacements of the sand/gypsum surface could be quantified by means of digital image correlation of plan view images taken every 60 s with an overhead camera (see Holohan et al., 2013, for details). Gradients in these horizontal surface displacements were used to calculate rotation ($E_{rot} = \frac{\partial v}{\partial x} - \frac{\partial u}{\partial y}$) and dilatation ($E_{dil} = -\frac{\partial u}{\partial x} - \frac{\partial v}{\partial y}$). Therefore, rotational components along fault-scarps can be interpreted as indicating sinistral (anti-clockwise) or dextral (clockwise) strike-slip. Dilatation, that is contraction or expansion, along fault scarps can be interpreted as indicating reverse or normal slip. To validate such interpretations of surface observations, and to resolve the 3-D geometry of the related structures, the sand/gypsum packs were soaked with water and orthogonal cross-sections were cut through them.

6.4 Results

6.4.1 InSAR displacements and analytical models

In order to describe the data modelled, and to later highlight the improvements made in using more complex BEM models and analogue experiments to explain these data, we first provide a summary of the main results of our previous article on Tendürek volcano (Bathke et al., 2013).

For both satellite tracks, we calculated the best-fit linear component (least squares) of the displacement rate at Tendürek volcano from the SBAS time-series analysis (Figs 6.3a and 6.3b). The displacement rate shows an elliptical pattern that covers the volcano edifice and reaches a maximum of ~11 mm/yr in radar line-of-sight (LOS) at the volcano summit. After decomposing the LOS displacement rates into vertical and E-W horizontal components (Figs 6.3c and 6.3d), it becomes evident that the displacement velocities are composed of a vertical subsidence with a maximum rate of ~10 mm/yr and a strong, westward-directed horizontal

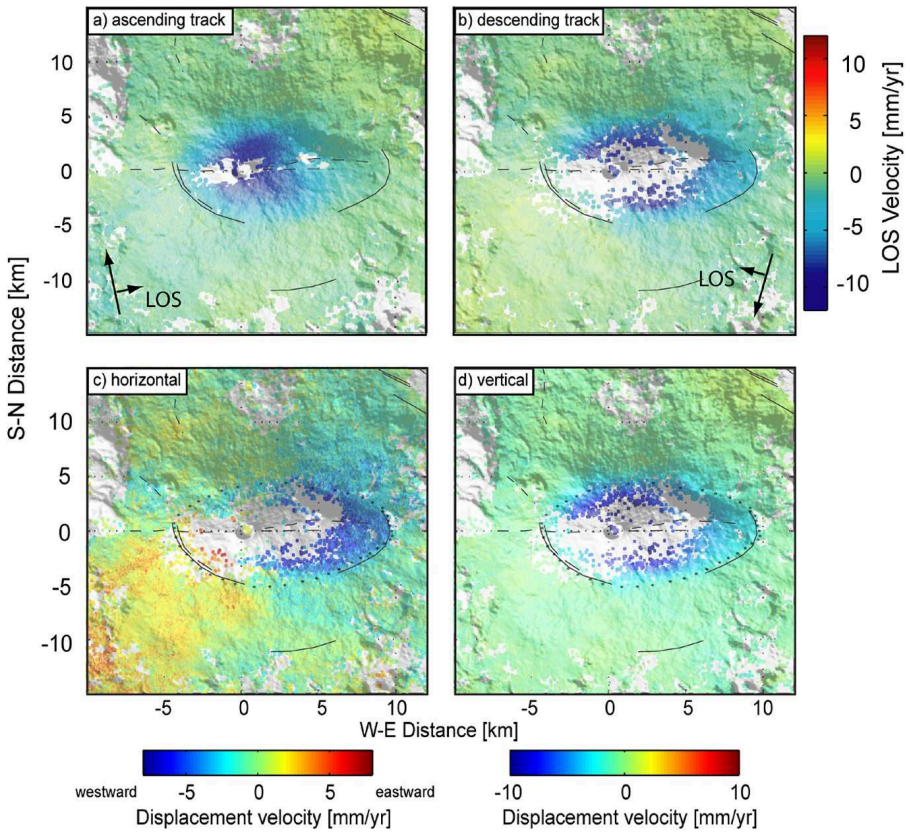

Figure 6.3: InSAR data: Surface displacement velocity data in satellite line-of-sight from SBAS time-series analysis of Envisat data (Bathke et al., 2013). The data span the time periods 2004–2009 and 2003–2010 for the ascending (a) and descending (b) tracks, respectively. (c) Horizontal and (d) vertical surface displacement velocities at Tendürek volcano between 2003 and 2010 from Envisat SAR data. Light grey dots mark the gradient in residual displacement (ring-like residual) of the past sill-only model and are coincident with the volcano's arcuate fracture system. Thin black lines mark inferred or observed faults from Fig. 6.1.

motion with a maximum of ∼7 mm/yr.

Previous analytical source modelling (Bathke et al., 2013) that involved a single rectangular dislocation source showed that an optimum sub-horizontal sill-like source would be located beneath the western crater at 0.8 to 3.0 km below sea level (or 4.3–6.5 km below the summit), with a spatial extent of 6 × 7 km and an annual contraction of ∼1–3 cm normal to the rectangular dislocation (see Fig. S17). Comparing this optimum model's surface displacements (see Fig. S17b) to the observed surface displacements, we get the residual surface displacements, that is those that cannot be explained by the sill-like source. The Root Mean Squared Error (RMSE) of this optimum model is 0.62 (see Figs S18a, S17c). The residuals contain a ring-like zone of high gradients in displacement that closely follow the arcuate fracture system observed at surface (Fig. 6.1 Bathke et al., 2013). We call this feature the 'ring-like residual' in the following sections.

6.4.2 Boundary element method: sill and ring-fault model

6.4.2.1 Model geometry

For computational convenience, we constrained the upper ellipse of the model ring-fault to have the same shape as the 'ring-like residual' described above, that is, the possible surface expression of the Tendürek ring-fault (see black dots in Fig. 6.3). In addition, we fixed the center of the upper ellipse, but allowed its outline to scale in $x-$ and $y-$directions. The vertical position of the upper ellipse could not lie above 2.4 km above mean sea level, while that of the

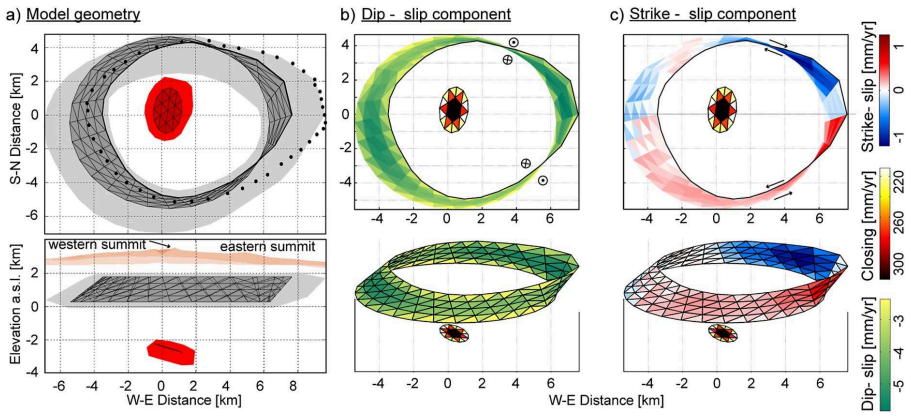

Figure 6.4: BEM modelling results: (a) Plan view: The dark grey mesh and the dark red mesh show the geometry of the ring-fault and the sill-like source that best explain the observed displacement velocity. The thick black lines mark the upper edge of the ring-fault. The light grey and red polygons show the range of alternative and similarly-well fitting mesh geometries. Bottom: Perspective view, colour coding same as plan view, but also with the topography of Tendürek volcano in orange. (b) Dip- and (c) strike-slip components (dextral-blue, sinistral-red) of the displacement rate along the triangular dislocations (TDs) of the optimum ring-fault model. Also shown is the closing rate along the TDs of the sill.

lower ellipse could not lie below 3 km below mean sea level. This is because intersection of the ring-fault with the free surface or the sill would have been numerically unstable. All other aspects of the ring-fault were free to vary. For the sill, the only constraint was that the dip should not exceed 25° (that is it should be near-horizontal).

The optimum combined ring-fault (dark grey) and sill (dark red) solution with the above-mentioned constraints is shown in Fig. 6.4a, below the topographic mesh of the volcano edifice (orange). The light grey and red volumes show the locations and orientations of alternative ring-fault and sill geometries, respectively, that similarly well explain the observed data (that is with similarly satisfactory misfit values; see the confidence bounds of model parameters in Table 6.1).

A consistent feature of all optimizations is that the ring-fault is outward-inclined below the western flank of the volcano and is inward-inclined on the opposite side, below the eastern flank of the volcano (Fig. 6.4a). Below the southern and northern flanks the ring-fault is consistently outward-inclined. The absolute dip values on different sides of the ring-fault are not well constrained. In the East and in the West, they vary between ∼25° and 65° (see Table S2). In the North and South, the dip values range from ∼30° to 80°, and are, in general, steeper than those in the West and East.

The upper and lower edges of the optimum ring-fault are located at 1.75 and 0.25 km above mean sea level, respectively. The uniform shear-traction of −91 kPa of the optimum ring-fault in the model, results in a maximum slip rate of 5 mm/yr in the dip-direction (Fig. 6.4b). The optimum elliptic sill in the model possesses major and minor axes of 2.72 and 1.8 km, respectively, and a dip-angle of 18° towards the east. It is located at a depth of 2.5 km below mean sea level or, equivalently, ∼5.9 km beneath the western summit crater of the volcano. The uniform normal traction of −10.1 MPa of the optimum sill results in a maximum closing rate of ∼30 cm/yr (Fig. 6.4b, Table 6.1). In terms of the geodetic moments calculated through modelling, we estimate a relative contribution of 22 per cent for the ring-fault and 78 per cent for the sill-like source. The geodetic moments of the sill and the ring-fault in all twenty models are shown in Fig. S18b. From these, it is clear that the contribution of the ring-fault to the total moment can vary between 14 per cent and 35 per cent. However, the relative contribution of the ring-fault to the surface displacement is likely to be underestimated by the geodetic moment as the ring-fault is shallower than the sill.

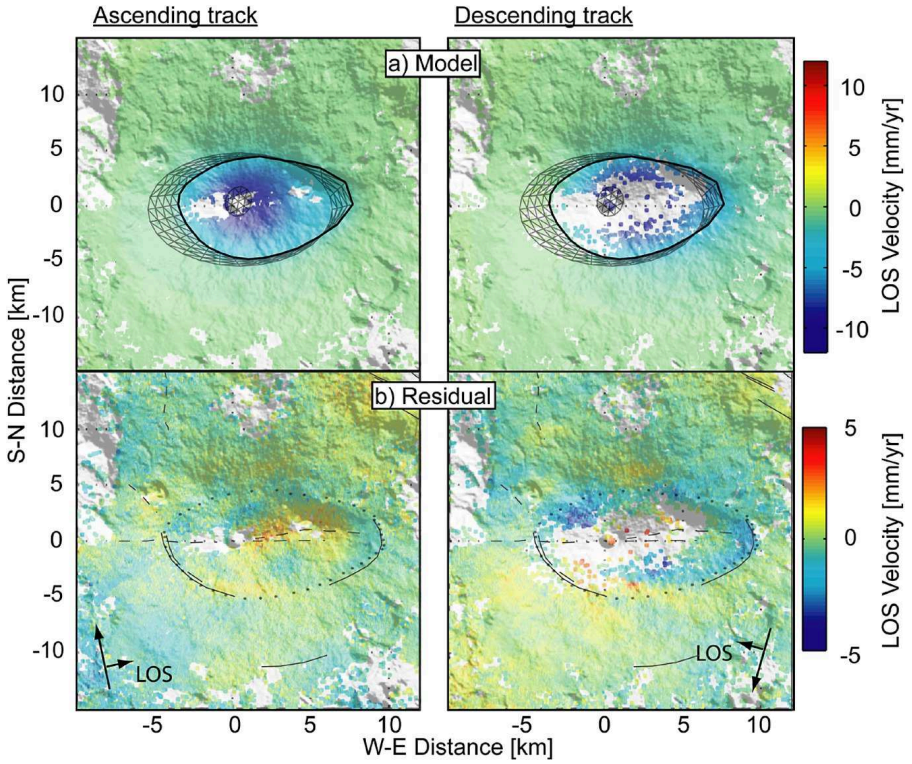

Figure 6.5: BEM model synthetic displacements: (a) Synthetic surface displacement in radar line-of-sight from our optimum deformation source model, which is composed of a sill-like source and a ring-fault. The optimum sill and ring-fault are superimposed in light grey, where the thick black line marks the upper edge of the ring-fault. (b) Bottom panels: Residual displacements between observation (Figs 6.3a and 6.3b) and BEM model (RMSE of 0.57). Light grey dots mark the gradient in residual (ring-like residual) that is observed when using a sill-only model and that coincides locally with an arcuate fracture system on the volcano. Thin black lines mark inferred or observed faults from Fig. 6.1.

6.4.2.2 Distribution of slip on the model ring-fault

The slip rates in the dip-direction and strike-direction of the TDs that comprise the optimum model ring-fault are shown in Figs 6.4b and 6.4c. The dip-slip component is largest, at about 5 mm/yr, in the eastern and the western sectors of the ring-fault. Slip sense is reverse on the outward-inclined western segments, and is normal on the inward inclined eastern segments. For the strike-slip component, there are two regimes of slip-sense: sinistral slip along the southern half of the ring-fault and dextral slip along the northern half.

6.4.2.3 Model surface displacements

The synthetic displacements of the optimum sill and ring-fault in the model fit the elliptic shape of the observed displacement velocities very well (RMSE of 0.57 mm/yr; see Figs 6.5 and S18a). A spatially correlated ring-like feature remains in the residuals, just inside the trace of the arcuate fracture system, but its values, which are within ±3 mm for the ascending track and within ±5 mm for the descending track (Fig. 6.3c), are close to the noise level of the data (Bathke et al., 2013). In close agreement with observations from InSAR (Fig. 6.3c) the synthetic surface displacements from our optimum ring-fault and sill in the BEM model (see black vectors in Fig. 6.6a) show that there is systematic westward horizontal movement towards the summit of the volcano.

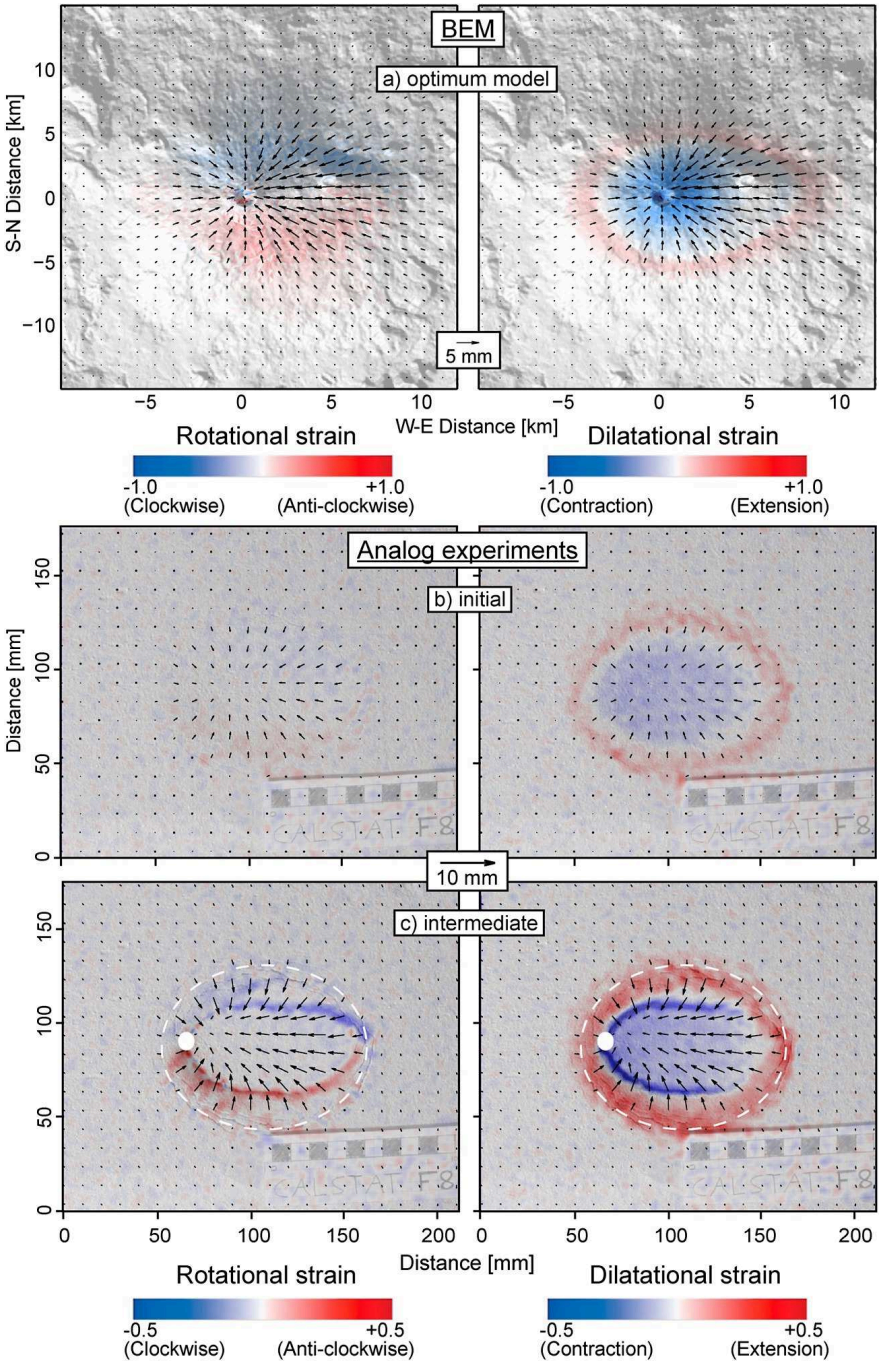

Figure 6.6: Cumulative strain components: Cumulative rotational (left) and dilatational (right) horizontal strain components on the surfaces of the BEM and analogue experiments: (a) the optimum BEM model (normalized to the maximum), (b) the analogue experiment at an early stage and (c) at an intermediate stage. Maximum subsidence in (b) and (c) is ∼2 mm and 8 mm, respectively. The white dashed line shows the outline of the underlying honey reservoir. The white circle indicates the approximate position of the off-centered conduit at depth. The black arrows show the vectors of the horizontal surface displacements.

6.4.2.4 Tests for alternative sources

Using the BEM, we tested if other source set-ups could also satisfactorily explain the observed displacement signal. Firstly, we tested for a sill-like source only, under the consideration of realistic topography. However, throughout various results the ring-like residual is noticeably larger (RMSE of 0.68; Figs S18a and S19) when compared to the models that include the ring-fault. Secondly, we tested an extended ellipsoidal source of deformation. In this case, large residual displacements appear on the volcano flanks. These are mostly caused by overestimated

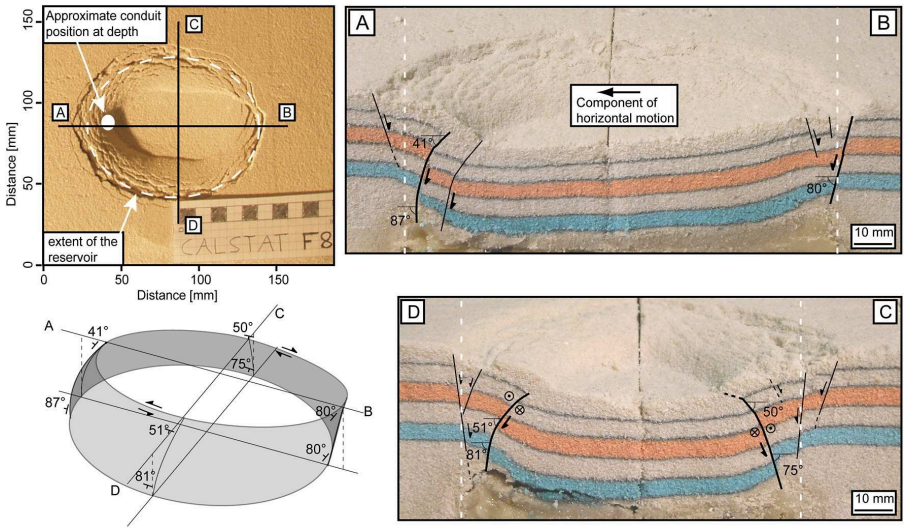

Figure 6.7: Cross sections and 3-D reconstruction of a ring-fault in a representative analogue experiment. The upper left image is a plan view of the final collapse structure (max. subsidence = c. 17 mm). Illumination is from the bottom left. The black lines mark the locations of the cross-sections shown to the right. The A-B cross section shows that the inner ring-fault comprises an inward-inclined normal segment at the trapdoor 'hinge' on the right side of the reservoir roof and an outward-inclined reverse segment on the left side. In the section D-C, the inner ring-fault is outward-inclined and reverse on both sides of the roof. It also has a strong strike-slip component (see Fig. 6.6c). Note that the inner ring-fault visible in the plan-view image is the dominant structure in the cross-sections in terms of displacement. The outer ring-fault splays from the inner ring-fault at the hinge, but it and the other faults in the extension zone are much less significant in terms of displacement. The lower left image is a schematic sketch of the inner ring-fault in three dimensions.

horizontal displacements. Also, the ring-like residual is more pronounced than in the model with a ring fault (RMSE of 0.66; Figs S18a and S20). Consequently we discard a sill-only source or an extended volumetric body as a viable source set-up.

Finally, we tested if only the ring-fault under the realistic topography could explain the observed data. We find that the point of maximum subsidence on the western summit is largely underestimated by 60 to 70 per cent. Therefore, the sill-like source in combination with the ring-fault is essential in the source set-up.

6.4.3 Analogue experiments

Deformation in our analogue experiments began with initial sagging of the roof above the reservoir, as is typical for a low 'depth to diameter' ratio ($T/D < 4$) (Roche et al., 2000; Kennedy et al., 2004, see also). Subsidence produced a central area of horizontal contraction surrounded by a peripheral area of horizontal extension (Fig. 6.6b). The area of extension commonly contained a ring-like or arcuate system of small tension fractures. With continued depletion of the honey reservoir, an inner ring-fault associated with mainly horizontal contraction developed (Fig. 6.6c). This was closely followed by the development of outer ring-like or arcuate faults associated with horizontal extension, which in some cases ultimately localized as one main outer ring fault (Fig. 6.7).

Following ring-fault formation, the analogue roofs typically subsided such that the area of maximum subsidence was off-centered with respect to the reservoir outline. This is often referred to as 'asymmetric' or 'trapdoor' subsidence in the caldera literature (Lipman, 1997, see). Intriguingly, the maximum subsidence of a roof with an off-centered conduit was located near the conduit in most cases (8 of 12 models run here).

Such off-centered collapse commonly led to a horizontal translation of the roof block within the central ring-fault (Fig. 6.6c). This translation was usually ultimately directed towards the

point of maximum subsidence, that is towards the off-centered conduit. In the example shown here (Fig. 6.6c), the horizontal translation is directed westwards, which results in mirrored dextral and sinistral strike-slip components along the 'northern' and 'southern' sections of the ring-fault, respectively.

The cross-sections (Fig. 6.7) through such a markedly off-centered (or 'asymmetric') collapse show that, near the 'western' area of maximum subsidence, the inner ring-fault dips outward and has a reverse slip-sense. On the opposite 'eastern' side of the reservoir roof, the inner ring-fault dips inward and has a normal slip-sense (Fig. 6.7, Profile A-B). In contrast the 'northern' and 'southern' segments of the inner ring-fault are both outward dipping and have an oblique-reverse slip-sense (Fig. 6.7, Profile D-C). Also noteworthy here is that the inner ring-fault is rooted at depth to the analogue reservoir's lateral margins.

6.5 Discussion

In this work we describe the deformation at Tendürek volcano in eastern Turkey, and explain it as a consequence of a shrinking sill-like body and a fully slipping ring-fault. We derive these insights from a combination of geodetic (InSAR) data, analogue subsidence experiments and numerical boundary element modelling.

In earlier works, ring-fault activity could be inferred based on deformation data, but a near complete ring of faulting was not identified as in our case. During inflation periods measured by InSAR at Sierra Negra volcano, Galápagos (Amelung et al., 2000; Jónsson, 2009), for instance, only a small part of a ring-fault ruptured or slipped, leading to a simple trapdoor-faulting episode. The trapdoor-faulting was simulated by analytical modelling techniques based on rectangular dislocations in a homogeneous elastic half-space. Similarly, Ronchin et al. (2013) used the Finite Element Method and seismic tomographic data from Rabaul caldera, Papua New Guinea, to constrain its heterogeneous subsurface geometry as well as the extent of a magma body. Then they used levelling data to invert for the pressure change within the inflating magma body and for slip on a rectangular dislocation that again represented only a segment of the caldera ring-fault. Additionally, the interaction of the fault segments with the underlying magma body at depth was not fully accounted for in either of these studies.

Our study considers interaction of a ring-fault and a contracting sill-like source as well as the effect of topography (see also Appendix 1). This level of complexity was possible by applying the BEM technique, similar to an earlier study of a subsidence period at Campi Flegrei (Beauducel et al., 2004). A difference to this earlier modelling work is that our work allowed for outward and inward dipping ring-fault geometries, as well as a strike-slip component of motion. The latter, in particular, led us to draw important conclusions for the general behaviour of ring-faults (see below).

6.5.1 BEM modelling assumptions

Our models give new insights into the deformation sources acting at Tendürek. Nevertheless, the modelling results depend on the model assumptions and the applied boundary conditions. Changing these might affect the optimum parameter values.

We here take into account the effect of topography and the interaction of complex sources, but not the effects of a heterogeneous crust. Although the latter might change the modelling results somewhat (Manconi et al., 2010; Wauthier et al., 2012), we do not have further constraints on the sub-surface crustal properties at Tendürek, e.g. from seismic or gravimetric data, so we assumed them to be homogeneous for simplicity.

We assume a constant dip-angle with depth along the ring-fault. This is unlikely to be true in reality, as seen in analogue (e.g. Fig. 6.7 here) and numerical models (Holohan et al., 2011, e.g.)

and as inferred at Rabaul caldera for instance (Saunders, 2001). Given the lack of independent constraints (from e.g. seismicity) at Tendürek, however, the computational effort of resolving such more complex models would be unrewarding at this stage.

An alternative source process to explain the 'ring-like residual' in the past sill-only model could be the compaction of caldera infill against a buried ring-fault scarp. However, we think that this is unlikely to be the main process generating the 'ring-like residual' at Tendürek. Based on our models of displacement along a buried fault, which should be broadly similar in effect to compaction against a buried fault scarp, the predominantly westward horizontal movement of the area within the ring-like residual appears to demand subsidence against a boundary that has a large overhang and a km-scale vertical extent. Preservation of such a large and shallowly-overhanging fault scarp seems unlikely; such scarp geometries are gravitationally highly unstable (Geshi et al., 2002, see).

6.5.2 New insights into the deep structure of Tendürek volcano

The BEM models resolve the 3-D architecture of the ring-fault beneath Tendürek to be compatible with a 'sliding-trapdoor' subsidence mechanism. Although the absolute dip angles along the ring-fault (Table S2) are not well constrained by surface displacements alone, there are several main features in the overall ring-fault geometry that were present in every model. Firstly and most importantly, the ring-fault architecture comprises segments that are inward-inclined and normal at the eastern volcano flanks and outward-inclined and reverse under the western volcano flanks. Secondly, segments along the northern and southern volcano flanks are resolved to be vertical or outward-inclined, with oblique-reverse or strike-slip slip-senses (Figs 6.4 and 6.6a). Thirdly, the strike-slip component along these segments is mirrored across an E-W axis running parallel to the long axis of the ring-fault's elliptical shape in plan-view. This circumferential variation in the ring-fault's three dimensional geometry and slip-sense accounts for the predominantly westward-directed horizontal motion seen in the InSAR data within the ring-fault (Figs 6.3, 6.4 and 6.6).

The data fit of the BEM model (18 model parameters; RMSE of 0.57, Fig. 6.5) is only slightly better than that of the simple analytical inversions made previously by using a rectangular dislocation in a half-space (10 model parameters; RMSE of 0.62, Fig. S17). As there is strong geologic and geodetic evidence for the existence of a ring-fault, however, the more complex BEM model presented here is more physically meaningful.

The inclusion of the ring-fault in source modelling affects the dimensions, but not the position, of the optimum sill-like source inferred in our earlier study (Bathke et al., 2013). The sill's dimensions decreased from 6.4×7.3 km to 2.7×1.8 km. The total volume change over seven years increased from ~ 3.29–4.55×10^{-3} km^3 as previously estimated to ~ 4.91–7.8×10^{-3} km^3 for the updated BEM models. The reduced size of the sill-like source in the new model is simply the consequence of an additional source, the ring-fault, which can independently account for a substantial portion of the observed surface displacements.

The tilt of the sill towards the East in our BEM models acts to account for some of the predominantly westward horizontal motion within the ring-fault. One explanation for this is that the model ring-fault is under-displaced with respect to nature, such that the model sill becomes tilted in order to help reproduce the asymmetric surface displacements. Supporting this interpretation is the fact that in models with a horizontal sill (Fig. S23), the dip-slip and strike-slip components on the ring-fault are noticeably (30–40 per cent) larger compared to those in the models with a tilted sill. In addition, the analogue experiments produce a similar ring-fault structure and a similar displacement pattern to that observed, but with a horizontal sill.

We tested again if the volume change of the sill-like source might be reasonable for a cool-

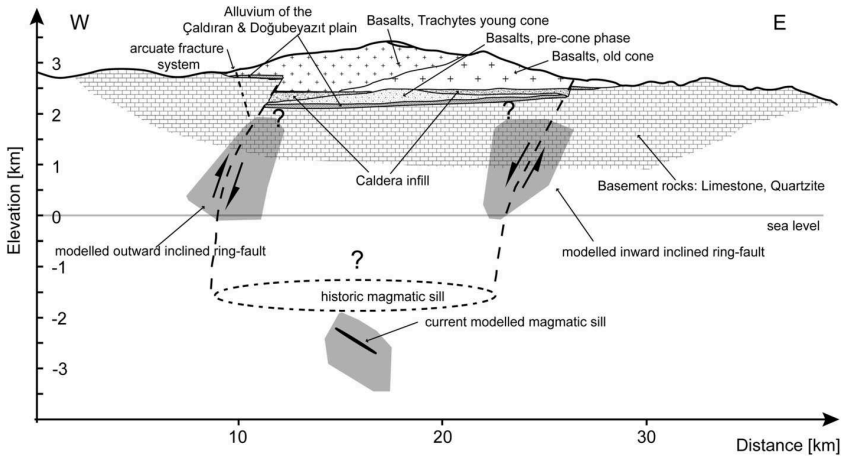

Figure 6.8: Schematic West-East cross-section through Tendürek volcano: Shown are the inferred ring-fault geometry and the sill location. Note the vertical exaggeration by a factor of two. The geologic units are projected from data of Yılmaz et al. (1998). The light gray polygons show the uncertainty in the location and geometry of the sill and the ring-fault based on our numerical modelling results. The dashed ellipse marks the speculative location, size and shape of an ancient magma reservoir whose evacuation caused the ring-fault to develop.

ing magmatic sill (Bathke et al., 2013, see also). Assuming that the sill had a conservative initial thickness of ∼30 m, the total initial volume of the magma body was 0.12 km^3 meaning that a 4.1–6.5 per cent volumetric change (previously 0.2 per cent assuming 50 m thickness) of this body would account for the estimated absolute volume change, during the time of our observation as constrained by InSAR. This volumetric change can still be explained by cooling and crystallization of liquid basaltic melt (density ∼2600 kg/m^3) to solid gabbro (density ∼3100 kg/m^3), which in the limit may result in a volume reduction of up to 7–16 per cent (Sigmundsson et al., 1997; Shirzaei et al., 2013; Bathke et al., 2013). Although a contribution to the observed displacement field from other naturally connected processes like hydrothermal activity and alteration (Tendürek shows fumarolic activity; Ölmez et al., 1994) cannot be precluded, the volume reduction attributable to the sill-like source is plausible for a cooling-contracting magmatic sill.

6.5.3 Ring-fault generation

The analogue experiments shown here produce almost identical ring-fault geometry and kinematics to those in the BEM models, and so they clearly support the structural plausibility of the resolved ring-fault architecture. They also reveal several insights into how such an architecture may have developed at Tendürek and elsewhere.

Firstly, the arcuate fractures at the surface and the 'ring-like residual' of the past sill-only models (Appendix S1) have been used to initially construct the outline of the ring-fault in our new models. The modelling results reveal, however, that the projection of the ring-fault to the surface does not coincide with the initially assumed fault position. This can be explained if the arcuate fractures at surface represent a peripheral extension zone rather than the trace of the ring-fault (Fig. 6.8). This hypothesis is supported by our analogue experiments where it is clear that the trace of the inner, outward-inclined, reverse ring-fault lies within an outer ring of extensional fractures (Fig. 6.6c). The fractures on Tendürek's flanks here correspond to the outer or peripheral fracture system, where inward-inclined normal faults may form with further subsidence (Fig. 6.7).

Secondly, low dip angles along the ring-fault in the BEM models could represent the upper part of the ring-fault, which steepens with depth as can be seen from the analogue experiments

(Figs 6.7 and 6.8).

Thirdly, it is unlikely that the sill currently inferred below Tendürek represents the magma chamber at the time of ring-fault formation. The analogue experiments show that the lower edge of a ring-fault is rooted to the lateral edge of a reservoir of similar diameter. In contrast, the ring-fault in the numerical models does not project down to the lateral edge of the sill-like source; rather, it is of a much greater diameter. Therefore, we infer that the ring-fault at Tendürek developed during ancient times by the depletion of an old magma-reservoir of a dimension that was similar to the diameter of the lower edge of the optimum modelled BEM ring-fault (Fig. 6.8). This is consistent with the blocking of old (probably >13 000 yr) summit derived lavas by the arcuate fracture system on the eastern flank of the volcano (Bathke et al., 2013). The depth of this ancient reservoir is unclear, because the ability to constrain the BEM models by surface displacement data only, is limited at greater depths. We suspect that this old ring-fault is presently being reactivated by a younger, cooling, and contracting sill.

Fourthly, the analogue experiments show that the formation of the 'sliding-trapdoor' ring-fault architecture at Tendürek may have been associated with strongly off-centered (or 'asymmetric') subsidence of the original magma chamber roof. While past results show that such asymmetric or trapdoor ring-fault geometry can form spontaneously (Roche et al., 2000; Holohan et al., 2013), our new results here indicate that it is favoured by an off-centered conduit. Assuming that the original ring-fault geometry is the same as that resolved today, it seems possible that the lateral position of the conduit during ring-fault formation was similar to the current off-centered position of the younger and deeper sill below the western volcano summit crater. This might indicate a long-term stability in the lateral position of the deep-level magma plumbing system at Tendürek. Alternatively, or perhaps complementarily, it may be that re-activation of the currently resolved trapdoor-like ring-fault, or perhaps even an asymmetric reactivation of an initially symmetric ring-fault system, could be currently promoted by the off-centered position of the present-day sill.

The reactivation of the ring-fault at Tendürek seems to be in its early phases. If it continues into the future, one could expect more distinct fault scarps to eventually form at the volcano surface. It remains unknown whether there has been any seismic activity along the ring-fault or underneath the volcano. A detailed seismological study at Tendürek has not been conducted so far, but our results indicate that it could be a fruitful subject of future research.

6.5.4 3-D ring-fault architecture at other ancient or active volcanoes

Finally, it is worth noting that the resolved 'sliding-trapdoor' ring-fault architecture at Tendürek is similar to that inferred by other approaches at several other caldera volcanoes. Examples based on field-evidence and interpreted through analogue models include ring-faults in the active calderas of Fernandina in the Galápagos Islands (Howard, 2010, Fig. 6.9a) and Miyakejima in Japan (Holohan et al., 2013). A particularly good example is the ring-fault system that accommodated much of the subsidence of the ancient Glen Coe caldera in Scotland (Fig. 6.9b). Here, exceptional field exposures reveal the ring-fault to be outward dipping on its northeastern side and inward dipping on its southwestern side. Dips measured on the northwestern and southeastern sides are near vertical. A similar asymmetric fault-geometry has been also inferred from modelling of associated seismicity occurring in 1996 at Bárðarbunga caldera, Iceland (Fichtner and Tkalčić, 2010). Here the ring-fault is thought to be outward-inclined and reverse in the West and vertical and normal in the East (Fig. 6.9c). Interestingly, the distribution of epicenters of more recent earthquakes related to a significant episode of magma migration at Bárðarbunga, appear to be compatible with this ring-fault geometry, in that they lie almost exclusively beyond and within the caldera on the NW and SE sides, respectively (Sigmundsson et al., 2015).

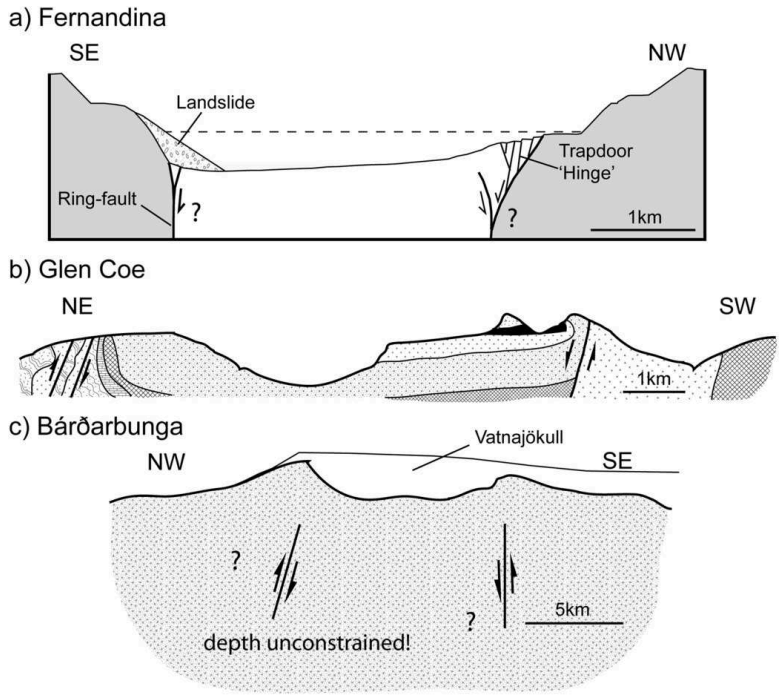

Figure 6.9: Other 'asymmetric' or 'sliding-trapdoor' ring-fault geometries in nature: (a) Cross-section through Fernandina caldera, Galápagos, showing asymmetric trapdoor-like faulting along a ring-fault, modified after Howard (2010) and Holohan et al. (2011). Dashed line indicates the position of the pre-collapse caldera floor (Simkin and Howard, 1970). (b) Cross-section through Glen Coe caldera, Scotland with the geologically determined ring-fault geometry modified after Clough et al. (1909). The newer maps of Moore and Kokelaar (1998) contain more structural detail in the central region of the caldera, but the main attributes of the main ring-fault are unchanged. (c) Schematic cross-section through Bárðarbunga volcano, Iceland, with the ring-fault geometry inferred from 1996 seismic activity by Fichtner and Tkalčić (2010). The bedrock below the Vatnajökull glacier is shown in grey (Gudmundsson and Högnadóttir, 2007) and its surface is vertically exaggerated by a factor of 2. Note that the depth and vertical extent of the ring-fault are not well constrained.

These examples suggest that sliding-trapdoor ring-fault geometries may be common in nature, at least where subsidence relative to reservoir diameter is relatively small. Such fault geometries may be also characteristic of non-volcanic subsidence phenomena, such as sinkhole formation or mine collapse. Importantly, such ring-fault geometries and their attendant strike-slip components have to date not been considered in inversions of earthquake source mechanisms at volcanoes (see Shuler et al., 2013, for overview). In agreement with a similar conclusion of Holohan et al. (2013), our results suggest that allowing for non-conical and non-dip-slip ring-fault geometries in such inversions may be an important step for more realistic earthquake source mechanism investigations.

6.6 Conclusions

1. We have used for the first time a combination of numerical modelling of spatially dense geodetic data and analogue subsidence experiments to reveal the three dimensional geometry and kinematics of a sub-surface ring-fault at a historically active volcano.

2. The geometry of the numerically modelled ring-fault at Tendürek volcano is a 'sliding-trapdoor' architecture that comprises inward-inclined normal segments on the eastern flanks and outward-inclined reverse segments on the western volcano flanks. The slip on the ring-fault entails dextral and sinistral strike-slip components along the northern and southern sides, respectively.

3. A contracting sill-like source that is centered below the western summit, but that is off-centered with respect to the ring-fault, is required to explain the geodetic observations also.

4. The plausibility of the resolved ring-fault architecture is independently supported by outcomes of analogue experiments. These experiments also indicate that the sliding-trapdoor-style fault architecture is generated by off-centered (or 'asymmetric') subsidence, which in turn may be promoted by an off-centered point of reservoir depletion.

5. Comparison of our results to field and seismological data at Glen Coe, Fernandina and Bárðarbunga calderas indicates that such an asymmetric ring-fault geometry may be common in nature and should therefore be considered in geophysical inversions of non-double couple earthquake source mechanisms at volcanoes.

Chapter 7

The rise, collapse, and compaction of Mt. Mantap from the 3 September 2017, North Korean nuclear test

Abstract

Surveillance of clandestine nuclear tests relies on a global seismic network, but the potential of spaceborne monitoring has been underexploited. Here, we determined the complete surface displacement field of up to 3.5 m of divergent horizontal motion with 0.5 m of subsidence associated with North Korea's largest underground nuclear test using satellite radar imagery. Combining insight from geodetic and seismological remote sensing, we found that the aftermath of the initial explosive deformation involved subsidence associated with sub-surface collapse and aseismic compaction of the damaged rocks of the test site. The explosive yield from the nuclear detonation with seismic modelling for 450 m depth was between 120–304 kt of TNT equivalent. Our results demonstrate the capability of spaceborne remote sensing to help characterize large underground nuclear tests.[1]

[1]Originally published as: Wang, T., Shi, Q., Nikkhoo, M., Wei, S., Barbot, S., Dreger, D., Bürgmann, R., Motagh, M., Chen, Q.-F. (2018): The rise, collapse, and compaction of Mt. Mantap from the 3 September 2017, North Korean nuclear test. - *Science*, 361, No. 6398, 166-170; doi:10.1126/science.aar7230

7.1 Main text

World peace benefits from the adherence to internationally negotiated nuclear-test-ban treaties that strive to promote the nonproliferation of nuclear weapons. In 2003, the Democratic People's Republic of Korea (North Korea) became the first country to withdraw from the 1968 Non-Proliferation treaty and started to conduct underground nuclear weapon tests with increasing intensity since 2006. On 3 September 2017, two seismic events separated by $\sim$ 8.5 minutes were detected in the North Korea's Punggye-ri nuclear test site. Soon thereafter, North Korea's state media reported the successful firing of a two-stage thermonuclear bomb test. The US Geological Survey and China Earthquake Networks Center determined a body wave magnitude (m_b) of 6.3 for the first event (NKNT 6), much larger than the five nuclear tests since 2006 (NKNT 1–5). Shortly after, the scientific community started to determine the location, focal mechanism, and yield of the explosion using seismic waveforms and satellite imagery (IRIS, 2017). Preliminary analysis revealed a predominantly isotropic explosive source located beneath Mt. Mantap (IRIS, 2017; Liu et al., 2018), which also hosted NKNT 2–5 (Fig. 7.1).

The source properties of previous North Korean underground nuclear tests have been extensively studied using seismic waveforms (Zhao et al., 2008; Ford et al., 2009; Selby, 2010; Wen and Long, 2010; Chun et al., 2011; Rougier et al., 2011; Zhao et al., 2012; Zhang and Wen, 2013; Zhao et al., 2014; Cesca et al., 2017; Patton and Taylor, 2011), but surface displacements associated with these explosions are rarely reported. Remote sensing with Synthetic Aperture Radar (SAR) is a powerful technique for monitoring deformation of the Earth's surface (Hu et al., 2014; Elliott et al., 2016) but its contribution to characterizing nuclear tests has been limited. The NKNT 4 conducted on 6 January 2016 has been studied using SAR interferometry, but the interpretation of interferometric phase is challenged due to the single imaging geometry (Wei, 2017). Tracking the amplitude features of the SAR images (so called pixel-offset tracking) is better suited when the interferometric phase is decorrelated (Michel et al., 1999). Moreover, pixel offsets can map displacement along the radar line-of-sight (LOS) and the satellite flying (azimuth) directions. In contrast to offset tracking of optical images, the SAR range offset is sensitive to the vertical displacement because of the slant-range imaging geometry, allowing for deriving three-dimensional (3-D) displacements (Pathier et al., 2006; Wang and Jónsson, 2015; Ruch et al., 2016; Schaefer et al., 2017). Here we rely on detailed 3-D displacements derived from sub-meter resolution SAR images together with seismic waveform data to reveal the complex processes that took place during and in the immediate aftermath of NKNT 6.

We measured the surface displacements caused by NKNT 6 through cross-correlating high-resolution spotlight radar images acquired by the German TerraSAR-X satellite, with an azimuth resolution of 1.1 m and a slant-range resolution as fine as 0.45 m (Fig. S24, Table S3). The accuracy of the offset measurement is about 1/10 of the imaging resolution (Bamler and Eineder, 2005). We combined the azimuth and range offsets from two ascending and two descending tracks to calculate the total 3-D surface displacements produced during and in the immediate aftermath of the explosion on a 300×300 m grid (Fig. 7.1 and Figs S26-S28; see supplementary information for details). The horizontal motions of up to 3.5 m show a divergent pattern at the top of Mt. Mantap with a central zone of subsidence of $\sim$0.5 m. We decomposed the 3-D displacements into vertical and horizontal directions along two topographic profiles across the top of Mt. Mantap (Fig. 7.1). The along-profile displacements show that the horizontal displacement is generally larger where the topography is steeper (the west and south flanks). However, the direction of motion does not follow the slope of the terrain but is nearly horizontal. This indicates that while there is strong topographic control on the surface displacement field caused by the buried explosion, it does not resemble the slope-parallel motions expected from triggered landslides. While optical imagery suggests isolated 10–100 m

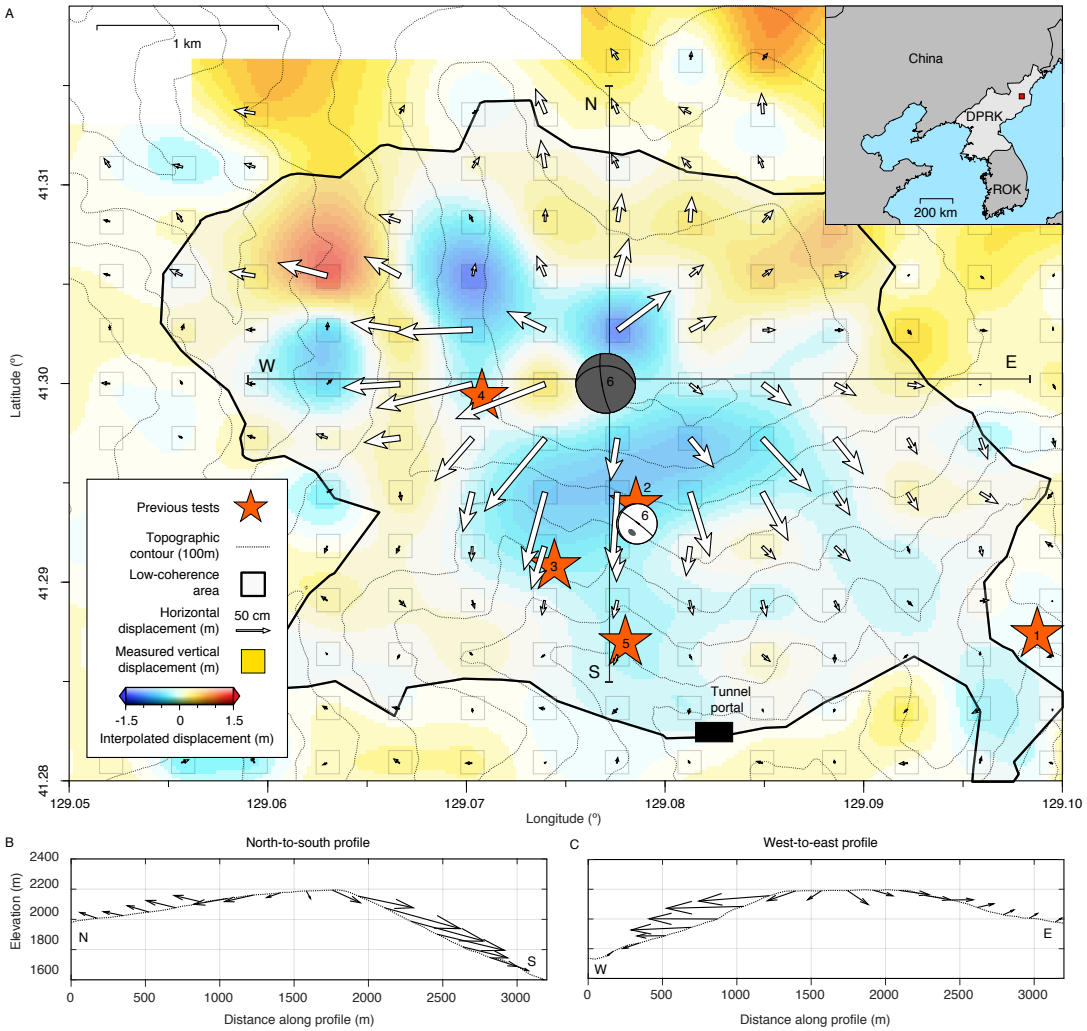

Figure 7.1: Three-dimensional (3-D) displacement associated with the 3 September 2017 North Korean Nuclear Test (NKNT 6). (A) 3-D displacements derived from radar imagery with arrows indicating horizontal, color indicating vertical motions spanning the explosion and ∼1 week of additional deformation. The uncertainties are shown in Fig. S27 and provided in Additional Dataset 1 with the displacements. Black outline derived from ALOS-2 coherence loss indicates the substantial surface disturbance and large displacement gradients caused by the explosion over an area of ∼9 km^2 (Figs S24 and S25). Thin gray lines are topographic contours at 100-m intervals. Red square in the upper right inset shows the location of Mt. Mantap. Red stars indicate the locations of NKNT 1–5 (IRIS, 2017; Wen and Long, 2010; Zhang and Wen, 2013; Wei, 2017), among which NKNT 2–5 were all located within the NKNT-6 low-coherence region, NKNT 1 on 9 October 2006 was in a different location (Selby, 2010). Beach balls show locations and focal mechanisms of the M_w 5.24 and M_w 4.47 events on 3 September 2017. (B) and (C) show 2-D (horizontal along the profile and vertical) displacements along two profiles across the top of Mt Mantap from north to south, and from west to east respectively. The elevations along the vertical axis in (B) and (C) are on scale.

scale landslide deposits (USKI, 2018), these appear to be debris flows localized in pre-existing channels that could not produce the large-scale horizontal motions we observed.

To resolve the horizontal location and depth of the detonation chamber, we set up numerical models that predict the surface displacements due to the expansion and subsequent collapse of an underground cavity embedded in a uniform elastic crust below realistic surface topography (Nikkhoo and Walter, 2015; Nikkhoo et al., 2017, Fig. 7.2). We constrained the 3-D location of the source by minimizing the misfit between predicted and observed surface displacements (Holland, 1975; Haupt and Haupt, 2004). The explosion and immediate collapse of a 300 m radius spherical cavity that includes the detonation chamber and the surrounding damaged material reproduced the horizontal displacement well but was not sufficient to explain the

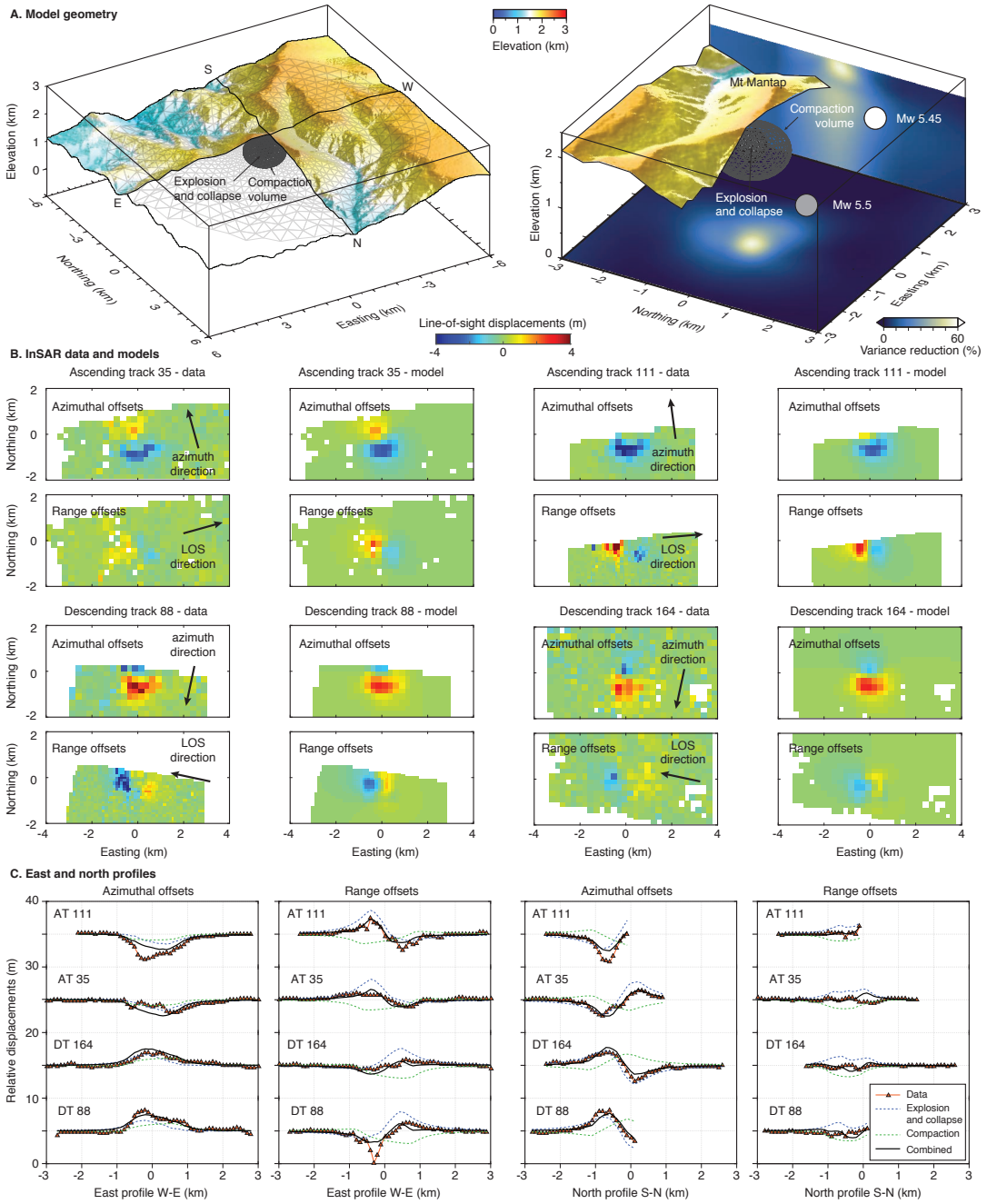

Figure 7.2: Model geometry and fit to the observed surface displacements. (A) Perspective view of the model with topography and variance reductions as a function of centroid position (both cross-sections are centred on the best fit location). We represent the first event, combining the explosion and immediate collapse, using a sphere of 300 m radius with a centroid located at a depth about 450 m below Mt Mantap. We model the aseismic subsidence detected with geodetic data about a week after the seismic events 1 and 2 with an ellipsoid of dimension $800 \times 800 \times 470$ m semi-axes, centred at 100 m deeper than the explosive source. The isotropic components of the moment tensors are represented as beach balls. (B) The observed and simulated surface displacements. (C) The west-east and south-north profiles of the surface displacements from the SAR observations and the best-fitting models. The dashed profiles represent the contributions of the explosion/collapse (Event 1) and the subsequent aseismic compaction on the surface displacement. We ignore the deformation caused by Event 2.

small vertical motion around Mt Mantap. A third, mostly aseismic process involving the compaction of a larger volume is invoked to explain the low uplift (Fig. 7.2A and Fig. S29). A similar compaction process has been inferred from the seismic analysis of other explosions (Patton and Taylor, 2011) and was observed in the weeks to months following underground

nuclear tests conducted in Nevada (Vincent et al., 2003). As we do not have any constraints on the geometry of the compaction zone, we assumed a generalized ellipsoidal geometry for it and inferred its dimensions by using the geodetic observations. We estimated the explosive source to be located at 129.078°E/41.300°N±50 m, 1750 ± 100 m above mean sea level, that is, 450 ± 100 m below the top of Mt. Mantap. Incorporating the large-scale compaction source into the model does not significantly influence our inferred epicentre of the explosion/collapse source (see supplementary information for details).

Assuming that the hypocentre of the first event coincides with the center of the spherical cavity we refined the relative location for the second seismic event using local seismic waveform records from the NorthEast China Seismic Array to Investigate Deep Subduction (NECsaids) (Wang et al., 2016) and regional data from South Korean sites archived at the Incorporated Research Institutions for Seismology (IRIS) (Fig. 7.3A) (see supplementary information for details). With the calibration from the first event and careful P-wave arrival picks of the second event (Figs S30 and S31), our grid search showed that the second event occurred 8 min30.76 s after the first event and is located about 700 m to the south. Due to the azimuthal gap in the station coverage, the east-west location (±700 m) is less well constrained compared with the north-south separation (±200 m with 96 per cent confidence) (Fig. 7.3C and Fig. S32). The refined location of the second implosive event is beneath the area of large subsidence and southward horizontal motion under the south flank of Mt. Mantap, between the initial explosion and the south portal of the tunnel system (Fig. 7.1).

We applied the generalized Cut-And-Paste (gCAP) method (Zhu and Ben-Zion, 2013) to the regional and local waveform data to invert for the full moment tensor solutions of the two seismic events, including isotropic (that is, explosive or implosive volume source), compensated-linear-vector-dipole (CLVD) (that is, ring faulting along a certain axis, like a collapse), and double-couple (that is, shear dislocation on planar fault) components (see supplementary information for details). Our preferred solution of the first event indicates a moment of 9.5×10^{16} N m ($M_w = 5.24$) and a 50 to 90 per cent positive isotropic component, and relatively small CLVD or double couple contributions (Figs S33-S36). The second seismic event ($M_w = 4.5$) has a large negative isotropic component (∼50 to 70 per cent of the total moment) (Figs S37-S38). While we obtained a high waveform cross-correlation coefficient between the data and synthetics for most of the waveform components of the first event (e.g. Fig. 7.3B), the noise level for the second event is larger, resulting in a much smaller variance reduction of the observations (Fig. S39). To overcome this limitation of the data, we drew insight on the moment tensor of the second event by directly comparing the waveforms with those of the first event. We multiplied the amplitude of the vertical-component waveforms of the second event by a factor of -60 and compared them with the waveforms of the first event at higher frequencies (∼0.2–0.9 Hz). The result (Fig. 7.3D and Fig. S39) shows very high waveform cross-correlation coefficients, even for some coda waves, supporting the close locations but opposite isotropic polarities of the two events (Liu et al., 2018).

Combining the depth constraints from geodesy and energy constraints from seismology, we can refine the explosive yield of the nuclear explosion (Teller et al., 1968; Denny and Johnson, 1991). We assumed the seismic velocity model MDJ2 (Ford et al., 2009) for the elastic earth structure. We based the overburden pressure on the best-fitting centroid source depth of 450 ± 100 m from the geodetic modelling. The medium in which the device was detonated was likely the granodiorite that lies beneath the stratified volcanic rocks that make up the high elevations of Mt. Mantap (Rougier et al., 2011). We assumed a gas porosity of 1 per cent for granitic rocks (Springer, 1966). Considering an isotropic seismic moment of magnitude $M_w = 5.05$ (the mean value of solutions fitting within 95 per cent of the maximum fit for a source depth of 450 m) and the possible range of source depths of 350–550 m, the yield estimates

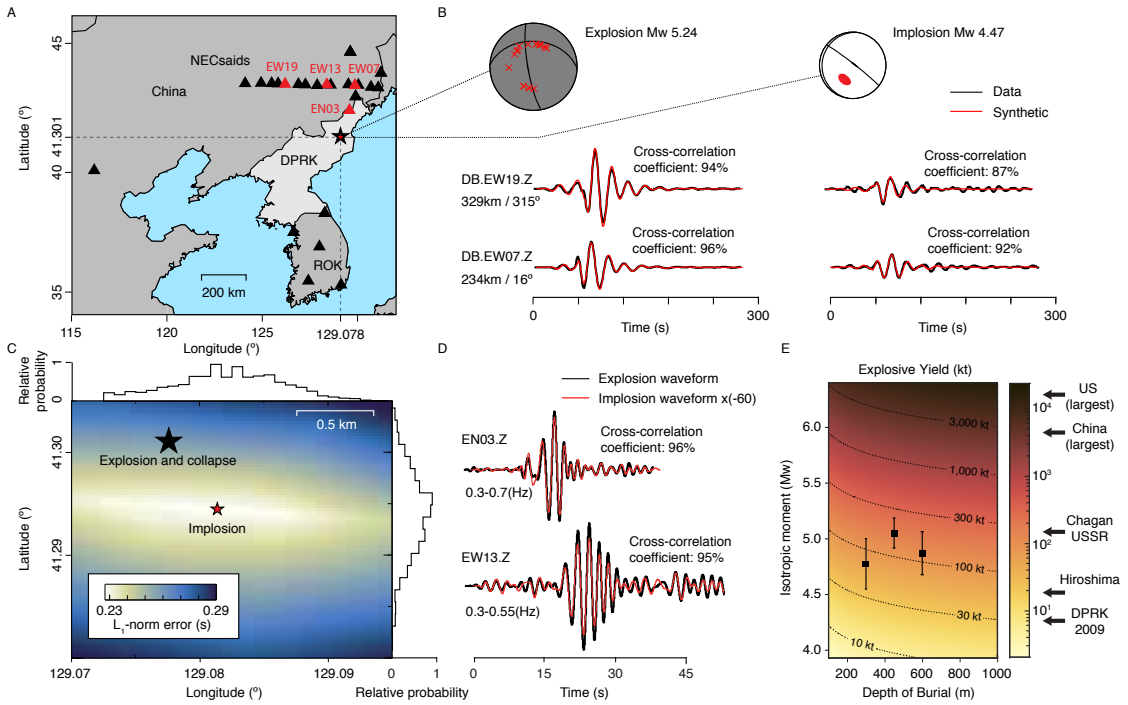

Figure 7.3: Analysis of seismic waves. (A) Station map of broadband seismometers with four stations in B and D highlighted in red. The black and red stars are the epicentre location of the first and second event, respectively. (B) Moment tensor solutions for the first explosive (left) and the second implosive (right) event, with vertical component of two representative stations shown at the bottom. Both data and synthetics are filtered between 0.02 Hz and 0.045 Hz. Station names are shown at the beginning of waveform pairs and distance (in km) and azimuth (in degree) are indicated below. (C) Grid search result (under L1 norm) for relocating the second event relative to the first event (black star). Marginal distribution for the epicentral position are plotted along the northing and easting axes. (D) Vertical component waveform comparison between the first (black) and the second (red) event at two representative stations, with the second event waveforms multiplied by -60. (E) Explosive yield with historical nuclear tests. The black dots and error bars show yields estimated based on the mean and standard deviation of tabulated moment within 95 per cent of the best fitting solutions with depths of 300 m, 450 m and 600 m, respectively.

range between 171 to 209 kt of TNT equivalent, with 191 kt corresponding to the best-fitting source parameters from geodetic and seismic data (Fig. 7.3E). Doubling the gas porosity results in an 8 per cent increase in the magnitude of estimated yield.

The source characteristics we derived from surface displacement and seismic waveforms are in remarkable agreement. The divergent horizontal motions and the moment tensor of the first event consistently suggest a predominant isotropic explosive source buried at shallow depth. The moment of the geodesy-derived models, assuming an empirical rigidity of 5.7 GPa (Springer et al., 2002), is $M_w = 5.5$, larger than the one inferred seismically ($M_w = 5.24$), because it includes slow deformation that did not generate seismic waves - with a total volume change of 0.01 km^3. The seismic analysis of the second event reveals an implosive seismic source that occurred south of the first event with a dominant negative isotropic component, suggesting an inverse process of the main explosion. This may reflect the combination of negative isotropic compaction of the over-pressured cavity and/or vertical collapse of the explosion chimney and nearby tunnel segments due to gravity, contributing to the subsidence on the south flank of Mt. Mantap (Fig. 7.4). The larger-scale compaction source in the geodetic model is independent of the first and second seismic events, and the post-explosion compaction of surrounding rocks may continue aseismically for an extended period, as seen in the Nevada underground nuclear test site with initial subsidence rates of ∼1–7 cm/yr (Vincent et al., 2003).

Our 3-D surface displacement measurements and elastic modelling incorporating realistic

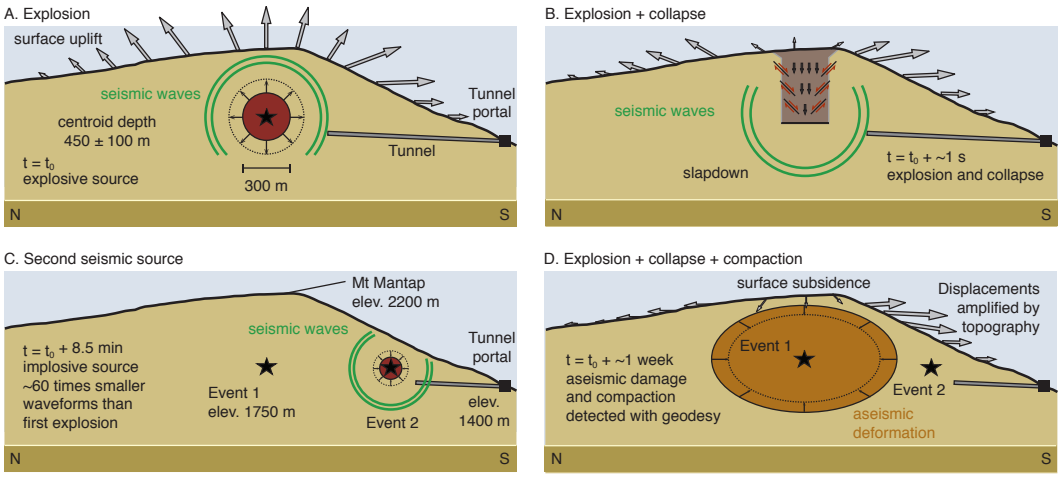

Figure 7.4: Summary deformation scenario for the 3 September 2007 North Korea's Nuclear test. The unfolding of events includes the succession of (A) explosive, (B) collapse, and (D) compaction processes, with different associated surface displacements. The implosive source (C) may be shallow and only contribute localized surface displacements. The radar imagery reveals the deformation (arrows in D) resulting from the three processes.

topography allow for locating the main explosive event within ±50 m assuming a uniform elastic medium, but a non-uniform structure and small-scale surficial processes (e.g., landslides) may bias our results. As the largest deformation occurred above the explosive source due to the chimneying and spalling effect (Patton and Taylor, 2011), the centroid of the modelled geodetic source may locate above the actual detonation point. Following the explosion, water was observed to be flowing from the tunnel portal (USKI, 2018). Assuming a slope of 2–4 degrees to provide drainage, the depth implied from the elevation of the tunnel entrance is about 600–700 m below the surface, consistent with a detonation point about 150 m deeper than the centroid of geodetic model.

Combining the available spaceborne geodetic and seismic records provided new insights into the mechanics of deformation surrounding North Korea's sixth underground nuclear test, revealing the explosion, collapse, and subsequent compaction sequence (Fig. 7.4). The modelling of the geodetic observations reduces the epicentral and depth uncertainties that otherwise hinder the analysis of seismic waveforms. The derived horizontal location of the first event is important to relatively relocate the second event, which likely indicates the collapse of the tunnel system of the test site. The inclusion of geodetic data also helps resolving the aseismic deformation processes that may follow nuclear tests. Finally, our findings demonstrate the capability of monitoring shallow underground nuclear tests using remote-sensing observations and seismic sensors.

Chapter 8

Summary and outlook

This research delivers new analytical solutions for triangular and rectangular dislocations in both elastic full-space and half-space. These solutions are free of artefact singularities and numerical instabilities in their configurations and thus, are well suited for high-resolution dislocation modelling applications. Furthermore, these solutions are scale-independent and can be applied to deformation modelling problems of various length scales.

Another contribution of this research is a compound dislocation model (CDM) that can simulate deformation fields associated with generalized pressurized cavities and magmatic intrusions. The CDM is composed of three mutually orthogonal rectangular dislocations (RDs). As the new solutions for the RDs possess full rotational degrees of freedom, the CDM may also take any arbitrary orientation in space. The CDM can be used in rapid source inversions without any prior knowledge on the deformation source geometry. This particular advantage of the CDM is crucial for hazard assessment and early warning systems. These features of the CDM have been illustrated through applying it to the 2015 co-eruptive deformations of Calbuco volcano. Moreover, the flexibility of the CDM for representing various generalized deformation sources also allows making use of multiple CDMs of various geometries to constrain complex plumbing systems of active volcanoes. The two-source deformation model of the 2013–2016 inflation at Copahue volcano has provided an image of the hydrothermal system that has been confirmed by both the recorded volcano-tectonic (VT) earthquakes and the observed displacements on tectonic fault scarps in the area.

Through applying the boundary element method (BEM) to the new solutions for the triangular dislocations (TDs) more sophisticated dislocation models have been developed in this dissertation. These models have been applied to more complex deformation problems, which involve realistic surface topography, arbitrary source geometries and stress interactions between deformation sources. The numerical modelling examples in this dissertation highlight that the fast and efficient numerical dislocation models make complex deformation problems tractable. The first example focuses on the 2013 pre-explosive inflation of Volcán de Colima in Mexico. The surface displacements have been simulated by using two ellipsoidal cavities, which represent two zones of pressurization in the main conduit system and one of its branches, respectively. The location of the latter coincides with the location of the post-explosive extrusion.

In the second case study the 3-D kinematics and geometry of an active ring-fault at Tendürek volcano in Turkey have been investigated. For this aim the source parameters of the ring-fault and a contracting sill-like source are inferred through inverting the observed surface displacements. Comparing the inversion results with sand-box analogue models of caldera collapse, the observed subsidence and sliding signal have been explained as a consequence of a 'sliding-trapdoor' ring-fault architecture. The inferred ring-fault consists of outward-inclined reverse segments and inward-inclined normal segments on the volcano's western and eastern flanks, respectively. This mechanism has been shown to be common in nature at different scales.

The last application example in this dissertation concerns the North Korea's sixth underground nuclear test conducted on 3 September 2017. In this case study, a dislocation model

that is composed of the TDs and CDM has been used to invert the observed surface displacements for the horizontal location and depth of the detonation cavity within the edifice of Mt. Mantap. It has been shown that due to the steep flanks of Mt. Mantap and the very shallow depth of the explosion the topography has a strong control on the deformation and thus, on the surface displacements. Combining the results from the dislocation model with focal mechanism solutions from seismic data analysis it has been shown that the inflation due to the initial explosion has been succeeded by subsidence due to subsurface collapse and compaction of the rocks surrounding the detonation cavity.

The presented modelling techniques and application case studies in this dissertation establish a unified framework for dislocation modelling, ranging from point source and finite analytical models to sophisticated numerical models of complex geometries and flexible boundary conditions. The application examples show that these models allow integration of more physical and geological constraints in deformation models and lead to a better understanding of the underlying processes of crustal deformations.

Future work: In this dissertation, the geodetic inversions that rely on numerical models have been conducted through non-linear optimization techniques, namely the genetic algorithm. This way, however, the uncertainties in the inferred source parameters due to observational and model errors cannot be assessed properly. This issue can be avoided through estimating the probability density functions (PDFs) of the estimated source parameters. Bayesian inversion approach along with a PDF sampling technique, such as Markov Chain Monte Carlo (MCMC), can be used for this purpose. However, the numerical deformation models and MCMC techniques are both computationally demanding and thus, combining these techniques in routine inversions requires further investigations on theoretical aspects of these methods and utilization of available tools for optimal parallel computations.

The developed mathematical models in this research can be further improved at various levels. Regardless of the assumption for the surface topography, the Earth's crust in both analytical and numerical models in this research is simulated as a uniform, isotropic elastic medium. This first-order approximation may result in large errors, if significant material heterogeneities be present in the host rocks. Another important point is that crustal rocks may not always deform elastically. Depending on the mechanical properties of the rocks and the intensity and timescale of the driving forces, various regimes such as brittle, plastic, viscoelastic or a combination thereof may govern the crustal deformations. Moreover, interactions between the host rocks and sources of heat and fluids, especially at active volcanoes, may result in significant thermoelastic and poroelastic deformations. Thus, for a more accurate modelling the sophisticated dislocation models must be enhanced to include realistic material heterogeneities and complex deformation regimes in their formulation. However, to achieve this goal it may be necessary to couple the dislocation modelling techniques with other numerical methods such as the finite element method.

Supplementary information

Supplementary information for Chapter 4: Copahue volcano, Chile

Introduction

This supplement contains figures and tables in support of the main document. The Fig. S1 shows InSAR data for the UAVSAR and satellite InSAR time series mean velocities spanning the 2013–2014 interval. Figures S2-S11 show pCDM modelling results for one- and two-source pCDM solutions for the 2013–2016 interval, with the final set of model figures for the 2013–2014 interval. Figures S12-S14 show the theoretical interpretation and comparison between pipe models and CDM models with similar shapes.

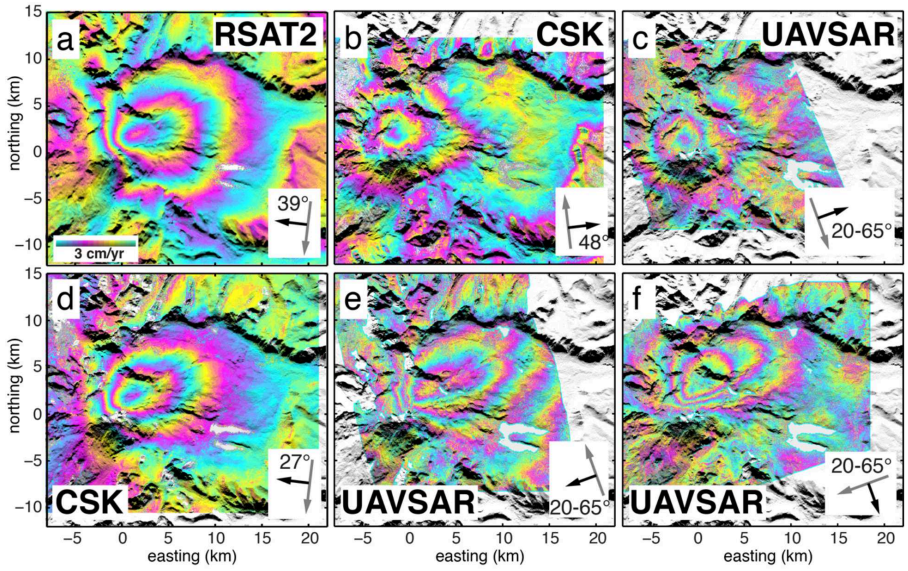

Figure S1: InSAR mean velocities for the 2013–2014 time-interval. The heading and radar look direction and incidence angle or angle range are indicated for each data set. Each velocity map is shown wrapped at 3 cm/yr velocity per color cycle. The satellites (a, b, d) show mean velocities from the time series portions shown in Fig. 4.3, whereas the airborne UAVSAR data are single interferograms divided by the time-interval (1 year).

Table S1: UAVSAR data acquisition dates.

Line	2013	2014	2015
158	March 25	April 24	March 28
253	March 25	April 28	March 30
346	March 25	April 24	March 28

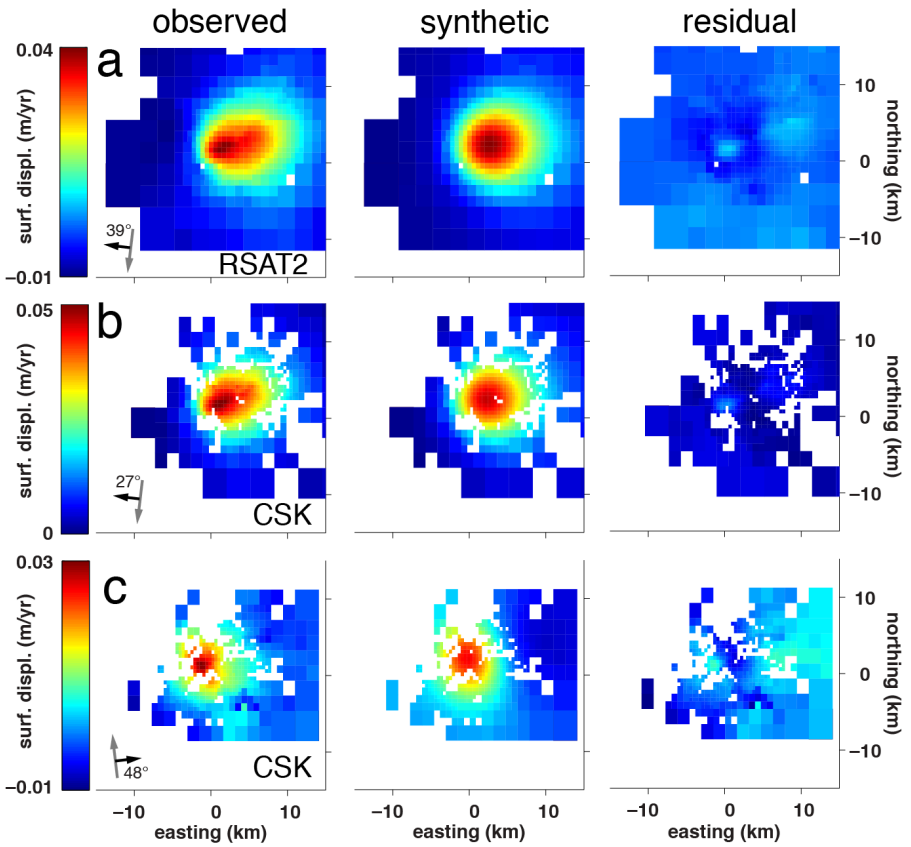

Figure S2: Single source pCDM solution modeled InSAR line-of-sight (LOS) surface displacement rates for the 2013.25–2016.4 time-interval. See Fig. 4.3 for more detailed explanation.

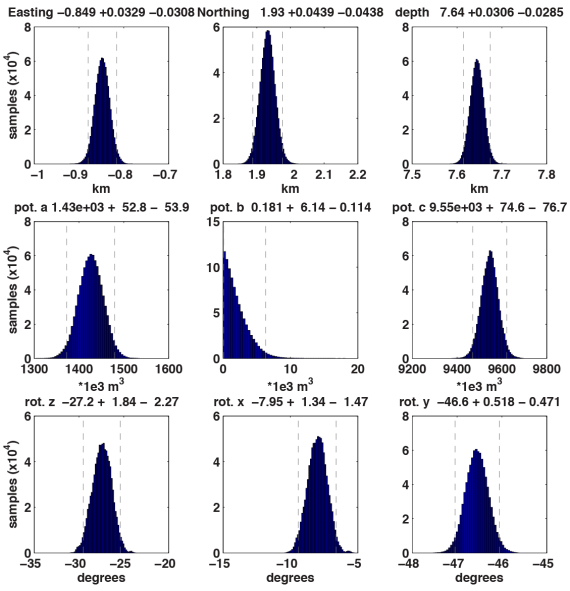

Figure S3: Single source pCDM solution posterior probability density functions (PDFs) for each parameter for the 2013.25–2016.4 data set solution. Number adjacent parameter label gives the mode value and the plus and minus 95 per cent confidence bounds and indicated in the PDF plots by dashed grey lines.

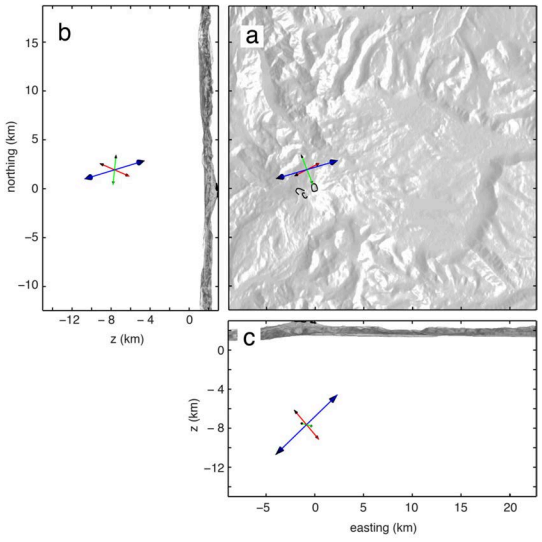

Figure S4: Single source pCDM solution for the 2013.25–2016.4 data set solution. (a) Map view of CDM source. Source vectors correspond to the potency a (red), potency b (green), potency c (blue), with arrow size proportionate to the values given in the PDF plots (Fig. S3). Map area corresponds to box shown in Fig. 4.1. (b) Side view from the west. (c) Side view from the south.

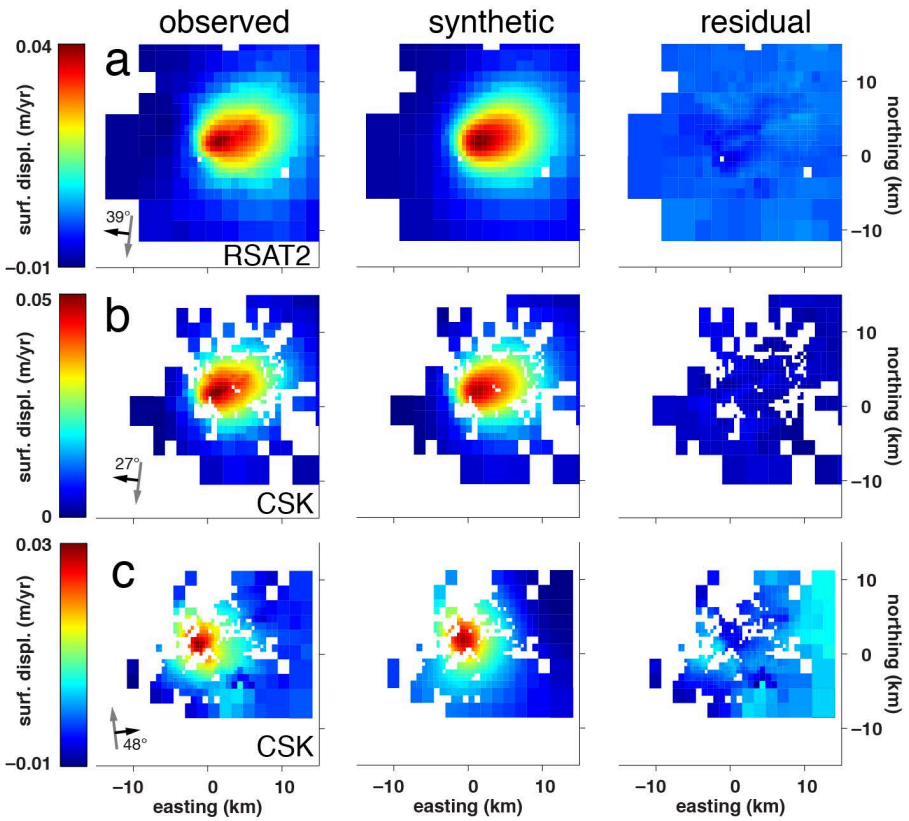

Figure S5: Two source pCDM solution modelled InSAR line-of-sight (LOS) surface displacement rates for the 2013.25–2016.4 time-interval. See Fig. 4.3 for more detailed explanation.

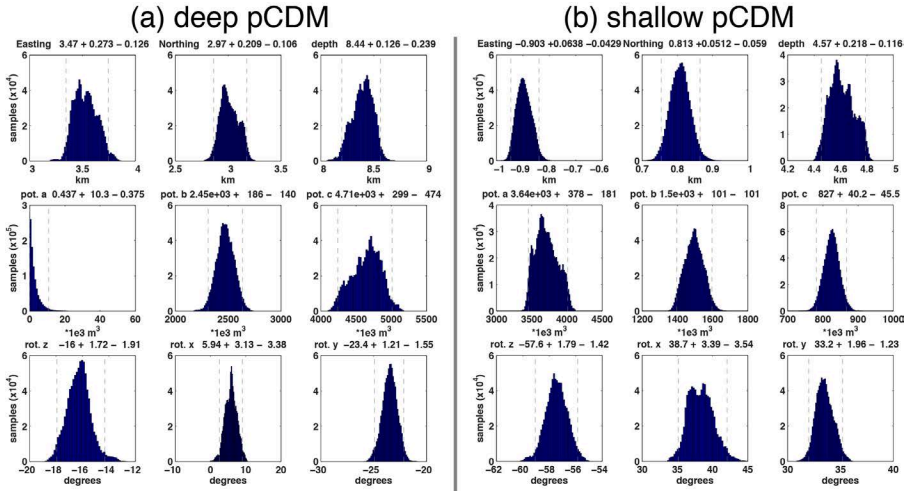

Figure S6: Two source pCDM solution posterior probability density functions (PDFs) for each parameter for the 2013.25–2016.4 data set solution. (a) Deep pCDM source. (b) Shallow pCDM source. Label for each parameter given above each subplot. Number adjacent parameter label gives the mode value and the plus and minus 95 per cent confidence bounds and indicated in the PDF plots by dashed grey lines.

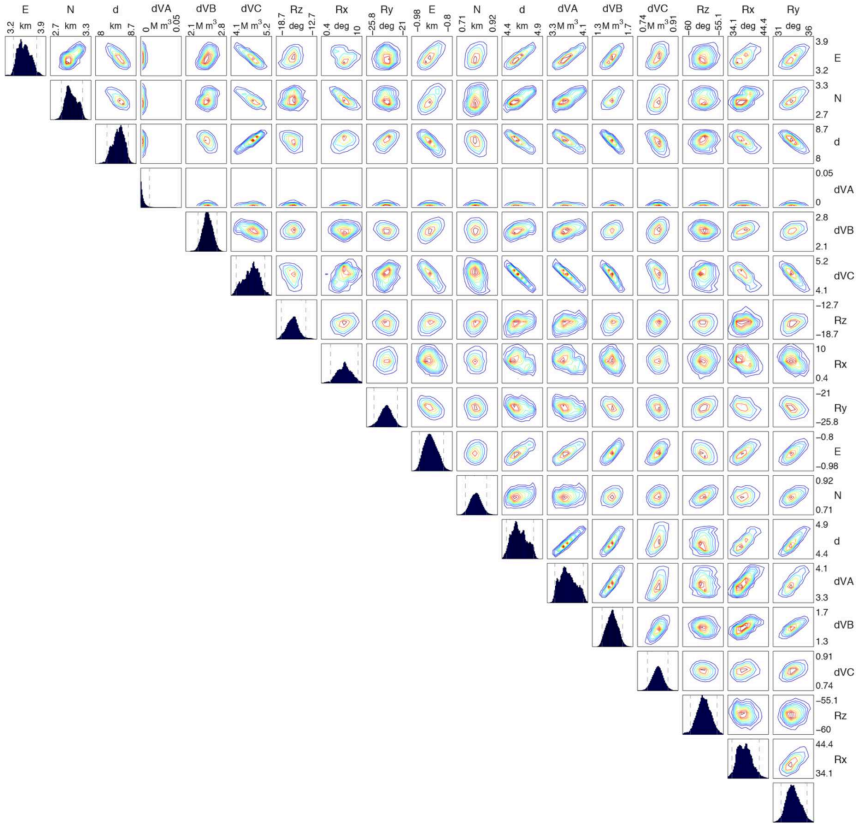

Figure S7: Two source pCDM solution model parameter covariances (contours) and posterior probability density functions (PDFs) for each parameter (on the diagonal) for the 2013.25–2016.4 data set solution. 95 per cent confidence bounds and indicated in the PDF plots by dashed grey lines. The labels at the top and right side give the parameter name and bounds (the first 9 values are for the first deep pCDM source, the plots for the lower right 9 are for the second pCDM source). For the PDFs on the diagonal the top label relates to the PDF bounds on the horizontal axis.

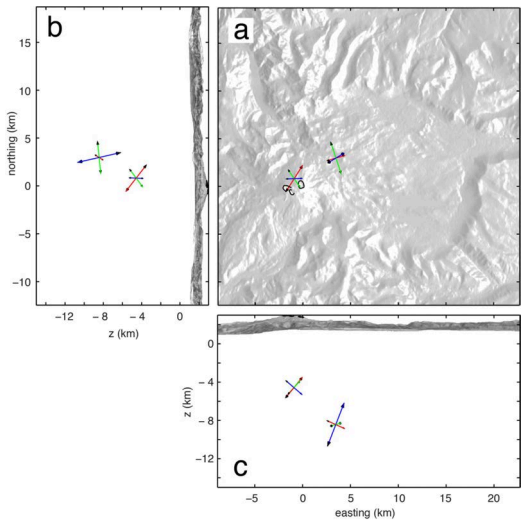

Figure S8: Two source pCDM solution for the 2013.25–2016.4 data set solution. (a) Map view of CDM source. Source vectors correspond to the potency a (red), potency b (green), potency c (blue), with arrow size proportionate to the values given in the PDF plots (Fig. S10). Map area corresponds to box shown in Fig. 4.1. (b) Side view from the west. (c) Side view from the south.

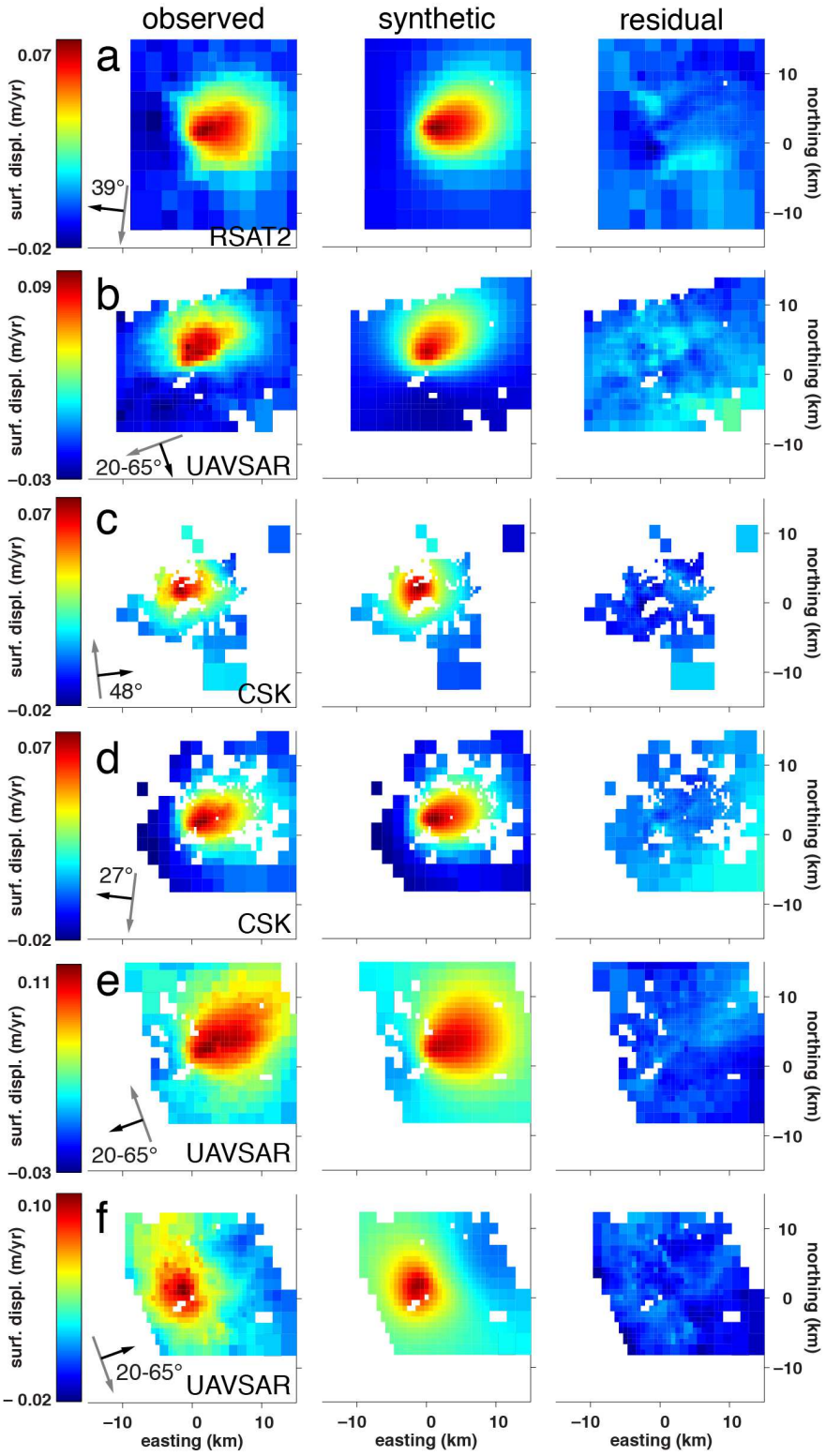

Figure S9: Two source pCDM solution modeled InSAR line-of-sight (LOS) surface displacement rates for the 2013.25–2014.33 time-interval. For each observed InSAR time series linear velocity (left column) we show the synthetic displacements given by the source model (middle column) and the residual (right column). For each data set: (a) RSAT2 descending, (b) UAVSAR heading 253, (c) CSK ascending, (d) CSK descending, (e) UAVSAR heading 346, (f) UAVSAR heading 158. For each the heading (grey arrow), look direction (black arrow), and incidence angle are indicated in the lower left corner.

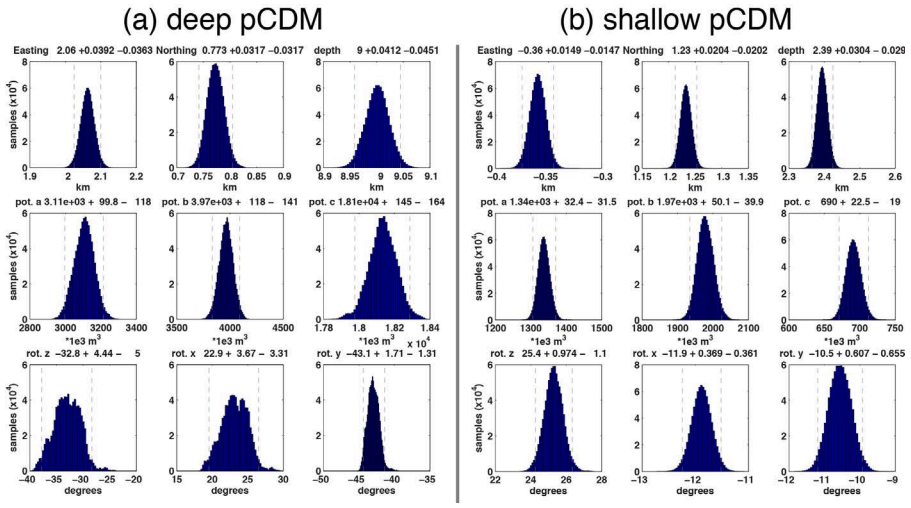

Figure S10: Two source pCDM solution posterior probability density functions (PDFs) for each parameter for the 2013.25–2014.33 data set solution. (a) Deep pCDM source. (b) Shallow pCDM source. Label for each parameter given above each subplot. Number adjacent parameter label gives the mode value and the plus and minus 95 per cent confidence bounds and indicated in the PDF plots by dashed grey lines.

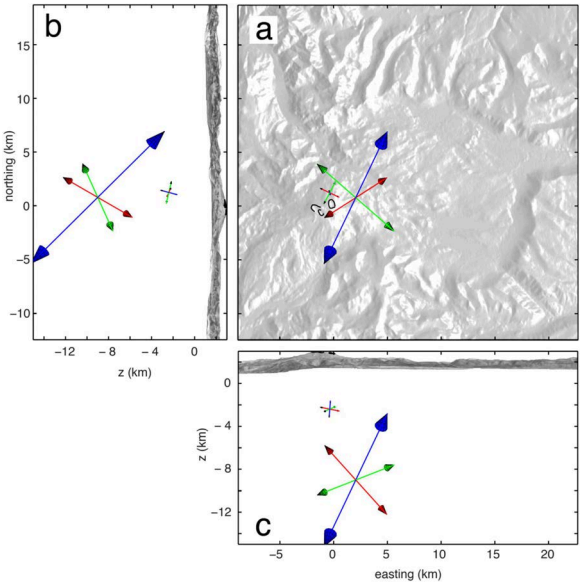

Figure S11: Two source pCDM solution for the 2013.25–2014.33 data set solution. (a) Map view of CDM sources. Source vectors correspond to the potency a (red), potency b (green), potency c (blue), with arrow size proportionate to the values given in the PDF plots (Fig. S3). Map area corresponds to box shown in Fig. 4.1. (b) Side view from the west. (c) Side view from the south.

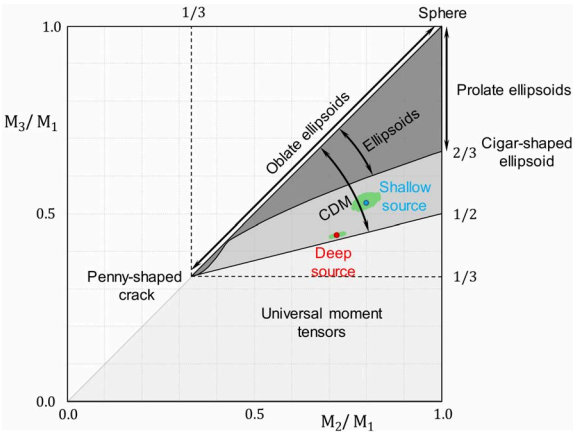

Figure S12: Location of the two CDM solutions on the moment ratio plot of Nikkhoo et al. (2017). The locations of the deep CDM (red dot) and shallower CDM (blue dot) are beyond the range for ellipsoids (dark grey) and fall within the area for pipe-like bodies (medium grey). Green area surrounding each dot shows the moment ratios for all 900000 kept solutions showing their spread in values and representing close to a 99 per cent confidence bounds.

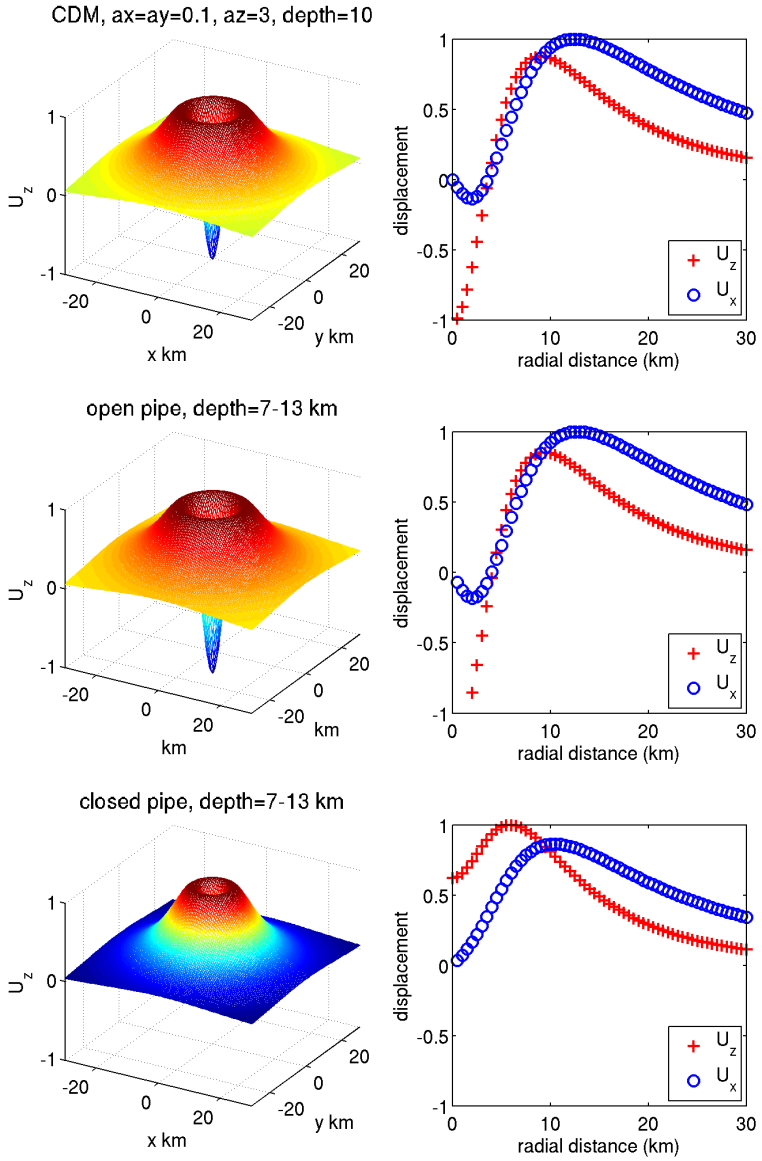

Figure S13: Comparison of vertically elongated (a) CDM, (b) open pipe, and (c) closed pipe analytical solutions. The pipe solutions are after Bonaccorso and Davis (1999). Each solution extends vertically from 7 to 13 km below the surface with a radial dimension of 0.1 km. The CDM solution is very close to that for an open conduit.

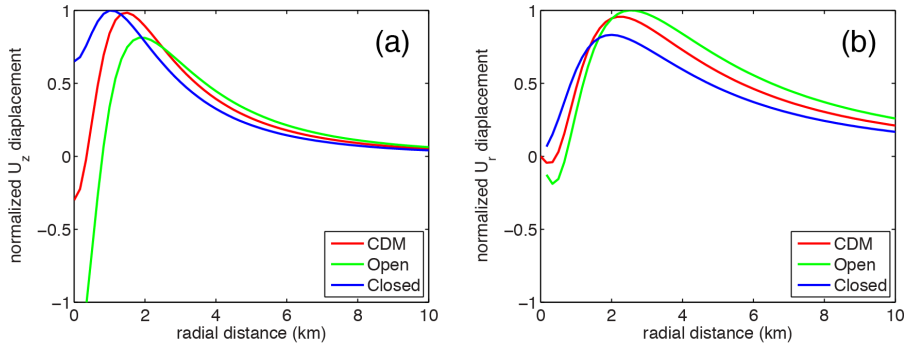

Figure S14: Comparison of shallow (depth = 2.5 km) vertically elongated (depth ±1.4 km) source surface displacements. Plots show modelled displacement profiles as a function of radial distance, normalized by the maximum of the vertical or radial displacements. (a) vertical, (b) horizontal. The pipe solutions are after Bonaccorso and Davis (1999). Each solution extends vertically from 3.9 to 1.1 km below the surface with a radial dimension of 0.25 km. The CDM solution is very close to that for an open conduit.

Supplementary information for Chapter 5: Volcán de Colima, Mexico

Supplementary Figures

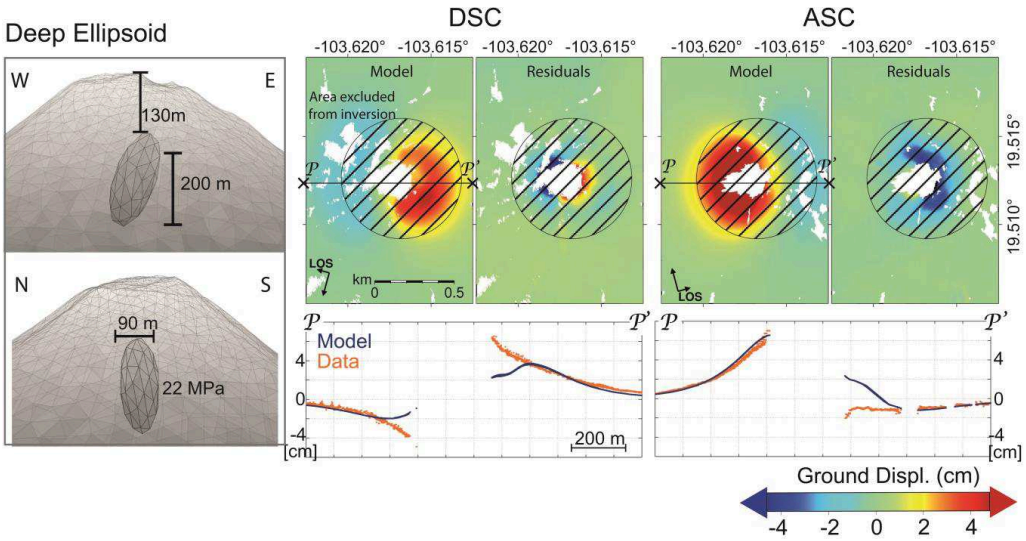

Figure S15: Optimization result for an ellipsoidal source excluding the near-field data. The resulting model is an inclined source located at greater depth than the single-source models. The residuals in the far field are near-zero in both the ascending and descending track, but extremely high in the summit region. This result is used to constrain the deeper source in the two-source model.

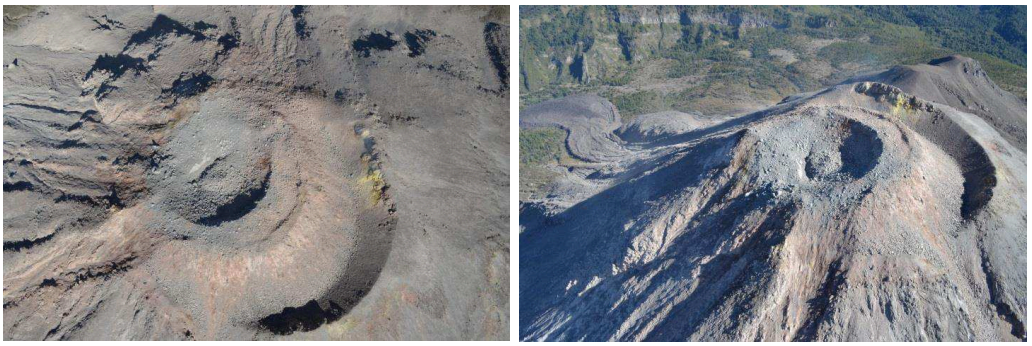

Figure S16: Photographs of the summit taken during an airplane overflight on January 10th, provided by Protección Civil Jalisco. These were used for the geocoded images shown in Figs 5.6 and 5.7. The new extrusion is clearly visible in the center of the crater left by the January 6th explosion.

Supplementary information for Chapter 6: Tendürek volcano, Turkey

Topographic influence

We tested the modelling of only a sill under the realistic topography by using the BEM (BEM-sill in the following). Intriguingly, a result as good as that obtained by using the analytic rectangular dislocation in a homogeneous elastic half-space (Fig. S17) could not be achieved. In addition, there is a strong ring-like residual (Fig. S19).

To further estimate the influence of the topography, we used the BEM-sill parameters and calculated the synthetic LOS displacement velocities (Fig. S20) with respect to a flat surface at 1900 m above the mean sea level, which is the mean elevation at Tendürek. The difference between both forward models, the one with the real topography (Fig. S19b) and the one with the flat surface (Fig. S21b), is a measure for the synthetic line-of-sight (LOS) displacement velocity that is caused by neglecting the topography (Fig. S22). This shows that the inclusion of the realistic topography into the model set-up is very important, as it may account for up to 40 percent of the observed signal in this case.

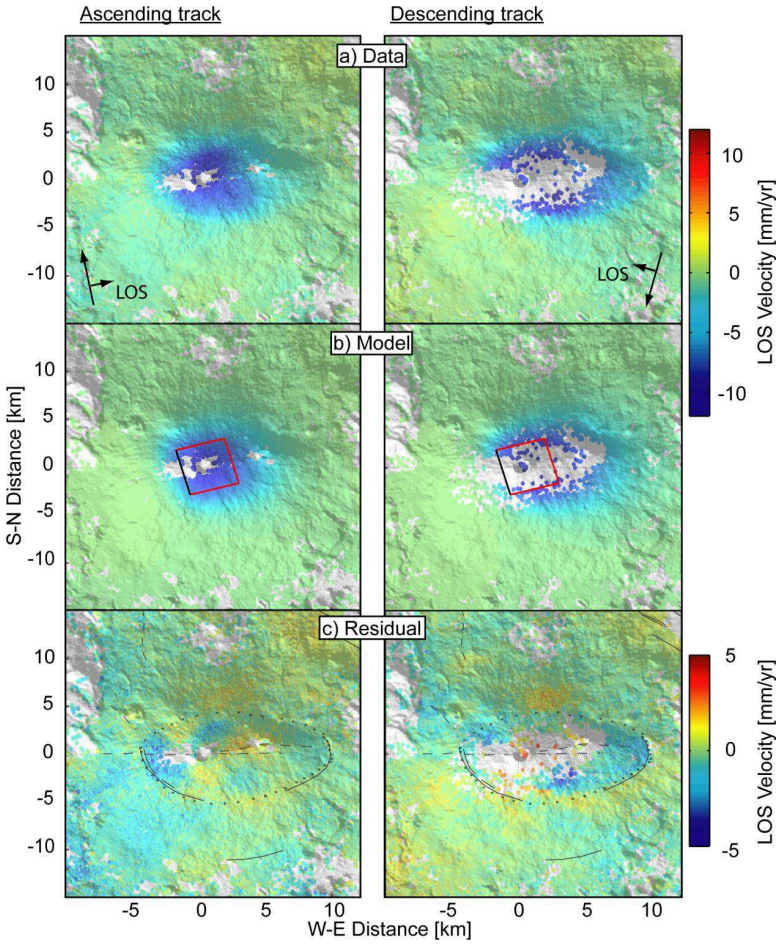

Figure S17: Optimum analytical rectangular sill model from Bathke et al. (2013): (a) Surface displacement velocity data from SBAS time-series analysis of Envisat data between 2004–2009 and 2003–2010 in the ascending and the descending track, respectively. (b) Synthetic surface displacement of the optimum sill-like deformation source model (rectangular dislocation) projected in the radar line-of-sight. The red quadrangle shows the approximate location and orientation of the optimum sill-like source; the black line marks the upper edge of the rectangular dislocation. (c) Residual displacements between observation and model. Light grey dots mark the surface trace of the inferred ring-fault (ring-like residual). Thin black lines mark inferred or observed faults from Fig. 6.1.

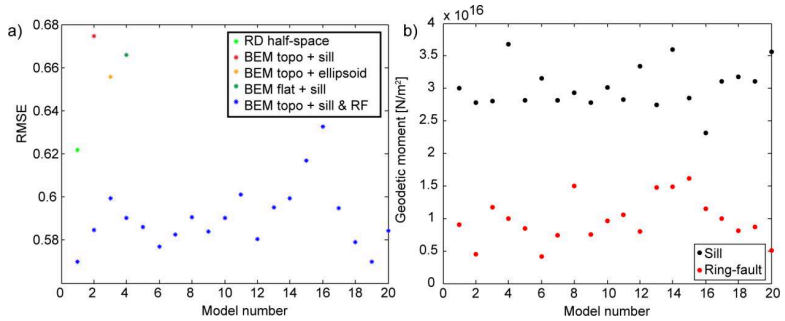

Figure S18: Modeling statistics: (a) Root mean square errors (RMSE) of the different models. Abbreviations: RD - rectangular dislocation, RF - ring-fault, topo - realistic topography, flat - no topography (b) Geodetic moments of the BEM sill vs. BEM ring-fault for all the optimizations.

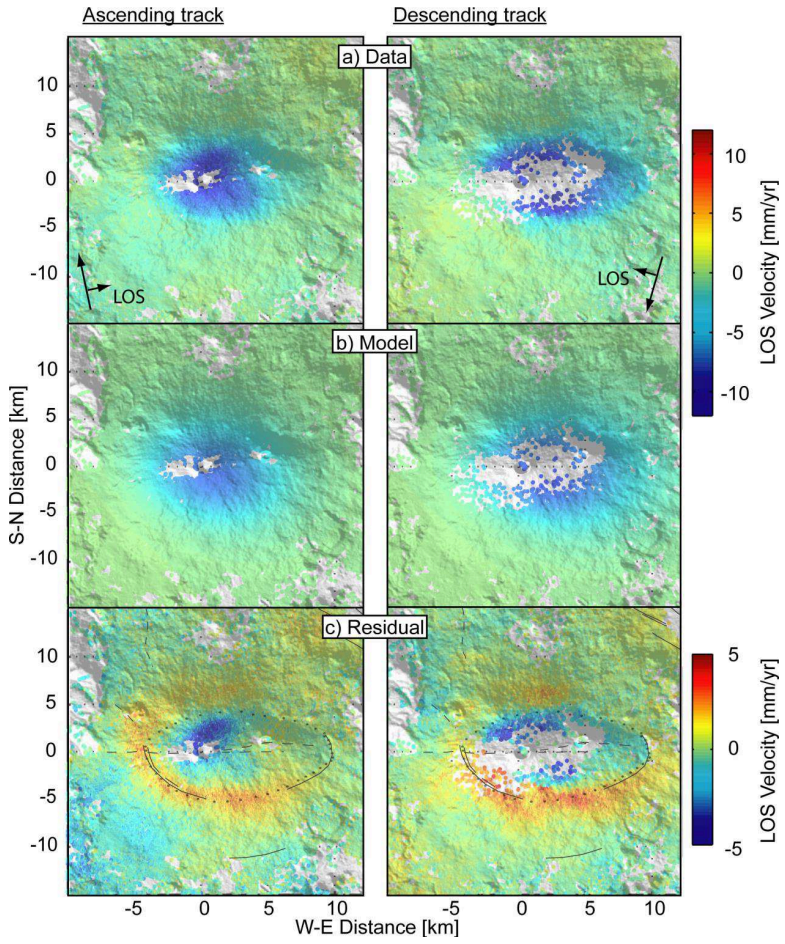

Figure S19: BEM sill only with realistic topography: (a) Surface displacement velocity data from SBAS time-series analysis of Envisat data between 2004–2009 and 2003–2010 in the ascending and the descending track, respectively. (b) Synthetic surface displacement, projected in the radar line-of-sight, of our optimum sill only BEM source model including realistic topography. (c) Residual displacements between observation and model. Light grey dots mark the surface trace of the inferred ring-fault. Thin black lines mark inferred or observed faults from Fig. 6.1.

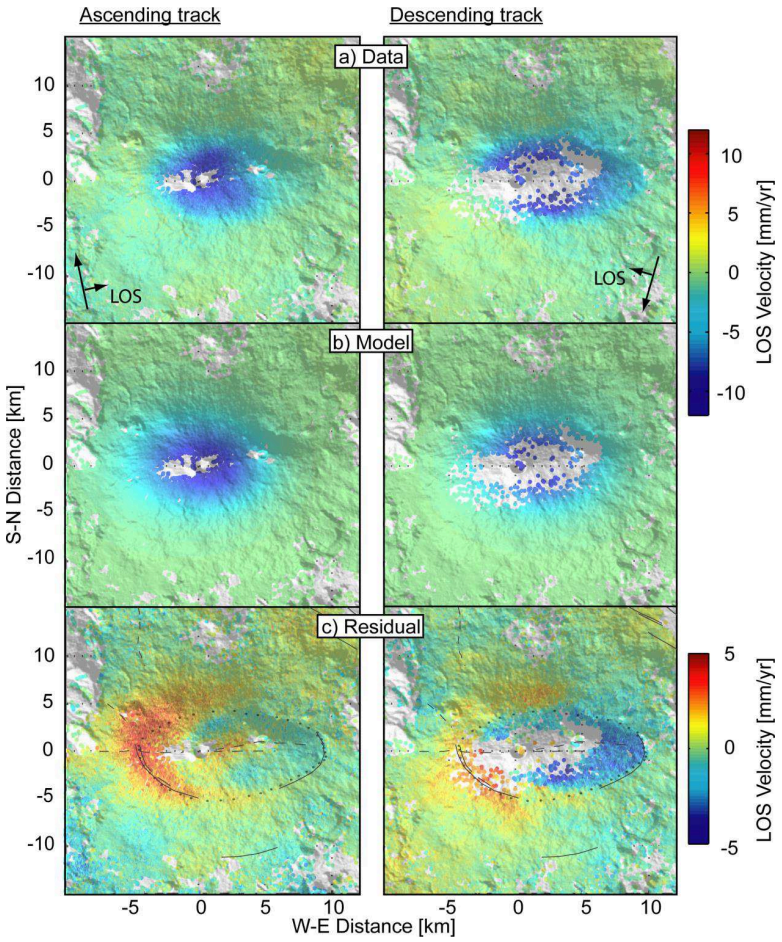

Figure S20: Ellipsoidal BEM source and realistic topography: (a) Surface displacement velocity data from SBAS time-series analysis of Envisat data between 2004–2009 and 2003–2010 in the ascending and the descending track, respectively. (b) Synthetic surface displacement, projected in the radar line-of-sight, of our optimum ellipsoidal BEM source model. (c) Residual displacements between observation and model. Light grey dots mark the surface trace of the inferred ring-fault. Thin black lines mark inferred or observed faults from Fig. 6.1.

Table S2: Dip angles of the ring-fault in the South, North, West and East quadrants (origin of the coordinate system in Fig. 6.5) based on the solutions of the different BEM models.

	South	North	West	East
Minimum	34	31	22	26
Optimum	64	67	35	46
Mean	62	63	42	43
Maximum	81	80	62	61
Orientation	outward	outward	outward	inward

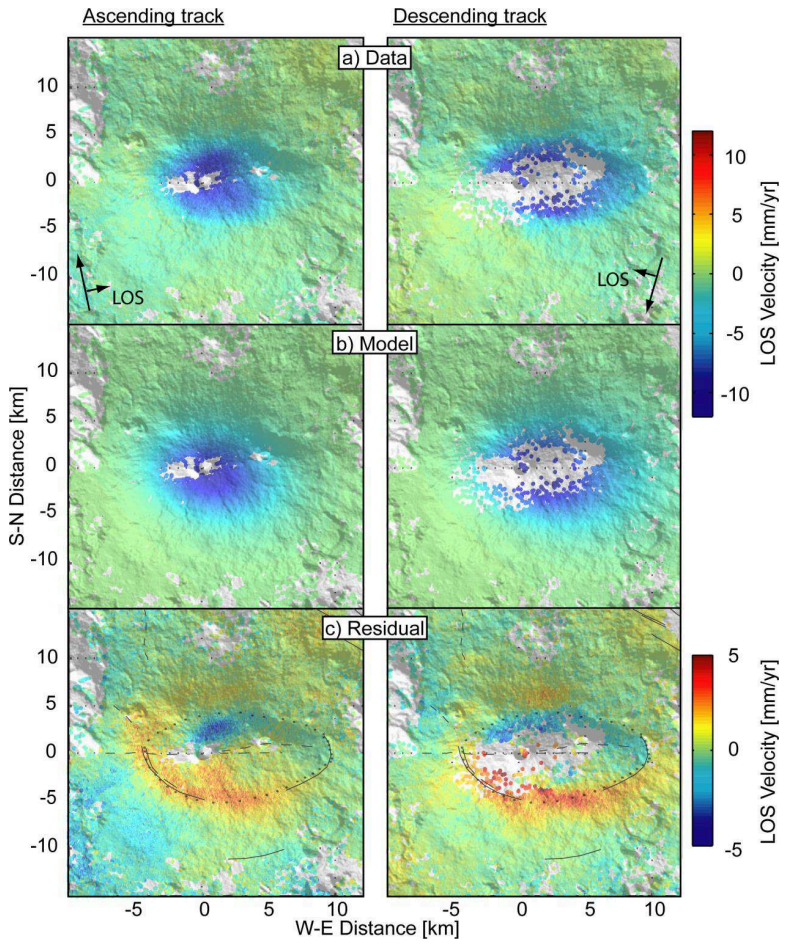

Figure S21: Flat topography and BEM sill: (a) Surface displacement velocity data from SBAS time-series analysis of Envisat data between 2004–2009 and 2003–2010 in the ascending and the descending track, respectively. (b) Synthetic surface displacement, projected in the radar line-of-sight, of our optimum sill-like BEM source model with respect to a flat surface at 1900 m above the mean sea level (mean elevation at Tendürek). (c) Residual displacements between observation and model. Light grey dots mark the surface trace of the inferred ring-fault. Thin black lines mark inferred or observed faults from Fig. 6.1.

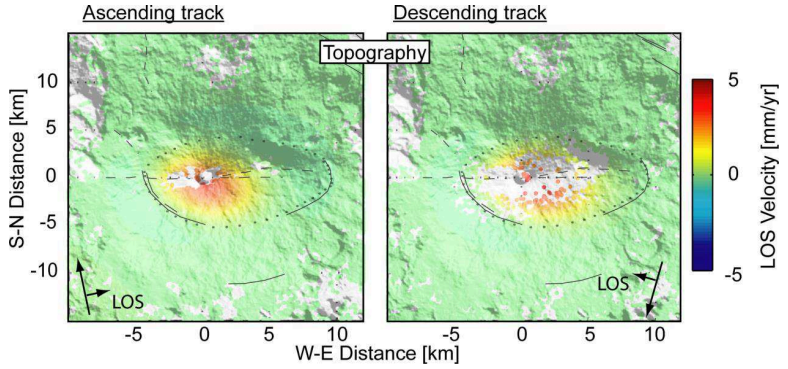

Figure S22: Topographic influence: Difference between synthetic surface displacements velocity of our BEM optimum sill like source shown in Fig. S19b (flat surface) and Fig. S18b (realistic topography). This is representative for the influence of the topography in the case of our optimum BEM sill-like source. Thin black lines mark inferred or observed faults from Fig. 6.1.

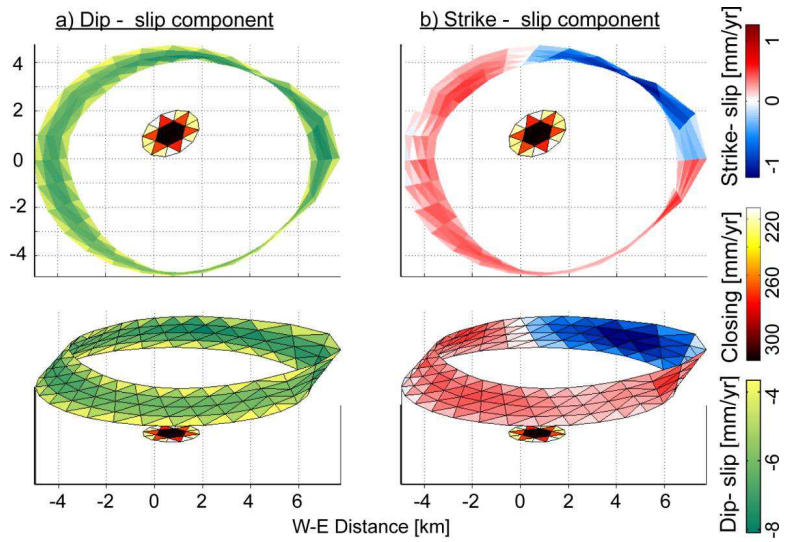

Figure S23: Slip distribution of a BEM model with a flat-lying sill-like source: (a) Dip- and (b) strike-slip components (dextral-blue, sinistral-red) of the displacement rate along the triangular dislocations of a ring-fault model with a horizontal sill. Also shown is the closing rate along the triangular dislocations of the sill.

Supplementary information for Chapter 7: Mt. Mantap nuclear test, North Korea

Synthetic Aperture Radar (SAR) image processing and 3-D displacement calculation

The Japanese ALOS-2, the European Sentinel-1A/B, and the German TerraSAR-X satellites all acquired SAR images spanning the sixth North Korean Nuclear Test (NKNT 6), conducted on 3 September 2017 at the Punggye-ri test site (Fig. S24 and Table S3). All these images are publicly available, either obtained free of charge (Sentinel-1) or via data allocations for scientific projects (ALOS-2 and TerraSAR-X). The resolution of Sentinel-1 data is too low to reveal any reliable information for this case.

A pair of ascending ALOS-2 images spanning the NKNT 6 was co-registered to generate an interferogram and a coherence map using our InSAR processing system (Wang et al., 2014; Jiang et al., 2017). The near-field interferometric phases are completely decorrelated due to the large displacement and substantial surface disturbance from the explosion, and therefore impossible to unwrap (Fig. S25A). Nevertheless, the level of coherence can be used to indicate the area of the surface disturbances caused by the explosion (Fig. S25B).

Four pairs of TerraSAR-X images from the German Aerospace Center (DLR) were processed to map the surface displacement associated with the underground nuclear test. Two pairs of TerraSAR-X Spotlight images covering the south part of the test area were acquired from ascending orbits (satellite travelling north) and descending orbits (satellite travelling south) with resolution of 1.1 m in azimuth and 0.45 m in range (the line-of-sight direction), and two additional pairs covering the whole test area were acquired from ascending and descending orbits with resolution of 1.1 m in azimuth and 0.9 m in range (For dataset information, see Fig. S24 and Table S3). These images provide a unique dataset to calculate a complete 3-D displacement map caused by the nuclear explosion (Fig. 7.1).

We co-registered the four datasets separately using their orbital information and a 30 m-resolution digital elevation model (DEM) from SRTM DEM (Wang et al., 2014). To estimate pixel offsets due to the explosion and possible subsequent collapse, we calculated the cross-correlation between distributed sub-images on the co-registered radar amplitude images. Cross-correlation windows with a dimension of 32-by-32 pixels were uniformly distributed to compute image offsets due to the explosion. The peak location in the obtained cross-correlation surface indicates the pixel offsets between the two sub-images in two dimensions (Michel et al., 1999). The TerraSAR-X range offsets from the ascending and descending orbit images measure ground displacement in their radar line-of-sight directions, which are about 34–48 degrees from the vertical with a component towards the west and east, respectively. The azimuth offsets measure along-track components, which are close to the north-south direction. We downsampled these offsets points using 200–250 m uniformly distributed grids to further improve the signal-noise-ratio. We calculated the standard deviation of offsets points outside of the disturbance area before and after downsampling (Table S3).

To calculate the 3-D displacement, we defined a grid with 300 m spacing across the test site. Values from the offsets along up to eight directions were combined to invert for the displacement in west-east, south-north and vertical directions for each grid element (Fig. 7.1 and Fig. S28) (Pathier et al., 2006; Wang and Jónsson, 2015). Where we have displacements from more than three independent measurements, we calculated the standard deviation from the residues of the 3-D displacement decomposition (Fig. S27). The 3-D displacement measurements were also decomposed along profiles into horizontal motions parallel to the profile and vertical dis-

placements (Fig. 7.1B and 7.1C). We then interpolated the 3-D displacement into a regular grid with 100 m resolution as shown in Fig. 7.2A and Fig. S26 with different components.

Dislocation modelling of the geodetic data

To infer the parameters of the deformation source associated with the 3 September 2017 underground nuclear test in North Korea, we applied the point-source version of the compound dislocation model (the point CDM; Nikkhoo et al., 2017) to the observed surface displacements. The point CDM is a half-space source model in which a flat free surface is implemented analytically. In principle, this procedure can be viewed as correcting the full-space solution for the free surface effect through adding some analytical correction terms to it. For irregular surface topographies, however, this needs to be performed numerically. For this purpose, we first simulated the surface topography as a continuous mesh of triangular dislocations (TDs; Nikkhoo and Walter, 2015). Then, using the TD mesh in a numerical scheme based on the boundary element method (BEM), we calculated the corrections that implement the effect of the realistic surface topography on the calculated surface displacements in our models (Crouch and Starfield, 1983; Kuriyama and Mizuta, 1993).

Also, through a minor modification in the point CDM formulation, we allowed for arbitrary positive and negative signs for the potencies. This way, one single point CDM was capable of simulating the superimposed effects of expansion and contraction due to the initial explosion and subsequent vertical collapse of the explosion chimney, respectively.

We used this source model in a non-linear inversion scheme based on the genetic algorithm (Holland, 1975; Haupt and Haupt, 2004) and inverted the surface displacements for the source parameters, including the horizontal location and depth as well as the potencies along the three axes of the source model (see Table S4). The presence of significant topographic effects in the surface displacements and accounting for these effects in the model provided strong constraints on the source depth in the inversions. The optimal model from this step fitted the best to the azimuthal offset data, yet the amplitude and extent of the model residuals for the range offsets were significant. This is because the azimuthal offsets exclusively depend on the horizontal displacements and the range offsets depend on both horizontal and vertical displacements.

The temporal resolution of our geodetic data, however, provides only a snapshot of the deformation signal, which is the superposition of the explosion, collapse and compaction processes. Therefore, the exact nature of the compaction source and its contribution to the total deformation signal cannot be resolved uniquely through inversions of the available geodetic data. However, we were able to simulate the general pattern of the deformation as a two-source model, one is the explosion plus collapse on the top, and the other is the compaction in a larger area (Fig. S29). Using numerical integration, we first extended the inferred point CDM to a finite ellipsoidal source which simulated the source of explosion and collapse with a better fit to the data. We then implemented a zone of compaction as a large ellipsoidal source, which surrounded the first inferred source of explosion and collapse. Best results were achieved for a large cavity of rather isotropic compaction, which contained almost the entire uppermost edifice of Mt. Mantap from the top to a few hundred meters below the inferred source of explosion and collapse (see Fig. 7.2, Fig. S29 and Table S5).

It must be noted that the incorporation of the source of compaction into the model did not significantly influence the inferred depth of the first source from the inversions, and was just to suggest one possible mechanism, which could explain the overall pattern of observed horizontal and vertical surface displacements in one framework under a few reasonable assumptions.

Relative relocation of the second event

We used regional waveform data recorded by a temporary broadband network installed in northeast China (Wang et al., 2016) and a few stations in the national broadband network of China and South Korea (Fig. 7.3A) to refine the location of the second event, relative to the epicentre of the main event. We used the main event epicentre location derived from the surface displacement field. Since the P-wave arrival times of the main event can be very well picked (Fig. S30), we firstly used these arrival picks to calibrate the paths and then applied the corrections to relocate the second event in a grid search optimization, similar to a master-event relocation, e.g., (Frémont and Malone, 1987). Because these two events are very close to each other, according to preliminary USGS reports, the master event approach is a good option for relocation. However, due to the coda wave from the main event, it is more difficult to pick the P-wave arrivals for the second event at these regional stations. To obtain reliable arrival picks, we filtered the data of the second event to relatively high frequency ranges (approximately 1.0 Hz and 8.0 Hz) to improve the picks (Fig. S31). With these picks, our relocation results using L1 and L2 norm for error calculation are shown in Fig. S32. Both results show that the second event is located about 700 m to the south of the main event, but the E-W component of the location estimates differ by ∼700 m. This difference is not unexpected, as the error ellipses are elongated in the E-W direction, primarily because there are no seismic stations in this direction. To better estimate the uncertainty of the relocation, we add random Gaussian noise to the arrival picks of the second event, assuming the maximum picking error of ±0.3 s. We repeat this process 1000 times and produce 1000 relocations (gray dots in Fig. S32), these locations also show elongated error ellipses (95 per cent confidence levels of the distributions) similar to that from the grid search result using original picks (background colour). We finally use the location from L1-normal solution for the second event (Fig. 7.3C in the main text).

Moment tensor inversion

To constrain the moment tensor solution of the main event, we conducted waveform inversion on the regional seismic waveform data using a generalized Cut-And-Paste method (gCAP; Zhu and Ben-Zion, 2013). The regional stations are the same as we used in the relocation procedure. We removed the instrument response from the raw data, converted the data into ground velocity, and then rotated the horizontal components into radial and tangential components. In the gCAP algorithm, the three-component waveform data at each station is cut into Pnl segments (vertical and radial components) and surface wave segments (vertical and radial component for Rayleigh wave and tangential component for Love wave), and fitted with the 1-D synthetics. Each component can have its own time shift to align the data and the synthetics, which can greatly reduce the sensitivity of the inversion to the imperfect velocity model. We used a modified 1-D velocity model for most of the stations, except BJT and HIA, for which we used the PREM model (Dziewonski and Anderson, 1981).

We filtered the Pnl waves to 0.01 Hz and 0.06 Hz and surface waves to 0.02 Hz and 0.045 Hz, which are the frequency ranges that can fit most of the components with decent cross-correlation coefficients (>0.9 on average). During the inversion, we experimentally place the source at the depth of 450 m as constrained by the geodetic data modelling, and grid searched for the best percentage of the deviatoric CLVD component (compensated linear vector dipole Knopoff and Randall, 1970), and isotropic volume-change component (Fig. S33). Our inversion result prefers a large percentage (80 per cent) of the positive isotropic component (explosion) in the full moment tensor solution and a total moment magnitude of 5.24 (Fig. S34). However, the waveforms cannot be fitted well if we assume a 100 per cent isotropic source (Fig. S33). The CLVD indicates a component of collapse in the vertical direction. Possible causes include: 1) triggering of

tectonic faults, 2) heterogeneous stress in the source region, 3) non-elastic deformation, 4) 3-D velocity structure and topography effects. Because the non-isotropic component is very small, it is difficult to distinguish the contribution of these factors with the data we have. Also note that there are some trade-offs between isotropic and the CLVD component (Fig. S33).

To test the impact of topography, we also use Spectral Element Method (SEM) (Tromp et al., 2008) to simulate 3-D synthetics with topography imposed on a background 1-D velocity model (Fig. S35). We place a pure explosion source at the depth of 450 m and generate synthetics at the stations used in the moment tensor inversion. We filter both the 3-D and 1-D synthetics to the same frequency ranges as we used in the inversion and display one of example station (EW06) in Fig. S36. As shown, the difference between the 3-D and 1-D synthetics in tangential component is very small at this frequency range, primarily because the corresponding wavelength (tens of kilometres) is much longer than that in the topography features (a few kilometres).

Similar to the P-wave arrival picks, the full moment tensor inversion of the second event is also more difficult due to the coda from the first event. With careful selection of the waveform components and frequency ranges, we can still obtain good fits for the Rayleigh waves at more than 10 stations, in particular for the vertical component (Fig. S38). A grid search for the isotropic and CLVD components of the second event indicates strong trade-offs between the two components, and the inversion did not converge as good as for the first event and the variance reduction is apparently lower (Fig. S38). Despite more local minimums present in the Hudson source type plot, the inversion still shows a concentration of minimums near a strong negative isotropic component value (about -55 per cent, implosion) with a moment magnitude of 4.5 (Fig. S37). To verify this result we multiplied the amplitude of the vertical-component waveforms of the second event by a factor of -60 (note the sign flip), and compared them with the waveforms of the first event at higher frequencies (∼0.2–0.9 Hz). The result (Fig. S39) shows very high waveform cross-correlation coefficients, even for some coda waves. The strong similarity of the flipped high-frequency waveforms therefore provides additional evidence for a large negative isotropic component of the second event, as well as for the close proximity of the two events.

Source radius and yield estimation

We considered the uncertainty in the isotropic scalar moment in estimating the source radius and explosive yield. First, all solutions fitting within 95 per cent of the best fitting solution (e.g., Figure S33) were tabulated, and then the mean and standard deviation were estimated. The mean and standard deviation of the isotropic moment was determined to be M_w =5.05 ± 0.13 N m. Using the relationship, $M_0^{ISO} = (\lambda + 2\mu)\,\delta V$ and the equation for the volume of a sphere, where the two Lame coefficients are assumed from the V_p, V_s and density values from model MDJ2 (Ford et al., 2009) the cavity radius is estimated to be 51 m.

It should be noted that the larger source radius of the geodetic modelling is the result of the integrative effect of all of the deformation processes that affect the surface displacement field, namely the explosion, collapse and compaction, as discussed in the paper. There are some trade-offs between the inferred parameters of the sources in the deformation model. The trade-offs could result in an overestimation of the geodetically estimated volume. Therefore, we did not use the radius derived from this volume for yield estimation. The seismic data have the resolution for separating the explosion and collapse precisely. Also, the isotropic moment is determined by inverting the regional waveform assuming different source depths. When the source is located at 600 m, we got very similar total moment as the other depth, however, the

isotropic percentage is smaller, therefore the corresponding isotropic moment is also smaller, resulted in smaller yield than depth of 450 m shown in Fig. 7.3E.

The Denny and Johnson (1991) model (see also Ford and Walter, 2013) relates the explosive yield to the isotropic scalar seismic moment, the V_p, V_s and density at the source, the overburden pressure and the gas porosity of the medium. We have assumed the MDJ2 model (Ford et al., 2009) for the elastic parameters, the overburden pressure is based on the best fitting geodetic centroid of 450 m. The medium in which the device was detonated is likely the granodiorite that lies beneath the stratified volcanic rocks that make up higher elevations of Mt. Mantap. We assumed a gas porosity of 1 per cent for granitic rocks (Springer, 1966). For the mean isotropic scalar moment of solutions fitting within 95 per cent of the best fit solution at 450 m depth the explosive yield is estimated to be 191 kt, with a 1 standard deviation range of 120 to 304 kt. Our preferred explosive yield for the event is 191 kt from the mean of acceptable solutions, however for completeness the yield of the best fitting solution (isotropic $M_w = 5.15$) is 265 kt.

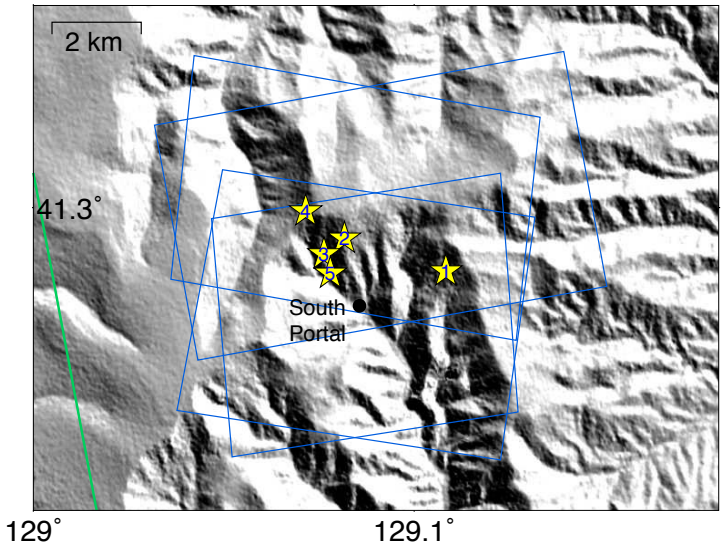

Figure S24: Punggye-ri nuclear test site with datasets. Green lines indicate the coverage of Japanese ALOS-2 and German TerraSAR-X image coverages respectively. Yellow stars indicate the locations of NKNT 1–5 from IRIS (2017); Wen and Long (2010); Zhang and Wen (2013); Wei (2017), respectively.

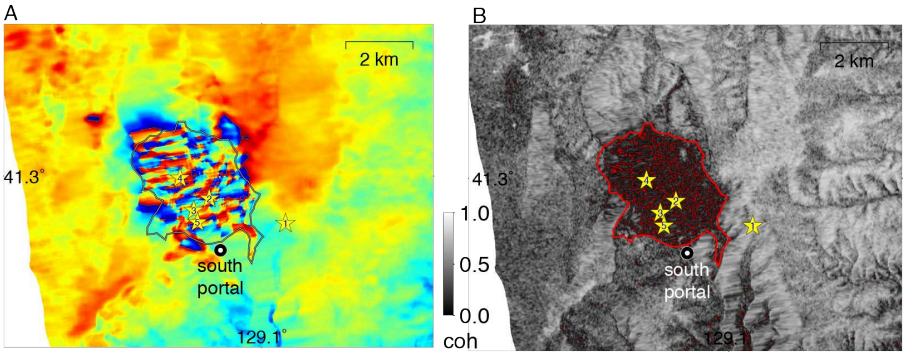

Figure S25: ALOS-2 interferogram (A) and coherence map (B). Yellow stars indicate the location of NKNT 1–5. Black circle is south portal. Red dots are low coherence pixels, from which the boundary polygon (red lines) was calculated.

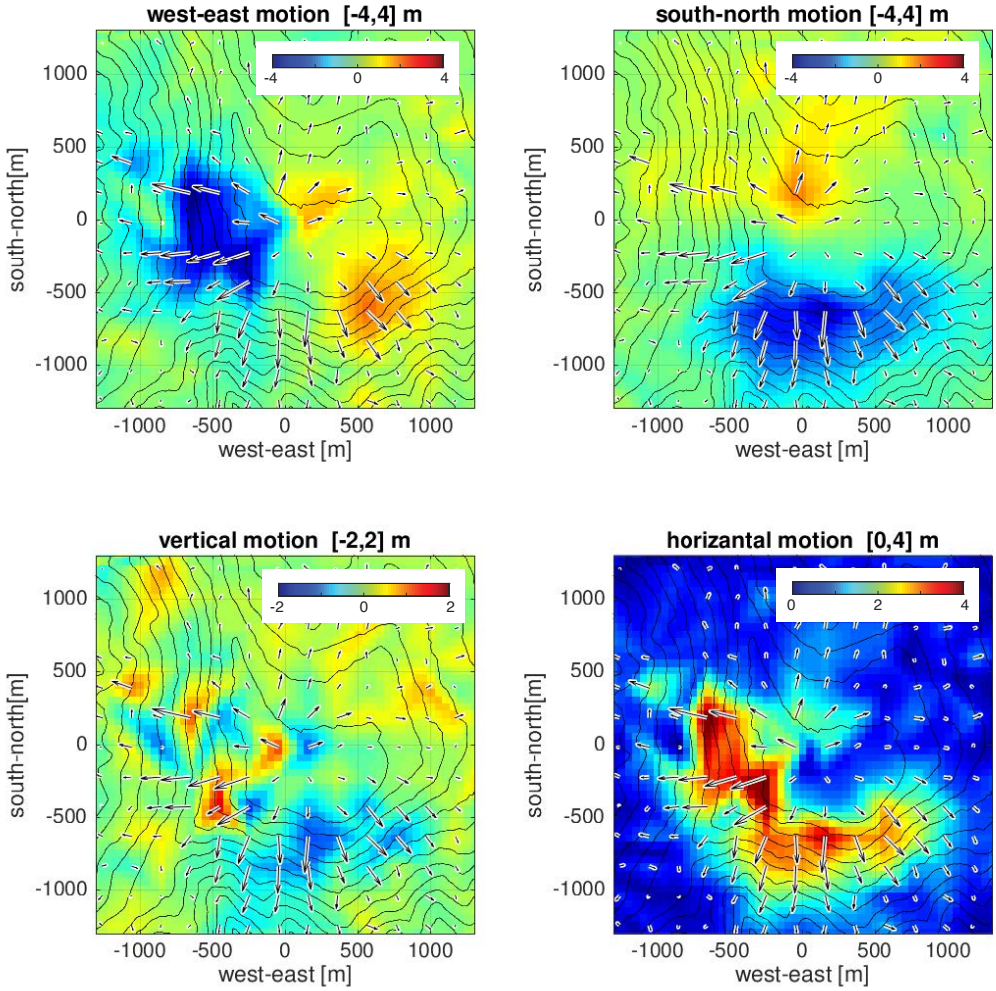

Figure S26: Horizontal and vertical displacements of grid-points spaced 100 m apart obtained from pixel offsets of four pairs of ascending and descending orbit TerraSAR-X images spanning NKNT 6 with topographic contours.

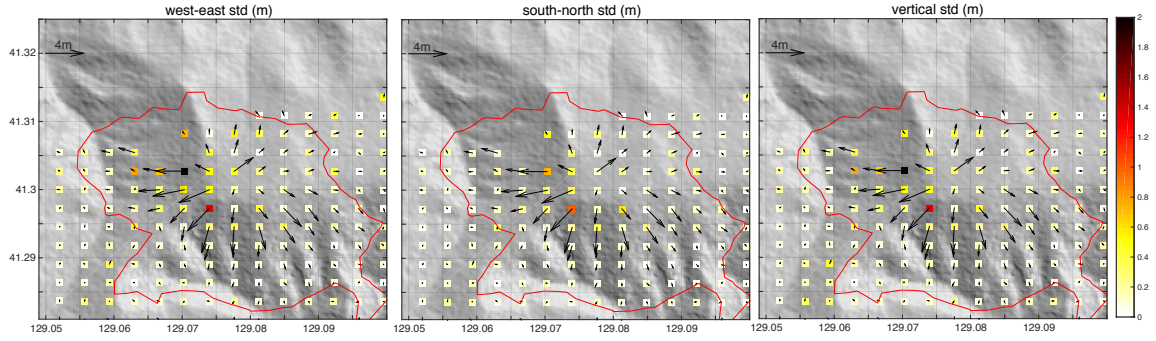

Figure S27: Standard deviations derived from the 3-D displacement decomposition. Note that only patches with measurements from more than 3 independent directions can be used to calculate residual standard deviations.

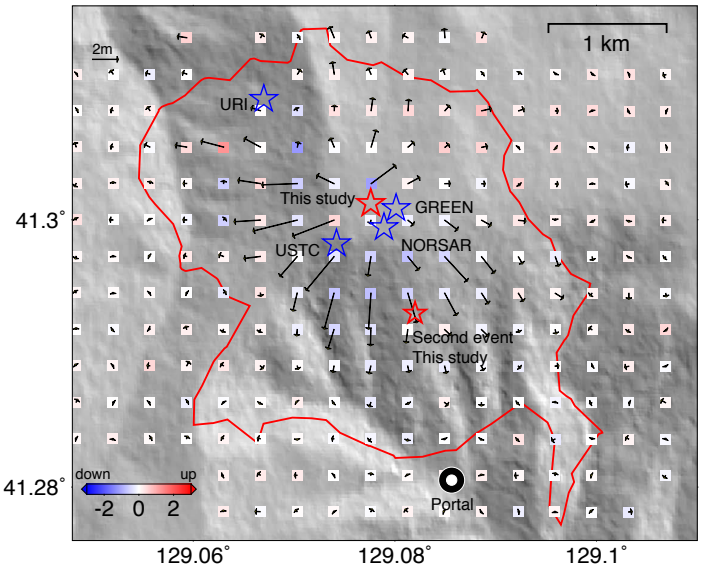

Figure S28: 3-D displacements calculated within 300 × 300 m grid before interpretation plotted with locations published from other institutes and this study. Locations are inferred from http://weilab.uri.edu/nk6/.

Table S3: SAR images processed. AT means ascending tracks, DT means descending tracks.

Satellites	Track	Resolution Az/Ra	Incidence Angle	Date yyyymmdd	useful information	3D/model
TerraSAR-X	DT88	1.1 m 0.45 m	48.3°	20170824 20170904	Azimuth offsets Range offsets	Azimuth offsets Range offsets
TerraSAR-X	AT111	1.1 m 0.45 m	46.2°	20170826 20170906	Azimuth offsets Range offsets	Azimuth offsets Range offsets
TerraSAR-X	DT164	1.1 m 0.86 m	35.6°	20170602 20170909	Azimuth offsets Range offsets	Azimuth offsets Range offsets
TerraSAR-X	AT35	1.1 m 0.86 m	33.7°	20170605 20170912	Azimuth offsets Range offsets	Azimuth offsets Range offsets
ALOS-2	AT130	5 m 6 m	36.3°	20170727 20170907	coherence	–

Table S4: Source parameters of an axi-symmetric point CDM ($\Delta V_x = \Delta V_y$) under realistic topography. "H" is the elevation of the source above mean sea level (MSL). The reference location is 129.077 598°E, 41.300 653°N.

E (km)	N (km)	H (km)	Potency $\Delta V_x = \Delta V_y$ (km^3)	Potency ΔV_z (km^3)
0.050	-0.150 (±50 m)	1.743 (±100 m)	0.003056	-0.000187

Table S5: Source parameters of the two deformation sources in the finite-source model. The centroids of both sources have the same coordinates as the point CDM in Table S4.

Source	Semi-major axes (m)	Potency ΔV_X (km^3)	Potency ΔV_Y (km^3)	Potency ΔV_Z (km^3)
Explosion and collapse	$a_X = a_Y = 300$ $a_Z = 300$	0.009008	0.007862	0.001288
Compaction	$a_X = a_Y = 800$ $a_Z = 460$	-0.006407	-0.004498	-0.005396

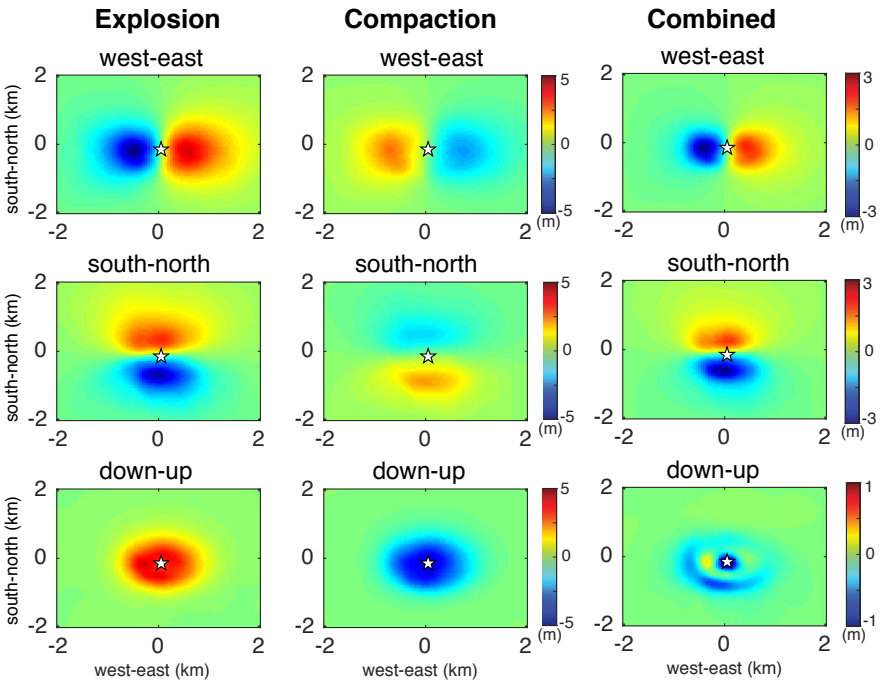

Figure S29: 3-D displacements predicted from our elastic model with explosion/collapse source, compaction source, and two sources combined.

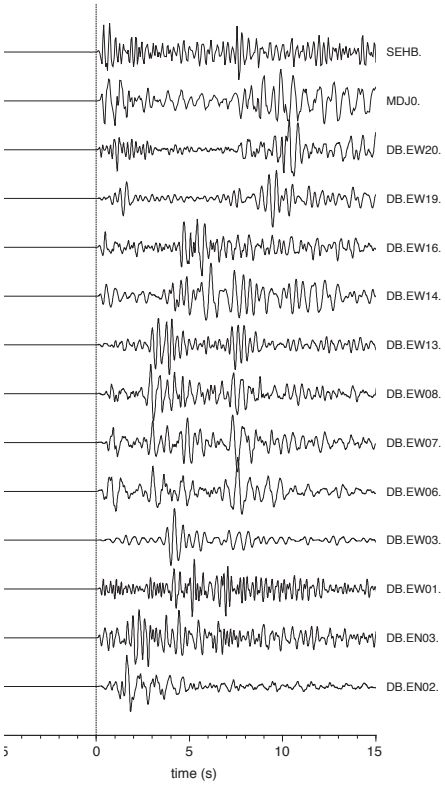

Figure S30: P-wave first arrival picks for the first event on the vertical components. The station names are indicated at the end of each seismogram.

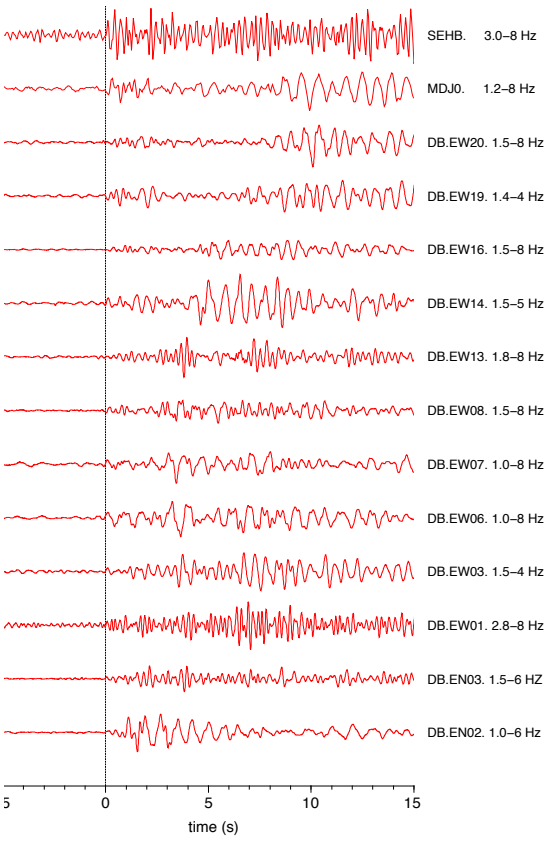

Figure S31: P-wave first arrival picks for the second event. Note that the waveform data has been filtered to relatively high frequency ranges (∼1–8 Hz) shown to the right of each trace.

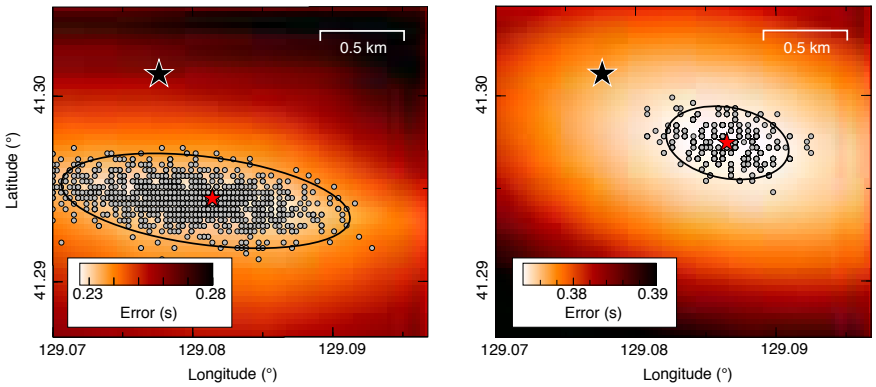

Figure S32: Relative relocation results of the second event by using path calibrations from the first event. The error of L1 and L2 norms are shown in the left and right, respectively. The black star indicates the epicentre location of the first event based on the deformation data, which is also the reference location. The red star shows the preferred location of the second event determined by grid search. The gray dots are the grid search results using the perturbed arrival times of the second event, assuming a random Gaussian distribution error in arrival time picks. We assume the maximum picking error is ±0.3 s, and the sampling process was conducted 1000 times (corresponding to 1000 gray dots). The ellipses represent the 95 per cent confidence levels of the distributions of gray dots.

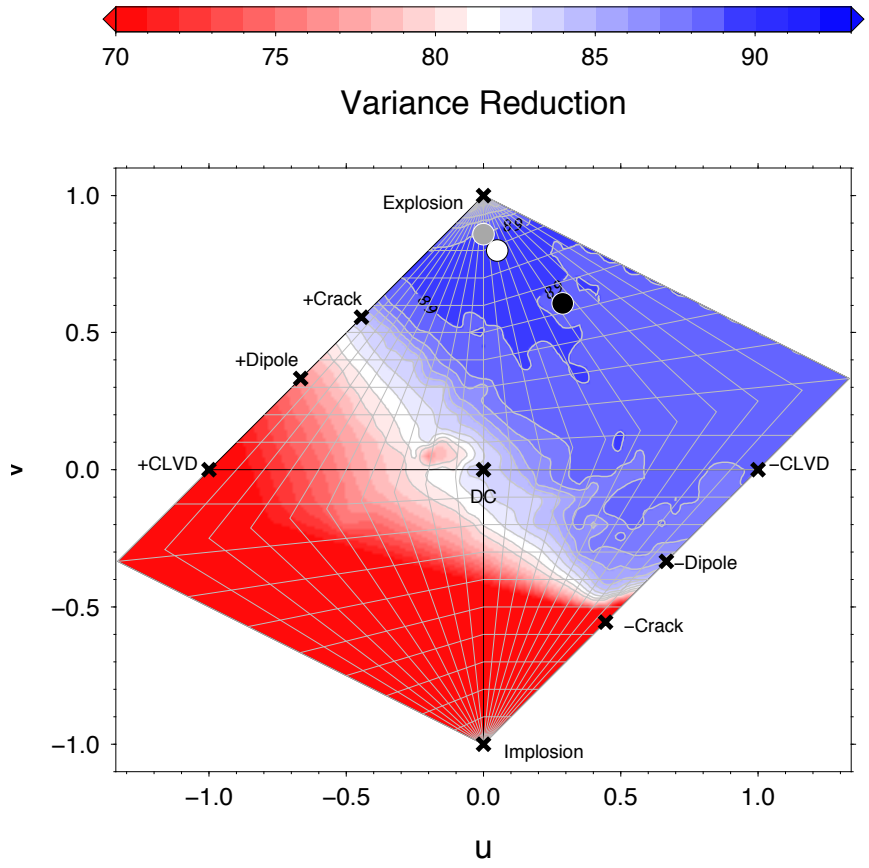

Figure S33: Grid search results for the CLVD and isotropic components of the first event using GCAP method. The Variance Reduction (VR) from the inversion is color coded on the Hudson source type plot (Hudson et al., 1989). The white circle indicates the preferred moment tensor (see more details of moment tensor and waveform fits in Fig. S34). The black dot displays the preferred moment tensor solution from Liu et al. (2018), the gray dot displays the moment tensor from an independent inversion result reported during AGU meeting 2017 (Dreger et al., Source-Type Inversion of the September 03, 2017 DPRK Nuclear Test 2017).

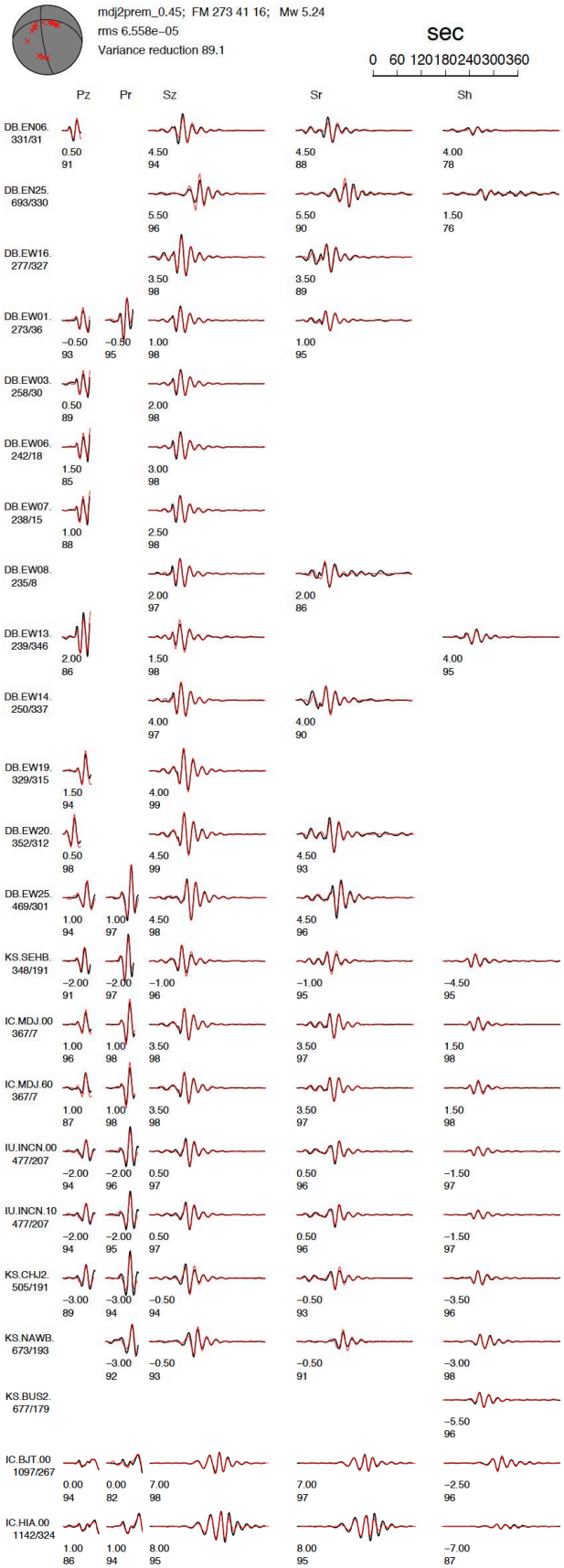

Figure S34: Waveform fits for the preferred moment tensor solution for the second event. Stations names are indicated at the beginning of waveform comparisons, with epicentre distance (front) and azimuth (back) shown below the station name. Black traces are observed waveforms and red traces are predicted waveforms. The numbers below each waveform segment are time shift in seconds and waveform cross-correlation coefficient in percentage.

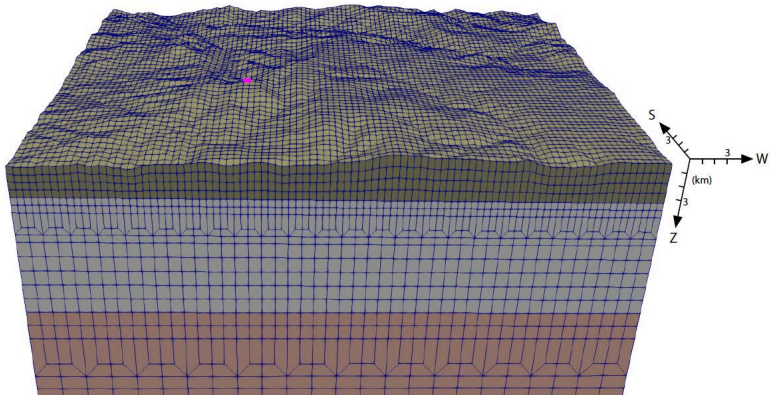

Figure S35: A portion of velocity model set-up for the 3-D Spectral Element Method (SEM) simulations with topography. The pink dot represents the epicentre location used for the simulation. A 1-D velocity model (MDJ2 model (Ford et al., 2009)) is used as the background model.

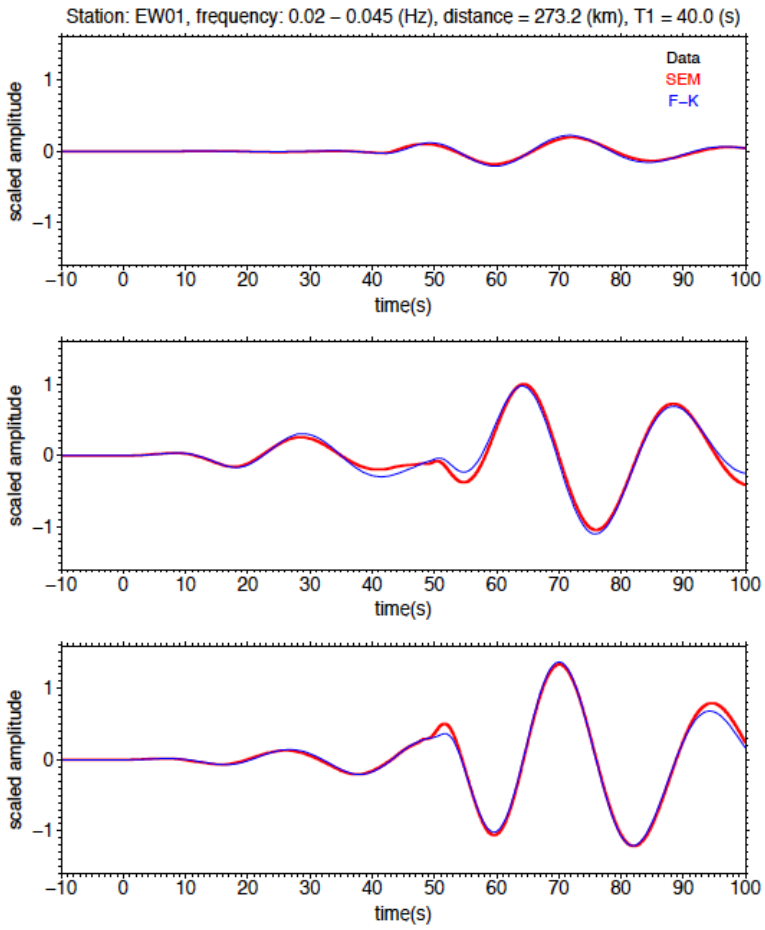

Figure S36: Waveform comparisons between the three component 3-D synthetics (red) with topography and 1-D synthetics (blue). Note the very small difference in the tangential component.

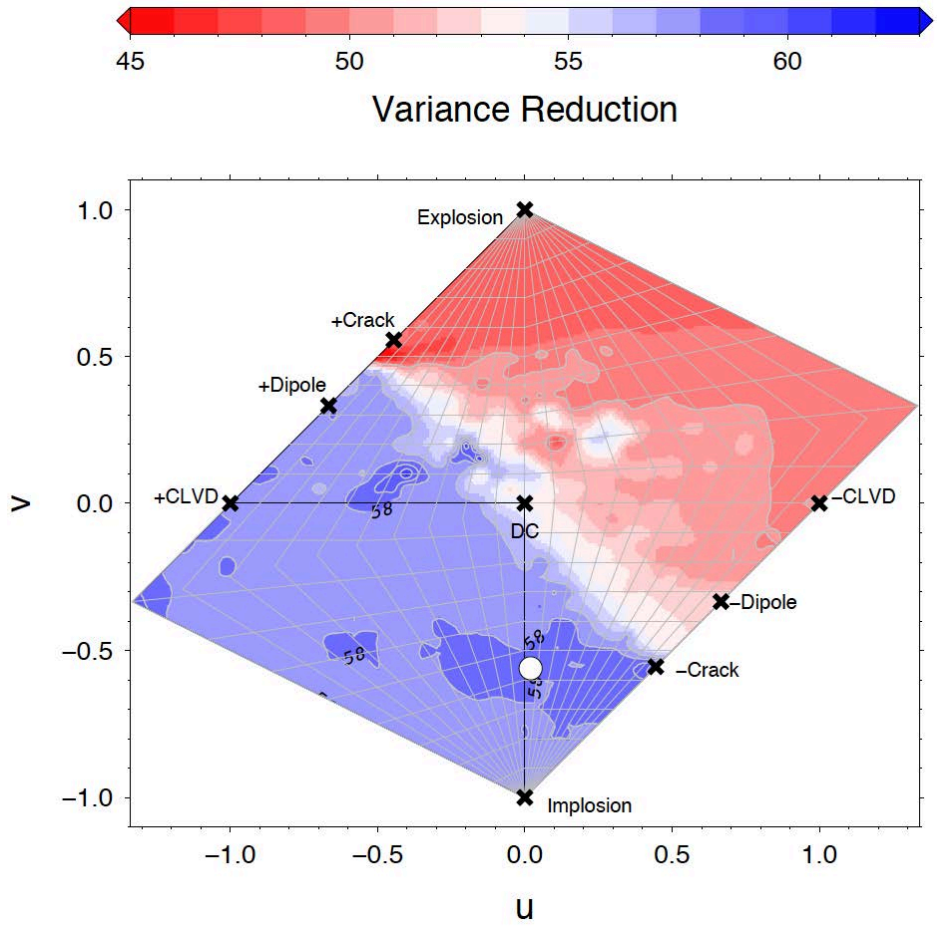

Figure S37: Grid search results for the CLVD and isotropic components of the second event using GCAP method. The Variance Reduction (VR) from the inversion is color coded on the Hudson source type plot (Hudson et al., 1989). The white circle indicates the preferred moment tensor (see more details of moment tensor and waveform fits in Fig. S38).

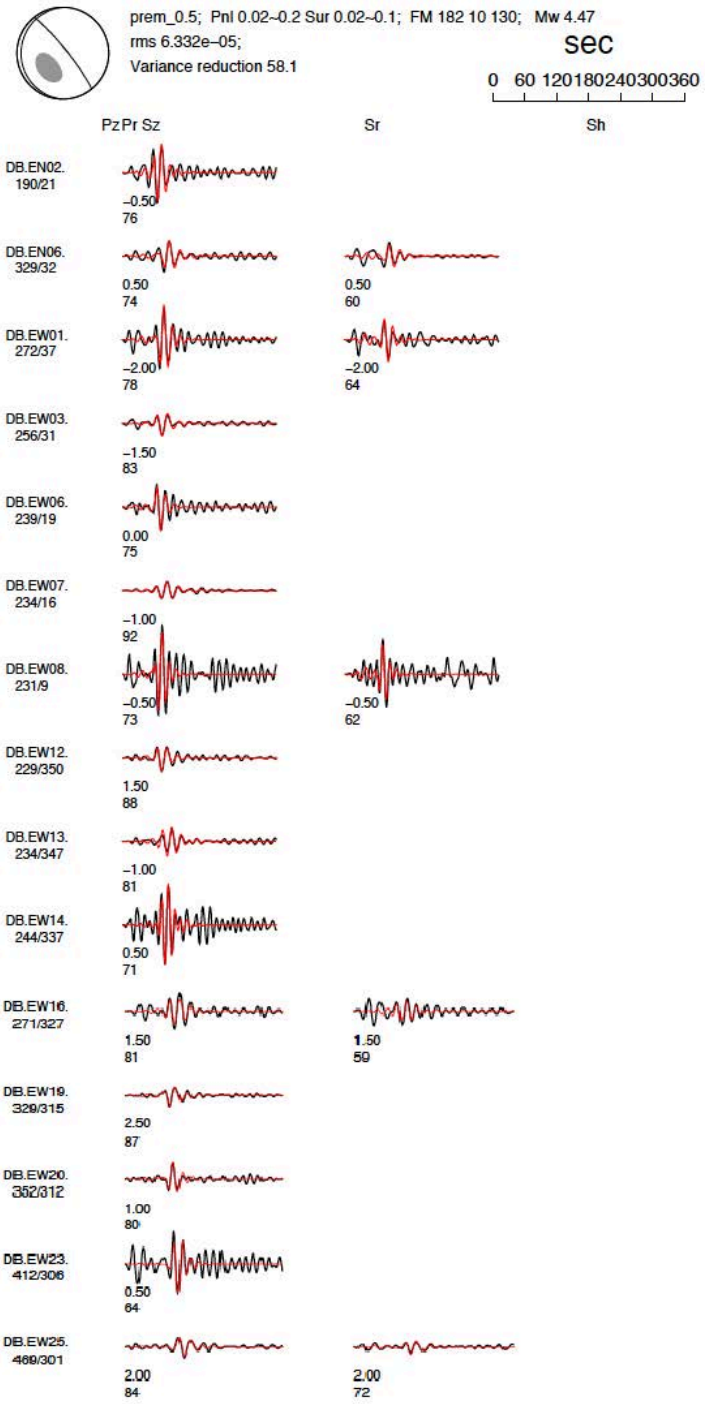

Figure S38: Waveform fits for the preferred moment tensor solution for the second event. Stations names are indicated at the beginning of waveform comparisons, with epicentre distance (front) and azimuth (back) shown below the station name. Black traces are observed waveforms and red traces are predicted waveforms. The numbers below each waveform segment are time shift in seconds and waveform cross-correlation coefficient in percentage.

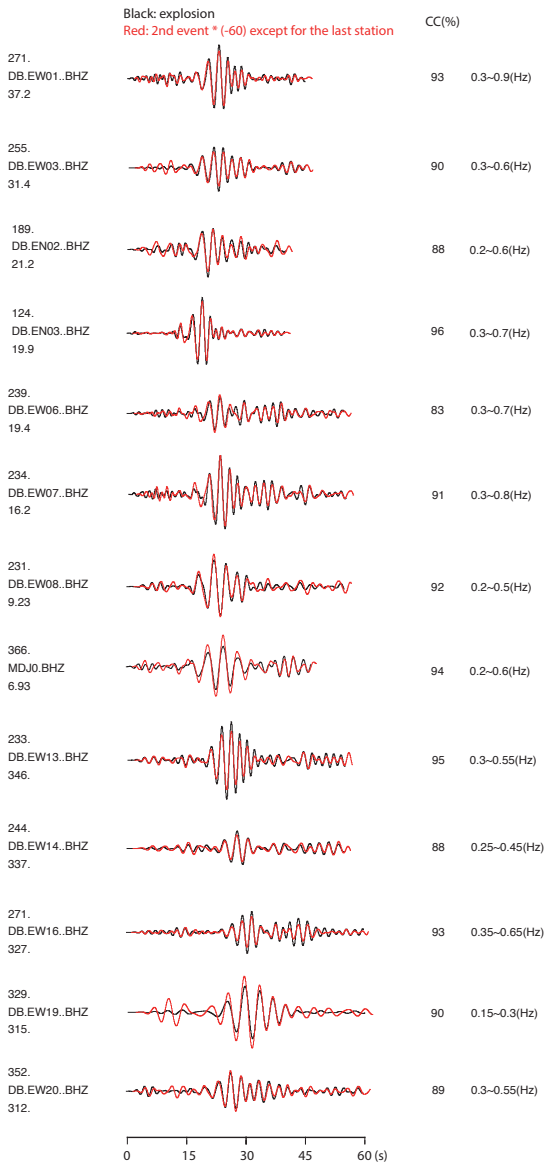

Figure S39: Vertical component waveform comparison between the first and the second event. Here the sign of the second event waveforms are flipped and the amplitude is enlarged by a factor of 60. The station names are shown at the beginning of each waveform pair with azimuth (in degree) and distance (in km) shown at the bottom and top, respectively. The waveform cross-correlation coefficients in percent and frequency ranges are displayed to the right of each trace.

Bibliography

Acocella, V. (2007). Understanding caldera structure and development: An overview of analogue models compared to natural calderas. *Earth-Science Reviews*, 85(3):125 – 160.

Agram, P. S., Jolivet, R., Riel, B., Lin, Y. N., Simons, M., Hetland, E., Doin, M. P., and Lasserre, C. (2013). New Radar Interferometric Time Series Analysis Toolbox Released. *EOS Transactions*, 94:69–70.

Agusto, M., Tassi, F., Caselli, A., Vaselli, O., Rouwet, D., Capaccioni, B., Caliro, S., Chiodini, G., and Darrah, T. (2013). Gas geochemistry of the magmatic-hydrothermal fluid reservoir in the Copahue-Caviahue Volcanic Complex (Argentina). *Journal of Volcanology and Geothermal Research*, 257(Supplement C):44–56.

Aki, K. and Richards, P. G. (2002). *Quantitative Seismology*. University Science Books, Saualito, California, second edition.

Albino, F. and Sigmundsson, F. (2014). Stress transfer between magma bodies: Influence of intrusions prior to 2010 eruptions at Eyjafjallajökull volcano, Iceland. *Journal of Geophysical Research: Solid Earth*, 119(4):2964–2975.

Amelung, F., Jónsson, S., Zebker, H., and Segall, P. (2000). Widespread uplift and 'trapdoor' faulting on Galápagos volcanoes observed with radar interferometry. *Nature*, 407:993–996.

Anderson, E. M. (1936). The Dynamics of the Formation of Cone-sheets, Ring-dykes, and Caldron-subsidences. *Proceedings of the Royal Society of Edinburgh*, 56:128–157.

Anderson, K., Lisowski, M., and Segall, P. (2010). Cyclic ground tilt associated with the 2004-2008 eruption of Mount St. Helens. *Journal of Geophysical Research: Solid Earth*, 115(B11). B11201.

Arámbula-Mendoza, R., Lesage, P., Valdés-González, C., Varley, N. R., Reyes-Dávila, G., and Navarro, C. (2011). Seismic activity that accompanied the effusive and explosive eruptions during the 2004-2005 period at Volcán de Colima, Mexico. *Journal of Volcanology and Geothermal Research*, 205(1):30–46.

Auker, M. R., Sparks, R. S. J., Siebert, L., Crosweller, H. S., and Ewert, J. (2013). A statistical analysis of the global historical volcanic fatalities record. *Journal of Applied Volcanology*, 2(1).

Bagnardi, M. and Amelung, F. (2012). Space-geodetic evidence for multiple magma reservoirs and subvolcanic lateral intrusions at Fernandina Volcano, Galápagos Islands. *Journal of Geophysical Research: Solid Earth*, 117(B10). B10406.

Bagnardi, M., Amelung, F., and Poland, M. P. (2013). A new model for the growth of basaltic shields based on deformation of Fernandina volcano, Galápagos Islands. *Earth and Planetary Science Letters*, 377-378(Supplement C):358–366.

Balbis, C., Petrinovic, I. A., and Guzmán, S. (2016). A contribution to the hazards assessment at Copahue volcano (Argentina-Chile) by facies analysis of a recent pyroclastic density current deposit. *Journal of Volcanology and Geothermal Research*, 327:288–298.

Bamler, R. and Eineder, M. (2005). Accuracy of Differential Shift Estimation by Correlation and Split-Bandwidth Interferometry for Wideband and Delta-k SAR Systems. *IEEE Geoscience and Remote Sensing Letters*, 2(2):151–155.

Bathke, H., Shirzaei, M., and Walter, T. R. (2011). Inflation and deflation at the steep-sided Llaima stratovolcano (Chile) detected by using InSAR. *Geophysical Research Letters*, 38(10). L10304.

Bathke, H., Sudhaus, H., Holohan, E., Walter, T. R., and Shirzaei, M. (2013). An active ring fault detected at Tendürek volcano by using InSAR. *Journal of Geophysical Research: Solid Earth*, 118(8):4488–4502.

Battaglia, M., Gottsmann, J., Carbone, D., and Fernández, J. (2008). 4D volcano gravimetry. *Geophysics*, 73(6):WA3–WA18.

Battaglia, M., Roberts, C., and Segall, P. (1999). Magma Intrusion Beneath Long Valley Caldera Confirmed by Temporal Changes in Gravity. *Science*, 285(5436):2119–2122.

Battaglia, M. and Segall, P. (2004). The Interpretation of Gravity Changes and Crustal Deformation in Active Volcanic Areas. *pure and applied geophysics*, 161(7):1453–1467.

Bean, C. J., De Barros, L., Lokmer, I., Métaxian, J.-P., O'Brien, G., and Murphy, S. (2014). Long-period seismicity in the shallow volcanic edifice formed from slow-rupture earthquakes. *Nature Geoscience*, 7:71–75.

Beauducel, F., Cornet, F. H., Suhanto, E., Duquesnoy, T., and Kasser, M. (2000). Constraints on magma flux from displacements data at Merapi volcano, Java, Indonesia. *Journal of Geophysical Research: Solid Earth*, 105(B4):8193–8203.

Beauducel, F., De Natale, G., Obrizzo, F., and Pingue, F. (2004). *3-D Modelling of Campi Flegrei Ground Deformations: Role of Caldera Boundary Discontinuities*, pages 1329–1344. Birkhäuser Basel.

Bernstein, M., Pavez, A., Varley, N., Whelley, P., and Calder, E. (2013). Rhyolite lava dome growth styles at Chaitén Volcano, Chile (2008-2009): Interpretation of thermal imagery. *Andean Geology*, 40(2):295–309.

Bilham, R. (2013). Societal and observational problems in earthquake risk assessments and their delivery to those most at risk. *Tectonophysics*, 584:166–173.

Bonaccorso, A. and Davis, P. M. (1999). Models of ground deformation from vertical volcanic conduits with application to eruptions of Mount St. Helens and Mount Etna. *Journal of Geophysical Research: Solid Earth*, 104(B5):10531–10542.

Bonafede, M., Dragoni, M., and Quareni, F. (1986). Displacement and stress fields produced by a centre of dilation and by a pressure source in a viscoelastic half-space: application to the study of ground deformation and seismic activity at Campi Flegrei, Italy. *Geophysical Journal of the Royal Astronomical Society*, 87(2):455–485.

Bonafede, M. and Ferrari, C. (2009). Analytical models of deformation and residual gravity changes due to a Mogi source in a viscoelastic medium. *Tectonophysics*, 471(1-2):4–13.

Bonali, F. (2013). Earthquake-induced static stress change on magma pathway in promoting the 2012 Copahue eruption. *Tectonophysics*, 608:127–137.

Bonali, F., Tibaldi, A., and Corazzato, C. (2015). Sensitivity analysis of earthquake-induced static stress changes on volcanoes: the 2010 Mw 8.8 Chile earthquake. *Geophysical Journal International*, 201(3):1868–1890.

Bonali, F. L., Corazzato, C., Bellotti, F., and Groppelli, G. (2016). *Active Tectonics and Its Interactions with Copahue Volcano*, pages 23–45. Springer Berlin Heidelberg.

Bottema, O. (2008). *Topics in Elementary Geometry*. Springer Science+Business Media, LLC.

Boussinesq, J. V. (1878). Équilibre élasticité d'un solide isotrope de masse négligeable, soumis à différents poids [Elastic equilibrium of a waitless isotropic solid under various loads]. *Comptes rendus de l'Académie des Sciences*, 86:1260–1263.

Bradley, A. M. and Segall, P. (2012). BEM simulation of Earth deformation, H-matrices and Green's functions. *AGU 2012, Poster T13E-2668*.

Bretón González, M., Ramírez, J. J., and Navarro, C. (2002). Summary of the historical eruptive activity of Volcán De Colima, Mexico 1519-2000. *Journal of Volcanology and Geothermal Research*, 117(1):21–46.

Brown, R. L. J. (1975). *A dislocation approach to plate interaction*. PhD thesis, Massachusetts Institute of Technology.

Brown, S. K., Auker, M., and Sparks, R. (2015). *Populations around Holocene volcanoes and development of a Population Exposure Index*, pages 223–232. Cambridge University Press.

Burgers, J. M. (1939). Some considerations on the fields of stress connected with dislocations in a regular crystal lattice. I. *Proceedings of the Koninklijke Nederlandse Akademie Van Wetenschappen*, 42:293–325.

Bürgmann, R., Rosen, P. A., and Fielding, E. J. (2000). Synthetic aperture radar interferometry to measure Earth's surface topography and its deformation. *Annual Review of Earth and Planetary Sciences*, 28:169–209.

Cai, W., Arsenlis, A., Weinberger, C. R., and Bulatov, V. V. (2006). A non-singular continuum theory of dislocations. *Journal of the Mechanics and Physics of Solids*, 54(3):561–587.

Carlson, B. C. (1995). Numerical computation of real or complex elliptic integrals. *Numerical Algorithms*, 10(1):13–26.

Carn, S. A., Fioletov, V. E., McLinden, C. A., Li, C., and Krotkov, N. A. (2017). A decade of global volcanic SO_2 emissions measured from space. *Scientific Reports*, 7:1–12.

Caselli, A., Agusto, M., Velez, M. L., Forte, P., Bengoa, C., Daga, R., Albite, J. M., and Capaccioni, B. (2016a). *The 2012 Eruption*, pages 61–77. Springer Berlin Heidelberg.

Caselli, A. T., Velez, M. L., Agusto, M., Liccioli, C., and Vaselli, O. (2016b). *Prehistoric to Historic Volcanic Activity at Copahue Volcano*, pages 49–59. Springer Berlin Heidelberg.

Cayol, V. and Cornet, F. H. (1997). 3D mixed boundary elements for elastostatic deformation field analysis. *International Journal of Rock Mechanics and Mining Sciences*, 34(2):275–287.

Cayol, V. and Cornet, F. H. (1998a). Effects of topography on the interpretation of the deformation field of prominent volcanoes—Application to Etna. *Geophysical Research Letters*, 25(11):1979–1982.

Cayol, V. and Cornet, F. H. (1998b). Three-dimensional modeling of the 1983-1984 eruption at Piton de la Fournaise Volcano, Réunion Island. *Journal of Geophysical Research: Solid Earth*, 103(B8):18025–18037.

Cesca, S., Heimann, S., Kriegerowski, M., Saul, J., and Dahm, T. (2017). Moment Tensor Inversion for Nuclear Explosions: What Can We Learn from the 6 January and 9 September 2016 Nuclear Tests, North Korea? *Seismological Research Letters*, 88(2A):300.

Chang, W.-L., Smith, R. B., Farrell, J., and Puskas, C. M. (2010). An extraordinary episode of Yellowstone caldera uplift, 2004-2010, from GPS and InSAR observations. *Geophysical Research Letters*, 37(23).

Chaussard, E. and Amelung, F. (2012). Precursory inflation of shallow magma reservoirs at west Sunda volcanoes detected by InSAR. *Geophysical Research Letters*, 39(21). L21311.

Chaussard, E., Amelung, F., and Aoki, Y. (2013). Characterization of open and closed volcanic systems in Indonesia and Mexico using InSAR time series. *Journal of Geophysical Research: Solid Earth*, 118(8):3957–3969.

Chen, C. W. and Zebker, H. A. (2000). Network approaches to two-dimensional phase unwrapping: intractability and two new algorithms. *Journal of the Optical Society of America A*, 17(3):401–414.

Chestler, S. R. and Grosfils, E. B. (2013). Using numerical modeling to explore the origin of intrusion patterns on Fernandina volcano, Galapagos Islands, Ecuador. *Geophysical Research Letters*, 40(17):4565–4569.

Chevallier, L. and Verwoerd, W. J. (1988). A numerical model for the mechanical behavior of intraplate volcanoes. *Journal of Geophysical Research: Solid Earth*, 93(B5):4182–4198.

Chiodini, G., Cardellini, C., Lamberti, M. C., Agusto, M., Caselli, A., Liccioli, C., Tamburello, G., Tassi, F., Vaselli, O., and Caliro, S. (2015). Carbon dioxide diffuse emission and thermal energy release from hydrothermal systems at Copahue-Caviahue Volcanic Complex (Argentina). *Journal of Volcanology and Geothermal Research*, 304:294–303.

Chouet, B. and Dawson, P. (2011). Shallow conduit system at Kilauea Volcano, Hawaii, revealed by seismic signals associated with degassing bursts. *Journal of Geophysical Research: Solid Earth*, 116(B12). B12317.

Chouet, B., Dawson, P., and Martini, M. (2008). Shallow-conduit dynamics at stromboli volcano, italy, imaged from waveform inversions. *Geological Society, London, Special Publications*, 307(1):57–84.

Chun, K.-Y., Wu, Y., and Henderson, G. A. (2011). Magnitude Estimation and Source Discrimination: A Close Look at the 2006 and 2009 North Korean Underground Nuclear Explosions. *Bulletin of the Seismological Society of America*, 101(3):1315–1329.

Clough, C. T., Maufe, H. B., and Bailey, E. B. (1909). The cauldron-subsidence of glen coe, and the associated igneous phenomena. *Quarterly Journal of the Geological Society*, 65(1-4):611–678.

Comninou, M. and Dundurs, J. (1975). The angular dislocation in a half space. *Journal of Elasticity*, 5(3-4):203–216.

Coxeter, H. S. M. (1969). *Introduction to Geometry*. JOHN WILEY & SONS, INC., Toronto.

Crouch, S. L. and Starfield, A. M. (1983). *Boundary Element Method in Solid Mechanics*. Allen and Unwin, London.

Currenti, G., Del Negro, C., and Ganci, G. (2007). Modelling of ground deformation and gravity fields using finite element method: An application to Etna volcano. *Geophysical Journal International*, 169(2):775–786.

Dahm, T. (2000). Numerical simulations of the propagation path and the arrest of fluid-filled fractures in the Earth. *Geophysical Journal International*, 141(3):623–638.

Davis, P. M. (1983). Surface deformation associated with a dipping hydrofracture. *Journal of Geophysical Research: Solid Earth*, 88(B7):5826–5834.

Davis, P. M. (1986). Surface deformation due to inflation of an arbitrarily oriented triaxial ellipsoidal cavity in an elastic half-space, with reference to Kilauea volcano, Hawaii. *Journal of Geophysical Research*, 91(B7):7429.

Denny, M. D. and Johnson, L. R. (1991). The explosion seismic source function: Models and scaling laws reviewed. In *Explosion Source Phenomenology*, pages 1–24. American Geophysical Union.

Di Traglia, F., Del Ventisette, C., Rosi, M., Mugnai, F., Intrieri, E., Moretti, S., and Casagli, N. (2013). Ground-based InSAR reveals conduit pressurization pulses at Stromboli volcano. *Terra Nova*, 25(3):192–198.

Dieterich, J. H. and Decker, R. W. (1975). Finite element modeling of surface deformation associated with volcanism. *Journal of Geophysical Research*, 80(29):4094–4102.

Dragoni, M. and Magnanensi, C. (1989). Displacement and stress produced by a pressurized, spherical magma chamber, surrounded by a viscoelastic shell. *Physics of the Earth and Planetary Interiors*, 56(3):316–328.

Dunbar, W. S. and Anderson, D. L. (1981). *The Displacement Discontinuity Method in Three Dimensions*, pages 153–173. Springer, Berlin, Heidelberg.

Dvorak, J. J. and Dzurisin, D. (1997). Volcano geodesy: The search for magma reservoirs and the formation of eruptive vents. *Reviews of Geophysics*, 35(3):343–384.

Dvorak, J. J. and Okamura, A. T. (1987). A hydraulic model to explain variations in summit tilt rate at Kilauea and Mauna Loa volcanoes. *US Geological Survey Professional Papers*, 1350(2):1281–1296.

Dziewonski, A. M. and Anderson, D. L. (1981). Preliminary reference Earth model. *Physics of the Earth and Planetary Interiors*, 25(4):297–356.

Dzurisin, D. (2007). *Volcano deformation: Geodetic monitoring techniques*. Springer-Praxis Books in Geophysical Sciences, Berlin.

Dzurisin, D., Lisowski, M., Poland, M. P., Sherrod, D. R., and Lahusen, R. G. (2008). Constraints and Conundrums Resulting from Ground-Deformation Measurements Made During the 2004-2005 Dome-Building Eruption of Mount St. Helens, Washington. professional paper 1750, US Geological Survey.

Dzurisin, D., Lisowski, M., and Wicks, C. W. (2009). Continuing inflation at Three Sisters volcanic center, central Oregon Cascade Range, USA, from GPS, leveling, and InSAR observations. *Bulletin of Volcanology*, 71(10):1091–1110.

Ebmeier, S. K., Biggs, J., Mather, T. A., and Amelung, F. (2013). On the lack of InSAR observations of magmatic deformation at Central American volcanoes. *Journal of Geophysical Research: Solid Earth*, 118(5):2571–2585.

Elliott, J., Walters, R., and Wright, T. (2016). The role of space-based observation in understanding and responding to active tectonics and earthquakes. *Nature Communications*, 7(13844).

Eshelby, J. D. (1957). The Determination of the Elastic Field of an Ellipsoidal Inclusion, and Related Problems. *Proceedings of the Royal Society A: Mathematical, Physical and Engineering Sciences*, 241(1226):376–396.

Farr, T. G., Rosen, P. A., Caro, E., Crippen, R., Duren, R., Hensley, S., Kobrick, M., Paller, M., Rodriguez, E., Roth, L., Seal, D., Shaffer, S., Shimada, J., Umland, J., Werner, M., Oskin, M., Burbank, D., and Alsdorf, D. (2007). The Shuttle Radar Topography Mission. *Reviews of Geophysics*, 45(2).

Feigl, K. L., Sarti, F., Vadon, H., McClusky, S., Ergintav, S., Durand, P., Bürgmann, R., Rigo, A., Massonnet, D., and Reilinger, R. (2002). Estimating Slip Distribution for the İzmit Mainshock from Coseismic GPS, ERS-1, RADARSAT, and SPOT Measurements. *Bulletin of the Seismological Society of America*, 92(1):138–160.

Fernández, J., Pepe, A., Poland, M. P., and Sigmundsson, F. (2017). Volcano geodesy: Recent developments and future challenges. *Journal of Volcanology and Geothermal Research*, 344(Supplement C):1–12. Volcano Geodesy: Recent developments and future challenges.

Ferrari, C., Bonafede, M., and Trasatti, E. (2015). Relations between pressurized triaxial cavities and moment tensor distributions. *Annals of Geophysics*, 58(4).

Fialko, Y., Khazan, Y., and Simons, M. (2001). Deformation due to a pressurized horizontal circular crack in an elastic half-space, with applications to volcano geodesy. *Geophysical Journal International*, 146(1):181–190.

Fialko, Y. and Pearse, J. (2012). Sombrero Uplift Above the Altiplano-Puna Magma Body: Evidence of a Ballooning Mid-Crustal Diapir. *Science*, 338(6104):250–252.

Fichtner, A. and Tkalčić, H. (2010). Insights into the kinematics of a volcanic caldera drop: Probabilistic finite-source inversion of the 1996 Bárðarbunga, Iceland, earthquake. *Earth and Planetary Science Letters*, 297(3):607–615.

Flamant, A. (1892). Sur la répartition des pressions dans un solide rectangulaire chargé transversalement [On the distribution of stresses in a rectangular solid under transverse load]. *Comptes rendus de l'Académie des Sciences*, 114:1465–1468.

Folguera, A., Ramos, V. A., Hermanns, R. L., and Naranjo, J. (2004). Neotectonics in the foothills of the southernmost central Andes ($37° - 38°$S): Evidence of strike-slip displacement along the Antiñir-Copahue fault zone. *Tectonics*, 23(5).

Folguera, A., Rojas Vera, E., Vélez, L., Tobal, J., Orts, D., Agusto, M., Caselli, A., and Ramos, V. A. (2016). *A Review of the Geology, Structural Controls, and Tectonic Setting of Copahue Volcano, Southern Volcanic Zone, Andes, Argentina*, pages 3–22. Springer Berlin Heidelberg.

Ford, S. R., Dreger, D. S., and Walter, W. R. (2009). Source analysis of the Memorial Day explosion, Kimchaek, North Korea. *Geophysical Research Letters*, 36(21). L21304.

Ford, S. R. and Walter, W. R. (2013). An Explosion Model Comparison with Insights from the Source Physics Experiments. *Bulletin of the Seismological Society of America*, 103(5):2937–2945.

Fournier, R. O. (1999). Hydrothermal processes related to movement of fluid from plastic into brittle rock in the magmatic-epithermal environment. *Economic Geology*, 94(8):1193–1211.

Fournier, T. J., Pritchard, M. E., and Riddick, S. N. (2010). Duration, magnitude, and frequency of subaerial volcano deformation events: New results from Latin America using InSAR and a global synthesis. *Geochemistry, Geophysics, Geosystems*, 11(1). Q01003.

Frémont, M.-J. and Malone, S. D. (1987). High precision relative locations of earthquakes at Mount St. Helens, Washington. *Journal of Geophysical Research: Solid Earth*, 92(B10):10223–10236.

Fukuda, J. and Johnson, K. M. (2010). Mixed linear–non-linear inversion of crustal deformation data: Bayesian inference of model, weighting and regularization parameters. *Geophysical Journal International*, 181(3):1441–1458.

Fukushima, Y., Cayol, V., and Durand, P. (2005). Finding realistic dike models from interferometric synthetic aperture radar data: The February 2000 eruption at Piton de la Fournaise. *Journal of Geophysical Research: Solid Earth*, 110(B3). B03206.

Gaeta, F. S., De Natale, G., Peluso, F., Mastrolorenzo, G., Castagnolo, D., Troise, C., Pingue, F., Mita, D. G., and Rossano, S. (1998). Genesis and evolution of unrest episodes at Campi Flegrei caldera: The role of thermal fluid-dynamical processes in the geothermal system. *Journal of Geophysical Research: Solid Earth*, 103(B9):20921–20933.

Galland, O., Holohan, E., van Wyk de Vries, B., and Burchardt, S. (2015). *Laboratory Modelling of Volcano Plumbing Systems: A Review*, pages 1–68. Advances in Volcanology. Springer Berlin Heidelberg.

Geshi, N., Shimano, T., Chiba, T., and Nakada, S. (2002). Caldera collapse during the 2000 eruption of Miyakejima Volcano, Japan. *Bulletin of Volcanology*, 64(1):55–68.

Gimbutas, Z., Greengard, L., Barall, M., and Tullis, T. E. (2012). On the Calculation of Displacement, Stress, and Strain Induced by Triangular Dislocations. *Bulletin of the Seismological Society of America*, 102(6):2776–2780.

Green, D. N., Neuberg, J., and Cayol, V. (2006). Shear stress along the conduit wall as a plausible source of tilt at Soufrière Hills volcano, Montserrat. *Geophysical Research Letters*, 33(10). L10306.

Grosfils, E. B. (2007). Magma reservoir failure on the terrestrial planets: Assessing the importance of gravitational loading in simple elastic models. *Journal of Volcanology and Geothermal Research*, 166(2):47–75.

Grosfils, E. B., McGovern, P. J., Gregg, P. M., Galgana, G. A., Hurwitz, D. M., Long, S. M., and Chestler, S. R. (2015). Elastic models of magma reservoir mechanics: a key tool for investigating planetary volcanism. *Geological Society, London, Special Publications*, 401(1):239–267.

Gudmundsson, A. (1988). Effect of tensile stress concentration around magma chambers on intrusion and extrusion frequencies. *Journal of Volcanology and Geothermal Research*, 35(3):179–194.

Gudmundsson, M. T. and Högnadóttir, T. (2007). Volcanic systems and calderas in the Vatnajökull region, central Iceland: Constraints on crustal structure from gravity data. *Journal of Geodynamics*, 43(1):153–169. Hotspot Iceland.

Gutenberg, B. and Richter, C. F. (1944). Frequency of earthquakes in California. *Bulletin of the Seismological Society of America*, 34(4):185–188.

Haupt, R. L. and Haupt, S. E. (2004). *Practical Genetic Algorithms*. JOHN WILEY & SONS, INC., Hoboken, New Jersey, second edition.

Hautmann, S., Gottsmann, J., Sparks, R. S. J., Costa, A., Melnik, O., and Voight, B. (2009). Modelling ground deformation caused by oscillating overpressure in a dyke conduit at Soufrière Hills Volcano, Montserrat. *Tectonophysics*, 471(1):87–95. Understanding stress and deformation in active volcanoes.

Hirth, J. P. and Lothe, J. (1982). *Theory of Dislocations*. JOHN WILEY & SONS, New York, second edition.

Holland, A. S. P., Watson, I. M., Phillips, J. C., Caricchi, L., and Dalton, M. P. (2011). Degassing processes during lava dome growth: Insights from Santiaguito lava dome, Guatemala. *Journal of Volcanology and Geothermal Research*, 202(1):153–166.

Holland, J. H. (1975). *Adaptation in Natural and Artificial Systems*. University of Michigan Press, Ann Arbor.

Holohan, E. P., Schöpfer, M. P. J., and Walsh, J. J. (2011). Mechanical and geometric controls on the structural evolution of pit crater and caldera subsidence. *Journal of Geophysical Research: Solid Earth*, 116(B7). B07202.

Holohan, E. P., Troll, V. R., van Wyk de Vries, B., Walsh, J. J., and Walter, T. R. (2008). Unzipping Long Valley: An explanation for vent migration patterns during an elliptical ring fracture eruption. *Geology*, 36(4):323–326.

Holohan, E. P., Walter, T. R., Schöpfer, M. P., Walsh, J. J., van Wyk de Vries, B., and Troll, V. R. (2013). Origins of oblique-slip faulting during caldera subsidence. *Journal of Geophysical Research: Solid Earth*, 118(4):1778–1794.

Hooper, A., Bekaert, D., Spaans, K., and Arıkan, M. (2012). Recent advances in SAR interferometry time series analysis for measuring crustal deformation. *Tectonophysics*, 514-517(Supplement C):1–13.

Howard, K. A. (2010). Caldera collapse: Perspectives from comparing Galápagos volcanoes, nuclear-test sinks, sandbox models, and volcanoes on Mars. *GSA Today*, 20:4–10.

Hu, J., Li, Z., Ding, X., Zhu, J., Zhang, L., and Sun, Q. (2014). Resolving three-dimensional surface displacements from InSAR measurements: A review. *Earth-Science Reviews*, 133:1–17.

Hu, J., Li, Z., Zhu, J., Ren, X., and Ding, X. (2010). Inferring three-dimensional surface displacement field by combining SAR interferometric phase and amplitude information of ascending and descending orbits. *Science China Earth Sciences*, 53(4):550–560.

Hudson, J. A., Pearce, R. G., and Rogers, R. M. (1989). Source type plot for inversion of the moment tensor. *Journal of Geophysical Research: Solid Earth*, 94(B1):765–774.

Hurwitz, D. M., Long, S. M., and Grosfils, E. B. (2009). The characteristics of magma reservoir failure beneath a volcanic edifice. *Journal of Volcanology and Geothermal Research*, 188(4):379–394.

Ibáñez, J., Pezzo, E. D., Bengoa, C., Caselli, A., Badi, G., and Almendros, J. (2008). Volcanic tremor and local earthquakes at Copahue volcanic complex, Southern Andes, Argentina. *Journal of Volcanology and Geothermal Research*, 174(4):284–294.

Ichihara, M., Kusakabe, T., Kame, N., and Kumagai, H. (2016). On volume-source representations based on the representation theorem. *Earth, Planets and Space*, 68(1):1–10.

IRIS (2017). Special Event: 2017 North Korean nuclear test. https://ds.iris.edu/ds/nodes/dmc/specialevents/2017/09/03/2017-north-korean-nuclear-test/. Accessed: 2018-04-21.

Ishimoto, M. and Lida, K. (1939). Observations of earthquakes registered with the microseismograph constructed recently. *Bulletin of Earthquake Research Institute, University of Tokyo*, 17:443–478.

James, M. R. and Varley, N. (2012). Identification of structural controls in an active lava dome with high resolution DEMs: Volcán de Colima, Mexico. *Geophysical Research Letters*, 39(22). L22303.

Jeyakumaran, M., Rudnicki, J. W., and Keer, L. M. (1992). Modeling slip zones with triangular dislocation elements. *Bulletin of the Seismological Society of America*, 82(5):2153–2169.

Jiang, H., Feng, G., Wang, T., and Bürgmann, R. (2017). Toward full exploitation of coherent and incoherent information in Sentinel-1 TOPS data for retrieving surface displacement: Application to the 2016 Kumamoto (Japan) earthquake. *Geophysical Research Letters*, 44(4):1758–1767. 2016GL072253.

Johnson, J. B., Lees, J. M., Gerst, A., Sahagian, D., and Varley, N. (2008). Long-period earthquakes and co-eruptive dome inflation seen with particle image velocimetry. *Nature*, 456:377–381.

Jones, R. H. and Stewart, R. C. (1997). A method for determining significant structures in a cloud of earthquakes. *Journal of Geophysical Research: Solid Earth*, 102(B4):8245–8254.

Jónsson, S. (2009). Stress interaction between magma accumulation and trapdoor faulting on Sierra Negra volcano, Galápagos. *Tectonophysics*, 471(1):36–44. Understanding stress and deformation in active volcanoes.

Jónsson, S., Zebker, H., Segall, P., and Amelung, F. (2002). Fault slip distribution of the 1999 Mw 7.1 Hector Mine, California, earthquake, estimated from satellite radar and GPS measurements. *Bulletin of the Seismological Society of America*, 92(4):1377–1389.

Kahl, M., Chakraborty, S., Costa, F., and Pompilio, M. (2011). Dynamic plumbing system beneath volcanoes revealed by kinetic modeling, and the connection to monitoring data: An example from Mt. Etna. *Earth and Planetary Science Letters*, 308(1):11–22.

Kazahaya, K., Shinohara, H., and Saito, G. (2002). Degassing process of Satsuma-Iwojima volcano, Japan: Supply of volatile components from a deep magma chamber. *Earth, Planets and Space*, 54(3):327–335.

Kelvin, S. W. T. (1848). Note on the integration of the equations of equilibrium of an elastic solid. *Cambridge and Dublin Mathematical Journal*, 3(76-99):87–89.

Kennedy, B., Stix, J., Vallance, J. W., Lavallée, Y., and Longpré, M.-A. (2004). Controls on caldera structure: Results from analogue sandbox modeling. *GSA Bulletin*, 116(5-6):515–524.

Kilburn, C. R. J. and Voight, B. (1998). Slow rock fracture as eruption precursor at Soufriere Hills Volcano, Montserrat. *Geophysical Research Letters*, 25(19):3665–3668.

King, G. C. P., Stein, R. S., and Lin, J. (1994). Static stress changes and the triggering of earthquakes. *Bulletin of the Seismological Society of America*, 84(3):935–953.

Knopoff, L. and Randall, M. J. (1970). The compensated linear-vector dipole: A possible mechanism for deep earthquakes. *Journal of Geophysical Research*, 75(26):4957–4963.

Komuro, H., Fujita, Y., and Kodama, K. (1984). Numerical and experimental models on the formation mechanism of collapse basins during the Green Tuff orogenesis of Japan. *Bulletin Volcanologique*, 47(3):649–666.

Kühn, D. and Dahm, T. (2004). Simulation of magma ascent by dykes in the mantle beneath mid-ocean ridges. *Journal of Geodynamics*, 38(2):147–159.

Kumagai, H., Maeda, Y., Ichihara, M., Kame, N., and Kusakabe, T. (2014). Seismic moment and volume change of a spherical source. *Earth, Planets and Space*, 66(1):1–10.

Kuriyama, K. and Mizuta, Y. (1993). Three-dimensional elastic analysis by the displacement discontinuity method with boundary division into triangular leaf elements. *International Journal of Rock Mechanics and Mining Sciences & Geomechanics Abstracts*, 30(2):111–123.

Lavallée, Y., Varley, N. R., Alatorre-Ibargüengoitia, M. A., Hess, K.-U., Kueppers, U., Mueller, S., Richard, D., Scheu, B., Spieler, O., and Dingwell, D. B. (2012). Magmatic architecture of dome-building eruptions at Volcán de Colima, Mexico. *Bulletin of Volcanology*, 74(1):249–260.

Lazo, J., Basualto, D., Bengoa, C., Cardona, C., Franco, L., Gil-Cruz, F., Hernández, E., Lara, L., Lundgren, P., Medina, R., Morales, S., Peña, P., Quijada, J., Samsonov, S., San Martin, J., and Valderrama, O. (2015). Spatial Distribution of b-value of the Copahue volcano during 2012-2014 eruptive period: Relationship between magmatic and hydrothermal system. In *EGU General Assembly Conference Abstracts*, volume 17 of *EGU General Assembly Conference Abstracts*, page 982.

Le Corvec, N., Walter, T. R., Ruch, J., Bonforte, A., and Puglisi, G. (2014). Experimental study of the interplay between magmatic rift intrusion and flank instability with application to the 2001 Mount Etna eruption. *Journal of Geophysical Research: Solid Earth*, 119(7):5356–5368. 2014JB011224.

Le Mével, H., Feigl, K. L., Córdova, L., DeMets, C., and Lundgren, P. (2015). Evolution of unrest at Laguna del Maule volcanic field (Chile) from InSAR and GPS measurements, 2003 to 2014. *Geophysical Research Letters*, 42(16):6590–6598.

Lee, W. H. K. and Valdes, C. M. (1985). HYPO71PC: a personal computer version of the HYPO71 earthquake location program. Open File Report 85-749, U.S. Geological Survey.

Lipman, P. W. (1997). Subsidence of ash-flow calderas: relation to caldera size and magma-chamber geometry. *Bulletin of Volcanology*, 59(3):198–218.

Lisowski, M. (2007). *Analytical volcano deformation source models*, pages 279–304. Springer Berlin Heidelberg, Berlin, Heidelberg.

Liu, J., Li, L., Zahradník, J., Sokos, E., Liu, C., and Tian, X. (2018). North Korea's 2017 Test and its Nontectonic Aftershock. *Geophysical Research Letters*. in press.

Lohman, R. B. and Simons, M. (2005). Some thoughts on the use of InSAR data to constrain models of surface deformation: Noise structure and data downsampling. *Geochemistry, Geophysics, Geosystems*, 6(1).

Long, S. M. and Grosfils, E. B. (2009). Modeling the effect of layered volcanic material on magma reservoir failure and associated deformation, with application to Long Valley caldera, California. *Journal of Volcanology and Geothermal Research*, 186(3):349–360.

López-Escobar, L., Parada, M. A., Hickey-Vargas, R., Frey, F. A., Kempton, P. D., and Moreno, H. (1995). Calbuco Volcano and minor eruptive centers distributed along the Liquiñe-Ofqui Fault Zone, Chile ($41^\circ - 42^\circ$ S): contrasting origin of andesitic and basaltic magma in the Southern Volcanic Zone of the Andes. *Contributions to Mineralogy and Petrology*, 119(4):345–361.

Love, A. E. H. (1944). *A treatise on the Mathematical Theory of Elasticity*. Dover Publications, New York.

Lu, Z., Dzurisin, D., Biggs, J., Wicks, C., and McNutt, S. (2010). Ground surface deformation patterns, magma supply, and magma storage at Okmok volcano, Alaska, from InSAR analysis: 1. Intereruption deformation, 1997-2008. *Journal of Geophysical Research: Solid Earth*, 115(B5). B00B02.

Lu, Z., Masterlark, T., Dzurisin, D., Rykhus, R., and Wicks, C. (2003). Magma supply dynamics at Westdahl volcano, Alaska, modeled from satellite radar interferometry. *Journal of Geophysical Research: Solid Earth*, 108(B7).

Lu, Z., Wicks, C., Dzurisin, D., Power, J. A., Moran, S. C., and Thatcher, W. (2002). Magmatic inflation at a dormant stratovolcano: 1996-1998 activity at Mount Peulik volcano, Alaska, revealed by satellite radar interferometry. *Journal of Geophysical Research: Solid Earth*, 107(B7).

Lundgren, P., Casu, F., Manzo, M., Pepe, A., Berardino, P., Sansosti, E., and Lanari, R. (2004). Gravity and magma induced spreading of Mount Etna volcano revealed by satellite radar interferometry. *Geophysical Research Letters*, 31(4).

Lundgren, P. and Lu, Z. (2006). Inflation model of Uzon caldera, Kamchatka, constrained by satellite radar interferometry observations. *Geophysical Research Letters*, 33(6).

Lundgren, P., Samsonov, S. V., López Velez, C. M., and Ordoñez, M. (2015). Deep source model for Nevado del Ruiz Volcano, Colombia, constrained by interferometric synthetic aperture radar observations. *Geophysical Research Letters*, 42(12):4816–4823.

Lundgren, P., Usai, S., Sansosti, E., Lanari, R., Tesauro, M., Fornaro, G., and Berardino, P. (2001). Modeling surface deformation observed with synthetic aperture radar interferometry at Campi Flegrei caldera. *Journal of Geophysical Research: Solid Earth*, 106(B9):19355–19366.

Maccaferri, F., Bonafede, M., and Rivalta, E. (2011). A quantitative study of the mechanisms governing dike propagation, dike arrest and sill formation. *Journal of Volcanology and Geothermal Research*, 208(1):39–50.

Maeda, I. (2000). Nonlinear visco-elastic volcanic model and its application to the recent eruption of Mt. Unzen. *Journal of Volcanology and Geothermal Research*, 95(1):35–47.

Maerten, F. (2010). *Geomechanics to Solve Geological Structure Issues: Forward, Inverse and Restoration Modeling*. PhD thesis, University of Montpellier II.

Maerten, F., Resor, P., Pollard, D., and Maerten, L. (2005). Inverting for Slip on Three-Dimensional Fault Surfaces Using Angular Dislocations. *Bulletin of the Seismological Society of America*, 95(5):1654–1665.

Malinverno, A. (2002). Parsimonious Bayesian Markov chain Monte Carlo inversion in a non-linear geophysical problem. *Geophysical Journal International*, 151(3):675–688.

Manconi, A., Walter, T. R., and Amelung, F. (2007). Effects of mechanical layering on volcano deformation. *Geophysical Journal International*, 170(2):952–958.

Manconi, A., Walter, T. R., Manzo, M., Zeni, G., Tizzani, P., Sansosti, E., and Lanari, R. (2010). On the effects of 3-D mechanical heterogeneities at Campi Flegrei caldera, southern Italy. *Journal of Geophysical Research: Solid Earth*, 115(B8). B08405.

Martel, S. J. and Muller, J. R. (2000). A Two-dimensional Boundary Element Method for Calculating Elastic Gravitational Stresses in Slopes. *Pure and Applied Geophysics*, 157(6):989–1007.

Massin, F., Ferrazzini, V., Bachèlery, P., Nercessian, A., Duputel, Z., and Staudacher, T. (2011). Structures and evolution of the plumbing system of Piton de la Fournaise volcano inferred from clustering of 2007 eruptive cycle seismicity. *Journal of Volcanology and Geothermal Research*, 202(1):96–106.

Massonnet, D., Briole, P., and Arnaud, A. (1995). Deflation of Mount Etna monitored by spaceborne radar interferometry. *Nature*, 375:567–570.

McTigue, D. F. (1987). Elastic stress and deformation near a finite spherical magma body: Resolution of the point source paradox. *Journal of Geophysical Research: Solid Earth*, 92(B12):12931–12940.

Meade, B. J. (2007). Algorithms for the calculation of exact displacements, strains, and stresses for triangular dislocation elements in a uniform elastic half space. *Computers & Geosciences*, 33(8):1064–1075.

Melnick, D., Folguera, A., and Ramos, V. A. (2006). Structural control on arc volcanism: The Caviahue-Copahue complex, Central to Patagonian Andes transition (38°S). *Journal of South American Earth Sciences*, 22(1):66–88.

Mériaux, C. and Lister, J. R. (2002). Calculation of dike trajectories from volcanic centers. *Journal of Geophysical Research: Solid Earth*, 107(B4):ETG 10–1–ETG 10–10.

Michel, R., Avouac, J.-P., and Taboury, J. (1999). Measuring ground displacements from SAR amplitude images: Application to the Landers Earthquake. *Geophysical Research Letters*, 26(7):875–878.

Milillo, P., Bürgmann, R., Lundgren, P., Salzer, J., Perissin, D., Fielding, E., Biondi, F., and Milillo, G. (2016). Space geodetic monitoring of engineered structures: The ongoing destabilization of the Mosul dam, Iraq. *Scientific Reports*, 6(37408).

Mindlin, R. D. (1936). Force at a Point in the Interior of a Semi-Infinite Solid. *Physics*, 7(5):195–202.

Mogi, K. (1958). Relations between the eruptions of various volcanoes and the deformations of the ground surfaces around them. *Bulletin of the Earthquake Research Institute*, 36:99–134.

Moore, I. and Kokelaar, P. (1998). Tectonically controlled piecemeal caldera collapse: A case study of Glencoe volcano, Scotland. *GSA Bulletin*, 110(11):1448–1466.

Muller, J. R., Ito, G., and Martel, S. J. (2001). Effects of volcano loading on dike propagation in an elastic half-space. *Journal of Geophysical Research: Solid Earth*, 106(B6):11101–11113.

Naranjo, J. A. and Polanco, E. (2004). The 2000 AD eruption of Copahue Volcano, Southern Andes. *Revista geológica de Chile*, 31(2):279–292.

Neuberg, J. (2000). Characteristics and causes of shallow seismicity in andesite volcanoes. *Philosophical Transactions of the Royal Society of London A: Mathematical, Physical and Engineering Sciences*, 358(1770):1533–1546.

Newhall, C. G. and Self, S. (1982). The volcanic explosivity index (VEI) an estimate of explosive magnitude for historical volcanism. *Journal of Geophysical Research: Oceans*, 87(C2):1231–1238.

Newman, A. V., Dixon, T. H., and Gourmelen, N. (2006). A four-dimensional viscoelastic deformation model for Long Valley Caldera, California, between 1995 and 2000. *Journal of Volcanology and Geothermal Research*, 150:244–269.

Newman, A. V., Dixon, T. H., Ofoegbu, G. I., and Dixon, J. E. (2001). Geodetic and seismic constraints on recent activity at Long Valley Caldera, California: evidence for viscoelastic rheology. *Journal of Volcanology and Geothermal Research*, 105(3):183–206.

Nikkhoo, M. and Walter, T. R. (2015). Triangular dislocation: an analytical, artefact-free solution. *Geophysical Journal International*, 201(2):1117–1139.

Nikkhoo, M., Walter, T. R., Lundgren, P. R., and Prats-Iraola, P. (2017). Compound dislocation models (CDMs) for volcano deformation analyses. *Geophysical Journal International*, 208(2):877–894.

Norini, G., Capra, L., Groppelli, G., Agliardi, F., Pola, A., and Cortes, A. (2010). Structural architecture of the Colima Volcanic Complex. *Journal of Geophysical Research: Solid Earth*, 115(B12). B12209.

Okada, Y. (1985). Surface deformation due to shear and tensile faults in a half-space. *Bulletin of the seismological society of America*, 75(4):1135–1154.

Okada, Y. (1992). Internal deformation due to shear and tensile faults in a half-space. *Bulletin of the Seismological Society of America*, 82(2):1018–1040.

Ölmez, E., Ercan, T., and Yıldırım, T. (1994). Volcanology and geothermal energy possibilities of the Tendürek area (Diyadin, Zilan, Çaldiran), Eastern Anatolia (Turkey). *Geol. Bull. Turkey*, 9:48–55. (in Turkish).

Parfitt, E., Wilson, L., and Head, J. (1993). Basaltic magma reservoirs: factors controlling their rupture characteristics and evolution. *Journal of Volcanology and Geothermal Research*, 55(1):1–14.

Pascal, K., Neuberg, J., and Rivalta, E. (2014). On precisely modelling surface deformation due to interacting magma chambers and dykes. *Geophysical Journal International*, 196(1):253–278.

Patanè, D., De Gori, P., Chiarabba, C., and Bonaccorso, A. (2003). Magma Ascent and the Pressurization of Mount Etna's Volcanic System. *Science*, 299(5615):2061–2063.

Pathier, E., Fielding, E. J., Wright, T. J., Walker, R., Parsons, B. E., and Hensley, S. (2006). Displacement field and slip distribution of the 2005 Kashmir earthquake from SAR imagery. *Geophysical Research Letters*, 33(20). L20310.

Patton, H. J. and Taylor, S. R. (2011). The apparent explosion moment: Inferences of volumetric moment due to source medium damage by underground nuclear explosions. *Journal of Geophysical Research: Solid Earth*, 116(B3).

Pearce, J. A., Bender, J. F., De Long, S. E., Kidd, W. S. F., Low, P. J., Güner, Y., Saroglu, F., Yilmaz, Y., Moorbath, S., and Mitchell, J. G. (1990). Genesis of collision volcanism in Eastern Anatolia, Turkey. *Journal of Volcanology and Geothermal Research*, 44(1):189–229.

Pearse, J. and Lundgren, P. (2013). Source model of deformation at Lazufre volcanic center, central Andes, constrained by InSAR time series. *Geophysical Research Letters*, 40(6):1059–1064.

Peltier, A., Staudacher, T., Bachèlery, P., and Cayol, V. (2009). Formation of the April 2007 caldera collapse at Piton de La Fournaise volcano: Insights from GPS data. *Journal of Volcanology and Geothermal Research*, 184(1):152–163. Recent advances on the geodynamics of Piton de la Fournaise volcano.

Persson, P.-O. and Strang, G. (2004). A Simple Mesh Generator in MATLAB. *SIAM Review*, 46(2):329–345.

Pinel, V., Hooper, A., De la Cruz-Reyna, S., Reyes-Davila, G., Doin, M. P., and Bascou, P. (2011). The challenging retrieval of the displacement field from InSAR data for andesitic stratovolcanoes: Case study of Popocatepetl and Colima Volcano, Mexico. *Journal of Volcanology and Geothermal Research*, 200(1):49–61.

Pinel, V. and Jaupart, C. (2003). Magma chamber behavior beneath a volcanic edifice. *Journal of Geophysical Research: Solid Earth*, 108(B2). 2072.

Pinel, V. and Jaupart, C. (2005). Caldera formation by magma withdrawal from a reservoir beneath a volcanic edifice. *Earth and Planetary Science Letters*, 230(3):273–287.

Pinel, V., Jaupart, C., and Albino, F. (2010). On the relationship between cycles of eruptive activity and growth of a volcanic edifice. *Journal of Volcanology and Geothermal Research*, 194(4):150–164.

Poland, M., Hamburger, M., and Newman, A. (2006). The changing shapes of active volcanoes: History, evolution, and future challenges for volcano geodesy. *Journal of Volcanology and Geothermal Research*, 150(1):1–13. The Changing Shapes of Active Volcanoes.

Pollard, D. D. and Holzhausen, G. (1979). On the mechanical interaction between a fluid-filled fracture and the earth's surface. *Tectonophysics*, 53(1):27–57.

Prats-Iraola, P., Scheiber, R., Marotti, L., Wollstadt, S., and Reigber, A. (2012). TOPS Interferometry With TerraSAR-X. *IEEE Transactions on Geoscience and Remote Sensing*, 50(8):3179–3188.

Pritchard, M. E. and Simons, M. (2002). A satellite geodetic survey of large-scale deformation of volcanic centres in the central Andes. *Nature*, 418:167–171.

Ratdomopurbo, A., Beauducel, F., Subandriyo, J., Agung Nandaka, I. G. M., Newhall, C. G., Suharna, Sayudi, D. S., Suparwaka, H., and Sunarta (2013). Overview of the 2006 eruption of Mt. Merapi. *Journal of Volcanology and Geothermal Research*, 261(Supplement C):87–97. Merapi eruption.

Reilinger, R., McClusky, S., Vernant, P., Lawrence, S., Ergintav, S., Cakmak, R., Ozener, H., Kadirov, F., Guliev, I., Stepanyan, R., Nadariya, M., Hahubia, G., Mahmoud, S., Sakr, K., ArRajehi, A., Paradissis, D., Al-Aydrus, A., Prilepin, M., Guseva, T., Evren, E., Dmitrotsa, A., Filikov, S. V., Gomez, F., Al-Ghazzi, R., and Karam, G. (2006). GPS constraints on continental deformation in the Africa-Arabia-Eurasia continental collision zone and implications for the dynamics of plate interactions. *Journal of Geophysical Research: Solid Earth*, 111(B5). B05411.

Remy, D., Froger, J. L., Perfettini, H., Bonvalot, S., Gabalda, G., Albino, F., Cayol, V., Legrand, D., and De Saint Blanquat, M. (2014). Persistent uplift of the Lazufre volcanic complex (Central Andes): New insights from PCAIM inversion of InSAR time series and GPS data. *Geochemistry, Geophysics, Geosystems*, 15(9):3591–3611.

Reverso, T., Vandemeulebrouck, J., Jouanne, F., Pinel, V., Villemin, T., Sturkell, E., and Bascou, P. (2014). A two-magma chamber model as a source of deformation at Grímsvötn Volcano, Iceland. *Journal of Geophysical Research: Solid Earth*, 119(6):4666–4683.

Richter, N., Poland, M. P., and Lundgren, P. R. (2013). TerraSAR-X interferometry reveals small-scale deformation associated with the summit eruption of Kilauea Volcano, Hawai'i. *Geophysical Research Letters*, 40(7):1279–1283.

Rivalta, E. and Segall, P. (2008). Magma compressibility and the missing source for some dike intrusions. *Geophysical Research Letters*, 35(4).

Roche, O., Druitt, T. H., and Merle, O. (2000). Experimental study of caldera formation. *Journal of Geophysical Research: Solid Earth*, 105(B1):395–416.

Ronchin, E., Masterlark, T., Martí Molist, J., Saunders, S., and Tao, W. (2013). Solid modeling techniques to build 3D finite element models of volcanic systems: An example from the Rabaul Caldera system, Papua New Guinea. *Computers & Geosciences*, 52(Supplement C):325–333.

Rosen, P. A., Gurrola, E. M., Agram, P. S., Sacco, G. F., and Lavalle, M. (2015). The InSAR Scientific Computing Environment (ISCE): A Python Framework for Earth Science. In *AGU Fall Meeting Abstracts*. Abstract IN11C-1789 presented at 2015 Fall Meeting, AGU, San Francisco, California.

Rosen, P. A., Hensley, S., Joughin, I. R., Li, F. K., Madsen, S. N., Rodríguez, E., and Goldstein, R. M. (2000). Synthetic Aperture Radar Interferometry. In *Proceedings of the IEEE*, pages 333–382. VOL. 88, NO.3.

Rosen, P. A., Hensley, S., Peltzer, G., and Simons, M. (2004). Updated repeat orbit interferometry package released. *Eos, Transactions American Geophysical Union*, 85(5):47–47.

Rougier, E., Patton, H. J., Knight, E. E., and Bradley, C. R. (2011). Constraints on burial depth and yield of the 25 May 2009 North Korean test from hydrodynamic simulations in a granite medium. *Geophysical Research Letters*, 38(16). L16316.

Ruch, J., Wang, T., Xu, W., Hensch, M., and Jónsson, S. (2016). Oblique rift opening revealed by reoccurring magma injection in central Iceland. *Nature Communications*, 7:12352.

Sadd, M. H. (2009). *Elasticity: theory, applications, and numerics*. Academic Press, second edition.

Saepuloh, A., Urai, M., Aisyah, N., Sunarta, Widiwijayanti, C., Subandriyo, and Jousset, P. (2013). Interpretation of ground surface changes prior to the 2010 large eruption of Merapi volcano using ALOS/PALSAR, ASTER TIR and gas emission data. *Journal of Volcanology and Geothermal Research*, 261(Supplement C):130–143. Merapi eruption.

Salzer, J. T., Nikkhoo, M., Walter, T. R., Sudhaus, H., Reyes-Dávila, G., Bretón, M., and Arámbula, R. (2014). Satellite radar data reveal short-term pre-explosive displacements and a complex conduit system at Volcán de Colima, Mexico. *Frontiers in Earth Science*, 2:12.

Sartoris, G., Pozzi, J. P., Philippe, C., and Le Moüel, J. L. (1990). Mechanical stability of shallow magma chambers. *Journal of Geophysical Research: Solid Earth*, 95(B4):5141–5151.

Saunders, S. J. (2001). The shallow plumbing system of Rabaul caldera: a partially intruded ring fault? *Bulletin of Volcanology*, 63(6):406–420.

Scavia, C. (1991). The displacement discontinuity method in the analysis of open cracks. *Meccanica*, 26(1):27–32.

Schaefer, L. N., Wang, T., Escobar-Wolf, R., Oommen, T., Lu, Z., Kim, J., Lundgren, P. R., and Waite, G. P. (2017). Three-dimensional displacements of a large volcano flank movement during the May 2010 eruptions at Pacaya Volcano, Guatemala. *Geophysical Research Letters*, 44(1):135–142. 2016GL071402.

Schultz, R. A. (1995). Limits on strength and deformation properties of jointed basaltic rock masses. *Rock Mechanics and Rock Engineering*, 28(1):1–15.

Segall, P. (1997). New insights into old earthquakes. *Nature*, 388(July):122–123.

Segall, P. (2010). *Earthquake and Volcano Deformation*. Princeton University Press, Princeton, New Jersey.

Segall, P. (2016). Repressurization following eruption from a magma chamber with a viscoelastic aureole. *Journal of Geophysical Research: Solid Earth*, 121(12):8501–8522. 2016JB013597.

Selby, N. D. (2010). Relative Locations of the October 2006 and May 2009 DPRK Announced Nuclear Tests Using International Monitoring System Seismometer Arrays. *Bulletin of the Seismological Society of America*, 100(4):1779–1784.

Shirzaei, M., Walter, T. R., and Bürgmann, R. (2013). Coupling of Hawaiian volcanoes only during overpressure condition. *Geophysical Research Letters*, 40(10):1994–1999.

Shuler, A., Ekström, G., and Nettles, M. (2013). Physical mechanisms for vertical-CLVD earthquakes at active volcanoes. *Journal of Geophysical Research: Solid Earth*, 118(4):1569–1586.

Sigmundsson, F., Hooper, A., Hreinsdóttir, S., Vogfjörd, K., Ófeigsson, B. G., Heimisson, E. R., Dumont, S., Parks, M., Spaans, K., Gudmundsson, G. B., Drouin, V., Árnadóttir, T., Jónsdóttir, K., Gudmundsson, M. T., Högnadóttir, T., Fridriksdóttir, H. M., Hensch, M., Einarsson, P., Magnússon, E., Samsonov, S., Brandsdóttir, B., White, R. S., Ágústsdóttir, T., Greenfield, T., Green, R. G., Hjartardóttir, A. R., Pedersen, R., Bennett, R. A., Geirsson, H., La Femina, P. C., Björnsson, H., Pálsson, F., Sturkell, E., Bean, C. J., Möllhoff, M., Braiden, A. K., and Eibl, E. P. S. (2015). Segmented lateral dyke growth in a rifting event at Bárðarbunga volcanic system, Iceland. *Nature*, 517:191–195.

Sigmundsson, F., Hreinsdóttir, S., Hooper, A., Árnadóttir, T., Pedersen, R., Roberts, M. J., Óskarsson, N., Auriac, A., Decriem, J., Einarsson, P., Geirsson, H., Hensch, M., Ófeigsson, B. G., Sturkell, E., Sveinbjörnsson, H., and Feigl, K. L. (2010). Intrusion triggering of the 2010 Eyjafjallajökull explosive eruption. *Nature*, 468:426–430.

Sigmundsson, F., Vadon, H., and Massonnet, D. (1997). Readjustment of the Krafla Spreading Segment to crustal rifting measured by satellite radar interferometry. *Geophysical Research Letters*, 24(15):1843–1846.

Simkin, T. and Howard, K. A. (1970). Caldera Collapse in the Galápagos Islands, 1968. *Science*, 169:429–437.

Sparks, R. S. J. (1997). Causes and consequences of pressurisation in lava dome eruptions. *Earth and Planetary Science Letters*, 150(3):177–189.

Sparks, R. S. J., Biggs, J., and Neuberg, J. W. (2012). Monitoring Volcanoes. *Science*, 335:1310.

Springer, D. L. (1966). P-wave coupling of underground nuclear explosions. *Bulletin of the Seismological Society of America*, 56(4):861.

Springer, D. L., Pawloski, G. A., Ricca, J. L., Rohrer, R. F., and Smith, D. K. (2002). Seismic Source Summary for All U.S. Below-Surface Nuclear Explosions. *Bulletin of the Seismological Society of America*, 92(5):1806.

Stein, R. S., King, G. C. P., and Lin, J. (1992). Change in Failure Stress on the Southern San Andreas Fault System Caused by the 1992 Magnitude = 7.4 Landers Earthquake. *Science*, 258(5086):1328–1332.

Steketee, J. A. (1958). On Volterra's dislocations in a semi-infinite elastic medium. *Canadian Journal of Physics*, 36(2):192–205.

Surono, Jousset, P., Pallister, J., Boichu, M., Buongiorno, M. F., Budisantoso, A., Costa, F., Andreastuti, S., Prata, F., Schneider, D., Clarisse, L., Humaida, H., Sumarti, S., Bignami, C., Griswold, J., Carn, S., Oppenheimer, C., and Lavigne, F. (2012). The 2010 explosive eruption of Java's Merapi volcano–A '100-year' event. *Journal of Volcanology and Geothermal Research*, 241-242(Supplement C):121–135.

Teller, E., Talley, W. K., Higgins, G. H., and Johnson, G. W. (1968). *The Constructive Uses of Nuclear Explosives*. McGraw-Hill.

Thomas, A. L. (1993). POLY3D: A three-dimensional, polygonal element, displacement discontinuity boundary element computer program with applications to fractures, faults, and cavities in the Earth's. Master's thesis, Stanford University.

Toda, S. and Stein, R. (2003). Toggling of seismicity by the 1997 Kagoshima earthquake couplet: A demonstration of time-dependent stress transfer. *Journal of Geophysical Research: Solid Earth*, 108(B12). 2567.

Trasatti, E., Cianetti, S., Giunchi, C., Bonafede, M., Agostinetti, N. P., Casu, F., and Manzo, M. (2009). Bayesian source inference of the 1993-1997 deformation at Mount Etna (Italy) by numerical solutions. *Geophysical Journal International*, 177(2):806–814.

Trasatti, E., Giunchi, C., and Bonafede, M. (2003). Effects of topography and rheological layering on ground deformation in volcanic regions. *Journal of Volcanology and Geothermal Research*, 122(1):89–110.

Tromp, J., Komattisch, D., and Liu, Q. (2008). Spectral-Element and Adjoint Methods in Seismology. *Communications in Computational Physics*, 3(1):1–32.

Ungar, A. A. (2010). *Barycentric Calculus in Euclidean and Hyperbolic Geometry A Comparative Introduction*. World Scientific Publishing Co. Pte. Ltd.

USKI (2018). North Korea's Punggye-ri Nuclear Test Site: Satellite Imagery Shows Post-Test Effects and New Activity in Alternate Tunnel Portal Areas. https://www.38north.org/2017/09/punggye091217/. Accessed: 2018-04-21.

Van Oosterom, A. and Strackee, J. (1983). The Solid Angle of a Plane Triangle. *IEEE Transactions on biomedical engineering*, BME-30(2):125–126.

Varekamp, J. C., Ouimette, A. P., Herman, S. W., Bermúdez, A., and Delpino, D. (2001). Hydrothermal element fluxes from Copahue, Argentina: A "beehive" volcano in turmoil. *Geology*, 29(11):1059–1062.

Varekamp, J. C., Ouimette, A. P., W., H. S., Flynn, K. S., Bermúdez, A., and Delpino, D. (2009). Naturally acid waters from Copahue volcano, Argentina. *Applied Geochemistry*, 24(2):208–220.

Varekamp, J. C., Zareski, J. E., Camfield, L. M., and Todd, E. (2016). *Copahue Volcano and Its Regional Magmatic Setting*, pages 81–117. Springer Berlin Heidelberg.

Velez, M. L., Euillades, P., Blanco, M., and Euillades, L. (2016). *Ground Deformation Between 2002 and 2013 from InSAR Observations*, pages 175–198. Springer Berlin Heidelberg.

Velez, M. L., Euillades, P., Caselli, A., Blanco, M., and Díaz, J. M. (2011). Deformation of Copahue volcano: Inversion of InSAR data using a genetic algorithm. *Journal of Volcanology and Geothermal Research*, 202(1):117–126.

Vincent, P., Larsen, S., Galloway, D., Laczniak, R. J., Walter, W. R., Foxall, W., and Zucca, J. J. (2003). New signatures of underground nuclear tests revealed by satellite radar interferometry. *Geophysical Research Letters*, 30(22). 2141.

Voight, B., Hidayat, D., Sacks, S., Linde, A., Chardot, L., Clarke, A., Elsworth, D., Foroozan, R., Malin, P., Mattioli, G., McWhorter, N., Shalev, E., Sparks, R. S. J., Widiwijayanti, C., and Young, S. R. (2010). Unique strainmeter observations of Vulcanian explosions, Soufrière Hills Volcano, Montserrat, July 2003. *Geophysical Research Letters*, 37(19). L00E18.

Voight, B., Sparks, R. S. J., Miller, A. D., Stewart, R. C., Hoblitt, R. P., Clarke, A., Ewart, J., Aspinall, W. P., Baptie, B., Calder, E. S., Cole, P., Druitt, T. H., Hartford, C., Herd, R. A., Jackson, P., Lejeune, A. M., Lockhart, A. B., Loughlin, S. C., Luckett, R., Lynch, L., Norton, G. E., Robertson, R., Watson, I. M., Watts, R., and Young, S. R. (1999). Magma flow instability and cyclic activity at soufriere hills volcano, montserrat, british west indies. *Science*, 283(5405):1138–1142.

Volterra, V. (1907). Sur l'équilibre des corps élastiques multiplement connexes. *Annal. Sci. de l'Ecole Norm. Supér.*, 24:401–517.

Wald, D. J. and Heaton, T. H. (1994). Spatial and Temporal Distribution of Slip for the 1992 Landers , California , Earthquake. *Bulletin of the Seismological Society of America*, 84(3):668–691.

Walter, T. R. (2008). *Facilitating Dike Intrusions into Ring-Faults*, volume 10 of *Developments in Volcanology*, pages 351–374. Elsevier.

Walter, T. R., Acocella, V., Neri, M., and Amelung, F. (2005). Feedback processes between magmatic events and flank movement at Mount Etna (Italy) during the 2002-2003 eruption. *Journal of Geophysical Research: Solid Earth*, 110(B10). B10205.

Walter, T. R., Legrand, D., Granados, H. D., Reyes, G., and Arámbula, R. (2013). Volcanic eruption monitoring by thermal image correlation: Pixel offsets show episodic dome growth of the Colima volcano. *Journal of Geophysical Research: Solid Earth*, 118(4):1408–1419.

Wang, T. and Jónsson, S. (2015). Improved SAR Amplitude Image Offset Measurements for Deriving Three-Dimensional Coseismic Displacements. *IEEE Journal of Selected Topics in Applied Earth Observations and Remote Sensing*, 8(7):3271–3278.

Wang, T., Jónsson, S., and Hanssen, R. F. (2014). Improved SAR Image Coregistration Using Pixel-Offset Series. *IEEE Geoscience and Remote Sensing Letters*, 11(9):1465–1469.

Wang, X., Chen, Q.-F., Li, J., and Wei, S. (2016). Seismic Sensor Misorientation Measurement UsingP-Wave Particle Motion: An Application to the NECsaids Array. *Seismological Research Letters*, 87(4):901–911.

Watts, A. B. and Burov, E. (2003). Lithospheric strength and its relationship to the elastic and seismogenic layer thickness. *Earth and Planetary Science Letters*, 213(1):113–131.

Wauthier, C., Cayol, V., Kervyn, F., and d'Oreye, N. (2012). Magma sources involved in the 2002 Nyiragongo eruption, as inferred from an InSAR analysis. *Journal of Geophysical Research: Solid Earth*, 117(B5). B05411.

Wegmüller, U. and Werner, C. (1997). Gamma SAR processor and interferometry software. In Guyenne, T.-D. and Danesy, D., editors, *Third ERS Symposium on Space at the service of our Environment*, volume 414 of *ESA Special Publication*, pages 1687–1692.

Wei, M. (2017). Location and source characteristics of the 2016 January 6 North Korean nuclear test constrained by InSAR. *Geophysical Journal International*, 209(2):762–769.

Wen, L. and Long, H. (2010). High-precision Location of North Korea's 2009 Nuclear Test. *Seismological Research Letters*, 81(1):26–29.

Wicks, C., Thatcher, W., and Dzurisin, D. (1998). Migration of Fluids Beneath Yellowstone Caldera Inferred from Satellite Radar Interferometry. *Science*, 282(5388):458–462.

Wicks, C. W., Dzurisin, D., Ingebritsen, S., Thatcher, W., Lu, Z., and Iverson, J. (2002). Magmatic activity beneath the quiescent Three Sisters volcanic center, central Oregon Cascade Range, USA. *Geophysical Research Letters*, 29(7).

Williams, C. A. and Wadge, G. (1998). The effects of topography on magma chamber deformation models: Application to Mt. Etna and radar interferometry. *Geophysical Research Letters*, 25(10):1549–1552.

Yang, X.-M., Davis, P. M., and Dieterich, J. H. (1988). Deformation from inflation of a dipping finite prolate spheroid in an elastic half-space as a model for volcanic stressing. *Journal of Geophysical Research: Solid Earth*, 93(B5):4249–4257.

Yılmaz, Y., Güner, Y., and Şaroğlu, F. (1998). Geology of the quaternary volcanic centres of the east Anatolia. *Journal of Volcanology and Geothermal Research*, 85(1):173–210.

Yoffe, E. H. (1960). The angular dislocation. *Philosophical Magazine*, 5(50):161–175.

Yun, S., Segall, P., and Zebker, H. (2006). Constraints on magma chamber geometry at Sierra Negra Volcano, Galápagos Islands, based on InSAR observations. *Journal of Volcanology and Geothermal Research*, 150(1):232–243.

Zhang, M. and Wen, L. (2013). High-precision location and yield of North Korea's 2013 nuclear test. *Geophysical Research Letters*, 40(12):2941–2946.

Zhao, L.-F., Xie, X.-B., Wang, W.-M., and Yao, Z.-X. (2008). Regional Seismic Characteristics of the 9 October 2006 North Korean Nuclear Test. *Bulletin of the Seismological Society of America*, 98(6):2571–2589.

Zhao, L.-F., Xie, X.-B., Wang, W.-M., and Yao, Z.-X. (2012). Yield Estimation of the 25 May 2009 North Korean Nuclear Explosion. *Bulletin of the Seismological Society of America*, 102(2):467–478.

Zhao, L.-F., Xie, X.-B., Wang, W.-M., and Yao, Z.-X. (2014). The 12 February 2013 North Korean Underground Nuclear Test. *Seismological Research Letters*, 85(1):130–134.

Zhu, L. and Ben-Zion, Y. (2013). Parametrization of general seismic potency and moment tensors for source inversion of seismic waveform data. *Geophysical Journal International*, 194(2):839–843.